博士論文

Theoretical study on ordered spin states in amorphous and chiral magnets
(アモルファスおよびカイラル磁性体における秩序スピン状態の理論研究)

Mai Hirobe (廣部 麻衣)

東北大学大学院 理学研究科 物理学専攻

令和３年

（別紙様式５）

論文内容要旨

(NO. 1)

氏　　名	HIROBE, Mai	提出年	令和３年
学位論文の 題　　目	Theoretical study on ordered spin states in amorphous and chiral magnets (アモルファスおよびカイラル磁性体における秩序スピン状態の理論研究)		

論文目次

Contents

Chapter 1

Overview

The ordered states of magnetic materials, such as ferromagnets, ferrimagnets, and anti-ferromagnets, have long been investigated. Spintronics aims to propose low-power-consumption magnetic devices by utilizing magnons, accompanied by such ordered spin states as collective excitation. In this doctoral thesis, we describe the results of theoretical studies on magnetically ordered states in amorphous and chiral magnetic materials, where recent experimental and theoretical studies have pointed out their potential applications to the low-power magnetic devices.

As for the amorphous magnets, with the renewed interest in heat and spin transport, we re-visit the magnetic spectrum of amorphous ferromagnet using modern simulation methods. We find two parabolas in the spectrum, the magnons at wavenumber 0Å^{-1} and another magnons at wavenumber 3Å^{-1}, which is similar to that observed in experiments. The physical interpretation of the second dip has long been unclear. We suggest it is due to the amorphous Umklapp scattering. The methods can easily be extended to study the spin transport properties in amorphous magnets and may pave the way to the spintronics applications.

In terms of spin transport via magnons, collective precession of magnetizations, crystalline magnetic materials have been utilized in the field of spintronics [1]. Recently, experimental attempts to utilize amorphous magnets as well have been made. However, their conclusions are controversial; The first observation has shown that amorphous magnetic materials can transport spins further than the corresponding crystal [2, 3]. Whereas following experiments cast doubt about the result [4, 5]. As a long-term goal, we aim to theoretically find if the amorphous magnets are capable of transporting spins. In the master course study, as a first step, we built a model to calculate magnon spectra in amorphous magnets. In the doctoral course study, we aim to understand the magnon spectra of first target material, amorphous ferromagnet Co_4P, by applying the model. The amorphous ferromagnet Co_4P has been extensively studied in the past [6, 7, 8], since its magnetic excitation has unique feature; The inelastic neutron scattering experiment shows a ‘roton-like’ excitation at wavenumber 3Å^{-1} [9]. Despite many efforts, the physical picture has been unclear. By utilizing numerical techniques we have developed so far [10] and recently developed [11], we have simulated thermal equilibrium spin states and magnetic spectra. The application of this method to $\mathrm{Co_4P}$ suggests the existence of magnons at wavenumber 0Å^{-1}, which follows the Bloch's law, and at wavenumber 3Å^{-1}. Our results, shown in Figs. 1.1(a)-(b), suggest its physical interpretation as amorphous Umklapp scattering [12]. The method used in the study can easily be extended to spin transport study for amorphous magnets, paving the way for theoretical studies on spintronics applications of amorphous magnets.

As for the chiral magnets, with the controlling magnetic skyrmions in mind, we theoretically study the mechanism and effects of the inter-skyrmion interactions in a two-dimensional model. We find that a deformation of a skyrmion shape makes the interaction weakly attractive. When the magneto-crystalline anisotropy is sufficiently large, the interaction becomes strongly attractive by forming a magnetic domain between two skyrmions. The creation of the magnetic domain, and thus the strength of the attraction, can be tuned in a wide range by changing the direction of an external field. The anisotropic inter-skyrmion attraction also affects the lattice structure of the skyrmion crystal phase. This model can easily be extended to the 3D systems and may pave the way for improving controlabilities of skyrmion magnetic memories.

Magnetic skyrmions, topologically stable nanometer-sized vortices, are potentially applicable as information carriers of a magnetic memory [13]. To improve the controllability of such devices, it is essential to control the trajectory of the skyrmions, i.e., by manipulating interactions between them. However, the control has been limited by the fact that only repulsive force acts between the typical isotropic skyrmions [14]. On the other hand, recent theoretical and experimental studies have revealed an attraction between skyrmions in some specific systems [15, 16, 17, 18]. Understanding the mechanism of the attractive interaction is important for academic and application purposes.

In this study, we find two mechanisms of attractive interaction, skyrmion distortion and magnetic domain formation, using a two-dimensional model [21]. We derive the analytical expression for the interaction between two skyrmions excited in the ferromagnetic (FM) phase. From the expression, we find that the distortion of skyrmions can change the sign of the interaction; The distorted skyrmions favor to be connected in the direction of elongation, to reduce the exchange interaction energy. When the easy-axes tilt from the direction of external magnetic field, i.e., due to the large magneto-crystalline anisotropy, magnetic domains are formed between two skyrmions. The energy profit from the exchange and anisotropic potential terms, from the domain area give rise to the strong attractive interaction [see Figs. 1.2(a)-(d)].

In terms of controlling the skyrmion trajectory, manipulating the strength of the attraction may be crucial. Since the skyrmion-skyrmion interactions are only visibly affect in the vicinity of the FM—skyrmion crystal (SkX) phase boundary, the strength of external magnetic field is automatically fixed at that of the critical field. Thus, it is hard to modify the attraction only via the strength of the magnetic field. We have found that, by changing the direction of the external magnetic field, the strength of the attraction can be tuned as

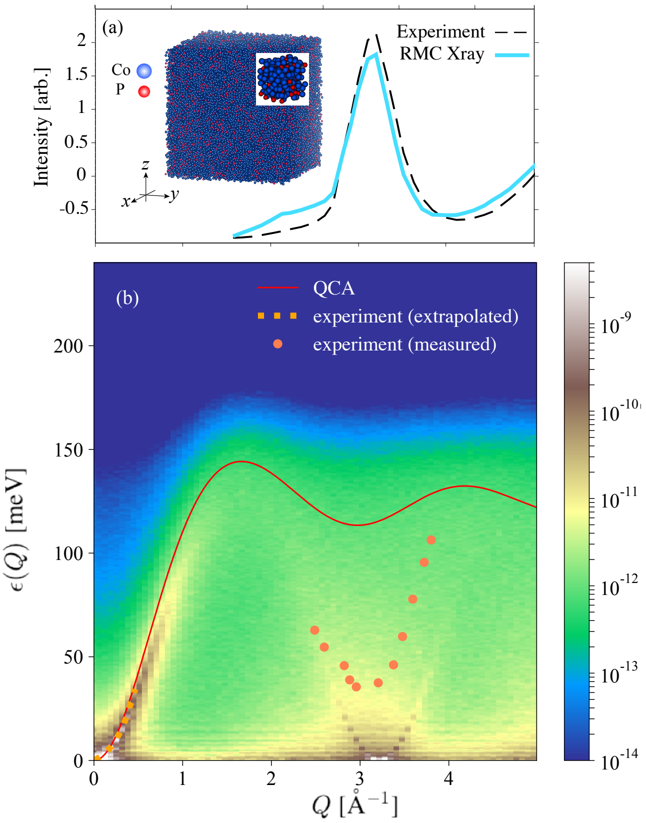

Fig.1.1 (a) Comparison of measured and calculated X-ray scattering intensity. Calculated scattering function (solid line) and measured one (dashed line) [19]. Inset is re-created amorphous atomic structure. (b) Magnetic excitation spectrum in Co_4P [20]. The spectrum from an approximation (red solid line) [8] and the experimental observation (orange dots) are overlaid for comparison [9].

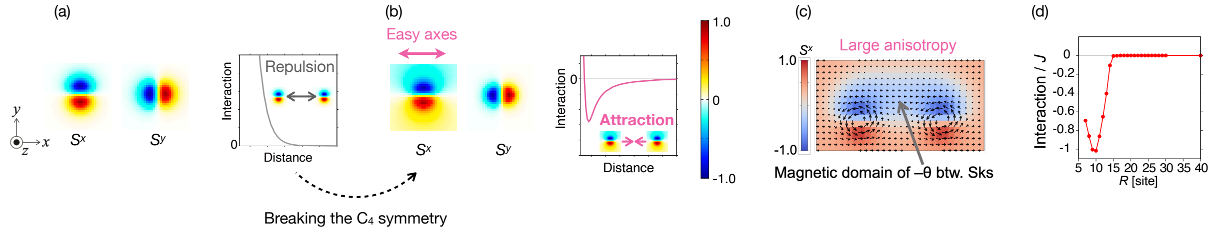

Fig.1.2 (a)-(b) Spatial spin distribution of a circular skyrmion and repulsive interaction (a) and an elongated skyrmion and attractive interaction (b). (c) x component of spin with magnetic domain between two skyrmions when magneto-crystalline anisotropy is sufficiently large. (d) Large attractive interaction, comparable to the spin exchange J, induced by the domain formation.

much as two orders of magnitude. This is because the tilted magnetic field makes the domain unstable [see Figs. 1.3(a)-(d)]. The 2D model can be easily extended to the three-dimensional systems. This work lays a theoretical foundation for improving the controllability of skyrmion magnetic memory and qubits.

We have found that the interaction between two elongated skyrmions is anisotropic; In the direction of domain formation, it is attractive. Given that the large anisotropic attraction appears, we expect that the interaction may also affect the SkX structures. Indeed, distorted triangular lattice appears, in the vicinity

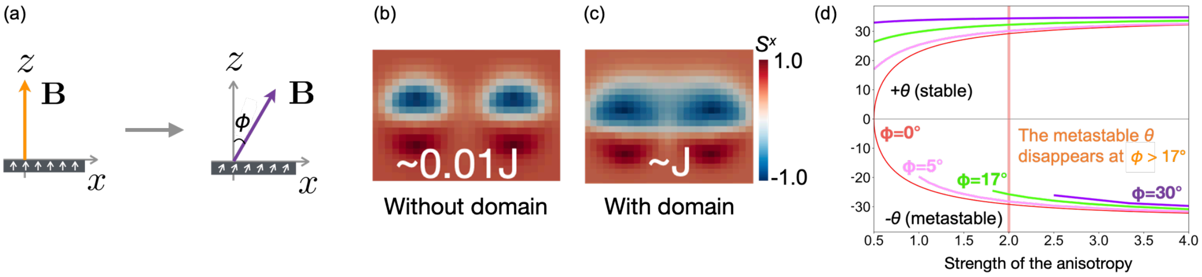

Fig.1.3 (a) External magnetic field is tilted in the x direction. (b)-(c) x component of two skyrmions without domain (b) and with domain (c) between them. (d) Controllable attractive interaction by means of the angle of the external magnetic field. It changes as much as two orders of magnitude.

of the SkX-FM phase boundary where the attractive interaction and skyrmion excitation energy may be comparable. In the resulting distorted triangular lattice, the interval of skyrmions along the direction of attraction is smaller than that of along the repulsion. Interestingly, the magnetic domain formed between the two skyrmions are expanded and connected to form domain wall skyrmion. This phase is qualitatively the same as that recently found experimentally [22]. We succeeded to find the qualitative mechanism of the domain wall skyrmions [see Figs. 1.4(a)-(c), and (e)]. In addition, we have found that the attraction expands the SkX phase in the 1D phase diagram of external magnetic field [see Fig. 1.4(d)]. In other words, the attraction expands the upper critical field of the elongated SkX phase. This new phase boundary corresponds to the field at which the energy loss of the skyrmion excitation balances with the energy profit of the attraction.

This thesis consists of 6 Chapters: In Chap. 2, we introduce the background and of the study. In Chap. 3, we explain numerical methods. Magnetically ordered states in amorphous ferromagnet Co_4P is discussed in Chap. 4, and that of the chiral magnet is shown in Chap. 5. Finally, we conclude in Chap. 6.

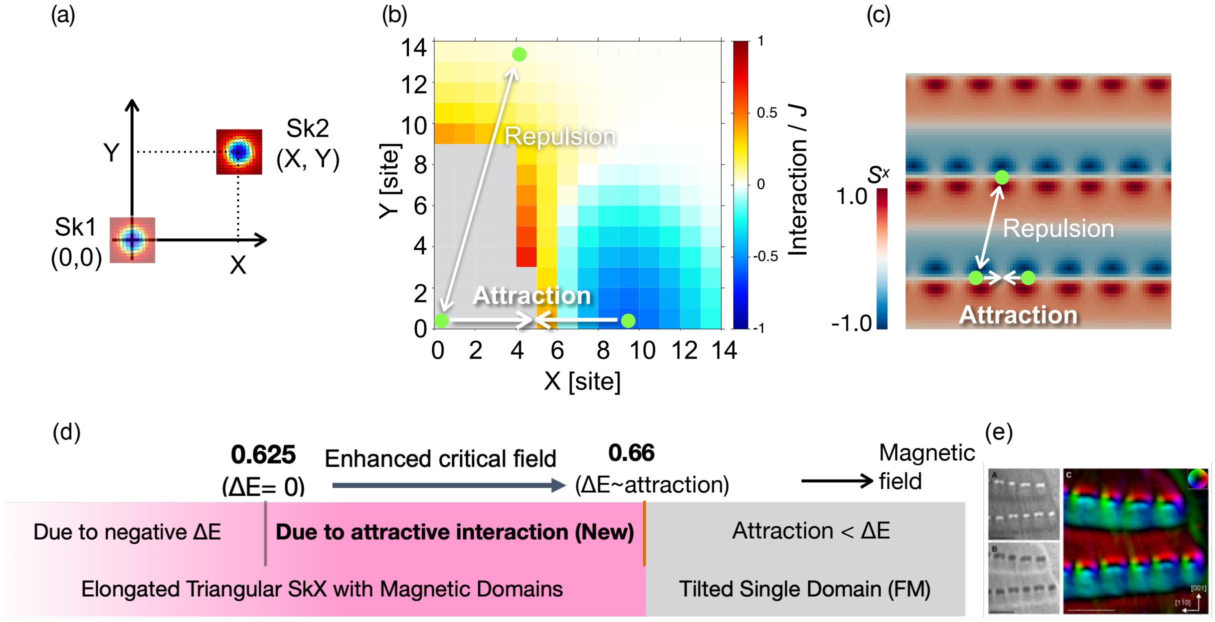

Fig.1.4 (a) Definition of the relative coordinates (X, Y) of two skyrmions, Sk1 and Sk2. (b) Inter-skyrmion interaction dependence of (X, Y). (c) Resulting skyrmion-lattice structure induced by the large anisotropic attraction. (d) 1D phase diagram in the vicinity of FM—SkX phase boundary. (e) Recent observation of the domain wall skyrmion, adopted from [22].

Chapter 2

Basics of spintronics

In this chapter, we introduce spintronics in Sec. 2.1 and related fundamental physics, which are important in this study. One of the key concept in spintronics is spin current, which is derived in ferromagnetic systems in Sec. 2.2.1. In this study, we focus on the magnon-mediated spin current, spin wave spin current. Magnons are introduced in Sec 2.2.2. The dynamics of magnons or magnetic moments are described in terms of the Landau-Lifshitz (LL) equation, which is derived in Sec. 2.2.3. Using the phenomenological damping term, Gilbert damping, the spin system can be relaxed to the energy-minimum states, as shown in Sec 2.2.4. The DM Hamiltonian, which plays key role in chiral magnetic systems, is briefly introduced in Sec 2.2.5.

2.1 Spintronics

The giant magneto-resistive effect (GMR), discovered by P. A. Grünberg and A. Fert in the late 1980s and awarded the Nobel Prize in Physics in 2007 [23, 24] was the catalyst for spintronics to gain significant attention. GMR and tunneling magnetoresistance (TMR) [25], which had already been discovered, utilize one of the ordered spin states, ferromagnets. In addition to using the ferromagnetic states, many phenomena based on the ferrimagnetic or anti-ferromagnetic spin states, especially related to the spin current (flow of the spin angular momentum), have been investigated in the past decades; A few of which include spin Hall effect [26, 27, 28], inverse spin Hall effect [29, 30, 31, 32], spin Seebeck effect [33, 34, 35, 36, 37, 38, 39, 40], spin Peltier effect [41, 42], spin pumping [43, 44, 45], magnetization oscillation induced by spin-transfer torque [46, 47, 48, 49], and current driven motions of magnetic structures such as magnetic domains and magnetic skyrmions (cf. Sec. 5.1) [50, 51, 52, 53, 54, 55]. In particular, the current driven motions of skyrmions are called skyrmion Hall effect, whereas the transverse effect is called topological Hall effect. For the spin current, see the next subsection. The main results in the field of spintronics, especially mentioned above, are summarized in Fig. 2.1(a)–(f) and Fig. 2.2.

The above works have mainly studied crystalline magnets, but recently there has also been a growing interest in spin ordered states in random arrangement of atoms; Attempts to utilize amorphous magnets in spintronics have been made for long years. Usually, however, the random atomic configurations are not utilized in terms of spin transport. This is the case in materials, i.e., CoFeB and GdFeCo. Recently, it has been pointed out that amorphous $\mathrm{Y_3Fe_5O_{12}}$ (YIG) with random atomic configuration may transport spins further than the corresponding crystal [2, 49, 56]. The schematic setup of the measurement is shown in Fig. 2.3. Their results suggest that it may be possible to transport spins in the system without perfect ordering. We note that crystal YIG is an insulator and spin are carried by spin waves, the precession of the magnetic moment, rather than electric current with spin polarization. Besides, another topic of recent interest in the field of spintronics is magnetic skyrmions, spin vortices with finite topological charge. They are nanometer-sized spin vortices with the finite topological number $\mathcal{N} = \frac{1}{4\pi}\int dr^2 \boldsymbol{n}(\boldsymbol{r})\cdot(\partial_x \boldsymbol{n}(\boldsymbol{r}) \times \partial_y \boldsymbol{n}(\boldsymbol{r}))$, where $\boldsymbol{n}(\boldsymbol{r})$ is a normalized spin vector at a position $\boldsymbol{r} = (x, y)$. The main reason why they are attracting much attention is their potential applications to magnetic memories (see Sec. 5.1 in detail) [13, 57]. They are observed for the first time in *crystal* chiral magnets in thermal equilibrium in 2009 [58, 59]. The Dzyaloshinskii-Moriya (DM) interaction [60, 61] is crucial to stabilize the skyrmion crystal (SkX) phase in the system. Experimental detection of the SkX phase are i.e., ac-susceptibility measurements [62], Fourier-space imaging by neutron small-angle scattering intensities [58], real-space imaging by Lorentz transmission electron microscopy [63], and detection of the topological Hall effect [64, 65].

2.2 Fundamental aspects in spintronics

2.2.1 Spin currents

A pure spin current, which is unaccompanied with charge, emerges in ferromagnets. Starting from a Heisenberg model

$$\mathcal{H} = -J \sum_{\langle i,j \rangle} \boldsymbol{S}_i \cdot \boldsymbol{S}_j, \tag{2.1}$$

where J is exchange constant, i, j are site indices, and angle brackets denote the nearest neighbor pairs of i and j. Each spin $\boldsymbol{S}_i$ feels an effective magnetic field

$$\boldsymbol{B}_{\text{eff}} = -\frac{J}{\mu} \sum_{\langle i,j \rangle} \boldsymbol{S}_j, \tag{2.2}$$

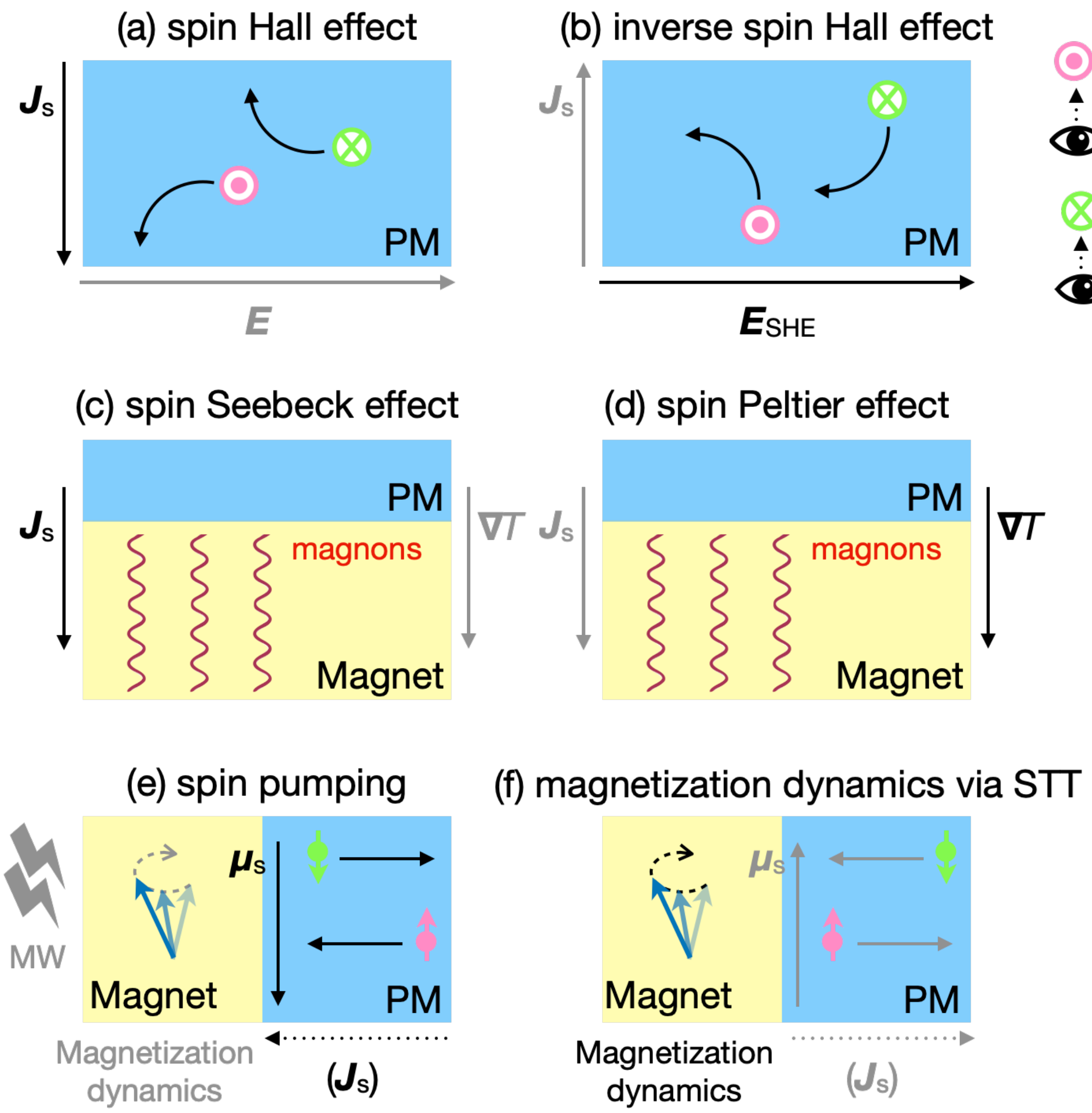

Fig.2.1 (a)-(f) Schematic images of the spin Hall effect (a), inverse spin Hall effect (b), spin Seebeck effect (c), spin Peltier effect (d), spin pumping (e), and magnetization dynamics induced by the spin transfer torque, STT (f). $\boldsymbol{J}_{\mathrm{s}}$, $\boldsymbol{J}_{\mathrm{c}}$, and PM in (a) respectively denote spin current, charge current and paramagnet. In (b), E_{SHE} represents inverse spin Hall electric field. $\boldsymbol{\nabla} T$ in (c) shows the temperature gradient. MW in (e) denotes microwave.

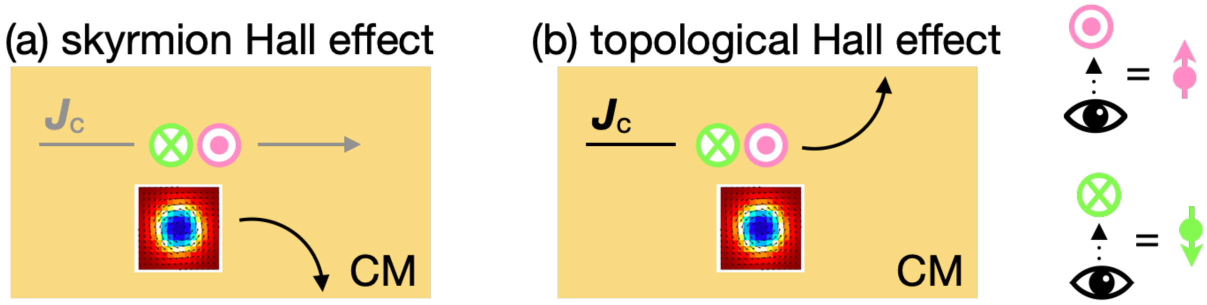

Fig.2.2 (a) Schematic image of the skyrmion Hall effect. (b) Schematic image of the topological Hall effect. CM in both panels means chiral magnet.

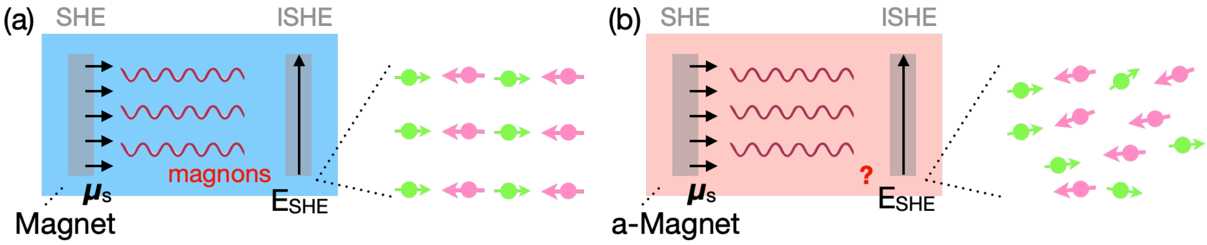

Fig.2.3 (a) Schematic experimental setup of the spin transport measurement conducted by Wesenberg et al., in the case of the crystal YIG (a) and that of the amorphous YIG, a-YIG (b). $\boldsymbol{J}_\mathrm{s}$, SHE, ISHE, and a-Magnet denote the spin accumulation, spin Hall effect, inverse spin Hall effect, and amorphous magnet, respectively.

where μ is the magnetic moment. Heisenberg equation of motion (for derivation, see Sec. 2.2.3) reads

$$\begin{aligned}\frac{d\boldsymbol{S}_i}{dt} &= \frac{1}{i\hbar}[\boldsymbol{S}_i, \mathcal{H}],\\ \frac{d\boldsymbol{S}_i}{dt} &= -\boldsymbol{S}_i \times \boldsymbol{B}_\mathrm{eff},\\ \frac{d\boldsymbol{S}_i}{dt} &= \boldsymbol{S}_i \times \frac{J}{\gamma_e}\sum_{\langle i,j\rangle} \boldsymbol{S}_j,\end{aligned} \tag{2.3}$$

where t is time and $\hbar$ is Dirac's constant, and γ_e is the gyromagnetic ratio. Let us convert above equation into a continuum equation using $\boldsymbol{S}_j \sim \boldsymbol{n}(\boldsymbol{r}_i) + \frac{1}{2}\frac{\partial^2 \boldsymbol{n}(\boldsymbol{r})}{\partial^2 \boldsymbol{r}}|_{\boldsymbol{r}=\boldsymbol{r}_i} \cdot \Delta\boldsymbol{r}^2$, where $\boldsymbol{r}_i$ and $\boldsymbol{r}_j$ are position vectors, $\boldsymbol{n}$ is the continuum spin vector, and $\Delta\boldsymbol{r} = \boldsymbol{r}_j - \boldsymbol{r}_i$. Substituting the approximation into Eq. (2.3) reads

$$\frac{d\boldsymbol{n}}{dt} = \frac{J(\Delta r)^2}{\gamma_e}\boldsymbol{n} \times \nabla^2\boldsymbol{n}, \tag{2.4}$$

where we rescaled the spin as $\gamma_e\boldsymbol{n} \to \boldsymbol{n}$. The relation $\boldsymbol{n} \times \nabla^2\boldsymbol{n} = \mathrm{div}(\boldsymbol{n} \times \nabla\boldsymbol{n})$ allows us to rewrite Eq. (2.3) in the form of

$$\frac{d\boldsymbol{n}}{dt} = J(\Delta r)^2 \mathrm{div}(\boldsymbol{n} \times \nabla\boldsymbol{n}), \tag{2.5}$$

which is equivalent to spin current equation of continuity

$$\frac{\partial\boldsymbol{n}}{\partial t} = -\frac{\gamma_e}{V}\mathrm{div}\boldsymbol{J}_s, \tag{2.6}$$

where V is the volume of the system and we defined the spin current as

$$\boldsymbol{J}_s = \boldsymbol{n} \times \nabla\boldsymbol{n}. \tag{2.7}$$

$\boldsymbol{J}_s$ is proportional to $\nabla \boldsymbol{n}$, reflecting that it is derived from exchange Hamiltonian. This form of spin current, called spin waves, can propagate in insulators and the interaction of spin waves lead to nonlinear effects [66, 67, 68, 10].

2.2.2 Magnon Hamiltonian

The Heisenberg Hamiltonian, Eq. (2.1), can be expressed in terms of magnons, quanta of the spin waves. An eigenfunction of spin operator, Θ_s^m, which has a magnitude S and z-component of m satisfies

$$\begin{aligned} S^+\Theta_s^m &= \sqrt{(S-m)(S+m+1)}\Theta_s^{m+1} \\ S^-\Theta_s^m &= \sqrt{(S+m)(S-m+1)}\Theta_s^{m-1} \\ S^z\Theta_s^m &= m\Theta_s^m \end{aligned} \tag{2.8}$$

For convenience, we will define a new operator $\hat{\mathfrak{m}}$

$$\hat{\mathfrak{m}} = S - S^z, \tag{2.9}$$

whose eigenvalue $\mathfrak{m} = S - m$ means the deviation of S^z from S. It can take values of $0, 1, 2, ..., 2S$. Focusing on the spin deviation, not spin itself, can lead us to define magnons, which are quasiparticle excitations of the spin waves. Here we use a new eigenfunction $F_s(\mathfrak{m})$, which explicitly shows the spin deviation, instead of Θ_s^m. Eq. (2.8) can be rewritten as (by substituting $m = S - \mathfrak{m}$)

$$\begin{aligned} S^+F_s(\mathfrak{m}) &= \sqrt{n(2S-\mathfrak{m}+1)}F_s(\mathfrak{m}-1) = \sqrt{2S}\sqrt{1-\frac{\mathfrak{m}-1}{2S}}\sqrt{n}F_s(\mathfrak{m}-1), \\ S^-F_s(\mathfrak{m}) &= \sqrt{(2S-\mathfrak{m})(\mathfrak{m}+1)}F_s(\mathfrak{m}+1) = \sqrt{2S}\sqrt{\mathfrak{m}+1}\sqrt{1-\frac{\mathfrak{m}}{2S}}F_s(\mathfrak{m}+1), \\ S^zF_s(\mathfrak{m}) &= (S-\mathfrak{m})F_s(\mathfrak{m}). \end{aligned} \tag{2.10}$$

Here we replaced Θ_s^{m+1} as $F_s(\mathfrak{m}-1)$ and Θ_s^{m-1} as $F_s(\mathfrak{m}+1)$. These equations are similar to those for bosons' creation and annihilation operators a, $a^\dagger$

$$\begin{aligned} aC(\mathfrak{m}) &= \sqrt{\mathfrak{m}}C(\mathfrak{m}-1), \\ a^\dagger C(\mathfrak{m}) &= \sqrt{\mathfrak{m}+1}C(\mathfrak{m}+1), \\ a^\dagger aC(\mathfrak{m}) &= \mathfrak{m}C(\mathfrak{m}), \end{aligned} \tag{2.11}$$

where $C(\mathfrak{m})$ is the $\mathfrak{m}$ particle sate with the same eigenenergy. We can show that

$$\begin{aligned} F_s(\mathfrak{m}) &= C(\mathfrak{m}), \\ S^z &= S - a^\dagger a = S - \hat{\mathfrak{m}}, \\ S^+ &= \sqrt{2S} f(S) a = \sqrt{2S}\sqrt{1-\frac{\mathfrak{m}}{2S}}a \quad (\mathfrak{m} \to \mathfrak{m}+1), \\ S^- &= \sqrt{2S} a^\dagger f(S) = \sqrt{2S} a^\dagger \sqrt{1-\frac{\mathfrak{m}}{2S}}. \end{aligned} \tag{2.12}$$

In general, bosons don't have a limited capacity of number of particles which have the same eigenenergy. However $\mathfrak{m}$ do have the upper limit of $2S$. This discrepancy can be ignored since

$$S^- F_s(2S) = 0, \tag{2.13}$$

a state which has $\mathfrak{m} \geq 2S+1$ don't have any physical meaning. Therefore we can express the spin operators in terms of the bosonic operators. These bosonic operators $a,\ a^\dagger$ are called Holstein-Primakoff operators.

The new operators satisfy following commutation relations

$$\begin{aligned} [S^+, S^-] &= 2S[f(S)a, a^\dagger f(S)], \\ &= 2S\sqrt{1-\frac{\mathfrak{m}}{2S}}(\mathfrak{m}+1)\sqrt{1-\frac{\mathfrak{m}}{2S}} - a^\dagger(1-\frac{\mathfrak{m}}{2S})a, \\ &= 2S^z, \end{aligned} \tag{2.14}$$

and

$$\begin{aligned} [S^+, S^z] &= -[\sqrt{2S}f(S)a, a^\dagger a], \\ &= -\sqrt{2S}f(S)[a, a^\dagger]a, \\ &= -S^+. \end{aligned} \tag{2.15}$$

In the following, we will derive the spin wave energy using Holstein-Primakoff operators. Substituting Eq. (2.12) into Eq. (2.1), expanding up to the lowest order of $\mathfrak{m}/2S$, $S^z = S - \hat{\mathfrak{m}},\ S^+ = \sqrt{2S}a,\ S^- = \sqrt{2S}a^\dagger$, and keeping only second-order terms of a, $a^\dagger$ leads to

$$\mathcal{H} = 2JS \sum_{\langle i,j \rangle} (a_i^\dagger a_i - a_i^\dagger a_j), \tag{2.16}$$

where we used the symmetry with respect to the indices ($i \neq j$):

$$\sum_{\langle i,j\rangle} a_i^\dagger a_i = \sum_{\langle i,j\rangle} a_j^\dagger a_j, \ \sum_{\langle i,j\rangle} a_i^\dagger a_j = \sum_{\langle i,j\rangle} a_i a_j^\dagger. \tag{2.17}$$

In order to diagonalize Eq. (2.16), we Fourier transform a and $a^\dagger$.

$$a_i = \frac{1}{\sqrt{N}} \sum_{\boldsymbol{Q}} e^{i\boldsymbol{Q}\cdot\boldsymbol{r}_i} a_{\boldsymbol{Q}}, \ a_i^\dagger = \frac{1}{\sqrt{N}} \sum_{\boldsymbol{Q}} e^{-i\boldsymbol{Q}\cdot\boldsymbol{r}_i} a_{\boldsymbol{Q}}^\dagger, \tag{2.18}$$

where N is the total number of spins. Substituting Eq. (2.18) into Eq. (2.16) obtains

$$\begin{aligned} \mathcal{H} &= 2JS \sum_{\boldsymbol{Q}} \sum_{\boldsymbol{\rho}} (1 - e^{-i\boldsymbol{Q}\cdot\boldsymbol{\rho}}) a_{\boldsymbol{Q}}^\dagger a_{\boldsymbol{Q}}, \\ &= 2zJS \sum_{\boldsymbol{Q}} (1-\gamma_{\boldsymbol{Q}}) a_{\boldsymbol{Q}}^\dagger a_{\boldsymbol{Q}} \ \left(\gamma_{\boldsymbol{Q}} = \frac{1}{z} \sum_{\boldsymbol{\rho}} e^{-i\boldsymbol{Q}\cdot\boldsymbol{\rho}}\right), \\ &= \sum_{\boldsymbol{Q}} \epsilon_{\boldsymbol{Q}} \mathfrak{m}_{\boldsymbol{Q}}, \end{aligned} \tag{2.19}$$

where $\boldsymbol{\rho}$ is the relative position between $\boldsymbol{r}_i$ and its neighbors, and z is the number of neighbors. Therefore a magnon of wavenumber $\boldsymbol{Q}$ has an eigenenergy

$$\epsilon_{\boldsymbol{Q}} = 2zJS(1-\gamma_{\boldsymbol{Q}}). \tag{2.20}$$

In the case of one-dimensional lattice,

$$\epsilon_Q = 2zJS(1-\cos Qa), \tag{2.21}$$

where a is the lattice parameter.

2.2.3 Derivation of the Landau-Lifshitz equation in ferromagnets

We derive the Lagrangian $\mathcal{L}_{\text{ex}}$ and the LL equation Eq. (2.3) in ferromagnets. The local magnetic moment per electron spin is $-g\mu_B S = -g\mu_B/2$, where g is electron's g-factor and μ_B is Bohr magneton. Magnetization M, magnetic moment per unit volume, is $M = -Ng\mu_B S/V$, where V is the sample volume. We treat spins as classical vectors with $|\boldsymbol{S}| = S$, and its direction, denoted two angles θ and ϕ, are the only variables,

$$\boldsymbol{n}(\boldsymbol{r}) = S \begin{pmatrix} \sin\theta(\boldsymbol{r})\cos\phi(\boldsymbol{r}) \\ \sin\theta(\boldsymbol{r})\sin\phi(\boldsymbol{r}) \\ \cos\theta(\boldsymbol{r}) \end{pmatrix}. \tag{2.22}$$

Using $|\Delta\boldsymbol{n}(\boldsymbol{r})| = S(\Delta\theta + \sin\theta\Delta\phi)$, the Heisenberg Hamiltonian becomes

$$\mathcal{H} = \frac{J}{2}\sum_{r}\{\nabla\boldsymbol{n}(\boldsymbol{r})\}^2 = \frac{J}{2}\int\frac{d^3r}{a^3}S(\Delta\theta + \sin\theta\Delta\phi). \tag{2.23}$$

Due to the commutation relation of spin operators, $[\hat{S}_i, \hat{S}_j] = i\hbar\epsilon_{ijk}\hat{S}_k$, we use path integral to get $\mathcal{L}_{\text{ex}}$. To this end we use the relation between $\mathcal{H}$ and action $\mathscr{S}$,

$$\langle\boldsymbol{n}_f|\, e^{-i\mathcal{H}(t_f - t_i)/\hbar}\, |\boldsymbol{n}_i\rangle = \int \mathcal{D}\boldsymbol{n}(t)\; e^{iS[\boldsymbol{n}(t)]/\hbar}, \tag{2.24}$$

$$\mathscr{S} = \int dt\mathcal{L}[\boldsymbol{n}(t)]. \tag{2.25}$$

We get

$$\mathcal{L}_{\text{ex}} = \int\frac{d^3r}{a^3}\hbar S\dot{\phi}(\cos\theta - 1) - \mathcal{H}. \tag{2.26}$$

The Euler-Lagrange equation of motion reads

$$\frac{\delta\mathcal{L}_{\text{ex}}}{\delta\theta} = \frac{d}{dt}\left(\frac{\partial\mathcal{L}_{\text{ex}}}{\partial\dot{\theta}}\right) - \frac{\partial\mathcal{L}_{\text{ex}}}{\partial\theta}, \tag{2.27}$$

$$\frac{\delta\mathcal{L}_{\text{ex}}}{\delta\phi} = \frac{d}{dt}\left(\frac{\partial\mathcal{L}_{\text{ex}}}{\partial\dot{\phi}}\right) - \frac{\partial\mathcal{L}_{\text{ex}}}{\partial\phi}. \tag{2.28}$$

So we obtain

$$\hbar S\sin\theta\dot{\phi} = -\frac{\delta\mathcal{H}}{\delta\theta}, \tag{2.29}$$

$$\hbar S\sin\theta\dot{\theta} = \frac{\delta\mathcal{H}}{\delta\phi}. \tag{2.30}$$

In terms of $\boldsymbol{n}$,

$$
\begin{aligned}
\frac{d\boldsymbol{n}}{dt} = S\dot{\theta}\begin{pmatrix}\sin\theta(\boldsymbol{r})\cos\phi(\boldsymbol{r})\\ \sin\theta(\boldsymbol{r})\sin\phi(\boldsymbol{r})\\ \cos\theta(\boldsymbol{r})\end{pmatrix} + S\dot{\phi}\begin{pmatrix}\sin\theta(\boldsymbol{r})\cos\phi(\boldsymbol{r})\\ \sin\theta(\boldsymbol{r})\sin\phi(\boldsymbol{r})\\ \cos\theta(\boldsymbol{r})\end{pmatrix} \\
=&\frac{1}{\hbar\sin\theta}\frac{\delta\mathcal{H}}{\delta\phi} - \frac{1}{\hbar}\frac{\delta\mathcal{H}}{\delta\theta} \\
=&\frac{S}{\hbar}\left[\boldsymbol{e}_\theta\left(\boldsymbol{e}_\phi\cdot\frac{\delta\mathcal{H}}{\delta\boldsymbol{n}}\right) - \boldsymbol{e}_\phi\left(\boldsymbol{e}_\theta\cdot\frac{\delta\mathcal{H}}{\delta\boldsymbol{n}}\right)\right]
\end{aligned}
\tag{2.31}
$$

Here we used the relations regarding general function $F(\theta,\phi)$,

$$\frac{\delta F}{\delta\theta} = S\left(\boldsymbol{e}_\theta\cdot\frac{\delta F}{\delta\boldsymbol{n}}\right), \tag{2.32}$$

$$\frac{\delta F}{\delta\phi} = S\sin\theta\left(\boldsymbol{e}_\phi\cdot\frac{\delta F}{\delta\boldsymbol{n}}\right). \tag{2.33}$$

In addition, using the vector formula, $\boldsymbol{A}\times\boldsymbol{B}\times\boldsymbol{C} = (\boldsymbol{A}\cdot\boldsymbol{C})\boldsymbol{B} - (\boldsymbol{A}\cdot\boldsymbol{B})\boldsymbol{C}$, we finally get

$$\hbar\frac{d\boldsymbol{n}}{dt} = S\left(\frac{\delta\mathcal{H}}{\delta\boldsymbol{n}}\times(\boldsymbol{e}_\theta\times\boldsymbol{e}_\phi)\right) = -\boldsymbol{n}\times\frac{\delta\mathcal{H}}{\delta\boldsymbol{n}}. \tag{2.34}$$

The right hand side acts as a torque and is called effective magnetic field, $\boldsymbol{H}_{\text{eff}} \equiv \frac{\delta\mathcal{H}}{\delta\boldsymbol{n}}$. This is the LL equation of motion. We note that the expression $\boldsymbol{H}_{\text{eff}} \equiv \frac{\delta\mathcal{H}}{\delta\boldsymbol{n}}$ also holds when $\mathcal{H}$ includes other terms such as anisotropy and Zeeman interactions [69, 70].

2.2.4 Landau-Lifshitz-Gilbert equation in ferromagnets

The equation Eq. (2.34) for $\boldsymbol{n}$ (in this context $\boldsymbol{n}$ is magnetization rather than spin per electron) can be rewritten as

$$\frac{d\boldsymbol{n}}{dt} = -\gamma_{\text{e}}\boldsymbol{n}\times\mathbf{B}. \tag{2.35}$$

Let us solve the equation when the magnetic field $\mathbf{B}$ is along the z-direction. Each component (x, y, and z) of the LL equation of motion for the magnetization $\boldsymbol{n}$ can be written as

$$\frac{dn_x}{dt} = -\gamma_{\text{e}}B_z n_y \tag{2.36}$$

$$\frac{dn_y}{dt} = \gamma_{\text{e}}B_z n_x \tag{2.37}$$

$$\frac{dn_z}{dt} = 0 \tag{2.38}$$

Differentiating Eq.(2.36) and substituting Eq.(2.37), $\frac{d^2n_x}{dt^2}$ is

$$\frac{d^2n_x}{dt^2} = -\gamma_{\mathrm{e}}B_z\frac{n_y}{dt} = -\gamma_{\mathrm{e}}^2B_z^2n_x \tag{2.39}$$

In a similar fashion, $\frac{d^2n_y}{dt^2}$ is

$$\frac{d^2n_y}{dt^2} = \gamma_{\mathrm{e}}B_z\frac{n_x}{dt} = -\gamma_{\mathrm{e}}^2B_z^2n_y \tag{2.40}$$

Eq.(2.39) and eq(2.40) are equations of motion for simple harmonic motion. Thus one can obtain their general solutions as follows

$$n_x(t) = A_x\mathrm{cos}(\omega t + \delta_x), \tag{2.41}$$

$$n_y(t) = A_y\mathrm{cos}(\omega t + \delta_y), \tag{2.42}$$

where A_x, A_y, δ_x, and δ_y are arbitrary constants (real numbers), and $\omega \equiv \gamma_{\mathrm{e}}B_z$. From Eq.(2.38), $\mathfrak{m}_z$ is constant. The LL equation of motion assumes that magnitude of magnetization $|\boldsymbol{n}| \equiv n_{\mathrm{s}}$ is constant. Using the relation

$$n_x^2 + n_y^2 + n_z^2 = n_s^2 \tag{2.43}$$

and assuming initial conditions : $n_x = A_x = A_y, n_y = 0$ at $t = 0$, one can obtain a particular solution as

$$n_x(t) = A_x\ \mathrm{cos}\omega t = n_{\mathrm{s}}\mathrm{sin}\theta\mathrm{cos}\omega t \tag{2.44}$$

$$n_y(t) = A_y\ \mathrm{sin}\omega t = n_{\mathrm{s}}\mathrm{sin}\theta\mathrm{sin}\omega t \tag{2.45}$$

$$n_z(t) = n_{\mathrm{s}}\mathrm{cos}\theta \tag{2.46}$$

where θ is the angle between z-axis and magnetization. The result means magnetization rotates around the direction of magnetic field **B** constantly. It has a frequency of $\omega = \gamma_{\mathrm{e}}B_z$. This motion is illustrated in figure 2.4.

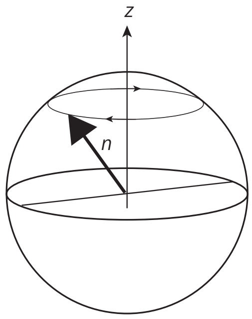

Fig.2.4 Schematic image of the solution A

The damping effect of magnetization can be introduced phenomenologically by so-called Gilbert-term and the equation of motion becomes the Landau-Lifshitz-Gilbert (LLG) equation,

$$\frac{d\boldsymbol{n}}{dt} = -\gamma_{\mathrm{e}}\boldsymbol{n} \times \mathbf{B} + \alpha\boldsymbol{n} \times \frac{d\boldsymbol{n}}{dt}, \tag{2.47}$$

where α is the Gilbert-damping constant. Each component (x, y, and z) of the Eq.(2.54) when $\mathbf{B} = B_z\mathbf{e}_z$ is

$$\frac{dn_x}{dt} = -\gamma_{\mathrm{e}}n_yB_z + \alpha\Big(n_y\frac{dn_z}{dt} - n_z\frac{dn_y}{dt}\Big) \tag{2.48}$$

$$\frac{dn_y}{dt} = \gamma_{\mathrm{e}}n_xB_z + \alpha\Big(n_z\frac{dn_x}{dt} - n_x\frac{dn_z}{dt}\Big) \tag{2.49}$$

$$\frac{dn_z}{dt} = \alpha\Big(n_x\frac{dn_y}{dt} - n_y\frac{dn_x}{dt}\Big) \tag{2.50}$$

In order to solve these equations analytically, let's keep the leading order terms in the deviation of $\boldsymbol{n}$ from the z-direction (n_x, n_y). These are the first-order of n_x and n_y. Then Eq.(2.48) - Eq.(2.50) can be written as

$$\frac{dn_x}{dt} = -\gamma_{\mathrm{e}}n_yB_z + \alpha\Big(n_y\frac{dn_z}{dt} - n_z\frac{dn_y}{dt}\Big) \tag{2.51}$$

$$\frac{dn_y}{dt} = \gamma_{\mathrm{e}}n_xB_z + \alpha\Big(n_z\frac{dn_x}{dt} - n_x\frac{dn_z}{dt}\Big) \tag{2.52}$$

$$\frac{dn_z}{dt} = 0 \tag{2.53}$$

Differentiating Eq.(2.51) and Eq.(2.52) under $\frac{dn_z}{dt} = 0$,

$$\frac{d^2n_x}{dt^2} = -\gamma_{\mathrm{e}}\frac{dn_y}{dt}B_z - \alpha n_z\frac{d^2n_y}{dt^2} \tag{2.54}$$

$$\frac{d^2n_y}{dt^2} = \gamma_{\mathrm{e}}\frac{dn_x}{dt}B_z + \alpha n_z\frac{d^2n_x}{dt^2} \tag{2.55}$$

Eq.(2.54) and Eq.(2.55) have the same structures. Substituting Eq.(2.52) and Eq.(2.55) to Eq.(2.54) (Eq.(2.51) and Eq.(2.54) to Eq.(2.55)),

$$(1+\alpha^2 n_z^2)\frac{d^2 n_x}{dt^2} + 2\alpha\gamma_{\mathrm{e}} n_z B_z \frac{dn_x}{dt} + \gamma_{\mathrm{e}}^2 B_z^2 n_x = 0 \tag{2.56}$$

$$(1+\alpha^2 n_z^2)\frac{d^2 n_y}{dt^2} + 2\alpha\gamma_{\mathrm{e}} n_z B_z \frac{dn_y}{dt} + \gamma_{\mathrm{e}}^2 B_z^2 n_y = 0 \tag{2.57}$$

Using

$$\gamma_{\mathrm{eff}} = \frac{\alpha\gamma_{\mathrm{e}} n_z B_z}{1+\alpha^2 n_z^2}, \tag{2.58}$$

$$\Omega_{\mathrm{eff}}^2 = \frac{\gamma_{\mathrm{e}}^2 B_z^2}{1+\alpha^2 n_z^2}, \tag{2.59}$$

Eq.(2.56) and Eq.(2.57) can be written as

$$\frac{d^2 n_x}{dt^2} + 2\gamma_{\mathrm{eff}} \frac{dn_x}{dt} + \Omega_{\mathrm{eff}}^2 n_x = 0 \tag{2.60}$$

$$\frac{d^2 n_y}{dt^2} + 2\gamma_{\mathrm{eff}} \frac{dn_y}{dt} + \Omega_{\mathrm{eff}}^2 n_y = 0 \tag{2.61}$$

Eq.(2.60) and Eq.(2.61) are the differential equation of forced oscillation, and in this case $\gamma_{\mathrm{eff}}^2 - \Omega_{\mathrm{eff}}^2 = \frac{-\gamma_{\mathrm{e}}^2 B_z^2}{(1+\alpha^2 n_z^2)^2} < 0$. Therefore the general solutions are

$$n_x(t) = A_x e^{-\gamma_{\mathrm{eff}} t} \cos(\omega t + \delta_x) \tag{2.62}$$

$$n_y(t) = A_y e^{-\gamma_{\mathrm{eff}} t} \cos(\omega t + \delta_y) \tag{2.63}$$

where $\omega = \sqrt{\Omega_{\mathrm{eff}}^2 - \gamma_{\mathrm{eff}}^2}$, and A_x, A_y, δ_x, and δ_y are constants. Note that the relation

$$n_x^2 + n_y^2 + n_z^2 = n_s^2 \tag{2.64}$$

is still valid. The result means magnetization rotates around the direction of magnetic field $\mathbf{B} // \mathbf{e}_z$ with a frequency of $\omega = \frac{\gamma_{\mathrm{e}}^2 B_z^2}{(1+\alpha^2 n_z^2)^2}$, but the precession angle decreases exponentially with time. It relaxes to align the z-direction after a while. This motion is illustrated in figure 2.5. Figure 2.6 shows one of the possible solutions of $n_x(t)$ in the case of $A_x = 1$.

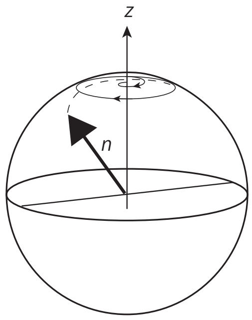

Fig.2.5 Schematic image of the solution B

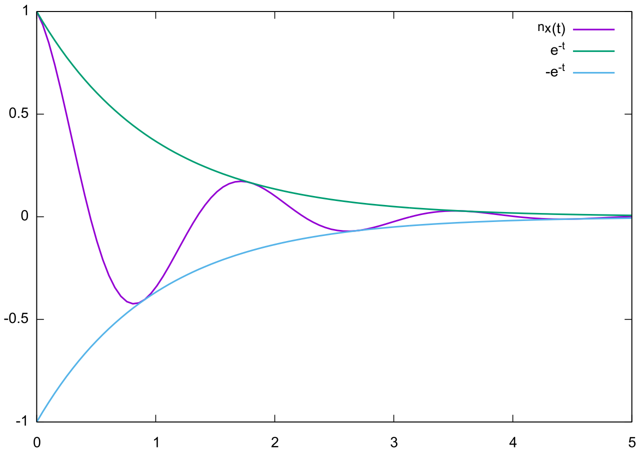

Fig.2.6 A plot of $n_x(\gamma_{\text{eff}} = 1, \omega = 3.5, A_x = 1, \delta_x = 0)$

The equation of motion of spins can be obtained in a different way, using the concept of the effective magnetic field. Let us find it by taking the functional derivative of the energy in the system (exchange, anisotropy with coefficient $\mathcal{K}$, and Zeeman terms),

$$F[\boldsymbol{n}] = \int d^3 r \mu_0 \Big(\frac{A}{2} n_s^2 \sum_{i=1,2,3} \frac{\partial \boldsymbol{n}}{\partial x_i} \cdot \frac{\partial \boldsymbol{n}}{\partial x_i} - \frac{\mathcal{K}}{2} n_s^2 n_z^2 - n_s \boldsymbol{n} \cdot \boldsymbol{B}\Big), \tag{2.65}$$

by

$$\mathbf{B}_{\text{eff}}(\mathbf{r}) = -\frac{1}{\mu_0 n_s} \frac{\delta F[\boldsymbol{n}]}{\delta \boldsymbol{n}(\mathbf{r})}. \tag{2.66}$$

Note that now $\boldsymbol{n}$ is a unit vector. When we increment $\boldsymbol{n}$ by $\delta \mathbf{n}$ to get $\boldsymbol{n} + \delta \boldsymbol{n}$, $F[\boldsymbol{n}]$ also increases to get $F[\boldsymbol{n} + \delta \boldsymbol{n}]$ as follows

$$F[\mathbf{n} + \delta \mathbf{n}] = \int d^3 r \mu_0 \Big(\frac{A}{2} n_s^2 \sum_{i=1,2,3} \partial_i (\mathbf{n} + \delta \mathbf{n}) \cdot \partial_i (\mathbf{n} + \delta \mathbf{n}) - \frac{\mathcal{K}}{2} n_s^2 (n_z + \delta n_z)^2 - n_s (\mathbf{n} + \delta \mathbf{n}) \cdot \boldsymbol{B}\Big). \tag{2.67}$$

The difference between $F[\mathbf{n} + \delta \mathbf{n}]$ and $F[\boldsymbol{n}]$ up to first-order of $\delta \mathbf{n}$ is

$$\begin{aligned} dF[\boldsymbol{n}] = F[\mathbf{n} + \delta \mathbf{n}] - F[\boldsymbol{n}] &= \int d^3 r \mu_0 \Big(A n_s^2 \sum_{i=1,2,3} \partial_i \boldsymbol{n} \cdot \partial_i \delta \mathbf{n} - \mathcal{K} n_s^2 n_z \delta n_z - n_s \delta \mathbf{n} \cdot \boldsymbol{B}\Big) &(2.68)\\ &= \int d^3 r \mu_0 \Big(A n_s^2 \sum_{i=1,2,3} \sum_{j=1,2,3} \partial_i n_j \partial_i \delta n_j - \mathcal{K} n_s^2 n_z \delta n_z - n_s \delta \mathbf{n} \cdot \boldsymbol{B}\Big) &(2.69)\\ &= \int d^3 r \mu_0 \Big(-A n_s^2 \sum_{i=1,2,3} \sum_{j=1,2,3} \partial_i^2 n_j \delta n_j - \mathcal{K} n_s^2 n_z \delta n_z - n_s \delta \mathbf{n} \cdot \boldsymbol{B}\Big) &(2.70)\\ &= \int d^3 r \mu_0 \Big(-A n_s^2 \nabla^2 \boldsymbol{n} - \mathcal{K} n_s^2 n_z \mathbf{e}_z - n_s \boldsymbol{B}\Big) \cdot \delta \mathbf{n}. &(2.71) \end{aligned}$$

From the definition of the functional derivative,

$$dF[\mathbf{y}(\mathbf{r})] = \int d^3r \frac{\delta F[\mathbf{y}(\mathbf{r})]}{\delta \mathbf{y}(\mathbf{r})} \cdot \delta \mathbf{y}(\mathbf{r}), \tag{2.72}$$

the effective field $\mathbf{B}_{\text{eff}}$ is given by

$$\mathbf{B}_{\text{eff}} = -\frac{1}{\mu_0 n_s} \frac{\delta F[\boldsymbol{n}]}{\delta \boldsymbol{n}(\mathbf{r})} = -\frac{1}{\mu_0 n_s} \Big(-A n_s^2 \nabla^2 \boldsymbol{n} - \mathcal{K} n_s^2 n_z \mathbf{e}_z - n_s \boldsymbol{B} \Big) = A n_s \nabla^2 \boldsymbol{n} + \mathcal{K} n_s n_z \mathbf{e}_z + \boldsymbol{B}. \tag{2.73}$$

Using above result, we can find the corresponding LL equation as

$$\frac{d\boldsymbol{n}}{dt} = -\gamma_{\text{e}} \boldsymbol{n} \times \mathbf{B}_{\text{eff}}, \tag{2.74}$$

where $\gamma_{\text{e}} > 0$ is assumed. Under the particular energy functional,

$$\frac{d\boldsymbol{n}}{dt} = -\gamma_{\text{e}} \boldsymbol{n} \times (A n_s \nabla^2 \boldsymbol{n} + \mathcal{K} n_s n_z \mathbf{e}_z + \boldsymbol{B}). \tag{2.75}$$

2.2.5 Dzyaloshinskii-Moriya interaction

In chiral magnets, DM interaction [60, 61] appears due to the inversion symmetry breaking. In the continuum limit, it looks like $\mathcal{H}_{\text{DM}} = -Da\boldsymbol{n} \cdot (\nabla \times \boldsymbol{n})$, with coefficient D. Indeed $\mathcal{H}_{\text{DM}}$ is anti-symmetric under the transform $\boldsymbol{r} \to -\boldsymbol{r}$. It is derived from the second-order perturbation of the spin-orbit coupling and exchange interaction, with respect to the crystal field. The spin-orbit coupling, $\mathcal{H}_{\text{SOI}} \propto Z/{r_{\text{e}}}^3 \boldsymbol{l} \cdot \boldsymbol{s}$, is the interaction between orbital angular momentum $\boldsymbol{l}$ and spin angular momentum $\boldsymbol{s}$ of electrons. Here Z is the atomic number and r_{e} is the distance between electron and the nucleus. It becomes pronounced for heavy elements where Z is large, such as platinum, gold, or lead.

Chapter 3

Methods

In this chapter, we introduce numerical methods used in the study. The atomistic spin dynamics (ASD), simulating spins per atom with the LLG equation, is the key concept used in the study of amorphous magnets. It is introduced in Sec. 3.1. To solve the LLG equation, we use Runge-Kutta method introduced in Sec. 3.2. When simulating the skyrmion configurations, we employ the Monte Carlo (MC) methods. The Metropolis MC is explained in Sec. 3.3 and exchange MC is in Sec. 3.4.

3.1 Atomistic spin dynamics

Atomistic spin models treat spins as they are distributing at each atoms. In short, this model separates electrons (fast variables) and atomistic spins (slow variables) like a spin system version of Born-Oppenheimer approximation [71, 72]. This model can be applied even when the macro-spin model (assuming there is only single domain in the system) is no longer valid. The dynamics of spins can be solved using the coupled LLG equation [11];

$$\frac{\partial \boldsymbol{S}_i}{\partial t} = -\gamma_e \boldsymbol{S}_i \times \boldsymbol{B}_{\mathrm{eff}} - \gamma_e \frac{\alpha}{S}[\boldsymbol{S}_i \times [\boldsymbol{S}_i \times \boldsymbol{B}_{\mathrm{eff}}]], \tag{3.1}$$

where $\boldsymbol{S}_i$ is a unit vector and $\boldsymbol{B}_{\mathrm{eff}} = -\frac{\partial \mathcal{H}}{\partial \boldsymbol{S}_i}$. To include temperature to the system, random torque term $-\gamma_{\mathrm{e}} \boldsymbol{S}_i \times \boldsymbol{g}_i$ is added to above equation,

$$\frac{\partial \boldsymbol{S}_i}{\partial t} = -\gamma_e \boldsymbol{S}_i \times (\boldsymbol{B}_{\mathrm{eff}} + \boldsymbol{g}_i) - \gamma_e \frac{\alpha}{S}[\boldsymbol{S}_i \times [\boldsymbol{S}_i \times (\boldsymbol{B}_{\mathrm{eff}} + \boldsymbol{g}_i)]], \tag{3.2}$$

where $\boldsymbol{g}_i$ represents a random torque. When we consider the system is classical, $\boldsymbol{g}_i$ doesn't affect the time spin-spin correlation in the system, and all the possible states are occupied following the equipartition law (see also Sec. 4.3). On the other hand, when we consider the system is quantum or semi-classical, we use the random force $\boldsymbol{g}(\boldsymbol{r},t)$ whose power spectrum follows quantum fluctuation-dissipation theorem [73, 11],

$$\langle g_a(\boldsymbol{r}_i,t)\rangle = 0;\ \langle g_a(\boldsymbol{r}_i)g_b(\boldsymbol{r}_j)\rangle_\omega = \delta_{ij}\delta_{ab}\frac{2\alpha}{\gamma_{\mathrm{e}}\mu\beta}\frac{\hbar\omega}{\mathrm{e}^{\beta\hbar\omega}-1}, \tag{3.3}$$

where a,b denote Cartesian coordinates, ω stands for the frequency, $\beta=(k_{\mathrm{B}}T)^{-1}$ is the inverse temperature with k_{B} is Boltzmann constant and T is temperature, $\langle\cdots\rangle$ denotes a time average, and $\langle\cdots\rangle_\omega$ shows a statistical average in the fourier space.

3.2 Solving the Landau-Lifshitz-Gilbert equation

In this section, we show the way of numerical integration of the LLG equation, Eq. (3.1). LLG equation is utilized in both studies of amorphous and chiral magnets. The specific definitions of the equations are respectively in Sec. 4.7 and Sec. 5.4.2. In the following, we show two main ways of solving the differential equation which can be applied to the LLG equations.

When we would like to numerically solve the the equation of motion only at 0 Kelvin (K), we can use both Heun and Runge-Kutta method. If we are to integrate an ordinary differential equation $\dot{y}=\frac{dy}{dx}=f(x,y)$ up to the second-order, we can use Heun method, in other words, Second-order Runge-Kutta method. The $(n+1)$-th variable y_{n+1} (where $n=\frac{\text{final value}\ -\ \text{initial value}}{h}$) is estimated to be

$$k_1 = hf(x_n,y_n), \tag{3.4}$$

$$k_2 = hf(x_n+h,y_n+k_1), \tag{3.5}$$

$$y_{n+1} = y_n+\frac{1}{2}(k_1+k_2)+\mathcal{O}(h^3), \tag{3.6}$$

or

$$k_1 = hf(x_n,y_n), \tag{3.7}$$

$$k_2 = hf(x_n+\frac{1}{2}h,y_n+\frac{1}{2}k_1), \tag{3.8}$$

$$y_{n+1} = y_n+k_2+\mathcal{O}(h^3). \tag{3.9}$$

The errors are of the order of $\mathcal{O}(h^3)$. Heun method evaluates y_{n+1} by taking average of the derivatives at (x_n,y_n) and (x_{n+1},y_{n+1}). The derivative at (x_{n+1},y_{n+1}) can be estimated using Euler method $y_{n+1}=y_n+hf(x_n,y_n)$ at (x_{n+1},y_{n+1}). It computes second-order derivatives f_{xx},f_{yy}, included in k_2 in Eq. (3.8) by utilizing Taylor expansion. Considering the derivative at two different points enables to achieve the second order accuracy:

$$
\begin{aligned}
y_{n+1} &= y_n + \frac{1}{2}(k_1 + k_2) \\
&= y_n + \frac{h}{2}\{f(x_n, y_n) + f(x_n + h, y_n + hf(x_n, y_n))\} \\
&= y_n + \frac{dy}{dx}h + \frac{1}{2}\frac{d^2y}{d^2x}h^2 + \mathcal{O}(h^3). \qquad (3.10)
\end{aligned}
$$

We note that we can further enhance the approximation precision using Fourth-order Runge-Kutta method. The derivatives are evaluated four times as

$$k_1 = hf(x_n, y_n), \tag{3.11}$$

$$k_2 = hf(x_n + \frac{1}{2}h, y_n + \frac{1}{2}k_1), \tag{3.12}$$

$$k_3 = hf(x_n + \frac{1}{2}h, y_n + \frac{1}{2}k_2), \tag{3.13}$$

$$k_4 = hf(x_n + h, y_n + k_3), \tag{3.14}$$

$$y_{n+1} = y_n + \frac{k_1}{6} + \frac{k_2}{3} + \frac{k_3}{3} + \frac{k_4}{6} + \mathcal{O}(h^5). \tag{3.15}$$

The errors are known to be of the order of $\mathcal{O}(h^5)$. When we integrate equations of motion in the following chapters, we use Heun method. Figure 3.1 shows the schematic image of the fourth-order Runge-Kutta method.

3.3 Classical Monte Carlo

In this section, we briefly explain classical Monte Carlo (MC). This method is used in the study of chiral magnets. In general, when the population of states that mainly contribute to an integral or mean value is very small, compared to all other states, it is very inefficient if one uses a method where all the states appear with the same probability. In order to avoid this, MC adopt a method where the states with larger contributions are preferentially generated from the beginning. This is the concept of the importance sampling. It uses a Markov process, a chain of states where each state is generate only from knowledge of the previous state.

Let's say that the current state is Σ. The probability of generating a next one Σ' is a function independent of time,

$$\mathcal{P}^{(t)} = \sum_{\Sigma'} \mathcal{T}(\Sigma|\Sigma')\mathcal{P}^{(t-1)}(\Sigma') \equiv T\mathcal{P}^{(t-1)}, \tag{3.16}$$

where $\mathcal{T}$ is called transition probability. The criterion of $\mathcal{T}$ so that it convergence to the one proportional to

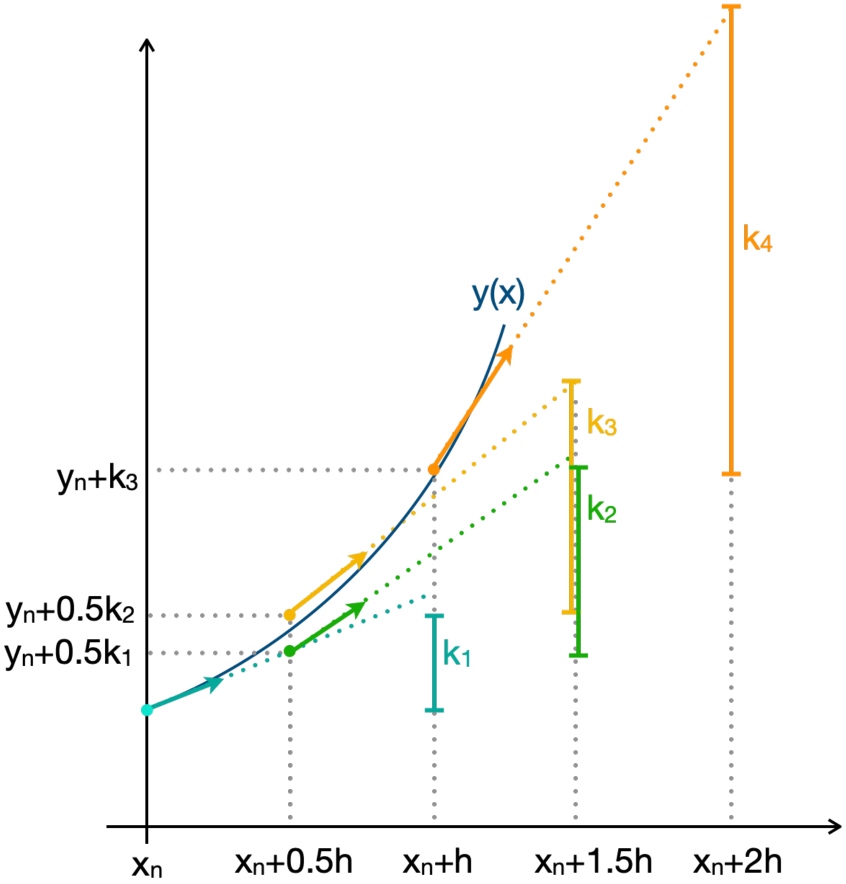

Fig.3.1 Schematic image of the approximation of the fourth-order Runge-Kutta method.

the desired weight W. In a system of particles with low concentration at high T, $W = e^{-E/k_{\mathrm{B}}T}$, where E is energy.

$$\mathcal{T}(\Sigma|\Sigma')W(\Sigma') = \mathcal{T}(\Sigma'|\Sigma)W(\Sigma). \tag{3.17}$$

The above equation is called detailed balance. In combination with the fact that the sum of the probabilities is 1, W is an eigenvector of the matrix $\mathcal{T}$ with eigenvalue 1:

$$\sum_{\Sigma'} \mathcal{T}(\Sigma|\Sigma')W(\Sigma') = W(\Sigma). \tag{3.18}$$

Sufficient conditions for $\mathcal{T}$ to be converged to the one proportional to the desired weight W, in the limit of $\lim_{t\to\infty}$, are that above detail balance and ergodicity (any state can appear after sufficiently long time, no matter which initial state you start from) are both satisfied.

One such algorithm, the Metropolis MC at arbitrary temperature T, is as follows.

step 1. Prepare an initial spin configuration (e.g. random state).

step 2. Randomly select one spin S_0 $(S_i|_{i=0})$.

step 3. Rotate S_0 by an arbitrary angle while leaving all other spins as they are. Then find the energy difference $\mathrm{d}E$ between the states before and after the rotation.

step 4. Generate a random number r between 0 and 1, and if $r < \exp(-\mathrm{d}E/k_\mathrm{B}T)$, accept the rotation.

step 5. Go back to step 2 and repeat.

We note that when $T = 0$, the acceptance probability of new state follows in this way; If the energy difference between new and old state, dE, is positive, the new (higher energy) state is always rejected since the acceptance probability P is

$$\begin{aligned} P &= \min\left(1,\ \lim_{T\to 0} \exp\left(-|\mathrm{d}E|/k_\mathrm{B}T\right)\right) \\ &= \min(1,\ 0) \\ &= 0. \end{aligned} \tag{3.19}$$

Otherwise, the new (lower energy) state will always be accepted since

$$\begin{aligned} P &= \min\left(1,\ \lim_{T\to 0} \exp\left(|\mathrm{d}E|/k_\mathrm{B}T\right)\right) \\ &= \min(1,\ \infty) \\ &= 1. \end{aligned} \tag{3.20}$$

3.4 Exchange Monte Carlo

In this section, we briefly explain exchange MC [74]. This method is used in the study of chiral magnets. The exchange MC is an efficient way of running several Metropolis MCs in parallel. The algorithm is schematically shown in Fig. 3.2. Each replica with different T runs the classical MC. At each MC step and each pair of the replicas, the spin configuration is swapped in probability $\exp(-\mathrm{d}E/k_\mathrm{B}\mathrm{d}T)$, where $\mathrm{d}T$ is the temperature difference between the pair. To ensure the efficiency, there are three necessary conditions as follows;

1. Each replica should be exchanged at nonzero probability. This is confirmed by checking the acceptance ratio of each replica pair.
2. Each replica should move around the whole temperature. This can be checked by tracking each replica.
3. The highest temperature should be high enough to avoid replica from being trapped at local minima.

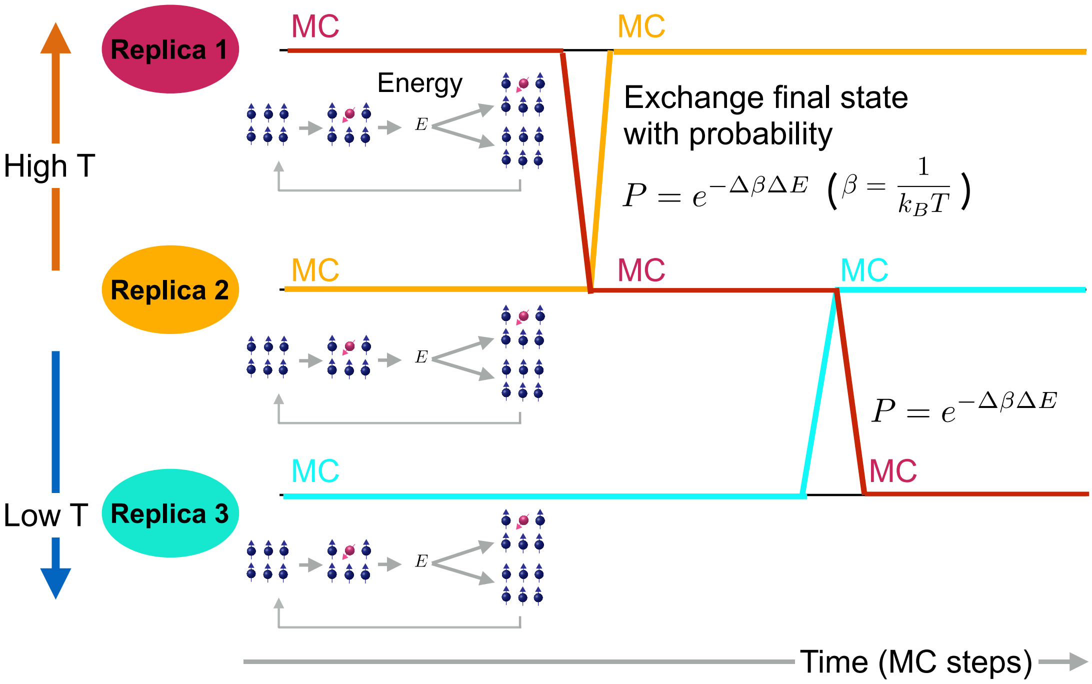

Fig.3.2 Schematic image of the algorithm of the exchange Monte Carlo.

Chapter 4

Magnetically ordered states in amorphous ferromagnet Co_4P

In this chapter, we discuss the spin dynamics and thermodynamics in amorphous ferromagnets, especially Co_4P. Recent experiment revealed that amorphous magnets may transport spin further than the corresponding crystal [49, 56, 2]. This suggests that amorphous magnets may be capable of transporting spin despite the random spin configurations. However, following experiments suggest controversial results [4, 5], partly because magnetic excitations in amorphous magnets have eluded accurate description since the 1970s, a time in which the computational power severely limited the scale and realism of calculations.

We present a realistic model of amorphous magnets and calculate entire spectrum of Co_4P. The model includes a realistic atomic structure and to all orders in the magnon-magnon interactions, for the first time, by combining reverse Monte Carlo and atomistic spin dynamics techniques [20].

First, we investigate the atomic structure of the material using reverse Monte Carlo. Distributing spins on the positions of the Co atoms, we get a spin model. By solving the LLG equation of the spins, we can calculate thermodynamic and magnon properties. To obtain the energy spectrum of the material, we derive the neutron scattering cross-section for amorphous magnets. Using the formula, we calculate the spectra with several different functional forms of the distance dependent exchange interaction. We compare the results with experiments, the spectrum from FCC Co, and that from the Quasi-crystalline approximation (QCA) [8].

In Figs. 4.1(a)-(d), we summarize the main results. Atomic structure from RMC is shown in real space in Fig. 4.1(a) and shown in reciprocal space in Fig. 4.1(b). One can see that the measured and calculated X-ray scattering functions agree well. As for the thermodynamic properties, magnetization of amorphous Co_4P and FCC Co are shown in Fig. 4.1(c). The red line with circle denotes the results of Co_4P and it decreases rapidly at low temperature region than that of the blue line with diamond, the result of the FCC Co. In Fig. 4.1(d), we show the magnetic excitations in amorphous Co_4P obtained from the spin-spin correlation in reciprocal

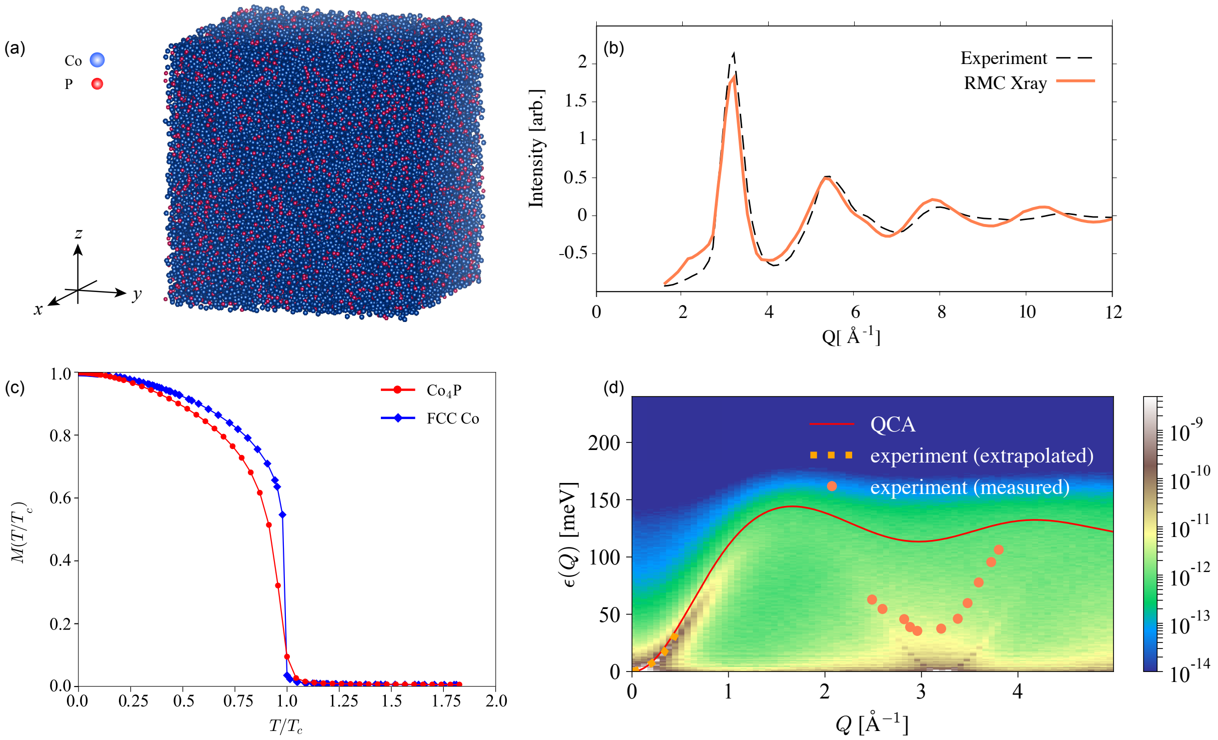

Fig.4.1 (a) Amorphous atomic structure from RMC in real space. (b) Comparison of measured and calculated X-ray scattering intensity. The orange solid line is calculated scattering function from RMC in reciprocal space and the dashed line is measured one [19]. (c) Magnetization of amorphous Co_4P (red line with circle) and FCC Co (blue line with diamond), obtained from ASD simulation. (d) Magnetic excitation spectrum in Co_4P. The red solid line shows the spectrum in QCA [8] , the orange dots show the experimental observation [9].

space. The resulted spectra almost quantitatively reproduces the experiment [9] especially at $Q \sim 0 \text{Å}^{-1}$, shown in orange dots. The theoretical approximation [8] is also plotted in the red solid line. At $Q \sim 0$ and high energy regions, it agrees well with the numerically obtained spectrum. At $Q \approx 3\,\text{Å}^{-1}$, close to the first Brillouin zone of the FCC Co and the first peak of the structure factor [see 4.1(b)], there is gapless parabolic dispersion. We interpret the second dip in terms of amorphous Umklapp scattering [12].

In this study, we found:

- A model which reproduces realistic atomic structure and includes magnon interactions up to all orders. It enables accurate calculation of the magnetic excitation spectra in amorphous magnets.
- Amorphous ferromagnet Co_4P has magnons which follow the Bloch's law, consistent with experiments and similar to that in crystal ferromagnets.
- There are clearly two dips in the magnetic excitation spectrum of Co_4P: first dip at wavenumber $Q \sim 0$ and second dip at $Q \sim 3\,\text{Å}^{-1}$.
- Magnons in energy spectrum placed at $Q \sim 0$ is quantitatively agree with the experimental observation.
- The energy spectrum looks similar to that of FCC Co up to the first Brillouin Zone but it is not periodic.
- Energy spectrum in QCA correctly predicts the spectra at $Q \sim 0$ and at high frequency region.

- The second dip, conventionally called “roton-like feature”, may be amorphous Umklapp scattering.
- Regardless of the choice of the asymptotic form of the exchange interactions, we find similar features in the spectra.

4.1 Amorphous ferromagnetism

Amorphous magnetism has attracted attention since the 1970s, in terms of both static and dynamic properties [75, 76, 77, 78]. Kaneyoshi has proved theoretically that amorphous ferromagnets can be stable with a large enough concentration of magnetic atoms (concentration of magnetic atoms should be larger than 0.329) [79]. At the Curie temperature $\mathrm{T_C}$, a second-order phase transition occurs and amorphous ferromagnetism appears. In the mean field approximation, in the vicinity of $\mathrm{T_C}$, the temperature dependence of the spontaneous magnetization follows the Curie-Weiss law $M(T) \propto \left(\frac{T_c-T}{T_c}\right)^{\xi}$, where $\xi \sim 0.4$, a little larger than 0.36 in the three-dimensional crystalline Heisenberg model [76].

In terms of the magnetically excited states, Mook et al. observed magnetic excitations by inelastic neutron scattering [9]. They found not only magnons at $Q \sim 0\text{Å}^{-1}$ but also “roton-like feature”, named after rotons in superfluid He^4 since both have a dip at finite wavenumber. The roton-like feature has a sharp peak near $Q \sim 3\text{Å}^{-1}$ with a finite gap.

In previous studies, the roton-like feature was believed to originate from short-range static correlation rather than dynamic effect (as rotons in liquid He). This is because the dip position corresponds to the first peak position of the dynamic structure factor $\mathscr{B}(Q,t)$,

$$\mathscr{B}(Q) = \mathscr{B}(Q,t)|_{t=0} = 1 + \int_0^{\infty} dr 4\pi r^2 \rho_0 (g(r)-1)\frac{\mathrm{sin}Qr}{Qr}, \tag{4.1}$$

where ρ_0 is the mean atomic density, $g(r)$ is the radial distribution function, $\rho(r)$ is atomic density as a function of distance r. We note that we ignore scattering term from mean atomic distribution $\int_0^{\infty} dr 4\pi r^2 \rho \frac{\mathrm{sin}Qr}{Qr}$ here, since this contribution is negligibly small in the limit of $r \to \infty$. Having said that, the concrete physical picture of the roton-like feature remains unknown.

As for magnons in amorphous magnets, Kaneyoshi showed theoretically that spin waves can be defined there too due to longer lifetime of magnons than typical precession periodicity of spin waves ($\sim$ ns) [80]. See section 4.4 for details. As magnons are the quasiparticle picture of spin waves (see Sec. 2.2.2), creation of magnons corresponds to decreasing of magnetization, so-called demagnetization. Theoretically, the demagnetization $\Delta M(T)$ can be expressed as [81, 82]

$$\begin{aligned}\Delta M(T) = M(0) - M(T) &= \frac{g\mu_B}{V}\sum_{\boldsymbol{Q}}\langle n_{\boldsymbol{Q}}\rangle \\ &= \frac{g\mu_B}{V}\frac{4\pi V}{(2\pi)^3}\int_0^{\infty} dk \frac{Q^2}{e^{\epsilon(Q)/k_{\mathrm{B}}T}-1} \\ &\sim \frac{g\mu_B}{V}\frac{4\pi V}{(2\pi)^3}\int_0^{\infty} dk \frac{Q^2}{e^{\mathcal{D}Q^2/k_{\mathrm{B}}T}-1} \\ &\propto \Gamma\left(\frac{3}{2}\right)\zeta\left(\frac{3}{2}\right)T^{3/2}, \end{aligned} \tag{4.2}$$

where $\langle n_{\boldsymbol{Q}}\rangle$ is thermal expectation value of magnon number at mode $\boldsymbol{Q}$, $n_{\boldsymbol{Q}}$ is magnon occupation number, $\Gamma(x)$ is Gamma function, $\zeta(x)$ is Riemann zeta function, and we assumed spin wave dispersion relation $\epsilon(Q) = \mathcal{D}Q^2$. Eq. (4.2) means magnetization decreases as $T^{3/2}$ if there are magnons with the dispersion relation of $\epsilon(Q) = \mathcal{D}Q^2$. We note that there could still be magnons with a different dispersion law which would have a different exponent. Experimentally, Cochrane et al. conducted magnetization measurement in Co$_4$P [83]. Demagnetization in amorphous ferromagnet Co$_4$P was confirmed to follows Bloch's law. We show the normalized measured demagnetization, $\frac{\Delta M(T)}{M(0)} = 1 - \frac{M(T)}{M(0)}$ where $M(0)$ is the saturation magnetization, in Fig.4.2.

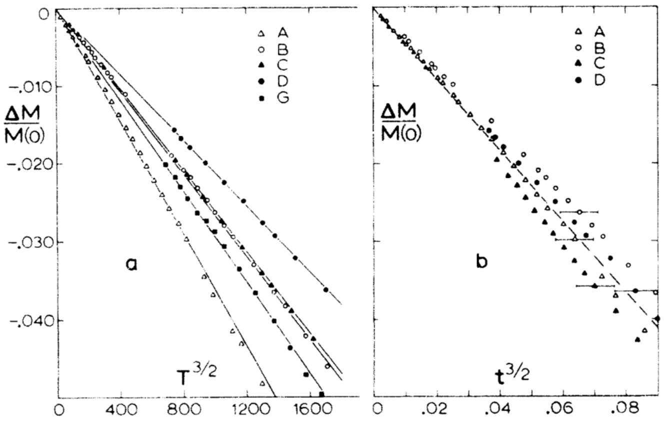

Fig.4.2 (a) Temperature $T^{3/2}$ vs. demagnetization $\frac{\Delta M(T)}{M(0)}$ of amorphous ferromagnet Co$_4$P measured by [83]. (b) Normalized temperature $\mathrm{t} \equiv (T/T_{\mathrm{C}})^{3/2}$ dependence of $\frac{\Delta M(T)}{M(0)}$, where T_{C} is the Curie temperature. The alphabet A, B, C, D, and G represents the five different samples of different concentration of P atoms: A is 23.6±1.0 %, B is 22.0 %, C is 20.3 %, D is 19.0 %, and G is 21 %. Copyright 1974, American Physical Society.

As for the magnetic excitation spectra, Kaneyoshi theoretically proposed quasi-crystalline approximation (QCA), an approximation for energy spectrum in amorphous ferromagnets [8]. See details in Sec. 4.4. Using this formalism he reproduced dips at finite wavenumbers, though energy gap of the dips is much larger than observed experimentally. Alben calculated magnetic spectra numerically under linear spin-wave approximation [6]. He directly calculated dynamic spin-spin correlation functions by using the structure of about 1000 amorphous magnetic atoms obtained from the dense random packing of hard spheres (DRPHS) [84, 85]. He reproduced the dip at $Q \sim 3$ Å^{-1} when he choose $\boldsymbol{Q}$ in such a way that it gives the biggest contribution to $\mathscr{B}(\boldsymbol{Q}, t)$. Roth and Singh obtained an effective medium approximation for magnetic excitations and found a dip with a smaller energy gap than that of QCA [86]. They interpreted the effect as exciting a few planes which are in phase, rather exciting many planes associated with the perfect ordering in crystals.

In the 1970s, numerical methods for modeling amorphous magnets was limited; Dense random packing of hard spheres (DRPHS) has been regarded to be able to reproduce the atomic arrangements in noncrystalline systems [84]. Previous studies have built DRPHS by hand, pouring about 4000 balls into a container and shaking them down [87]. They determined the average number of nearest neighbors to be $\sim$ 9.3, which is similar to that of liquid helium (8.5-9.7) [88], and the mean atomic density was $\sim$ 0.63. Later Gaskell combined the hand-build model and computer simulation to relax the structure by minimizing the elastic energy. However, these traditional methods are not capable of reproducing realistic 3D spin configuration which agrees with experimentally observed scattering functions.

To model the amorphous magnetic properties, the classical Heisenberg model with exchange coupling has been widely used;

$$H = -\sum_{\langle i,j \rangle} J(r_{ij}) \boldsymbol{S}_i \cdot \boldsymbol{S}_j, \tag{4.3}$$

where $J(r_{ij})$ is a distance-dependent isotropic exchange interaction between two spins separated by distance $r_{ij} \equiv |\boldsymbol{r}_j - \boldsymbol{r}_i|$.

4.2 Structural investigation using reverse Monte Carlo

Reverse Monte Carlo (RMC) provides a way of creating an amorphous structure from experimental data, such as X-ray diffraction and neutron diffraction data. It obtains a possible atomic position that reproduces these experimental data. RMC is originally developed by R. L. Mcgreevy and L. Pusztai [89] and improved by Gereben O. et al. [90]. [For the user guide, visit https://www.szfki.hu/ nphys/rmc++/downloads.html]. We use the latter to create an amorphous structure.

The algorithm is to minimize a cost function χ^2_{ij} for an atom type of i and j, which analogues to normal Monte Carlo which minimizes total energy of the system. This is schematically shown in Fig. 4.3. The definition of χ^2_{ij} is

$$\chi^2_{ij} = \frac{\sum_Q (S^C_{ij}(Q) - S^E_{ij}(Q))^2}{\sigma^2_{ij}}, \tag{4.4}$$

where $S^C_{ij}(Q)$ and $S^E_{ij}(Q)$ denote simulated and measured data as a function of wavenumber Q, respectively.

σ_{ij} represents a standard deviation for the cost function χ^2_{ij}, the value of which is also a parameter in the RMC simulation. Here $S^C_{ij}(Q)$ and $S^E_{ij}(Q)$ are the values in reciprocal space. To compare them, RMC first Fourier transforms $g_{ij}(r)$, which is either called radial distribution function or the pair correlation function. It is defined as

$$g_{ij}(r) = \frac{n_{ij}(r)}{4\pi r^2 dr \rho_0 c_j}, \tag{4.5}$$

where $n_{ij}(r)$ is the number of atoms of type j at distance r from another atom of type i, $4\pi r^2 dr$ is the volume of a spherical shell and $\rho_0 c_j = \rho_j$ is the number density of atom at j. We note that, since the atomic configuration from RMC is not unique, we take the configurational average when we study magnetic properties.

RMC avoids to be trapped in local minima, by accepting costly moves with probability exp$[-(\chi^2_{\mathrm{new}} - \chi^2_{\mathrm{old}})]$ [90]. This probability is the equilibrium distribution W_0, which appears in

$$\sum_{\Sigma'} \mathcal{T}(\Sigma'|\Sigma) W_0(\Sigma) = \sum_{\Sigma'} \mathcal{T}(\Sigma|\Sigma') W_0(\Sigma'). \tag{4.6}$$

The equation ensures that there is a state with minimum χ^2 due to the principle of detailed balancing, same as Eq (3.17),

$$\mathcal{T}(\Sigma'|\Sigma) W_0(\Sigma) = \mathcal{T}(\Sigma|\Sigma') W_0(\Sigma'), \tag{4.7}$$

where Σ and Σ' respectively denote current and next state and $\mathcal{T}$ is the transition matrix.

RMC is one of the sophisticated alternatives to the empirical random sphere packings in the early days. When constructing the structures, we treat atoms as hard spheres and ignore chemical bondings. We can also include some structural properties; In the case of Co$_4$P, we impose that P should be well mixed with Co atoms by requiring that two P atoms never touch [19]. This is included as a coordination number constraint in RMC, imposing the extra cost for P-P pairs closer than 2.75 Å.

As input experimental data, we use X-ray, neutron, and polarized neutron scattering data for Co$_4$P taken by Sadoc et al. [19]. We start from an FCC lattice, which has a similar coordination number of 12 to the average coordination of Co$_4$P (=11.54) [19]. The typical system size for the calculations is 62500 hard spheres (Co: 50000, P: 12500). The lattice parameter, the size of each side of the cubic box, is 97.71 Å and the number density ρ is 0.067 Å^{-3} [91]. We also consider the finite temperature effect in the analysis by empirically setting the mean square displacement of the atoms $\sigma = 0.015$ for both Co and P as this gives a good fit for the data. This means we assume the distribution of the atomic displacements from the equilibrium positions x_d follow the normal distribution $f(x_d)$.

The RMC procedure is as follows. Firstly, we create a random mixture of Co and P atoms as a ratio of 4:1. Secondly, we start to randomize the atomic positions so that it reproduces the experimental scattering data.

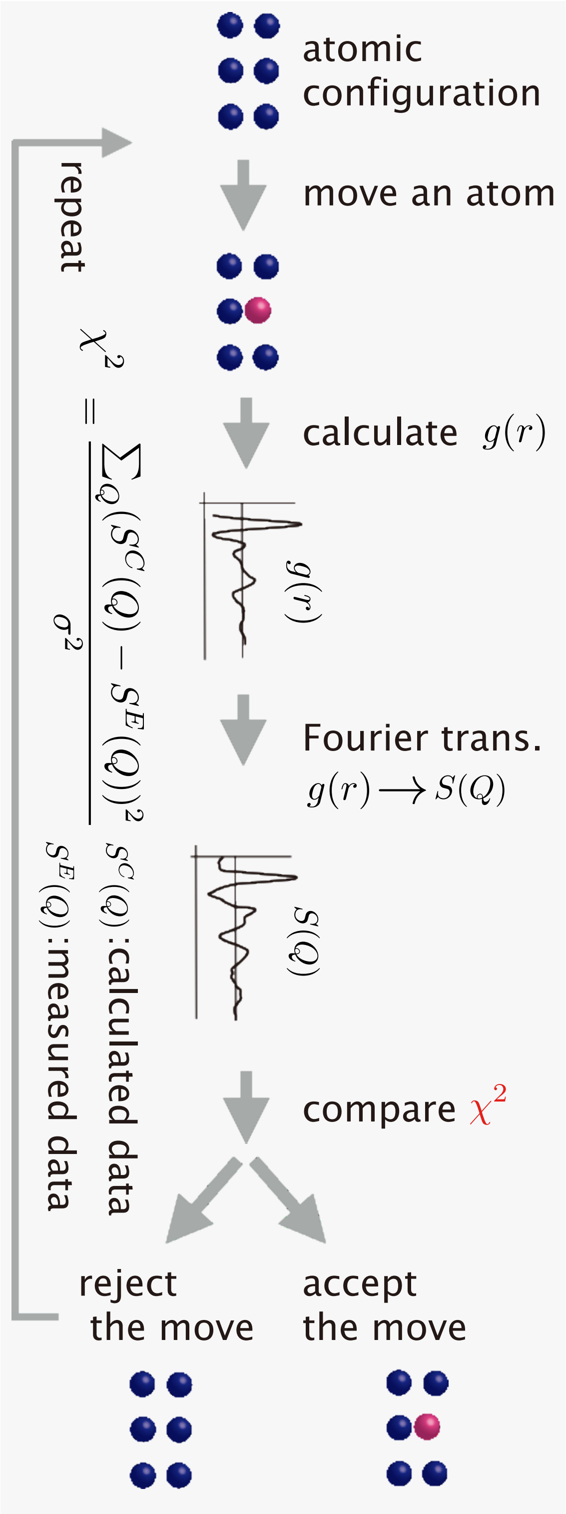

Fig.4.3 Schematic description of the reverse Monte Carlo algorithm

This move includes swaps of Co and P atoms. After some swaps, the probability of accepting the swap will be very low, as this move changes the structure a lot. We thus allow swaps for a relatively short period (about 4 hours) for efficiency. This time scale is determined by watching the acceptance rate, how the tried swaps were accepted. Thirdly, we stop swapping and keep fitting to the experimental data for a longer period (about 8 days). Lastly, we use a smaller (0.1Å, half the mesh as before) mesh of the space and run it for a long period (about 2 days) to get more accurate configurations.

4.3 Finite temperature effect

We include random force term $-\gamma_e \boldsymbol{s}_i \times \boldsymbol{g}_i$ in LLG equation to simulate finite temperature effect.

$$\frac{\partial \boldsymbol{s}_i}{\partial t} = -\gamma \boldsymbol{s}_i \times [\boldsymbol{B}_i + \boldsymbol{g}_i] - \gamma \frac{\alpha}{s} [\boldsymbol{s}_i \times [\boldsymbol{s}_i \times [\boldsymbol{B}_i + \boldsymbol{g}_i]], \tag{4.8}$$

where $\boldsymbol{g}_i$ represents a random force. Eq. (4.8) is called stochastic LLG equation. The Gilbert term was introduced phenomenologically [92]. This random force is Gaussian process

$$\langle \boldsymbol{g}_i \rangle = 0, \quad \langle g_i^\alpha(t) g_j^\beta(t') \rangle = 2d\delta_{ij}\delta_{\alpha\beta}\delta(t-t'), \tag{4.9}$$

where d is the power spectrum of $g(t)$ following $d = k_B T$. Eq. (4.9) shows that the random force at different t and different site, or different coordination has no correlation. $\boldsymbol{g}_i$ does not affect the time spin spin correlation in the system, and all the possible states are occupied following the equipartition law. When we consider the system is purely classical, we use the white noise random force with $d = \mathrm{const}$. In other words, the system follows classical fluctuation-dissipation theorem which states that fluctuation in equilibrium state and dissipation in non-equilibrium state both develop in the same way [93]

$$\mathrm{Im}[\chi^{\alpha\beta}(t)] = \frac{\omega}{2k_B T} \langle \delta s_i^\alpha(t) \delta s_j^\beta(0) \rangle, \tag{4.10}$$

where δs_i^α represents fluctuation of α-component of magnetization at site i, and $\chi^{\alpha\beta}(t-t')$ is a response function corresponding to a external field $h_\beta(t)$ defined as

$$\delta s_i^\alpha(t) = \int_{-\infty}^{t} dt' \chi^{\alpha\beta}(t-t') h_\beta(t') + \mathcal{O}(h_\beta^2). \tag{4.11}$$

When we consider the system is quantum or semi-classical, we use the random force $\boldsymbol{g}(t)$ whose power spectrum follows quantum fluctuation-dissipation theorem,

$$\langle g_a(\boldsymbol{r}_i,t)\rangle = 0;\ \langle g_a(\boldsymbol{r}_i)g_b(\boldsymbol{r}_j)\rangle_\omega = \delta_{ij}\delta_{ab}\frac{2\alpha}{\gamma_{\mathrm{e}}\mu\beta}\frac{\hbar\omega}{\mathrm{e}^{\beta\hbar\omega}-1}. \tag{4.12}$$

4.4 Quasi-crystalline approximation for spin wave spectra

In quasi-crystalline approximation (QCA) [8], energy spectrum $\epsilon^{\mathrm{QCA}}(\boldsymbol{Q})$ in amorphous ferromagnets is given by

$$\epsilon^{\mathrm{QCA}}(\boldsymbol{Q}) = \int J(r_{ij})g(r_{ij})(1-e^{i\boldsymbol{Q}\cdot\boldsymbol{r}_{ij}})d^3r_{ij}, \tag{4.13}$$

where $\boldsymbol{r}_{ij} = \boldsymbol{r}_i - \boldsymbol{r}_j$ is the difference of position vectors, $\boldsymbol{r}_i$ and $\boldsymbol{r}_j$. Above expression is a replacement of the energy for crystal

$$\epsilon(\boldsymbol{Q}) = \sum_j J_{ij}(1-e^{i\boldsymbol{Q}\boldsymbol{r}_{ij}}). \tag{4.14}$$

Eq. (4.13) is derived under the Heisenberg Hamiltonian, Eq. (4.3).

In order to derive the above equation Eq. (4.13), Kaneyoshi use a high-density expansion, assuming that the structure of the amorphous magnets is well modeled by the DRPHS. In other words, he drops higher-order correlation functions of a random function that represents the positions of atoms. He also takes an average of the Green function over all possible configurations of magnetic atoms. The resulting general expression of spin-wave energy is determined by

$$E - \epsilon^{\mathrm{QCA}}(\boldsymbol{Q}) - \Gamma_{\boldsymbol{Q}}(E) - \frac{1}{E-\epsilon^{\mathrm{QCA}}(\boldsymbol{Q})}\Sigma_{\boldsymbol{Q}}(E) = 0, \tag{4.15}$$

where $\Gamma_{\boldsymbol{Q}}(E)$ and $\Sigma_{\boldsymbol{Q}}(E)$ are obtained by the factorization approximation [76] as

$$\begin{aligned}
&\Big\{E - \epsilon^{\mathrm{QCA}}(\boldsymbol{Q}) - \Gamma_{\boldsymbol{Q}}(E) - \frac{1}{E-\epsilon^{\mathrm{QCA}}(\boldsymbol{Q})}\Sigma_{\boldsymbol{Q}}(E)\Big\}\langle G(E)_{\boldsymbol{Q}\boldsymbol{Q}'}\rangle = \Delta_{\boldsymbol{Q}}(E)\delta(\boldsymbol{Q}-\boldsymbol{Q}'),\\
&\Gamma_{\boldsymbol{Q}}(E) = (2Sp)^2\int d\boldsymbol{Q}_1 M_2(\boldsymbol{Q},\boldsymbol{Q}_1)\frac{(J_{\boldsymbol{Q}-\boldsymbol{Q}_1}-J_{\boldsymbol{Q}_1})(J_{\boldsymbol{Q}_1-\boldsymbol{Q}}-J_{\boldsymbol{Q}})}{E-\epsilon^{\mathrm{QCA}}(\boldsymbol{Q}_1)} + \dots,\\
&\Sigma_{\boldsymbol{Q}}(E) = \Big[2Sp\int d\boldsymbol{Q}_1 M_2(\boldsymbol{Q},\boldsymbol{Q}_1)(J_{\boldsymbol{Q}-\boldsymbol{Q}_1}-J_{\boldsymbol{Q}_1})\Big]^2 + \dots,\\
&\Delta_{\boldsymbol{Q}}(E) = \mathcal{N} + 2Sp\int d\boldsymbol{Q}_1 M_2(\boldsymbol{Q},\boldsymbol{Q}_1)\frac{J_{\boldsymbol{Q}-\boldsymbol{Q}_1}-J_{\boldsymbol{Q}_1}}{E-\epsilon^{\mathrm{QCA}}(\boldsymbol{Q}_1)}\\
&\qquad - \frac{2Sp}{E-\epsilon^{\mathrm{QCA}}(\boldsymbol{Q})}\int d\boldsymbol{Q}_1 M_2(\boldsymbol{Q},\boldsymbol{Q}_1)(J_{\boldsymbol{Q}-\boldsymbol{Q}_1}-J_{\boldsymbol{Q}_1}) + \dots,\\
&M_2(\boldsymbol{Q},\boldsymbol{Q}_1) = \langle\rho_a(\boldsymbol{Q}-\boldsymbol{Q}_1)\rho_a(\boldsymbol{Q}_1-\boldsymbol{Q})\rangle.
\end{aligned} \tag{4.16}$$

E is an eigenvalue of the Hamiltonian, $G(E)_{\boldsymbol{Q}\boldsymbol{Q}'}$ is the corresponding Green function in reciprocal space, $J_{\boldsymbol{Q}}$ is the exchange interaction in reciprocal space, $\mathcal{N}$ is total number of magnetic atoms per unit volume, $p \equiv \frac{n}{(2\pi)^3}$, and $\rho_a(\boldsymbol{Q}) = \rho'(\boldsymbol{Q}) - \langle \rho'(\boldsymbol{Q}) \rangle_{\mathrm{r}}$, where $\rho'(\boldsymbol{Q}) = \frac{1}{n}\sum_i \exp(-i\boldsymbol{Q}\boldsymbol{r}_i)$ is a random function depending on the position of magnetic atoms, $M_2(\boldsymbol{Q}, \boldsymbol{Q}_1) = \langle \rho_a(\boldsymbol{Q} - \boldsymbol{Q}_1) \rangle_{\mathrm{r}}$, and $\langle ... \rangle_{\mathrm{r}}$ denotes the configuration average over all possible ones. Here the factorization approximation is

$$\begin{aligned}\langle \rho_a(\boldsymbol{Q} - \boldsymbol{Q}_1, \boldsymbol{Q}_2)\rho_a(\boldsymbol{Q}_2 - \boldsymbol{Q}_3, \boldsymbol{Q}_4)\rangle &= \langle \rho_a(\boldsymbol{Q} - \boldsymbol{Q}_1)\rho_a(\boldsymbol{Q}_1 - \boldsymbol{Q})\rangle \delta(\boldsymbol{Q} - \boldsymbol{Q}_3)\delta(\boldsymbol{Q}_1 - \boldsymbol{Q}_2)\delta(\boldsymbol{Q}_3 - \boldsymbol{Q}_4) \\ &+ \langle \rho_a(\boldsymbol{Q} - \boldsymbol{Q}_1)\rho_a(\boldsymbol{Q}_1 - \boldsymbol{Q})\rangle \langle \rho_a(\boldsymbol{Q} - \boldsymbol{Q}_2)\rho_a(\boldsymbol{Q}_2 - \boldsymbol{Q})\rangle \delta(\boldsymbol{Q}_2 - \boldsymbol{Q}).\delta(\boldsymbol{Q}_4 - \boldsymbol{Q}_2) \quad (4.17)\end{aligned}$$

The stability of the spin waves in amorphous ferromagnets is estimated by comparing the inverse lifetime of the states $|\boldsymbol{Q}\rangle$ with that of the spin waves. The imaginary part of the states, which is proportional to the inverse lifetime, can be estimated from $\mathrm{Im}[\Gamma_{\boldsymbol{Q}}(E)]$ due to the relation

$$\begin{aligned}\langle G(E)_{\boldsymbol{Q}\boldsymbol{Q}'}\rangle &= \frac{\Delta_{\boldsymbol{Q}}(E)\delta(\boldsymbol{Q} - \boldsymbol{Q}')}{\left\{E - \epsilon^{\mathrm{QCA}}(\boldsymbol{Q}) - \Gamma_{\boldsymbol{Q}}(E) - \frac{1}{E - \epsilon^{\mathrm{QCA}}(\boldsymbol{Q})}\Sigma_{\boldsymbol{Q}}(E)\right\}} \\ &\propto \left\{E - \epsilon^{\mathrm{QCA}}(\boldsymbol{Q}) - \left[\Gamma_{\boldsymbol{Q}}(E) + \frac{\Sigma_{\boldsymbol{Q}}(E)}{E - \epsilon^{\mathrm{QCA}}(\boldsymbol{Q})}\right]\right\}^{-1}. \quad (4.18)\end{aligned}$$

Expanding the $\mathrm{Im}[\Gamma_{\boldsymbol{Q}}(E)]$ up to the first order of $\boldsymbol{Q}$, it follows

$$\mathrm{Im}[\Gamma_{\boldsymbol{Q}}(E)] \sim (2Sp)^2 \int d\boldsymbol{Q}_1 M_2(\boldsymbol{Q}, \boldsymbol{Q}_1) \frac{(J_{\boldsymbol{Q}-\boldsymbol{Q}_1} - J_{\boldsymbol{Q}_1})(J_{\boldsymbol{Q}_1-\boldsymbol{Q}} - J_{\boldsymbol{Q}})}{E - \epsilon^{\mathrm{QCA}}(\boldsymbol{Q}_1)} = \mathcal{O}(k^7), \quad (4.19)$$

$$M_2(\boldsymbol{Q}, \boldsymbol{Q}_1) = \mathcal{O}((k - k_1)^2). \quad (4.20)$$

When the spin waves have long wavelengths, $\mathrm{Im}[\Gamma_{\boldsymbol{Q}}(E)]$ is much smaller than that of the typical frequency of spin waves, which obeys $\sim Q^2$. Therefore we can define the spin waves even in amorphous ferromagnets, as far as the wavelength is sufficiently large. Later, we show that QCA can produce some dips at finite wavenumbers, but they are very shallow compared with the experiment.

In Appendix A, we note how our energy spectrum using JAMS (the name of our program), $\epsilon^{\mathrm{JAMS}}(Q)$, is quantitatively related to the QCA spectrum. We confirm that our spectra $\epsilon^{\mathrm{JAMS}}(Q)$ obtains quantitatively equivalent dispersion relation to QCA. This means we should get a very good agreement between QCA and JAMS in the small Q region, which is indeed confirmed later.

4.5 Inelastic neutron scattering cross-section for amorphous magnets

Neutron scattering is widely used technique to investigate structures and energy spectrums also in amorphous Co_4P [19]. Following a book [94], we derive suitable expression of cross-section for magnetic inelastic scattering, which can also be used in amorphous magnetic systems. See Appendix B for detailed derivation. We assume the amorphous magnetic systems, in particular Co_4P, can be approximated by the Heisenberg Hamiltonian; The dynamical fluctuations in length of the magnetic moment may be ignored.

Here we just summarize the results. The differences between crystal and amorphous systems may be:

1. "lattice parameter" is length of the unitcell (*crystal*) or that of whole system (repeating unit) (*amorphous*)
2. "lattice vector" is what span the unitcell (*crystal*) or that span whole system (repeating unit) (*amorphous*)
3. The statement "assuming all site is the center of symmetry" cannot be applied for amorphous systems. (cf. Eq. (B.59) and Eq. (B.67))

The cross-section of unpolarized neutron for amorphous magnets may be

$$\begin{aligned} \mathcal{S}(\boldsymbol{Q},\omega) = \frac{g_n^2 r_0^2}{2\pi\hbar} (\mathscr{C}^2(Q))^2 \sum_{ab} \left(\delta_{ab} - \hat{Q}_a \hat{Q}_b\right) \sum_{i,j} \mathrm{e}^{-\mathrm{i}\boldsymbol{Q}\cdot\boldsymbol{r}_{ij}} \\ \times \int_{-\infty}^{\infty} \mathrm{d}t \mathrm{e}^{-\mathrm{i}\omega t} \Big[\langle S_a(\boldsymbol{r}_i, 0) S_b(\boldsymbol{r}_j, t) \rangle - \langle S_a(\boldsymbol{r}_i) \rangle \langle S_b(\boldsymbol{r}_j) \rangle \Big] \end{aligned} \tag{4.21}$$

where $\boldsymbol{Q}$ is the neutron scattering vector, $\hat{\boldsymbol{Q}} = \boldsymbol{Q}/|\boldsymbol{Q}|$ is the unit vector of $\boldsymbol{Q}$, $\gamma_n = 1.931$ is the neutron's g-factor, $r_0 = e^2/m_e c^2 = 0.28179 \times 10^{-12}$ cm is the classical electron radius, $\mathscr{C}(Q) = \frac{g_s}{g} \bar{j}_0(Q)$ is the atomic form factor where the values, $\bar{j}_0(Q)$ for Co, are taken from the table [95].

4.6 Reproduction of scattering functions from experiment

In order to study the magnetic properties, we need to first equilibrate the system at a fixed temperature to find thermal equilibrium spin states. After that, we also perform time averaging to collect the fluctuations from the thermal equilibrium. In amorphous systems, one should also take a configurational average, averaging over multiple solutions of the amorphous structures. This is to collect the fluctuations of atomic structures in amorphous systems. We create10 independent amorphous configurations and all the magnetic calculations, shown in the following, are averaged over the 10 replicas. The averaged results are found to be almost the same as that of a single result, maybe due to the large system. Hamiltonian reads

$$\mathcal{H} = -\sum_{i \neq j} J(r_{ij}) \boldsymbol{S}(\boldsymbol{r}_i) \cdot \boldsymbol{S}(\boldsymbol{r}_j) - \mu \boldsymbol{B} \cdot \sum_i \boldsymbol{S}(\boldsymbol{r}_i). \tag{4.22}$$

As for the magnetic moment of Co atoms, we use the experimental value $\mu = 1.0\mu_{\mathrm{B}}$ [9]. The spin vectors $\boldsymbol{S}(\boldsymbol{r}_i)$ mean the same ones as $\boldsymbol{S}_i$ in Eq. (4.3) and the position vector of the spins are explicitly shown. The exchange interaction $J(r_{ij})$ is assumed to be distance dependent though it is not necessarily up to the nearest neighbors. The form of $J(r_{ij})$ in amorphous magnets is unclear, thus we tested several asymptotic forms.

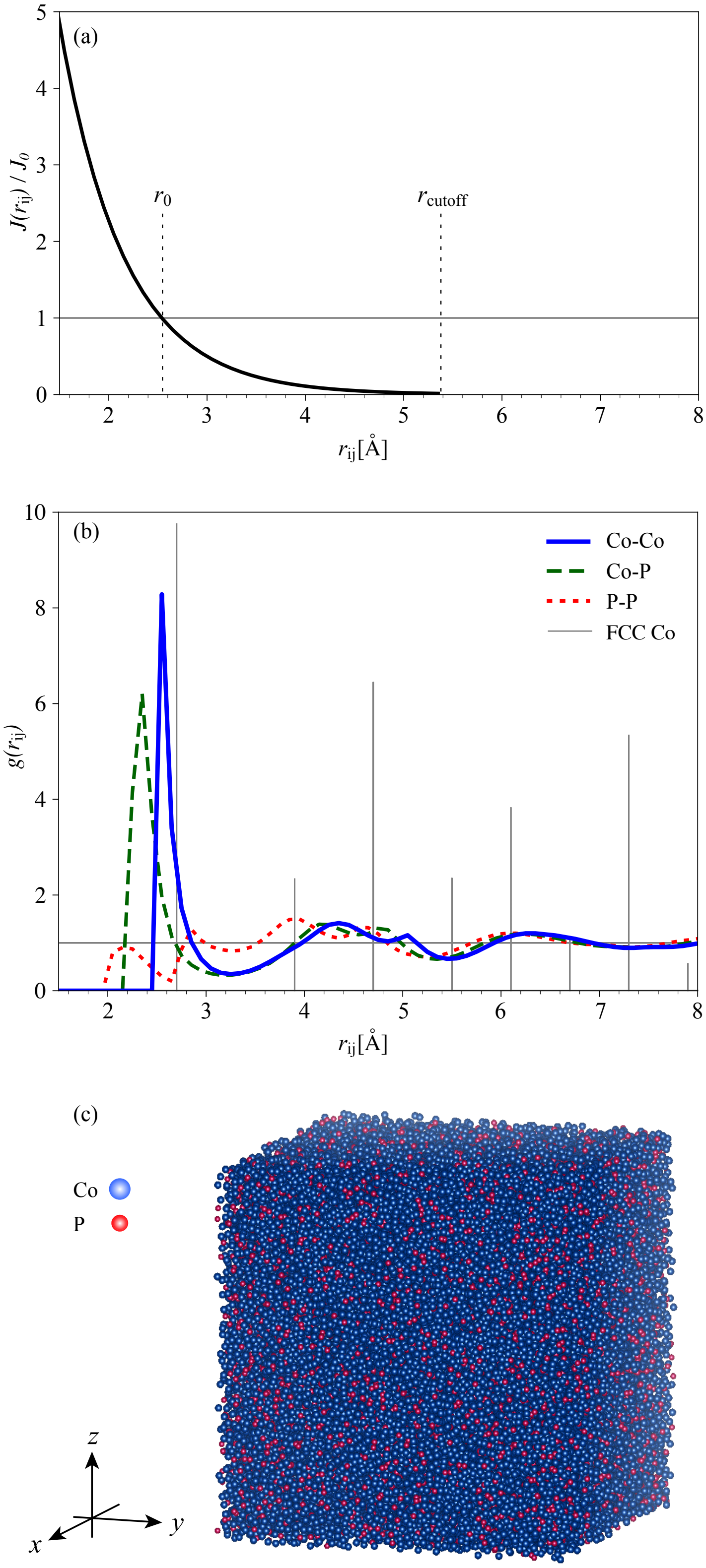

Fig.4.4 (a) Distance dependent spin-spin exchange interaction $J(r_{ij})$. The cutoff r_{cutoff} is introduced at $r_{\text{cutoff}} = 5.45$Å. This means $J(r_{ij}) = 0$ if $r_{ij} > r_{\text{cutoff}}$. (b) Pair correlation functions $g(r_{ij})$ of Co-Co, Co-P, and P-P in amorphous Co_4P and Co-Co in FCC Co. These are generated from RMC. (c) Real space image of an amorphous atomic configuration generated from RMC with 62500 atoms. Blue spheres stand for Co atoms and red spheres show P atoms.

One such example is an exponentially decaying one, shown in Fig. 4.4(a),

$$J_{\mathrm{exp}}(r_{ij}) = J_0 \mathrm{exp}\left(-\frac{r_{ij} - r_0}{w}\right), \tag{4.23}$$

where typical choice of the parameters in the following are $J_0 = 6.733$ meV, $r_0 = 2.54$ Å and $w = 0.66$ Å. Another example is RKKY-like [76], where the sign of exchange coefficient oscillates with distance,

$$J(r_{ij}) = -J_0 \frac{2k_F(r_{ij} - r_0)\mathrm{cos}\{2k_F(r_{ij} - r_0)\} - \mathrm{sin}\{2k_F(r_{ij} - r_0)\}}{\{2k_F(r_{ij} - r_0)\}^4}, \tag{4.24}$$

where k_F scales the length scale of the oscillation. As different exchange interaction forms did not give significant differences (shown later), we use the exponential one in the following main results. We impose $J_{exp}(r_{ij}) = 0$ when $r_{ij} > 5.45$ Å to reduce the calculation time.

One can see that the P atoms are almost homogeneously distributed and P atoms rarely touch each other, from the pair correlation functions $g(r_{ij})$ in Fig. 4.4(b). There is no strong peak of the P-P pair correlation and the largest peak is at ~ 4.0 Å, much larger than the P diameter. The double-peaked structure of $g(r_{ij})$ of the Co-Co distribution, i.e., around 4.4 Å and 5.0 Å, is one of the familiar features of amorphous metalloids [76]. This feature is also found in our result. The average number of neighbors of each pair is as follows: Co-Co=7.53, Co-P=1.96, P-P=0.30. In Fig 4.4(c), an example of real-space amorphous structure created from RMC is shown. In Fig. 4.5 we show the comparison of the scattering functions from RMC and the experimental data. The latter is used as an input of the RMC simulation. The calculated results all agree well with the experimentally observed ones. As a whole, we can say that the RMC process reproduces a realistic structure of amorphous Co_4P. Since the magnetic moments are mainly on Co atoms [96], so P atoms are essentially voids in the amorphous Co.

4.7 Magnon properties and Bloch's law

To calculate magnetic properties, we extract magnetic atoms Co from the structure obtained from RMC and ignore nonmagnetic P atoms. Putting spins on top of each Co atom gives rise to a spin model. In Fig. 4.6, we display the model. We use LLG equation to simulate the time dependence of each spin. This is our original idea, combining RMC and LLG equations together for calculating magnetic properties in amorphous systems. The damping constant of LLG equation is $\alpha = 0.01$ and we introduce finite temperature effect via a stochastic field, a quantum thermostat [11]. This thermostat is capable of providing reliable results for thermodynamic properties until the Curie temperature [97, 98].

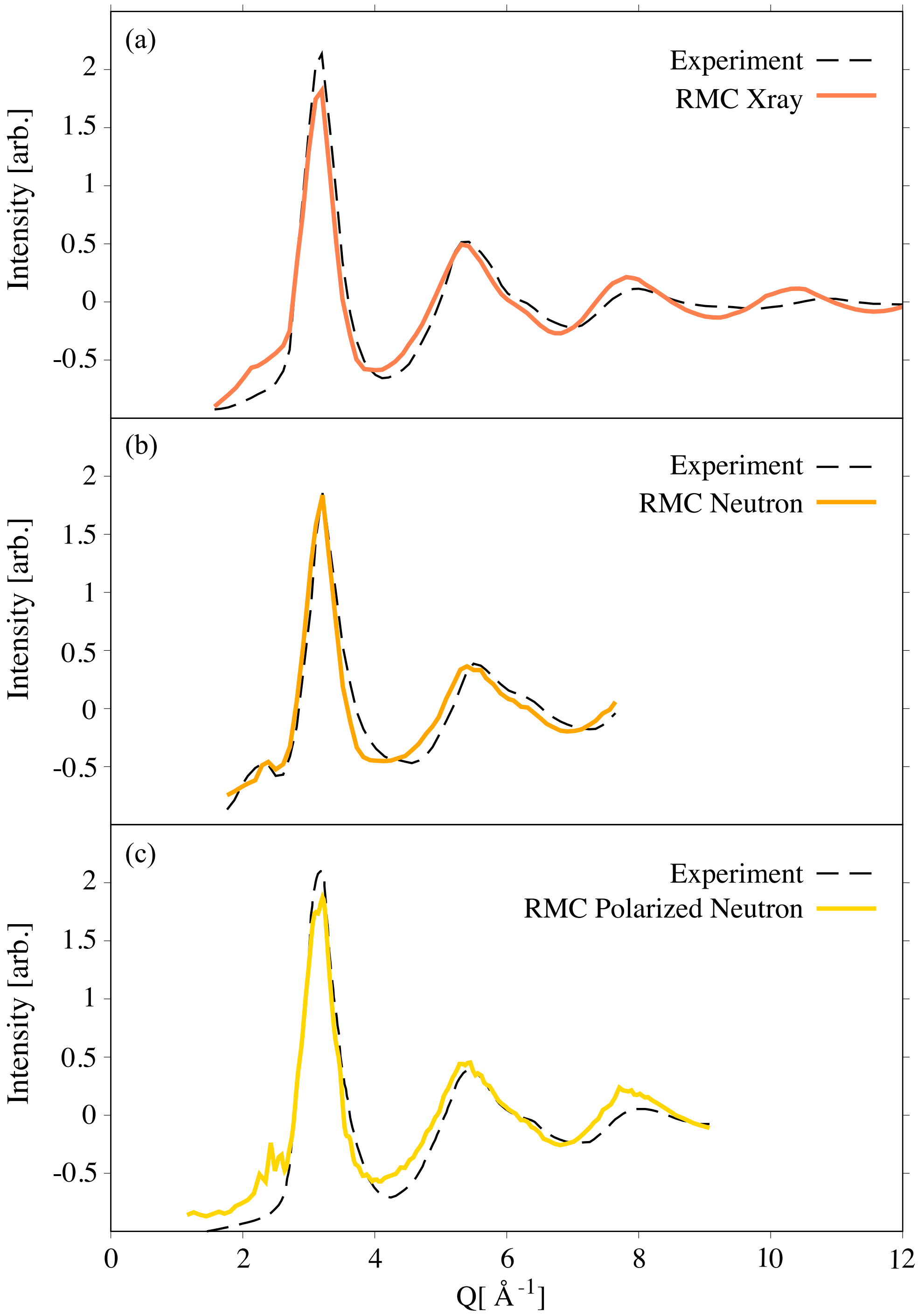

Fig.4.5 (a) X-ray, (b) neutron and (c) polarized neutron scattering functions in Co_4P, calculated from RMC (the solid line) and measured in exeriment [19] (the dotted line).

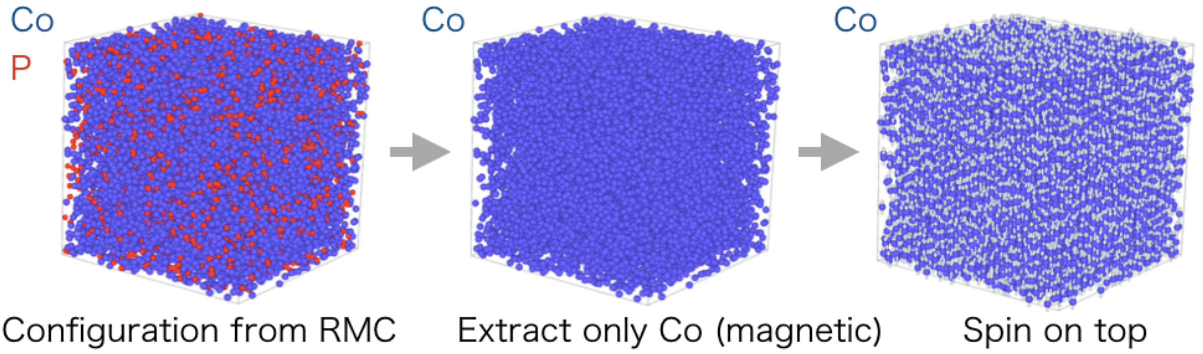

Fig.4.6 Schematic explanation of construction of the spin model. We extract Co atoms from the RMC structure, put spins on the top, and simulate the spin dynamics by LLG.

In Fig. 4.7(a), we show reduced magnetization vs. temperature for amorphous Co_4P and crystalline FCC Co,

$$\boldsymbol{M}(T) = \left\langle \frac{1}{N} \sum_{i=1}^{N} \boldsymbol{S}_i \right\rangle_T , \tag{4.25}$$

where $\boldsymbol{M}(T)$ is normalized magnetization and $\langle ... \rangle_T$ means thermal average. We determine T_C from the peak position of the susceptibility $\chi(T)$,

$$\chi(T) \propto \frac{\langle M(T) \rangle_T^2 - \langle M^2(T) \rangle_T}{k_\mathrm{B} T}. \tag{4.26}$$

In both cases, the magnetization decreases following the Bloch's law, $M(T) = 1 - B_{3/2}(T/T_C)^{3/2}$ at low temperature. The constant of Bloch's law in the amorphous system is larger than that of the crystal system, meaning that the magnetization of the former system decreases faster than in the latter case. This result is consistent with the experimental observation in the same material [83]. We find $B_{3/2} = 0.16$ in the case of FCC Co, almost the same as that observed, $B_{3/2} = 0.17$ [76]. In the Co_4P case, we find the constant to be $B_{3/2} = 0.22$. This larger value may be due to the randomness of the atomic positions in the amorphous system [76]; In QCA, Kaneyoshi suggests that the random structure of the system modifies the spin wave stiffness constant D as

$$D \sim \left(\partial^2 \epsilon / \partial Q^2\right)_{Q=0} - \tilde{D}, \tag{4.27}$$

where $\tilde{D}$ is attributed to the atomic position randomness. The value $B_{3/2} = 0.22$ is about the half of the measured one $B_{3/2} \sim 0.4$ [83]. This means that the magnetization reduces more rapidly in reality than that in our calculations. The difference between the calculated and measured value of $B_{3/2}$ are also found in previous studies; In experiments, $B_{3/2}$ deduced from the spin wave stiffness D, measured by neutron scattering, is often smaller than that from $M(T)$. One possibility for this discrepancy is that non-collinearities in the magnetic ground state, because of some antiferromagnetic interactions, i.e., superexchange via P atoms or local anisotropies [99]. This remains one of the possibilities since they are not included in our model Hamiltonian. Near T_C, we can see that $M(T)$ in FCC Co drops faster than that of amorphous $\mathrm{Co_4P}$. This may suggest that structural disorders broaden the critical behavior associated with the second-order phase transition.

4.8 Energy spectra and magnetic excitations

Our main interest is the unusual roton-like excitation in the spectrum. To understand the magnetic excitations, we calculate it using the spin-spin correlation functions in the Fourier space and plot the neutron scattering cross section, Eq. (4.21). We note that amorphous systems don't have a well-defined reciprocal lattice vector momentum – due to the lack of translational symmetry. This means we cannot use Bloch's theorem in the system. However, we can still study magnetic excitations using a sample vector $\boldsymbol{Q}$; It is the scattering vector of a neutron beam in experiments. In our simulations, it evaluates the Fourier transformation of the spin-spin correlations from all spins in the system. The evaluation of the spin-spin correlation function has been very difficult to treat analytically in the previous studies; For amorphous systems it cannot be evaluated easily, even in the framework of the linear spin wave theory. Our approach allows us to output the correlations after solving the spin dynamics of the many-body non-linear LL equations, and the higher-order correlations are implicitly included. Hence, we do not approximate the spin-spin correlations.

In the calculated spectrum, Figs. 4.8(a) and (b), we find a quadratic dispersion of magnons, which is consistent with the experiment and the QCA. As Bloch's law comes from the assumption of a quadratic dispersion, the spectral result is in agreement with our thermodynamic calculations. In the crystalline case, Fig. 4.8(a), the linewidth of magnons follows $\Gamma \sim \alpha\omega$. Whereas in the amorphous case, Fig. 4.8(b), one can see a broadening which expresses a shorter lifetime of them. In Figs. 4.8(b), we have shown the approximate spectrum in the QCA [8],

Our simulations suggest that the QCA fairly predicts the magnons at $Q \sim 0$ and a diffusive high energy region of the magnetic excitations. In addition, we find a sharply peaked parabola placed at $Q \approx 3$ Å^{-1} where the first peak of the static structure factor appears. The minimum of the second parabola is positioned at a larger wave number and much lower energies than the second parabola from the QCA. Even though the second dip is gapless, differently from the experiment, the linewidth is so narrow that indicates the comparable lifetime with the magnons at $Q \sim 0$. Interestingly, the QCA hasn't predicted this dip and it does appear in addition to the dips from QCA predictions. We attribute the second parabola to amorphous Umklapp scattering, spin waves with smaller wavelength than that of $Q \sim 0$. This was initially suggested in neutron scattering measurements [12] but here our models do not include any experimental ambiguities.

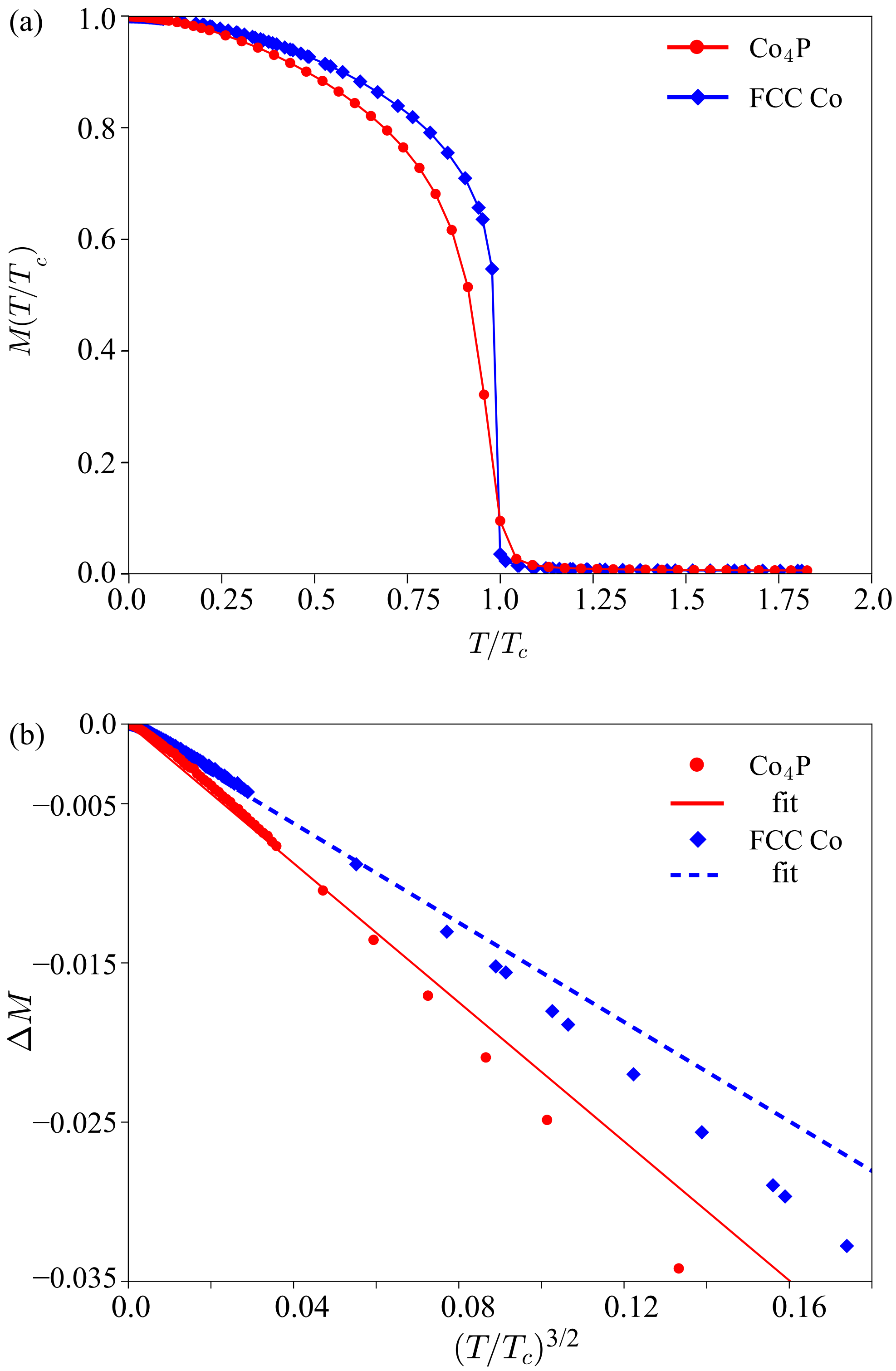

Fig.4.7 (a) Temperature dependence of the magnetization in crystal lattice and amorphous Co_4P. $T_{\rm C} \sim$ 500K in both cases. (b) Normalized temperature $(T/T_{\rm C})^{3/2}$ dependence of the reduced magnetization $\Delta M = M(T/T_{\rm C}) - 1$ in Co_4P and FCC Co. Solid and dashed lines show fits to the Bloch's law, $\Delta M = -B_{3/2}(T/T_{\rm C})^{3/2}$.

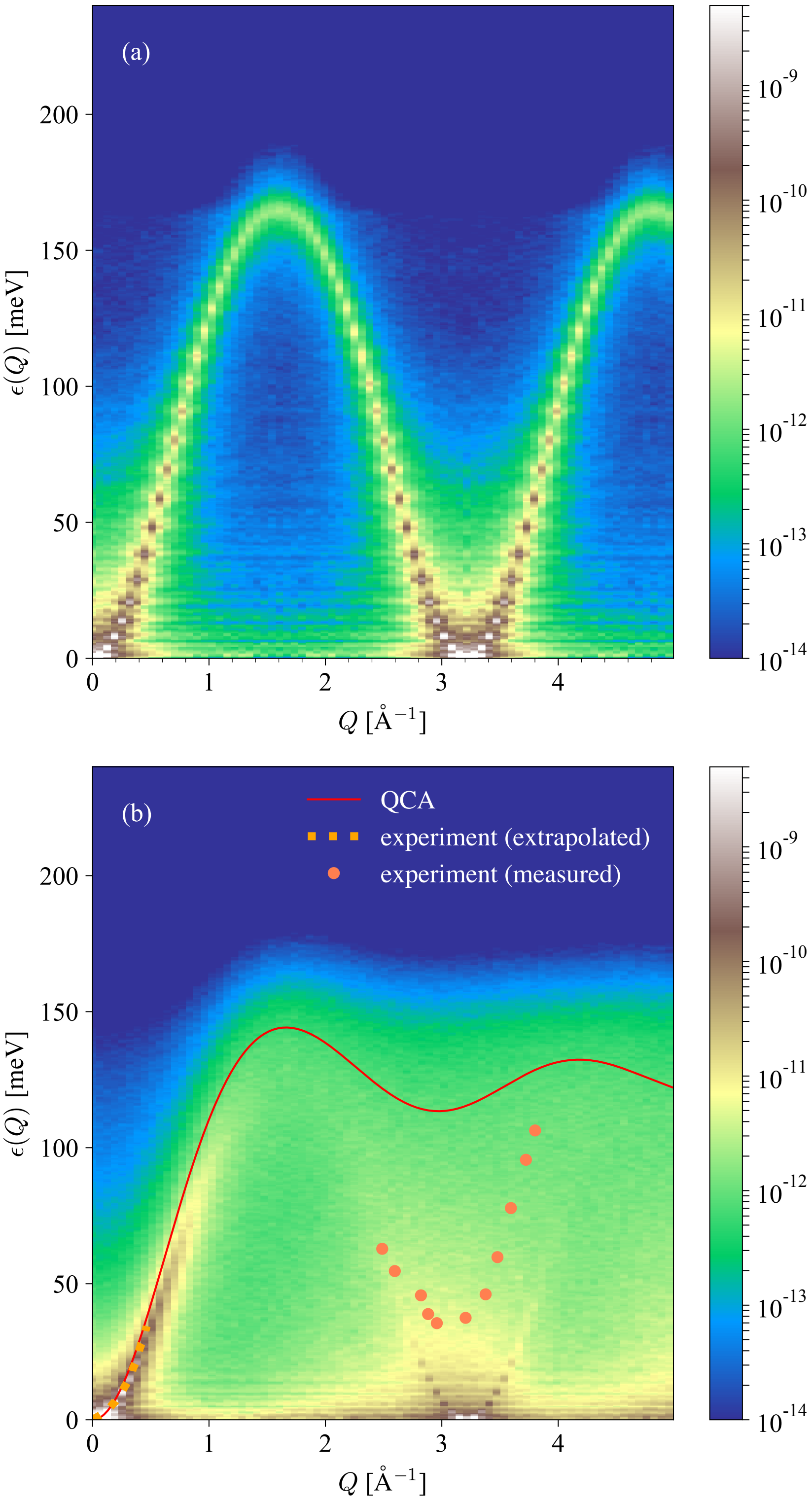

Fig.4.8 (a) Spin wave spectrum of crystalline FCC Co. We use the quantum thermostat at temperature $T = 300K$. The color shows the neutron scattering cross section in Eq.(4.21). (b) Calculated and the QCA spin wave spectrum. The red solid line shows the QCA prediction. The dashed orange line denotes the magnons and the orange dots denote roton-like features, observed in Co$_4$P by [9]. The same parameters are used for both simulations.

4.9 Additional aspects regarding spectra

4.9.1 Dependence on the different asymptotic form of $J(r_{ij})$

To see how the different spatial dependence of $J(r_{ij})$ affect the spectra, we tested many different forms of $J(r_{ij})$. However, just a few of them are shown as examples: exponentially decaying one with the longer decay length and RKKY-like shapes. In Fig. 4.9, we show the relative relations of exchange interaction and the pair-correlation function of Co-Co and the magnetic excitations in the case of exponential decay with longer interaction range, $w = 2.91$ Å. Fig. 4.9(b) shows that the QCA prediction, shown in the red solid line, agrees with the spectrum of higher energy region. In Figs. 4.10, and 4.11, we show the results when the exchange function is RKKY-like. We choose parameters in such a way that it exhibits ferromagnetic state. In this case, we don't see much difference from the exponential function cases. Regardless of the qualitative differences in $J(r_{ij})$, we always find the second dip. We note that the energy scale just reflects the amplitude of J_0 and does not affect the shape of the spectra. We also tested Gaussian form with different range (not shown) and find all the spectra are qualitatively the same.

4.9.2 Dependence on the average coordination number

To see the average coordination number $\mathscr{X}$ dependence of the spectra, we use constant exchange, $J_{ij} = J_0\mathscr{O}(\mathscr{T} - r_{ij})$, where $\mathscr{O}(r)$ is a step function. We note that this assumption also helps us to separate disorder in exchange interaction and disorder in atomic configuration. Exchange interaction length $\mathscr{T}$ is the only parameter in the system, changing averaged coordination number. $\mathscr{X}$ is the $g^{\mathrm{Co-Co}}(r)$ of smaller system, with 16384 atoms. We use a classical thermostat at $T = 10\mathrm{K} \ll T_{\mathrm{C}}$ so that the magnon distribution has enough values at high energies.

In Fig. 4.12 and Fig. 4.13, we show the average coordination number dependence of the energy spectra, ranging from $\mathscr{X} = 5$ to $\mathscr{X} = 32$. Regardless of the number of average neighbours, there is always the magnons near $Q \sim 0$ Å^{-1}. When the average neighbours is larger than 8, the spectrum starts to obey the QCA shown in red solid line in Fig. 4.12 and Fig. 4.13. This again suggests when the average number of the nearest neighbor is large enough, QCA may be a good approximation and is consistent with the fact that QCA is a high-density expansion.

4.9.3 Effect of P vacancy

In Fig.4.14, we compare magnetic spectra of $\mathrm{Co_4Co}$, where we put Co atoms where originally occupied by P atoms. This is to see if the different P vacancy gap the second dip at $Q \sim 3$Å^{-1}. Co atoms are dense in the

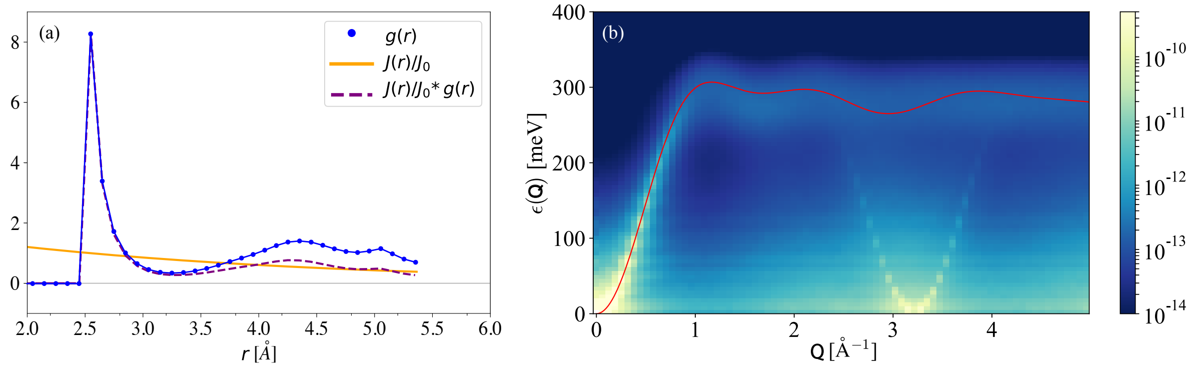

Fig.4.9 (a) Relative relation between $J(r_{ij})$, $g(r)$, and $J(r_{ij})g(r)$. $J(r_{ij})$ is the exponential decay with $J_0 = 13.466$ meV, $r_0 = 2.54$ Å, and $w = 2.91$Å. (b) Spin wave spectrum of amorphous Co$_4$P with classical thermostat at 10 K. The Red line shows the QCA theory.

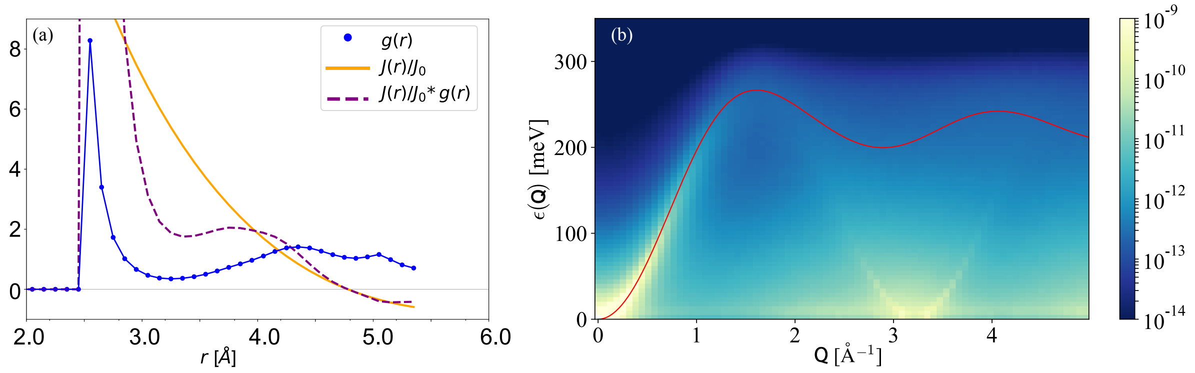

Fig.4.10 (a) Relative relation between $J(r_{ij})$, $g(r)$, and $J(r_{ij})g(r)$. $J(r_{ij})$ is RKKY-like with $J_0 = 163.7439$ meV, $r_0 = 0.0$ Å, and $k_F = 0.47$Å^{-1}. (b) Spin wave spectrum of amorphous Co$_4$P with classical thermostat at 10 K. Red line shows the QCA theory.

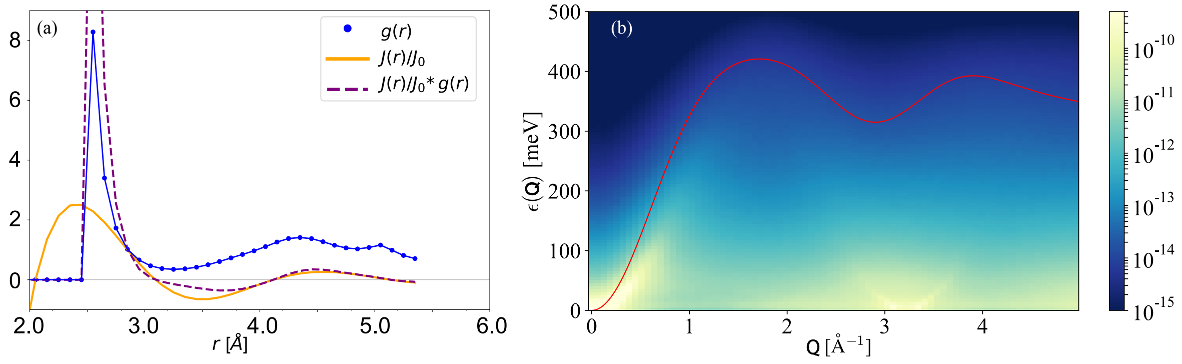

Fig.4.11 (a) Relative relation between $J(r_{ij})$, $g(r)$, and $J(r_{ij})g(r)$. $J(r_{ij})$ is RKKY-like with $J_0 = -4787.9$ meV, $r_0 = 0.6$ Å, and $k_F = 1.55$Å^{-1}. (b) Spin wave spectrum of amorphous Co$_4$P with classical thermostat at 10 K. The Red line shows the QCA theory.

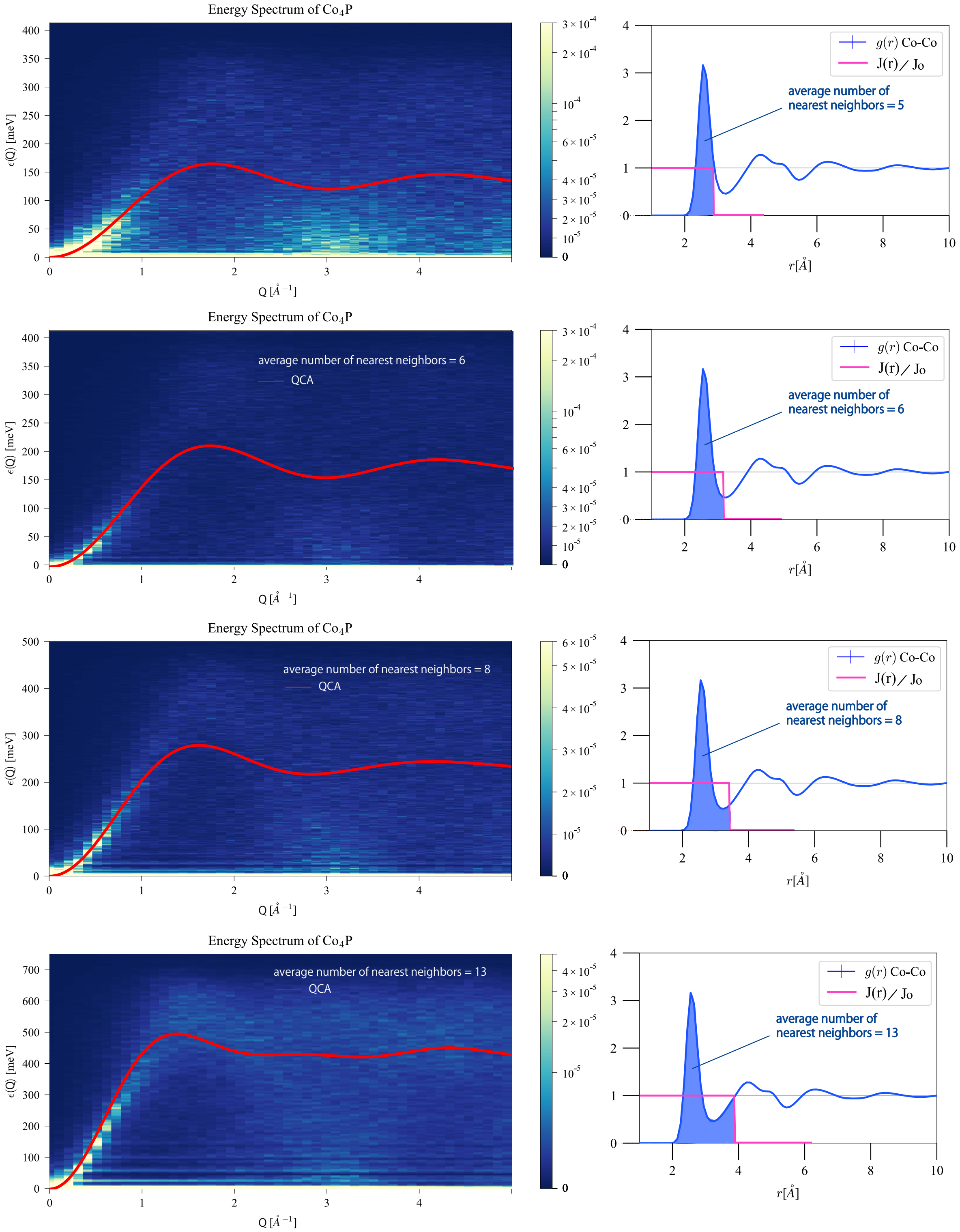

Fig.4.12 Spin wave spectrum of amorphous Co$_4$P when (a) $\mathscr{X}=5$, (b) $\mathscr{X}=6$, (c) $\mathscr{X}=8$, and (d) $\mathscr{X}=13$. $J(r_{ij})$ is the step function.

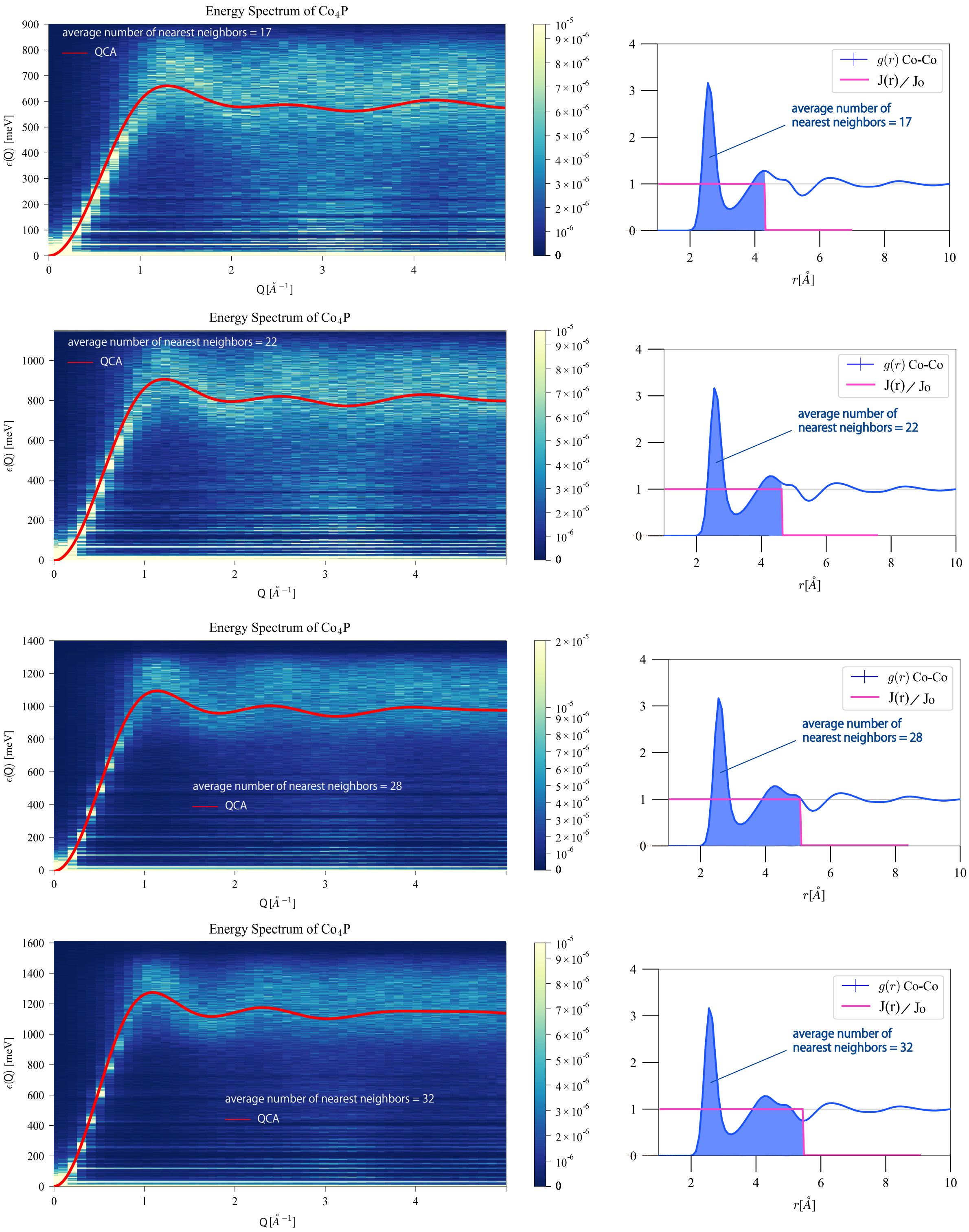

Fig.4.13 Spin wave spectrum of amorphous Co$_4$P when (e) $\mathscr{X} = 17$, (f) $\mathscr{X} = 22$, (g) $\mathscr{X} = 28$, and (h) $\mathscr{X} = 32$. $J(r_{ij})$ is the step function.

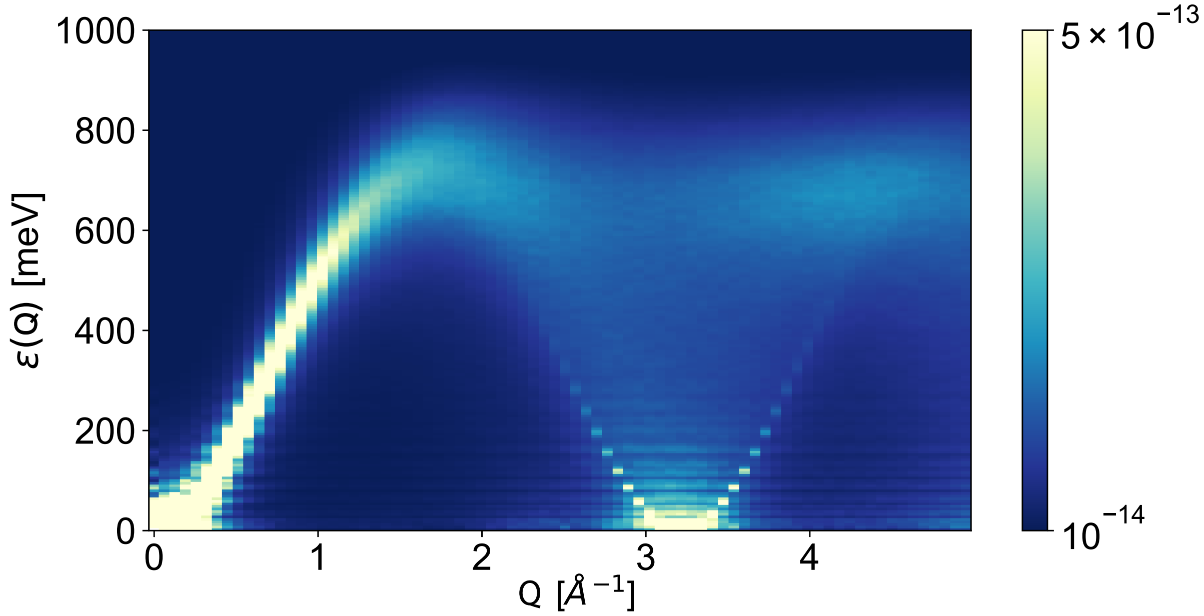

Fig.4.14 Spin wave spectrum of amorphous Co₄Co with classical thermostat at 10 K. $J(r_{ij})$ is the exponential decay with $J_0 = 26.932$ meV, $r_0 = 2.54$ Å, and $w = 0.66$Å.

model and the P concentration is 0%. On the other hand, the results shown so far, i.e., Fig.4.8(b), are the case of 20% concentration. We find that the overall feature does not sensitively depend on the P concentration.

4.10 Conclusion

In conclusion, we have succeeded to built a model for amorphous Co_4P and calculated magnetic properties. We reproduce experimental results, peak positions of static structure factors, Bloch's law in demagnetization, and spin wave stiffness constant of magnons at wavenumber~ 0, without assuming complicated long-range exchange interactions. Also, we find a bright sharp dip in the spin wave spectrum, which is centered at the same wavenumber as the 'roton-dip' measured in Co_4P. Though the dip is gapless, different from the original experiment by Mook et al., it does have a narrow linewidth. This sharp second parabola suggests that there exist low energy magnetic excitations in very short length scales. We attribute this to Umklapp scattering in amorphous ferromagnets [12]. Shirane et al. have pointed out the original experiment only measures one channel, $\mathcal{S}(\boldsymbol{Q},\omega)_{-+}$, of $\mathcal{S}(\boldsymbol{Q},\omega)_{+-} - \mathcal{S}(\boldsymbol{Q},\omega)_{-+}$, which may lead to an experimental artifact to observe the dip. $\mathcal{S}(\boldsymbol{Q},\omega)_{+-} - \mathcal{S}(\boldsymbol{Q},\omega)_{-+}$ should be plotted instead to remove any contributions from phonons and elastic scattering. Our simulation supports gapless magnons and Shirane's argument. The broad spectrum at higher energies indicates a strong scattering or short lifetime of excitations. Our model can be used regardless of the magnetism, which means that this can also be applied to antiferromagnetism or spin-glass systems. We expect it is also a good start to studying spin transport properties in amorphous systems in the field of spintronics. We hope this study encourages many researchers to explore exotic magnets and find many ways to utilize them in the field of spintronics.

Chapter 5

Magnetically ordered states in anisotropic 2D chiral magnets

In this chapter, we discuss the spin configurations in two-dimensional (2D) chiral magnets, especially magnetic skyrmions with the topological number,

$$\mathcal{N} = \frac{1}{4\pi} \int d^2 r \boldsymbol{n}(\boldsymbol{r}) \cdot (\partial_x \boldsymbol{n}(\boldsymbol{r}) \times \partial_y \boldsymbol{n}(\boldsymbol{r})) = \pm 1. \tag{5.1}$$

Recent theory and experiment revealed that the magnetic skyrmions in chiral magnets may be capable of an information carrier of the magnetic memories and computer devices, utilizing their topological stability [13, 57]. To enhance the device controllability, it may be crucial to manipulate the inter-skyrmion interactions. Typically, the skyrmion-skyrmion interaction between two circular symmetric skyrmions is known to be only repulsive. Recently, however, attractive inter-skyrmion interactions are found to appear in some specific chiral magnets; In a system with frustrated exchange coupling [100] and in the three-dimensional (3D) cone phase [17, 18]. However, the general mechanism of the appearance of the attraction has been unclear and thus the manipulation of the interaction has been impossible.

In this study, we theoretically investigate the 2D chiral magnet with in-plane anisotropy. We analytically derive an approximated interaction potential at a distance and numerically study the interaction under an in-plane magnetic field and/or a magneto-crystalline anisotropy [21]. In general, the magneto-crystalline anisotropy depends on the crystal plane direction to the film [101, 102, 103, 22]. We consider a (011) film to break the C_4 symmetry in spin space to create distorted skyrmions. Furthermore, we study the SkX configurations induced by attractive interactions. By changing the strength of the external magnetic field and the magneto-crystalline anisotropy constant, we investigate the optimal lattice structures in detail.

In Figs. 5.1(a)-(d), we summarize the calculation setups in (a) isotropic system where the magnetic field

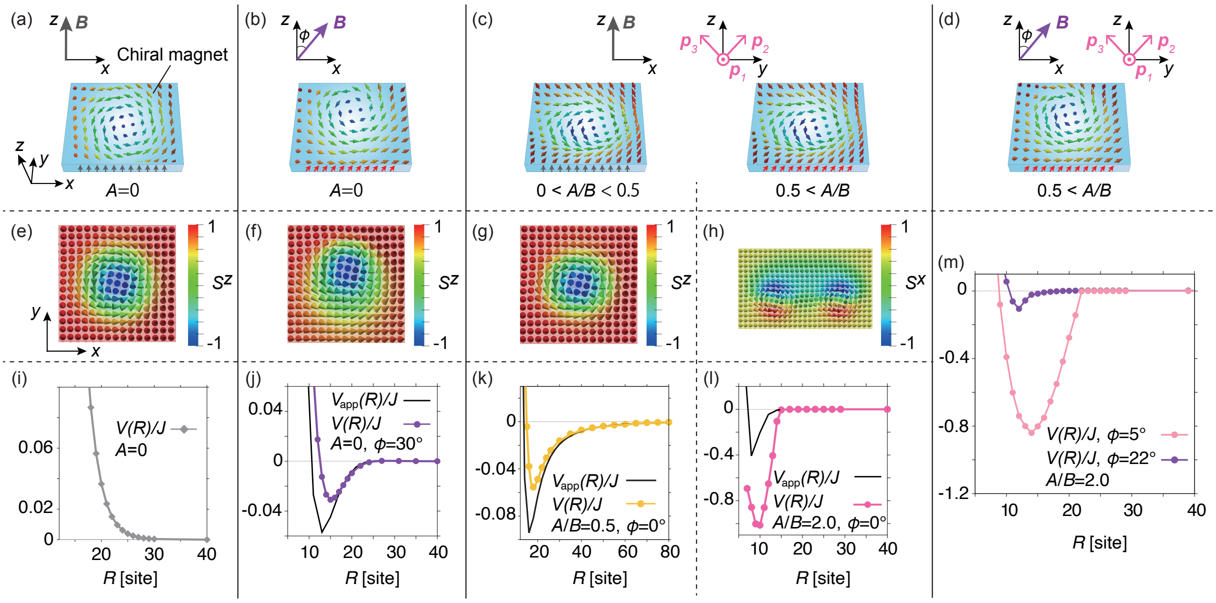

Fig.5.1 (a)-(d) Calculation setups (a) in an isotropic geometry where the magnetic field $\boldsymbol{B}$ points to the perpendicular direction z, (b) in an in-plane magnetic field with the tilting angle ϕ, (c) under a magnetocrystalline anisotropy with three hard axes $\hat{\boldsymbol{p}}_{1,2,3}$ and anisotropy constant A, and (d) in both in-plane magnetic field and the magnetic anisotropy. The parameters $(BJ/D^2$, ϕ, $A/B)$ are (e) (0.75, 0, 0), (f) (0.75, 30°, 0), (g) (0.75, 0, 0.5), and (h) that of a bounded skyrmion pair with (0.75, 0, 2.0). (i)-(m) Inter-skyrmion interaction potential in each case. The parameters are the same. Reproduced from [21]. Copyright 2021, American Physical Society.

$\boldsymbol{B}$ points to the perpendicular direction $\boldsymbol{B} \parallel \boldsymbol{e}_z$, (b) under the in-plane magnetic field with tilting angle ϕ, (c) under the magnetocrystalline anisotropy with the three hard axes $\hat{\boldsymbol{p}}_{1,2,3}$ and anisotropy constant A, and (d) under both the tilted magnetic field and the magnetic anisotropy. Figure 5.1(e)-(h) shows the typical single-skyrmion shape in each case. We plot inter-skyrmion potentials in each setup in Fig. 5.1(i)-(m).

In this study, we found the following things:

- The analytic expression of approximated inter-skyrmion interaction, $V_{\rm app}(R)$, at a distance R can be obtained from a single skyrmion configuration.
- $V_{\rm app}(R)$ correctly predicts the interaction $V(R)$ at a large distance.
- There are two mechanisms of inducing the attractive interactions: a small deformation of skyrmion shape and formation of magnetic domain between two skyrmions.
- A small distortion of skyrmions and the formation of the magnetic domain can induce small and large attractions, respectively.
- The attractive interaction induces elongated triangular bimeron lattice with magnetic domains in the background, as a ground state.
- 1D skyrmion chain appears as an excitation in the FM phase.
- There is a range of the magnetic field where the SkX is sustained by the attractive interaction.
- The attraction can be tuned in the range over double-digit by the in-plane magnetic field.

5.1 Magnetic skyrmions

Magnetic skyrmions are nanometer-sized spin vortices with the finite topological number $\mathcal{N}$. People are interested in them due to the potential applications as an information carrier of magnetic memories and computing devices, utilizing their topological stability [13, 57]. Skyrmions were originally suggested as an elementary excitation by T. Skyrme in nuclear physics [104], whereas skyrmions found in chiral magnets form a skyrmion crystal (SkX) which appears in thermal equilibrium [59] and stabilized due to the Dzyaloshinskii-Moriya (DM) interaction [60, 61]. These skyrmions are found in chiral magnets, i.e., B20-type alloys MX ($M=$ Mn, Fe, Co; $X=$ Si, Ge) [58, 63] and β-Mn type Co-Zn-Mn alloys [101]. Experimental identification of the skyrmionic spin textures are conducted by the ac-susceptibility measurements [62], Fourier-space imaging by neutron small-angle scattering intensities [58], real-space imaging by Lorentz transmission electron microscopy [63], and detection of the topological Hall effect [64, 65].

In order to expand skyrmion-hosting materials, with the aim of utilizing a magnetic skyrmion for an information carrier, many attempts have been conducted both theoretically and experimentally. The basic materials to stabilize skyrmions are non-centrosymmetric magnets, such as chiral magnets and the polar magnets, GaV_4S_8 and GaV_4Se_8 [105, 106]. The Bloch-type skyrmions are found in the former case and the Néel-type skyrmions are observed in the latter case. Some of the skyrmion hosting materials are multiferroic, such as the chiral magnet Cu_2OSeO_3 [107, 108, 109] and the polar magnets GaV_4S_8 and GaV_4Se_8, suggesting the possibility of controlling skyrmion motions by means of the electric field [110, 111, 112]. Strong DM interactions are also induced in multilayer systems of magnetic layer and heavy metal layers, such as iron mono-, bi-, and tri- layers on an Ir substrate. The system hosts atomic-scale skyrmions [113, 114, 115, 116, 117]. At room temperature, multilayer stacks of Pt/CoFeB/MgO, Pt/Co/Ta, and Pt/Co/MgO stabilize skyrmions [118, 119, 120]. In addition, recently the centrosymmetric magnets Gd_2PdSi_3 [121] and $GdRu_2Si_2$ [122] are also found to host skyrmions: The former is because of a triangular lattice structure which is geometrically frustrated [123] and the latter is due to the four-spin interactions via itinerant electrons. The very small skyrmions ($\sim$ 2 nm in diameter) are found in these materials, which is appealing not only for the possible new mechanism of stabilizing skyrmions but also for the potential applicability to the high-density magnetic storage. We note that spin configurations with different topological charge from the Bloch and the Néel skyrmions with $\mathcal{N}=1$, such as anti-skyrmions with charge $\mathcal{N}=-1$ [124, 125] and merons with charge $\mathcal{N}=1/2$ [102, 22], have also been observed.

In this study, we focus on chiral magnets, FeGe and Co-Zn-Mn alloys, a few examples of them, stabilize either stable or meta-stable skyrmions in the wide region in the temperature–magnetic field phase diagram. The temperature range includes room temperature and the magnetic field range expands up to $\sim$ 0.5 T [101, 126, 127, 102, 128, 103, 129]. In FeGe, even at zero-field, robust skyrmions are observed [130]. Though in a bulk chiral magnet, the SkX phase is restricted to a small area in the vicinity of the Curie temperature [58], the SkX phase expands until 0 K in thin films [63, 131, 132, 107, 133].

5.1.1 Analysis of a typical model of chiral magnets

Let us analyze the most fundamental Hamiltonian composed of three terms. This model is the minimum model to exhibit SkX phase as a ground state,

$$F_{\text{typ.}}[\boldsymbol{n}] = \int \frac{d^2r}{a^2} f_{\text{typ.}}[\boldsymbol{n}(\boldsymbol{r}), \boldsymbol{\nabla}\boldsymbol{n}(\boldsymbol{r})], \tag{5.2}$$

$$f_{\text{typ.}}[\boldsymbol{n}(\boldsymbol{r}), \boldsymbol{\nabla}\boldsymbol{n}(\boldsymbol{r})] = \frac{Ja^2}{2}[(\partial_x \boldsymbol{n})^2 + (\partial_y \boldsymbol{n})^2] + Da\boldsymbol{n} \cdot (\boldsymbol{\nabla} \times \boldsymbol{n}) - \boldsymbol{B} \cdot \boldsymbol{n}. \tag{5.3}$$

The form of the DM interaction, the second term of $f_{\text{typ.}}[\boldsymbol{n}(\boldsymbol{r}), \boldsymbol{\nabla}\boldsymbol{n}(\boldsymbol{r})]$, in chiral magnets is in general given by $a\boldsymbol{D} \cdot (\partial_x \boldsymbol{n} \times \boldsymbol{n} + \partial_y \boldsymbol{n} \times \boldsymbol{n})$, where $\boldsymbol{D} \parallel [111]$ in i.e., MnSi and Co-Zn-Mn alloys. Theoretically, a Monte Carlo simulation has found that $\boldsymbol{D} = \boldsymbol{e}_x(\boldsymbol{e}_y)$ along $x(y)$ direction reproduces qualitatively the same phase diagram of $\boldsymbol{B} = B\boldsymbol{e}_z$ as observed experimentally [134, 63]. The sign of D determines the helicity of the skyrmions, the winding direction of the in-plane spin components, and the sign of the topological charge $\mathcal{N} = \pm 1$. The 1D phase diagram under $\boldsymbol{B} = B\boldsymbol{e}_z$ is schematically shown in Fig. 5.2. This is found by another Monte Carlo analysis under the same Hamiltonian $f_{\text{typ.}}$ at 0K [55]. When $B = 0$, Helix phase propagating in the x direction with wavenumber Q (shown in the low field region in Fig. 5.2) is written as

$$\mathbf{n}_{\text{2DHL}} = (0, \text{cos}Qx, \text{sin}Qx). \tag{5.4}$$

Its length scale is estimated as $\sim D/J$ by

$$\frac{\partial f_{\text{typ.}}}{\partial Q} = Ja^2Q - Da = 0 \tag{5.5}$$

$$\rightarrow (\text{preferred Q}) = \frac{D}{Ja}. \tag{5.6}$$

By inserting $\mathbf{n}_{\text{2DHL}}$ into above energy functional, the energy of Helix is found to be $E_{\text{2DHL}} = -\frac{D^2}{2J}$. The phase boundaries are of the same order of E_{2DHL}; When the energy profit from Zeeman energy overcomes E_{2DHL}, the SkX phase appears. Indeed SkX phase emerges at intermediate field, $B > B_{\text{cr1}} \sim 0.23D^2/J$ and ferromagnetic phase (FM) appears at high field, $B > B_{\text{cr2}} \sim 0.78D^2/J$ [55]. In the 3D model, on the other hand, the SkX phase is no longer a ground state, since the 3D cone phase has lower energy. The cone phase, twists along the z direction, can only appear in the 3D model and hence SkX remains the ground state in the

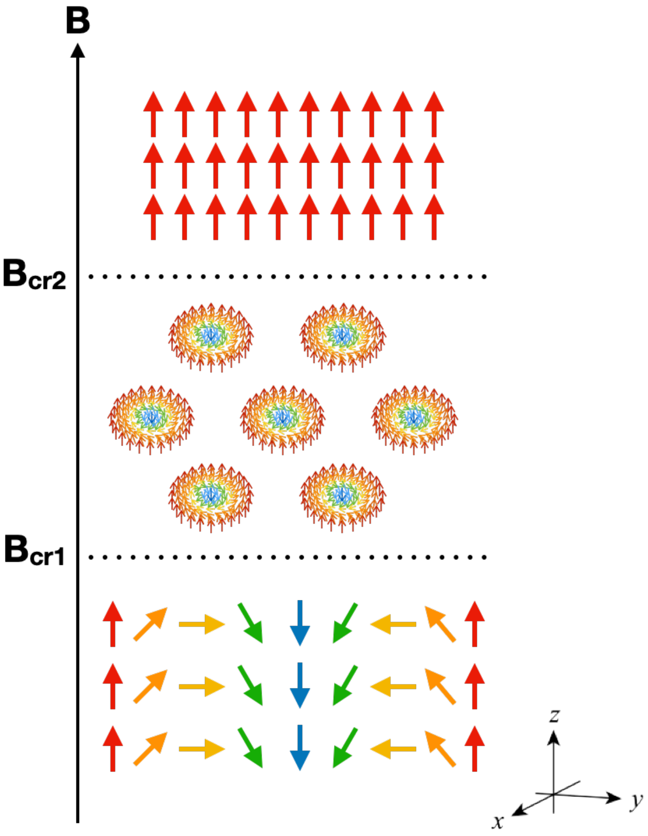

Fig.5.2 1D phase diagram of external magnetic field $\boldsymbol{B} = B\boldsymbol{e}_z$. Helix, SkX, and FM phase appears respectively at low, intermediate, and high field. Helix–SkX phase boundary is denoted by B_{cr1} and SkX–FM phase boundary is B_{cr2}.

2D model.

5.2 Inter-skyrmion repulsions / attractions in isotropic / anisotropic systems

It may be crucial to manipulate inter-skyrmion interactions to enhance the device controllability. Note that we consider inter-skyrmion interactions between those embedded in a uniform background spins (FM state). Typically, the skyrmion-skyrmion interaction is known to be repulsive and decays exponentially in a 2D circular symmetric chiral magnet, under out-of-plane magnetic field [135, 14].

However, by taking the 3D magnetic structures into account, the attractive inter-skyrmion interactions are explained both in a bulk and a thin film [16, 17, 18]. The attractive interaction accompanied with the magnetization softening in the vicinity of the Curie temperature is also reported [136]. There are a few other ways known to induce the attractions, besides chiral magnets: With the frustrated exchange interactions, oscillatory property of the inter-skyrmion interaction, between repulsion and attraction, are found [100, 137]; In the case of a polar magnet, anisotropic interactions are found between two skyrmions in a tilted background FM state, and they are connected in a certain direction [138]; In centrosymmetric magnetic films, a tightly bound pair of two skyrmions, called biskyrmions, are reported. They are stabilized due to the dipole-dipole interaction combined with the easy-axis anisotropy [139, 140, 141, 142]. The interactions between two skyrmions with higher topological charge, $\mathcal{N} > 1$, are also studied in Refs. [143, 144].

5.3 Analytic expression of the interaction

We consider a thin film and use a continuum model, assuming that spin configuration varies slowly compared to the lattice parameter a in space. The energy density is expressed as

$$F[\boldsymbol{n}] = \int \frac{d^2r}{a^2} f[\boldsymbol{n}(\boldsymbol{r}), \boldsymbol{\nabla}\boldsymbol{n}(\boldsymbol{r})] \tag{5.7}$$

$$f[\boldsymbol{n}(\boldsymbol{r}), \boldsymbol{\nabla}\boldsymbol{n}(\boldsymbol{r})] = \frac{Ja^2}{2}[(\partial_x \boldsymbol{n})^2 + (\partial_y \boldsymbol{n})^2] + Da\boldsymbol{n}\cdot(\boldsymbol{\nabla}\times\boldsymbol{n}) + U_{\mathrm{c}}(\boldsymbol{n}, \boldsymbol{\nabla}\boldsymbol{n}). \tag{5.8}$$

The coordinate axes are taken in such a way that the x-y plane is the in-plane. f stands for the energy per one spin, $\boldsymbol{n}(\boldsymbol{r})$ is the direction of the magnetization and a 3D unit vector, J is the spin-exchange interaction coefficient, D is the magnitude of the the DM interaction, a is the lattice parameter of the original lattice model, and $U_{\mathrm{c}}(\boldsymbol{n}, \boldsymbol{\nabla}\boldsymbol{n})$ expresses the anisotropy potential in the spin space which is a function of $\boldsymbol{n}$ and $\boldsymbol{\nabla}\boldsymbol{n} = (\partial_x \boldsymbol{n}, \partial_y \boldsymbol{n})$. We assume there is a stationary solution of a ferromagnetic state $\boldsymbol{n}(\boldsymbol{r}) = \hat{\boldsymbol{t}}$, in the system. This solution is stabilized by a magnetic field $B \parallel \hat{\boldsymbol{t}}$, and in this case, the anisotropy potential is

$$U_{\mathrm{c}}(\boldsymbol{n}, \boldsymbol{\nabla}\boldsymbol{n}) = -B\hat{\boldsymbol{t}}\cdot\boldsymbol{n}. \tag{5.9}$$

The uniform solution $\hat{\boldsymbol{t}}$ emerges as either stable or metastable in the vicinity of the FM – SkX phase boundary at least. We focus on the interaction between two such isolated skyrmions in the region.

Let's evaluate the inter-skyrmion interaction at a distance. We assume that a single-skyrmion state $\boldsymbol{n}_{1\mathrm{sk}}(\boldsymbol{r})$ is a stationary solution, where a skyrmion located at $\boldsymbol{r} = \boldsymbol{0}$ is embedded in a FM configuration, i.e.,

$$\boldsymbol{n}_{1\mathrm{sk}}(\boldsymbol{0}) = -\hat{\boldsymbol{t}}, \boldsymbol{n}_{1\mathrm{sk}}(\infty) = \hat{\boldsymbol{t}}. \tag{5.10}$$

Using above state $\boldsymbol{n}_{1\mathrm{sk}}$, we obtain a spin state of two skyrmions located at points

$$\mathrm{P}_{\pm} : \boldsymbol{r} = \pm\boldsymbol{R}/2 \tag{5.11}$$

by adding two vector fields,

$$\boldsymbol{n}_{\pm}(\boldsymbol{r}) = \boldsymbol{n}_{1\mathrm{sk}}(\boldsymbol{r} \mp \boldsymbol{R}/2), \tag{5.12}$$

utilizing the stereographic projection [135]. We introduce

$$\mathcal{R} : S^2 \mapsto S^2 \tag{5.13}$$

as a rotation operator about $\boldsymbol{e}_z \times \hat{\boldsymbol{t}}$ by angle $\arccos(\boldsymbol{e}_z \cdot \hat{\boldsymbol{t}})$, with $\boldsymbol{e}_\alpha$ $(\alpha = x, y, z)$ is the unit vector along the α direction. Fig. 5.3 schematically shows that the rotation $\mathcal{R}$ maps $\boldsymbol{e}_z$ to $\hat{\boldsymbol{t}}$, i.e.,

$$\mathcal{R}\boldsymbol{e}_z = \hat{\boldsymbol{t}}, \tag{5.14}$$

and the x-y plane the plane which is perpendicular to $\hat{\boldsymbol{t}}$. The stereographic projection

$$p : \mathbb{C} \cup \infty \mapsto S^2 \tag{5.15}$$

maps a complex number $u = u_1 + iu_2$ to a 3D unit vector in a following way;

$$p(u) = \frac{2u_1, 2u_2, 1 - |u|^2}{1 + |u|^2}. \tag{5.16}$$

The double-skyrmion state is thus given by

$$\boldsymbol{n}_{2\mathrm{sk}} = \mathcal{R}p[p^{-1}\mathcal{R}^{-1}(\boldsymbol{n}_+) + p^{-1}\mathcal{R}^{-1}(\boldsymbol{n}_-)]. \tag{5.17}$$

The detailed calculations can be found in Appendix C. The interaction potential is defined as the energy difference of a double-skyrmion state and two single-skyrmion states concerning the FM state:

$$V(\boldsymbol{R}) = \int \frac{d^2r}{a^2} \left[f(\boldsymbol{n}_{2\mathrm{sk}}) - f(\boldsymbol{n}_+) - f(\boldsymbol{n}_-) + f(\hat{\boldsymbol{t}}) \right]. \tag{5.18}$$

After extensive calculations (see Appendix D for details), we identify that $V(\boldsymbol{R})$ at a large distance may be given by

$$V_{\mathrm{app}}(\boldsymbol{R}) = \frac{1}{a^2} \int_\Gamma \epsilon_{ij}(A_{-+} - A_{+-})_i dl_j, \tag{5.19}$$

$$(A_{+-})_i = \frac{\partial^2 f(\hat{\boldsymbol{t}})}{\partial n_\alpha \partial(\partial_i n_\beta)} \delta n_{+,\alpha} \delta n_{-,\beta} + \frac{\partial^2 f(\hat{\boldsymbol{t}})}{\partial(\partial_k n_\alpha)\partial(\partial_i n_\beta)} (\partial_k \delta n_{+,\alpha}) \delta n_{-,\beta} \tag{5.20}$$

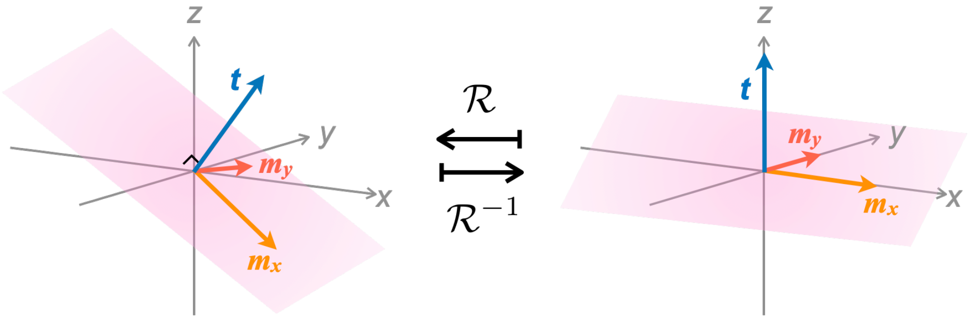

Fig.5.3 Definition of the rotational operater $\mathcal{R}$ and its inverse operator $\mathcal{R}^{-1}$ which acts in the spin space. The operator $\mathcal{R}^{-1}$ maps $\hat{\boldsymbol{t}}$ to $\boldsymbol{e}_z$ and the plane orthogonal to $\hat{\boldsymbol{t}}$ to the x-y plane. The vector $\boldsymbol{m} = \mathcal{R}^{-1}(\boldsymbol{n})$ stands for the magnetization whose z component is always parallel to the direction of the uniform stationary solution $\hat{\boldsymbol{t}}$. The projection of $\boldsymbol{n}$ to the $\mathcal{R}\boldsymbol{e}_x$, $\mathcal{R}\boldsymbol{e}_y$, and $\mathcal{R}\boldsymbol{e}_z$ corresponds to m_x, m_y and $m_z = \hat{\boldsymbol{t}}$, respectively.

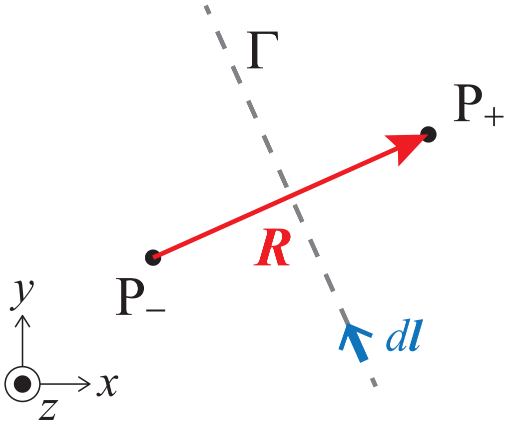

Fig.5.4 Schematic geometry considered for calculating the inter-skyrmion interaction. The two skyrmions are placed at P_+ and P_-. The line integral along Γ approximates the interaction between the skyrmions, as shown by Eq. (5.19). Reproduced from [21]. Copyright 2021, American Physical Society.

where Γ shows the orthogonal bisector of the segment $\mathrm{P}_+\mathrm{P}_-$, $d\boldsymbol{\ell}$ is the line element of Γ along $\boldsymbol{e}_z \times \boldsymbol{R}$ (see Fig. 5.4), ϵ_{ij} expresses the Levi-Civita symbol, and we imply to sum up repeated indices, where Roman (Greek) indices stand for the components in the coordinate (spin) space and return the values x and y (x, y and z). Here, we use $\delta\boldsymbol{n}$ to express the projection vector of $\boldsymbol{n}$ on the perpendicular plane to $\hat{\boldsymbol{t}}$, i.e., $\delta\boldsymbol{n} \equiv \boldsymbol{n} - (\boldsymbol{n}\cdot\hat{\boldsymbol{t}})\hat{\boldsymbol{t}}$. To derive Eq. (5.20), we assumed that $\delta\boldsymbol{n}_\pm$ on the integral path Γ is sufficiently small so that approximated $\boldsymbol{n}_\pm$ are given by

$$\boldsymbol{n}_\pm = \sqrt{1 - |\delta\boldsymbol{n}_\pm|^2}\,\hat{\boldsymbol{t}} + \delta\boldsymbol{n}_\pm \simeq \hat{\boldsymbol{t}} + \delta\boldsymbol{n}_\pm. \tag{5.21}$$

We note that the approximated potential, Eqs. (5.19) and (5.20), can be used to other continuum spin models as far as they have a FM state and a confined skyrmion in it as stable spin configurations.

5.3.1 Anisotrpic potential

As the anisotropy potentials, we consider the Zeeman field and the magneto-crystalline anisotropy. The Zeeman field contributes to $U_{\rm c}$ as

$$U_{\rm c}^{(\rm Ze)}(\boldsymbol{n}, \boldsymbol{\nabla}\boldsymbol{n}) = -\boldsymbol{B}_{\rm ex} \cdot \boldsymbol{n}(\boldsymbol{r}), \tag{5.22}$$

where $\boldsymbol{B}_{\rm ex}$ expresses a uniform magnetic field.

The lowest-order contribution of the magneto-crystalline anisotropy on a 3D cubic lattice is given by [145]

$$U_{\rm c}^{(\rm mc,3D)}(\boldsymbol{n}, \boldsymbol{\nabla}\boldsymbol{n}) = \sum_{\nu=1,2,3} \left\{ A(\boldsymbol{n} \cdot \hat{\boldsymbol{p}}_\nu)^4 - \frac{Ka^2}{2}[\partial_\nu(\boldsymbol{n} \cdot \hat{\boldsymbol{p}}_\nu)]^2 \right\}, \tag{5.23}$$

where A and K show the anisotropy coefficients, $\hat{\boldsymbol{p}}_{1,2,3}$ are the unit vectors along crystalline axes, and the derivative along $\hat{\boldsymbol{p}}_\nu$ is denoted by ∂_ν. We consider a (011) thin film, not a (001) thin film which is typically considered, since the crystal orientation would result in distorted skyrmions. This is due to the breaking of the C_4 symmetry in the spin space. The magneto-crystalline anisotropy in this case is expressed with $\hat{\boldsymbol{p}}_1 = \boldsymbol{e}_x$, $\hat{\boldsymbol{p}}_2 = (\boldsymbol{e}_y + \boldsymbol{e}_z)/\sqrt{2}$, and $\hat{\boldsymbol{p}}_3 = (-\boldsymbol{e}_y + \boldsymbol{e}_z)/\sqrt{2}$. In a 2D film, we can ignore ∂_z since it is sufficiently thin along the z axis. The resulting anisotropy potential is given by

$$U_{\rm c}^{(\rm mc,011)}(\boldsymbol{n}, \boldsymbol{\nabla}\boldsymbol{n}) = A\left[n_x^4 + \frac{(n_y+n_z)^4}{4} + \frac{(-n_y+n_z)^4}{4}\right] - \frac{Ka^2}{4}\left[2(\partial_x n_x)^2 + (\partial_y n_y)^2 + (\partial_y n_z)^2\right]. \tag{5.24}$$

5.3.2 Concrete expression for the interaction

Using Eq. (5.8) and the anisotropic potential $U_{\rm c} = U_{\rm c}^{\rm Ze} + U_{\rm c}^{(\rm mc,011)}$, Eq. (5.20) becomes

$$\begin{aligned}
&(A_{+-})_i \\
&= Ja^2(\partial_i \delta\boldsymbol{n}_+) \cdot \delta\boldsymbol{n}_- \\
&- Da(\delta\boldsymbol{n}_+ \times \delta\boldsymbol{n}_-)_i \\
&- Ka^2(\partial_x \delta n_{+,x})\delta n_{-,x}\delta_{i,x} \\
&- \frac{Ka^2}{2}\left[(\partial_y \delta n_{+,y})\delta n_{-,y} + (\partial_y \delta n_{+,z})\delta n_{-,z}\right]\delta_{i,y}.
\end{aligned} \tag{5.25}$$

We next discuss how each term contributes to the inter-skyrmion interaction.

Circular symmetric case

In the circular symmetric case, where the perpendicular external magnetic field is applied $\boldsymbol{B}_{\text{ex}} = B\boldsymbol{e}_z$ and no magneto-crystalline anisotropy is assumed $A = K = 0$. Obviously the uniform solution for this setup is $\hat{\boldsymbol{t}} = \boldsymbol{e}_z$. In this case, the only contribution becomes finite is the J term; The contribution from the D term of Eq. (5.25) vanishes due to $\delta\boldsymbol{n}_+ \times \delta\boldsymbol{n}_- \parallel \hat{\boldsymbol{t}} = \boldsymbol{e}_z$. The J term at a distance is given by

$$V_{\text{app}}(\boldsymbol{R}) = 2J \int_{\Gamma} \epsilon_{ij} \left(\partial_i \delta\boldsymbol{n}_-\right) \cdot \delta\boldsymbol{n}_+ dl_j, \tag{5.26}$$

with the partial integration using $\delta\boldsymbol{n}_\pm(\infty) = 0$. The obtained expression is the same as the consequence of the baby Skyrme model [135]. In addition, we can also evaluate Eq. (5.26) in the same manner. In fact we indeed reproduce a repulsive inter-skyrmion interaction $V_{\text{app}}(\boldsymbol{R}) \propto Ja^2 K_0(\sqrt{B/J}|\boldsymbol{R}|)$, where (r, φ) is the polar coordinates with respect to the center of the skyrmion, and $K_n(z)$ is the modified Bessel function of n-th order. The approximated behavior is known to be $K_n(z) \sim \sqrt{\pi/2z}e^{-z}$ when $z \to \infty$. To obtain the above interaction, we use the asymptotic solution of one skyrmion, $\delta\boldsymbol{n}_{1\text{sk}}(r, \varphi) \sim K_1(\sqrt{B/Ja^2}r)(-\sin\varphi, \cos\varphi, 0)$.

Effect of skyrmion deformation

We emphasize that it is a subtle energy balance between the x and y components of the inner product in the integrand of Eq. (5.26) that decides the sign of the interaction. In the above case, it results in the repulsive inter-skyrmion interaction. To see this point, let us rewrite Eq. (5.26), by choosing $\boldsymbol{R} = R\boldsymbol{e}_x$, as

$$V_{\text{app}}(R\boldsymbol{e}_x) = 2J \int_{-\infty}^{\infty} \sum_{\alpha = x, y} \left[\partial_x m_\alpha(R/2, y)\right] m_\alpha(-R/2, y) dy, \tag{5.27}$$

where $\boldsymbol{m} \equiv \mathcal{R}^{-1}(\boldsymbol{n}_{1\text{sk}})$, and m_x and m_y are the in-plane components of $\boldsymbol{n}$ which are projected on the perpendicular plane to $\hat{\boldsymbol{t}}$ [see Fig. 5.3]. Fig. 5.5 shows the plot of x and y components of the $\boldsymbol{m}$ and $\partial_x \boldsymbol{m}$ in the x-y plane. We numerically obtain $\boldsymbol{m}$ as a stationary solution of the LLG equation (see Methods). We also plot $\boldsymbol{m}$ and $\partial_x \boldsymbol{m}$ along $x = \pm R_{\text{ref}}$ for various $U_{\text{c}}(\boldsymbol{n}, \boldsymbol{\nabla}\boldsymbol{n})$ in Fig. 5.5, where we set R_{ref} to be similar to the skyrmion radius. Figure 5.5(a) is the result for $U_{\text{c}}(\boldsymbol{n}, \boldsymbol{\nabla}\boldsymbol{n}) = -Bn_z$, from which one may see that the product of the x (y) components contributes negatively (positively) to Eq. (5.27). In case (a), the summation of these terms results in small positive value, a repulsive interaction. This subtle balance can be easily changed by the skyrmion deformations either by tilting the external magnetic field [Fig. 5.5(b)] or by offering the magneto-crystalline anisotropy [Fig. 5.5(c)]. In Figs. 5.5(b) and 5.5(c), we can see that the contribution from the x (y) components becomes larger (smaller) and the resulting interaction becomes attractive.

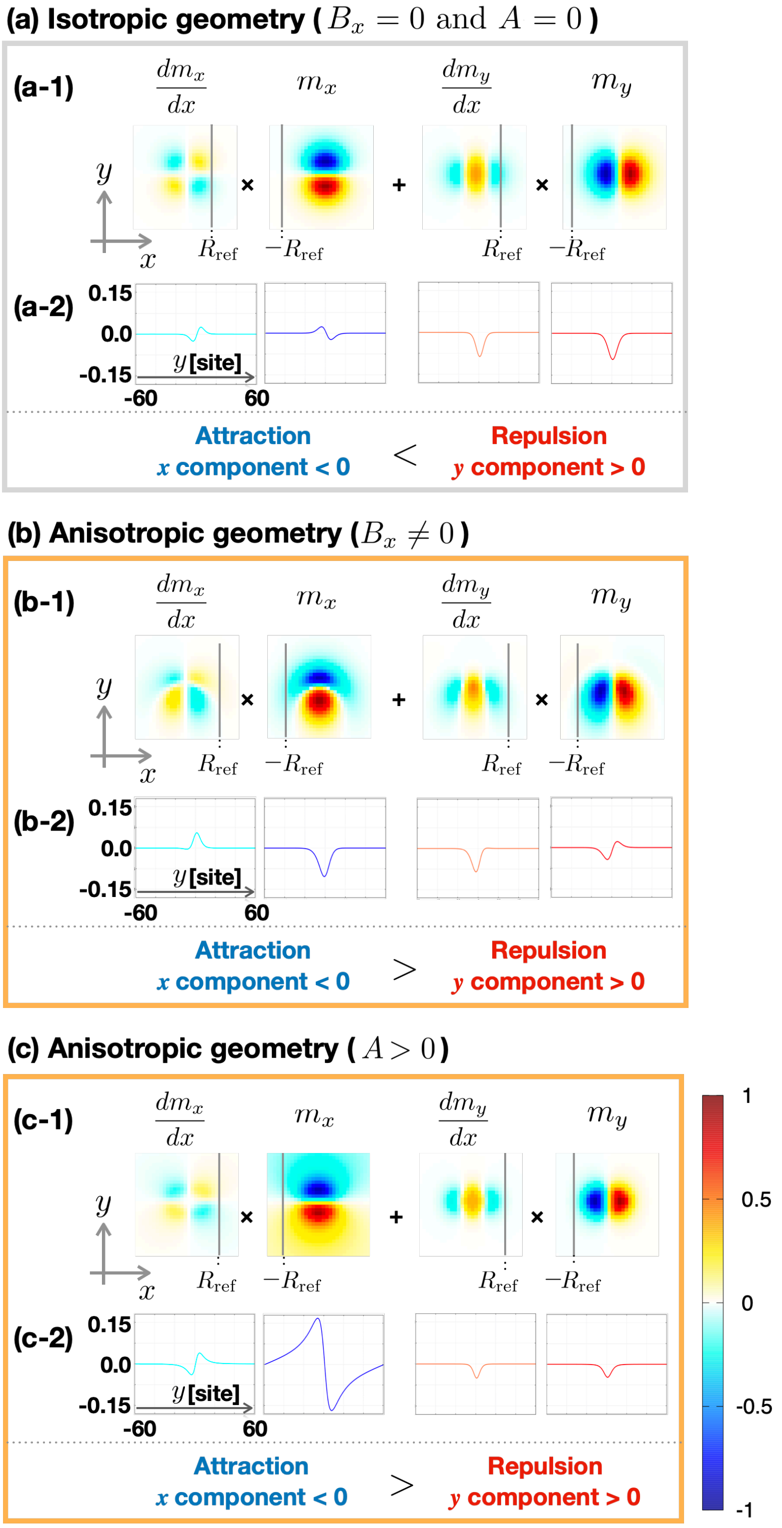

Fig.5.5 Summary of the each term, x and y components, of the integral Eq. (5.27) in (a) circular skyrmions and (b), (c) distorted skyrmions. Under the anisotropic potential $U_{\rm c} = U_{\rm c}^{\rm (Ze)} + U_{\rm c}^{\rm (mc,011)}$, we numerically obtain the single-skyrmion solution $\boldsymbol{n}_{\rm 1sk}$. Panels are for (a) $\boldsymbol{B}_{\rm ex} \parallel \boldsymbol{e}_z$ and $A = K = 0$, (b) $\boldsymbol{B}_{\rm ex} \parallel (\sin 30^\circ, 0, \cos 30^\circ)$ and $A = K = 0$, and (c) $\boldsymbol{B}_{\rm ex} \parallel \boldsymbol{e}_z$, $A \neq 0$, and $K = 0$, respectively. (a-1)-(c-1) Color plots shows the spatial distributions of $\partial_x m_x, m_x, \partial_x m_y$, and m_y in the thin film plane. $\boldsymbol{m} \equiv \mathcal{R}^{-1}(\boldsymbol{n}_{\rm 1sk})$. (a-2)–(c-2) y dependences of $\partial_x m_x(R/2, y), m_x(-R/2, y), \partial_x m_y(R/2, y)$, and $m_y(-R/2, y)$ from left to right at $R/2 = R_{\rm ref} = 10$. The integrals of $\partial_x m_x(R/2, y) m_x(-R/2, y)$ and $\partial_x m_y(R/2, y) m_y(-R/2, y)$ for y give rise to negative and positive values, respectively. The sum of the two contributions are positive in (a) and negative in (b) and (c), respectively. Reproduced from [21]. Copyright 2021, American Physical Society.

Effect of the D term

The D term in Eq. (5.25) also becomes finite to when the background magnetization is somehow tilted from the z axis, $\hat{\boldsymbol{t}} \neq \boldsymbol{e}_z$. The contribution of the D term can be given in terms of $\boldsymbol{m} = \mathcal{R}^{-1}(\boldsymbol{n}_{\text{1sk}})$. Suppose that double-skyrmions are located in a background magnetization $\hat{\boldsymbol{t}} = (\cos\chi\sin\phi, \sin\chi\sin\phi, \cos\phi)$ with their relative position being $\boldsymbol{R} = R\boldsymbol{e}_x$. Using $\delta\boldsymbol{n} = \mathcal{R}(m_x, m_y, 0)$, the D term contributes to the interaction as

$$\begin{aligned}
&\frac{2D}{a}\int_{-\infty}^{\infty} dy(\delta\boldsymbol{n}_+ \times \delta\boldsymbol{n}_-)_x \\
&= \frac{2D}{a}\sin\phi\cos\chi\int_{-\infty}^{\infty} dy\left[m_x\left(-\frac{R}{2}, y\right)m_y\left(\frac{R}{2}, y\right) - m_x\left(\frac{R}{2}, y\right)m_y\left(-\frac{R}{2}, y\right)\right].
\end{aligned} \tag{5.28}$$

We note that this term, Eq. (5.28), indeed vanishes when the skyrmion configuration is a simple spin rotation of that under the potential $U_{\text{c}}(\boldsymbol{n}, \boldsymbol{\nabla}\boldsymbol{n}) = -Bn_z$, due to the symmetry: $m_x(-R/2, y) = m_x(R/2, y)$ and $m_y(-R/2, y) = -m_y(R/2, y)$ [see Fig. 5.5(a)]. Therefore there should be an additional deformation of the skyrmion shape for the nonzero contribution. Roughly speaking, we can say that the above contribution, Eq. (5.28), is smaller than the contribution from the J term Eq. (5.27) by a factor of $\sin\phi\cos\chi$. The concrete values depend on how much the skyrmion is deformed under the anisotropic potentials. In Secs. 5.5 and 5.6, we will numerically show that the contribution of the D term is negligible at large distance R but is comparable to that from the J term for small R.

Effect of the K term

When $K \neq 0$, the K term in Eq. (5.25) should also be taken into consideration. To evaluate the effect, we consider the interaction of skyrmions aligned along the x axis. Let's assume that the uniform background magnetization is in the z direction, i.e., $\hat{\boldsymbol{t}} = \boldsymbol{e}_z$, for simplicity. The approximate interaction at a large distance is obtained as

$$V_{\text{app}}(R\boldsymbol{e}_x) = 2(J-K)\int_{-\infty}^{\infty}\left[\partial_x m_x(R/2, y)\right]m_x(-R/2, y)dy + 2J\int_{-\infty}^{\infty}\left[\partial_x m_y(R/2, y)\right]m_y(-R/2, y)dy. \tag{5.29}$$

From the equation above, the K term modifies the weight of the x component in Eq. (5.27). According to the expression, if K is negative and $K < -J(I_x + I_y)/|I_x|$ is satisfied, where $I_\alpha = \int_{-\infty}^{\infty}\left[\partial_x m_\alpha(R/2, y)\right]m_\alpha(-R/2, y)dy$, the interaction becomes attractive even when the skyrmion is not distorted at all. However, we find that $K/J < -1.6$ is required so that $K/J < -(I_x + I_y)/|I_x|$ is satisfied (see Table 5.1). For the evaluation, we use the spin configuration shown in Fig. 5.5(a). Such a strong anisotropy accompanies the deformation of skyrmions anyway, and the shape of which is no more circular. The deformation modifies the inter-skyrmion interaction via the J term, which is already discussed. Thus,

I_α/J R[site]	I_x	I_y
18	-0.007457	0.137210
16	-0.019489	0.061040
14	-0.050069	0.285613
12	-0.122373	0.501477

Table 5.1 Example of R dependence of the values of the integrand $I_\alpha,\ \alpha = x, y$, when $A = 0$ under the perpendicular magnetic field.

in the following calculations, we discard the K term for simplicity and investigate two specific situations (i) under a in-plane magnetic field and (ii) under the onsite magnetic anisotropy A.

5.4 Micromagnetic simulation

5.4.1 Model Hamiltonian

To numerically survey the interactions and stable spin structures, we use the classical spin and a 2D square lattice model. The Hamiltonian reads

$$\begin{aligned} H = &- J \sum_{\boldsymbol{r}} \boldsymbol{S}_{\boldsymbol{r}} \cdot (\boldsymbol{S}_{\boldsymbol{r}+\boldsymbol{e}_x} + \boldsymbol{S}_{\boldsymbol{r}+\boldsymbol{e}_y}) \\ &- D \sum_{\boldsymbol{r}} (\boldsymbol{S}_{\boldsymbol{r}} \times \boldsymbol{S}_{\boldsymbol{r}+\boldsymbol{e}_x} \cdot \boldsymbol{e}_x + \boldsymbol{S}_{\boldsymbol{r}} \times \boldsymbol{S}_{\boldsymbol{r}+\boldsymbol{e}_y} \cdot \boldsymbol{e}_y) \\ &+ \sum_{\boldsymbol{r}} U(\boldsymbol{S}_{\boldsymbol{r}}), \end{aligned} \tag{5.30}$$

where $\boldsymbol{S}_{\boldsymbol{r}}$ is the unit spin vector at $\boldsymbol{r} \in \{an_x\boldsymbol{e}_x + an_y\boldsymbol{e}_y \,|\, n_x, n_y \in \mathbb{Z}\}$, J and D are the same ones as those already defined in the continuum model, and $U(\boldsymbol{S}_{\boldsymbol{r}})$ is the general anisotropy potential, the continuum model counterpart of which is $U_{\mathrm{c}}(\boldsymbol{n}, \boldsymbol{\nabla}\boldsymbol{n})$. The Hamiltonian (5.30) is the discretized version of the continuum model Eq. (5.8). It is obtained by replacing $\boldsymbol{n}(\boldsymbol{r})$ with $\boldsymbol{S}_{\boldsymbol{r}}$, $\partial_i\boldsymbol{n}(\boldsymbol{r})$ with $(\boldsymbol{S}_{\boldsymbol{r}+\boldsymbol{e}_i} - \boldsymbol{S}_{\boldsymbol{r}})/a$, and $\int d^2r/a^2$ with $\sum_{\boldsymbol{r}}$, respectively. Note that we evaluate $\boldsymbol{n}(\boldsymbol{r})$, the above replacement is implied in the following calculations.

As an anisotropy potential, we consider the Zeeman field and the magneto-crystalline anisotropy of a (011) thin film. The breaking of the C_4 symmetry is crucial for the skyrmion deformation that induces an attractive inter-skyrmion interaction, and thus we choose the (011) film rather than (001). Although the 2D lattice grid of a (011) plane is not square, we use a square lattice for simplicity; We use discretized $U_{\mathrm{c}}^{(\mathrm{mc},011)}$ on the square lattice. This approximation is justified when the size of the skyrmion is much larger than the lattice parameter.

The resulting anisotropy potential, including the Zeeman field of Eq. (5.22), is given by

$$\begin{aligned} U(\boldsymbol{S}_{\boldsymbol{r}}) =& -\boldsymbol{B}_{\text{ex}} \cdot \boldsymbol{S}_{\boldsymbol{r}} \\ &+ A\left[(S^x_{\boldsymbol{r}})^4 + \frac{(S^y_{\boldsymbol{r}} + S^z_{\boldsymbol{r}})^4}{4} + \frac{(-S^y_{\boldsymbol{r}} + S^z_{\boldsymbol{r}})^4}{4}\right] \\ &+ K\left[S^x_{\boldsymbol{r}} S^x_{\boldsymbol{r}+\boldsymbol{e}_x} + \frac{1}{2}(S^y_{\boldsymbol{r}} S^y_{\boldsymbol{r}+\boldsymbol{e}_y} + S^z_{\boldsymbol{r}} S^z_{\boldsymbol{r}+\boldsymbol{e}_y})\right]. \end{aligned} \tag{5.31}$$

In the rest of the paper, we independently discuss changes of the inter-skyrmion interaction due to (i) an in-plane magnetic field and (ii) the onsite magneto-crystalline anisotropy (the A term). In both calculations, we choose $K = 0$ as discussed in Sec. 5.3.2. In case (i), we apply the in-plane magnetic field along the x axis and use the anisotropy potential given by

$$U_{\text{i}}(\boldsymbol{S}_{\boldsymbol{r}}) = -B(S^z_{\boldsymbol{r}} \cos\phi + S^x_{\boldsymbol{r}} \sin\phi), \tag{5.32}$$

where ϕ is the angle between the external magnetic field to the z axis. In case (ii), we apply an external magnetic field perpendicular to the film and use the anisotropy potential

$$U_{\text{ii}}(\boldsymbol{S}_{\boldsymbol{r}}) = -BS^z_{\boldsymbol{r}} + A\left[(S^x_{\boldsymbol{r}})^4 + \frac{(S^y_{\boldsymbol{r}} + S^z_{\boldsymbol{r}})^4}{4} + \frac{(-S^y_{\boldsymbol{r}} + S^z_{\boldsymbol{r}})^4}{4}\right]. \tag{5.33}$$

5.4.2 Skyrmion-skyrmion interactions

We calculate the inter-skyrmion interaction in the following way; Firstly, we find the energy of a metastable single-skyrmion state, $E_{1\text{sk}}$, and that of a metastable double-skyrmion state, $E_{2\text{sk}}(\boldsymbol{R})$ where the two skyrmions are placed at relative position $\boldsymbol{R}$. Also, we find the energy of the FM state of $\boldsymbol{S}_{\boldsymbol{r}} = \hat{\boldsymbol{t}}$, E_{ferro}, since this gives the standard of the energy. The above stationary states can be found by numerically integrating the Landau–Lifshitz–Gilbert (LLG) equation,

$$\frac{d\boldsymbol{S}_{\boldsymbol{r}}}{dt} = -\boldsymbol{S}_{\boldsymbol{r}} \times \boldsymbol{B}_{\text{eff}} + \alpha \boldsymbol{S}_{\boldsymbol{r}} \times \frac{d\boldsymbol{S}_{\boldsymbol{r}}}{dt}, \tag{5.34}$$

where $\boldsymbol{B}_{\text{eff}} = -\delta H/\delta \boldsymbol{S}_{\boldsymbol{r}}$ is the effective magnetic field, H is Hamiltonian given in Eq. (5.30), and α is the damping constant. Note that the temperature is kept at absolute zero in the study. We fixed the positions of skyrmions by using a strong pinning field at the skyrmion cores. The pinning field is only on one site. The inter-skyrmion interaction is generally expressed as

$$V(\boldsymbol{R}) = E_{2\text{sk}}(\boldsymbol{R}) - 2E_{1\text{sk}} + E_{\text{ferro}}, \tag{5.35}$$

which is the discrete model version of the continuum model, given in Eq. (5.18).

5.4.3 Stable SkX structure

In order to seek the ground state lattice structures of the model Hamiltonian, we used two kinds of Monte Carlo (MC) algorithms, the exchange MC [74] and the Metropolis MC. The typical system size used is 72 sites $\times 72$ sites $\times 1$ site with the periodic boundary conditions in x and y directions. We first run the exchange MC to efficiently find the thermal-equilibrium configurations with the temperature range of $0.01J \le k_\mathrm{B}T \le J/2$. Here, 30 replicas are empirically used in the simulation. After the thermalization, we seek the state with the lowest energy at $k_\mathrm{B}T = 0.01J$ during the MC simulation of a few tens of thousands of steps. Finally, we use the lowest-energy state of $k_\mathrm{B}T = 0.01J$ as an initial state of the Metropolis MC, and run with $T = 0$ until it converges to find the energy-minimum state.

5.4.4 Parameters

We fix $J = 1, D = 0.5$, and $a = 1$ in the study. We confirmed that, with the parameters, the SkX phase appears in the same magnetic field range as the previous studies have reported, $B_\mathrm{cr1} \le B \le B_\mathrm{cr2}$, where the two critical fields are $B_\mathrm{cr1} \simeq 0.23D^2/J$ and $B_\mathrm{cr2} \simeq 0.78D^2/J$, respectively [55, 146]. The triangular skyrmion lattice constant $4\pi Ja/(\sqrt{3}D)$ [13] corresponds to the diameter of an isolated skyrmion $2R_\mathrm{sk}$ in the vicinity of the FM–SkX phase boundary. Our choice of the parameters obtain the skyrmion diameter as $2R_\mathrm{sk} = 14.6a (R_\mathrm{sk} = 7.3a)$, which means that R_sk is satisfactorily larger than a, validiating the use of the square grid for a (011) thin film (see Sec. 5.4.1).

5.5 Appearance of attractive interactions under tilted magnetic field

Using the anisotropy potential $U_\mathrm{i}(\boldsymbol{S_r})$ defined in Eq. (5.32), we show the ϕ, the angle from z axis, dependence of the inter-skyrmion interaction. The previous work [15] has already investigated a similar system and found that the interaction becomes anisotropic. We reproduce these results and additionally show that the attractive interaction appears at a larger distance than that of the authors of Ref. [15] have studied.

Figures 5.6(a), (b), and (c) show the interaction potential $V(R)$, numerically obtained one, for skyrmions along the x direction at a distance R for $\phi = 17^\circ, 22^\circ$, and 30°, respectively. The approximated interaction $V_\mathrm{app}(R)$ defined in Eq. (5.19), as well as the first and second terms of Eq. (5.25), are also shown. They are also evaluated with the numerically obtained single skyrmion shape as the stationary solution of the LLG equation. In all cases, the attractive interaction appears for a large R. Interestingly, the attraction becomes larger for larger ϕ, though the interaction energy remains as small as a few percent of J.

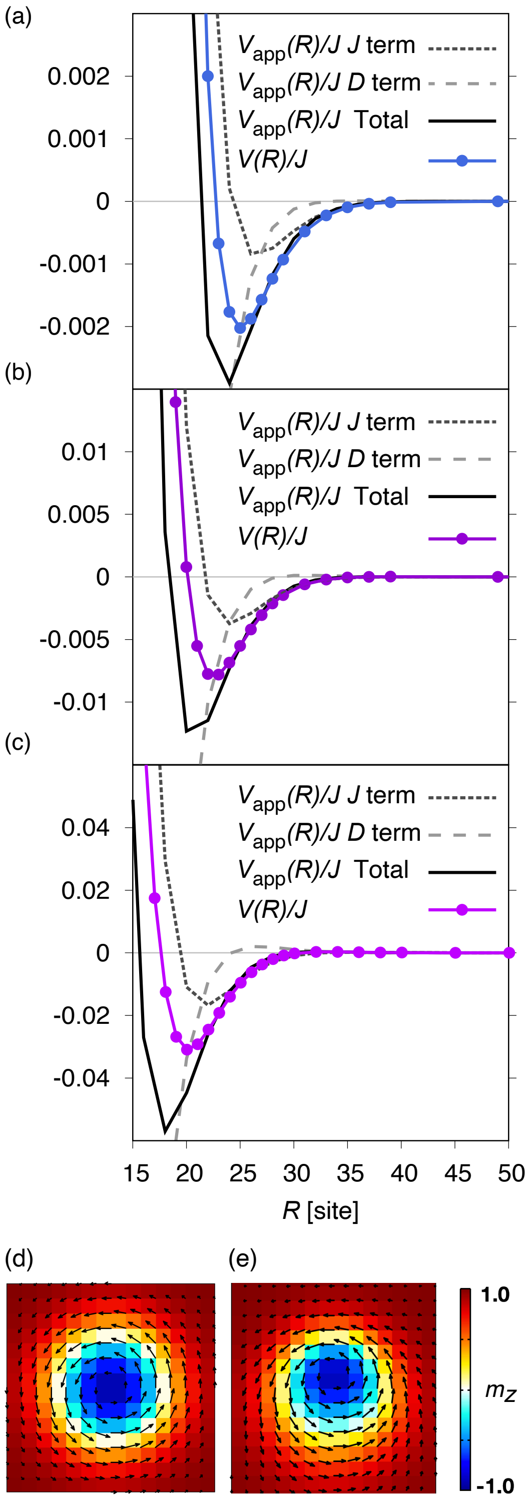

Fig.5.6 (a)-(c) Inter-skyrmion interaction $V(R)$ between two skyrmions aligned along x under a tilted magnetic field of strength $BJ/D^2 = 0.73$ and tilting angle (a) $\phi = 17^\circ$, (b) $\phi = 22^\circ$, and (c) $\phi = 30^\circ$. The numerically calculated interaction $V(R)$, the approximate interaction $V_{\text{app}}(R)$, and the J term (deformation) and D term (tilting background) in Eq. (5.25) are shown. (d),(e) Spin configuration $\boldsymbol{m} = (\boldsymbol{S_r} \cdot (\boldsymbol{e}_y \times \hat{\boldsymbol{t}}), S_{\boldsymbol{r}}^y, \boldsymbol{S_r} \cdot \hat{\boldsymbol{t}})$ of a single skyrmion for (d) $\phi = 0^\circ$ and (e) $\phi = 30^\circ$, where the arrows stand for the vector $\boldsymbol{m}$ projected on the thin film plane (x-y) and the color plot expresses $m_z \parallel \hat{\boldsymbol{t}}$. Tilting of the external magnetic field hardly causes the rotation of the skyrmion shape in spin space but deforms the shape to induce attractive interaction.

$V_{\mathrm{app}}(R)$ agrees very well with $V(R)$ when R is larger than the distance which minimizes $V(R)$. By comparing them we find the origin of the attraction mainly comes from the J term. At around the potential minimum, the D term also contributes to the interaction as much as that from the J term.

We describe the appearance of the attractive force using the deformation of a single skyrmion. In Fig. 5.5(b), we plot $\boldsymbol{m}$ and $\partial_x \boldsymbol{m}$ for $\phi = 30°$. The distribution of m_x (m_y) along the x axis enlarges (shrinks) compared with that for $\phi = 0$ [Fig. 5.5(a)]. As ϕ increases, $V_{\mathrm{app}}(R)$ for a fixed R ($\gtrsim 2R_{\mathrm{sk}}$) decreases and eventually becomes minus, due to the negative (positive) contributions to Eq. (5.27) from the x (y) component . Eq. (5.28) also contributes to the appearance of the attraction, which is seen from Fig. 5.5(b).

The magnetization profile $\boldsymbol{m} = (\boldsymbol{S}_{\boldsymbol{r}} \cdot (\boldsymbol{e}_y \times \hat{\boldsymbol{t}}), S^y_{\boldsymbol{r}}, \boldsymbol{S}_{\boldsymbol{r}} \cdot \hat{\boldsymbol{t}})$ of single-skyrmion at $\phi = 0°$ and $30°$ are also plotted in Figs. 5.6(d) and (e), respectively. This profile convinces that the skyrmion configuration is indeed different from the simple rotation of the shape at $\phi = 0$ in spin space but with the additional deformation, leading to the change in the sign of the interaction.

The interaction between two deformed skyrmions depends on the relative direction as well, which is also discussed in Ref. [15]. Figure 5.7 shows the relative position $\boldsymbol{R} = (X, Y)$ dependence of the interaction potential. The potential has a minimum in the direction of the in-plane magnetic field, i.e., the x axis in this study. On the other hand, the inter-skyrmion interaction along the y axis enlarges as ϕ increases. This feature reproduces the result in Ref. [15]. However, Ref. [15] has not mentioned the attractive interaction since they have investigated smaller distances, up to $R = 14$ site in our parameter.

5.6 Appearance of attractive interactions with the magneto-crystalline anisotropy

Next, we consider skyrmion deformation from the magneto-crystalline anisotropy $U_{\mathrm{ii}}(\boldsymbol{S}_{\boldsymbol{r}})$ shown in Eq. (5.33). Interestingly, when the crystalline anisotropy (A term) dominates the Zeeman term, the resulting easy axes for the magnetization tilt from the z axis. The three hard axes, $\boldsymbol{p}_1$, $\boldsymbol{p}_2$, and $\boldsymbol{p}_3$, prefers the z-x plane. In Sec. 5.6.1, we calculate such preferred direction for the FM state $\hat{\boldsymbol{t}}$. The interaction between two skyrmions embedded in the FM state $\hat{\boldsymbol{t}} = \boldsymbol{e}_z$ and $\hat{\boldsymbol{t}} \neq \boldsymbol{e}_z$ are discussed in Sec. 5.6.2. In the following, we treat only the $A > 0$ case, because the qualitative behavior of the interaction is the same regardless of the sign of A [see Sec. 5.6.1].

5.6.1 Preferred spin direction under the magnetic anisotropy

When the Zeeman term is neglected, the magneto-crystalline anisotropy $U_{\mathrm{ii}}(\boldsymbol{S}_{\boldsymbol{r}})$ with $A > 0$ has the eight preferred orientations: $\boldsymbol{S}_{\boldsymbol{r}} = (\pm 1/\sqrt{3}, 0, \pm\sqrt{2/3})$ and $(\pm 1/\sqrt{3}, \pm\sqrt{2/3}, 0)$. The external magnetic field along the z axis resolves the degeneracy of eight directions, and the new easy axes are the ones having the biggest

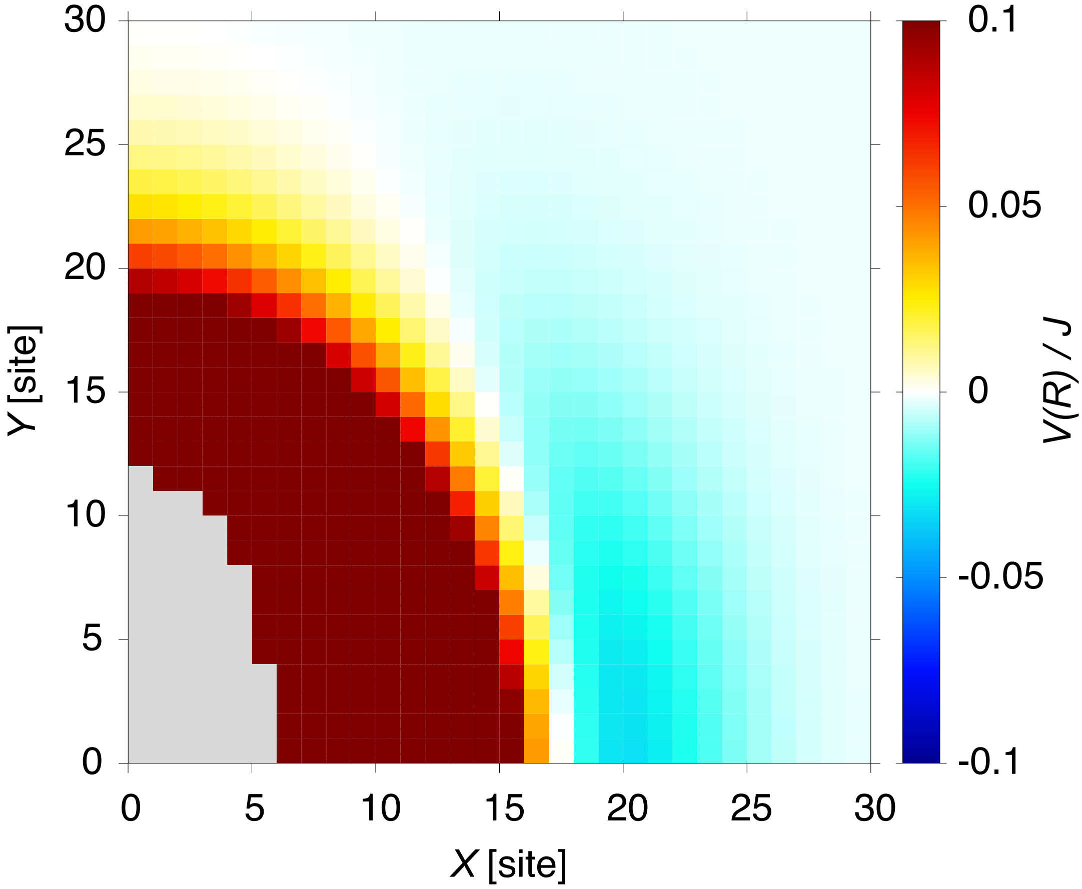

Fig.5.7 Inter-skyrmion interaction potential $V(\boldsymbol{R})$ between two skyrmions with relative position $\boldsymbol{R} = (X, Y)$ in a tilted magnetic field. The strength is $BJ/D^2 = 0.73$ and the tilting angle is $\phi = 30^\circ$ in the x axis. Reproduced from [21]. Copyright 2021, American Physical Society.

z component, i.e., $(\pm 1/\sqrt{3}, 0, \sqrt{2/3})$. The spin orientation eventually changes from $(\pm 1/\sqrt{3}, 0, \sqrt{2/3})$ to $\boldsymbol{e}_z$ as the Zeeman energy becomes large. The preferred spin direction is obtained by using a uniform FM state

$$\boldsymbol{S_r} = \hat{\boldsymbol{t}} = (\sin\theta, 0, \cos\theta), \tag{5.36}$$

and minimizing the one spin energy

$$E(\theta) = A\left(\sin^4\theta + \frac{1}{2}\cos^4\theta\right) - B\cos\theta \tag{5.37}$$

with regard to θ. The energy minimum can be found at $\theta = 0$ (i.e., $\hat{\boldsymbol{t}} = \boldsymbol{e}_z$) when $A/B \leq 0.5$, but it disappears (changes to a local maximum) when $A/B > 0.5$ (i.e., $\hat{\boldsymbol{t}}$ deviates from $\boldsymbol{e}_z$). This is because $d^2E/d\theta^2\big|_{\theta=0} = -2A + B$. Fig. 5.8 shows the resulted preferred angle θ vs. A/B. Note that there are two degenerate preferred directions $\hat{\boldsymbol{t}}_\pm = (\pm\sin\theta, 0, \cos\theta)$ since $E(\theta)$ is an even function of θ. The two magnetic

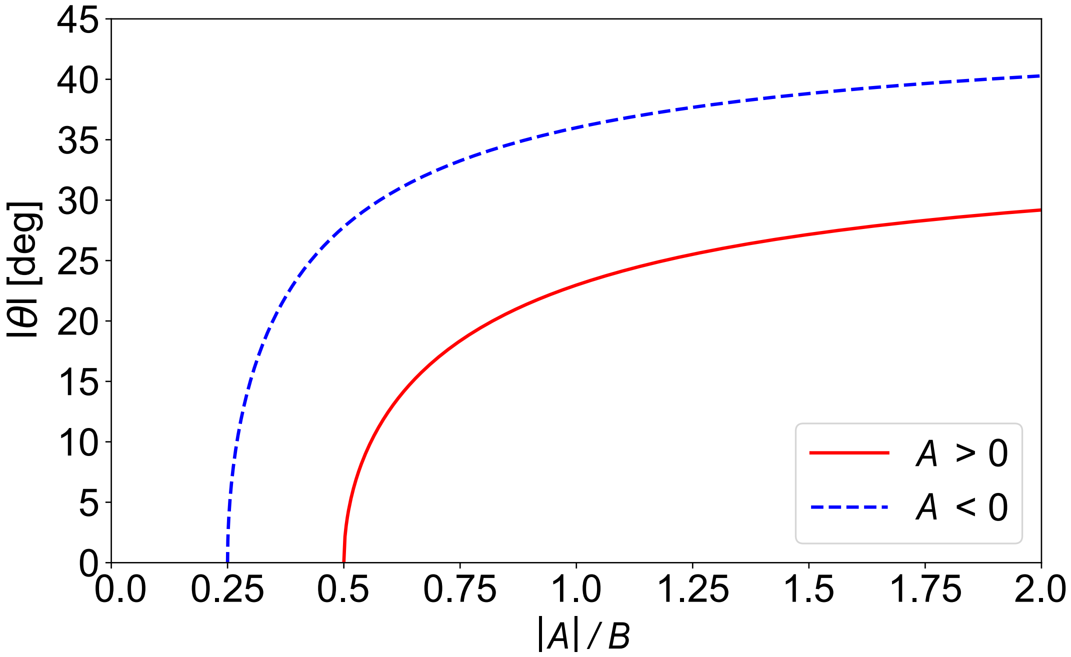

Fig.5.8 Resulted favorable angle θ of a FM state as a function of $|A|/B$. In the case of $A > 0$ ($A < 0$), the spins are angled in the x (y) direction. Once the magnetic anisotropy dominates the Zeeman energy, when $A/B > 0.5$ or $-A/B > 0.25$, the preferred angle becomes finite and spins are tilted from the z axis. Reproduced from [21]. Copyright 2021, American Physical Society.

domains of $\boldsymbol{S_r} = \hat{\boldsymbol{t}}_\pm$ indeed appear when the anisotropy is sufficiently strong [see Sec. 5.7].

Let's think about what happens when $A < 0$, the magneto-crystalline anisotropy prefers the spins to be $\boldsymbol{S_r} = (\pm 1, 0, 0)$ and $(0, \pm 1, \pm 1)/\sqrt{2}$. Combined with the Zeeman term, the easy axes result in lying in the y-z plane in the spin space. The angle from the z axis can be calculated in a similar way as in the $A > 0$ case, and the dashed curve in Fig. 5.8 shows the result. In the case of $A < 0$, θ becomes finite for $|A|/B > 0.25$.

The magneto-crystalline anisotropy leads to the skyrmion deformation even when $\hat{\boldsymbol{t}} = \boldsymbol{e}_z$. In Fig. 5.9, we show the single skyrmion shape with $BJ/D^2 = 0.70$ for $A = 0$ (a), $A = 0.5B$ (b), and $A = -0.25B$ (c), which indicates that the skyrmion shape for $A > 0$ ($A < 0$) is elongated in the x (y) direction. It is sufficient to investigate the $A > 0$ case only, because our interest is the effect of the skyrmion deforms on the inter-skyrmion interaction. Although the might be small quantitative changes in the interaction due to the spin configuration near the skyrmion, the behavior is qualitatively the same for both cases, $A > 0$ and $A < 0$. We thus discuss only the case of $A > 0$ in detail.

5.6.2 Inter-skyrmioin potential in single domain

Let's discuss the inter-skyrmion interaction in the single domain, the spins are tilted from the z axis either by $+\theta$ or $-\theta$. We start from the simple case where $\hat{\boldsymbol{t}} = \boldsymbol{e}_z$. When $A/B \lesssim 0.5$, the skyrmions are distorted under the magneto-crystalline anisotropy and the background spins are along the z axis. Figure 5.10(a) shows

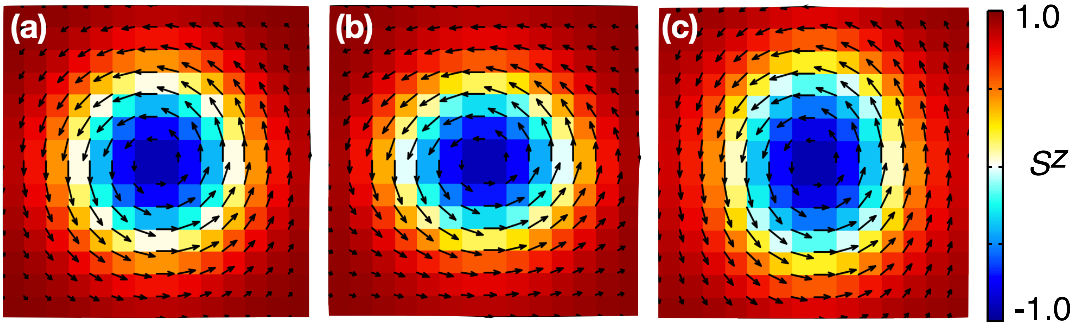

Fig.5.9 Stable shape of the single-skyrmion (a) $A = 0$, (b) $A = 0.5B$, and $A = -0.25B$ and at $BJ/D^2 = 0.70$. These are obtained as a stationary solution by numerically solving the LLG equation. The arrows denote the spin vector $\boldsymbol{S}_{\boldsymbol{r}}$ projected to the x-y plane, $S^x_{\boldsymbol{r}}$ and $S^y_{\boldsymbol{r}}$, and the color plot indicates $S^z_{\boldsymbol{r}}$. The circular shape at $A = 0$ (a) is elongated laterally (in the x direction) and vertically (in the y direction) for $A > 0$ (b) and $A < 0$ (c), respectively. Reproduced from [21]. Copyright 2021, American Physical Society.

the numerically obtained interaction potential $V(R)$ between the two skyrmions alinged along the x axis with $BJ/D^2 = 0.75$ at $A/B = 0.0, 0.1, 0.25, 0.33, 0.4$, and 0.5. The attractive interaction appears at $R \gtrsim 2R_{\text{sk}}$, and it becomes stronger for larger anisotropy constant A/B. However, even in the case of $A/B = 0.5$, the potential depth remains shallow (a few percent of J), which is the same order of magnitude as that under the in-plane magnetic field. We also plot the interaction for analytic approximation $V_{\text{app}}(R)$ calculated from the single-skyrmion shape. It well reproduces $V(R)$ at a large distance and up to around the potential minimum. For example, when $A/B = 0.4$ where the potential minimum is located at $R = 18$ site, the two curves almost become identical at $R \geq 20$.

Because the background magnetizations are not tilted, $\hat{\boldsymbol{t}} = \boldsymbol{e}_z$, for $A/B \leq 0.5$, there is only the J term which gives a finite contribution to A_{+-} [see Eq. (5.25)]. Therefore, we can see that the attractive interaction purely originates from the deformation of the skyrmion shape as discussed in Sec. 5.3.2. Figs. 5.5(c) and 5.9(b) indicate that the skyrmion deforms in such a way that the profile of the x component, $S^x_{\boldsymbol{r}}$, expands, which enhance the negative component to Eq. (5.27), giving rise to the attractive interaction along the x direction.

When $A/B > 0.5$, the situation changes drastically. We show the interaction $V(R)$ of two skyrmions lined up along the x axis with $BJ/D^2 = 1.0$ and at $A/B = 0.67, 1.0$, and 2.0 in Fig. 5.11(a), (b), and (c), respectively. The background spins are tilted from the z axis in these cases. The contributions to the approximate interaction $V_{\text{app}}(R)$ are both from the J term and the D term. They are also shown in the same plot. Interestingly, $V(R)$ in Fig. 5.11 appears to be much stronger than $V_{\text{app}}(R)$ especially around the potential minimum, which is very different from Fig. 5.10. The attractive interaction becomes as large as $0.1J$ to J for $A/B \gtrsim 0.5$. One may see that the preferred distance for skyrmions, the distance which minimizes $V(R)$, is smaller than that of Fig. 5.10. This is due to the different skyrmion size because of the different value of B;

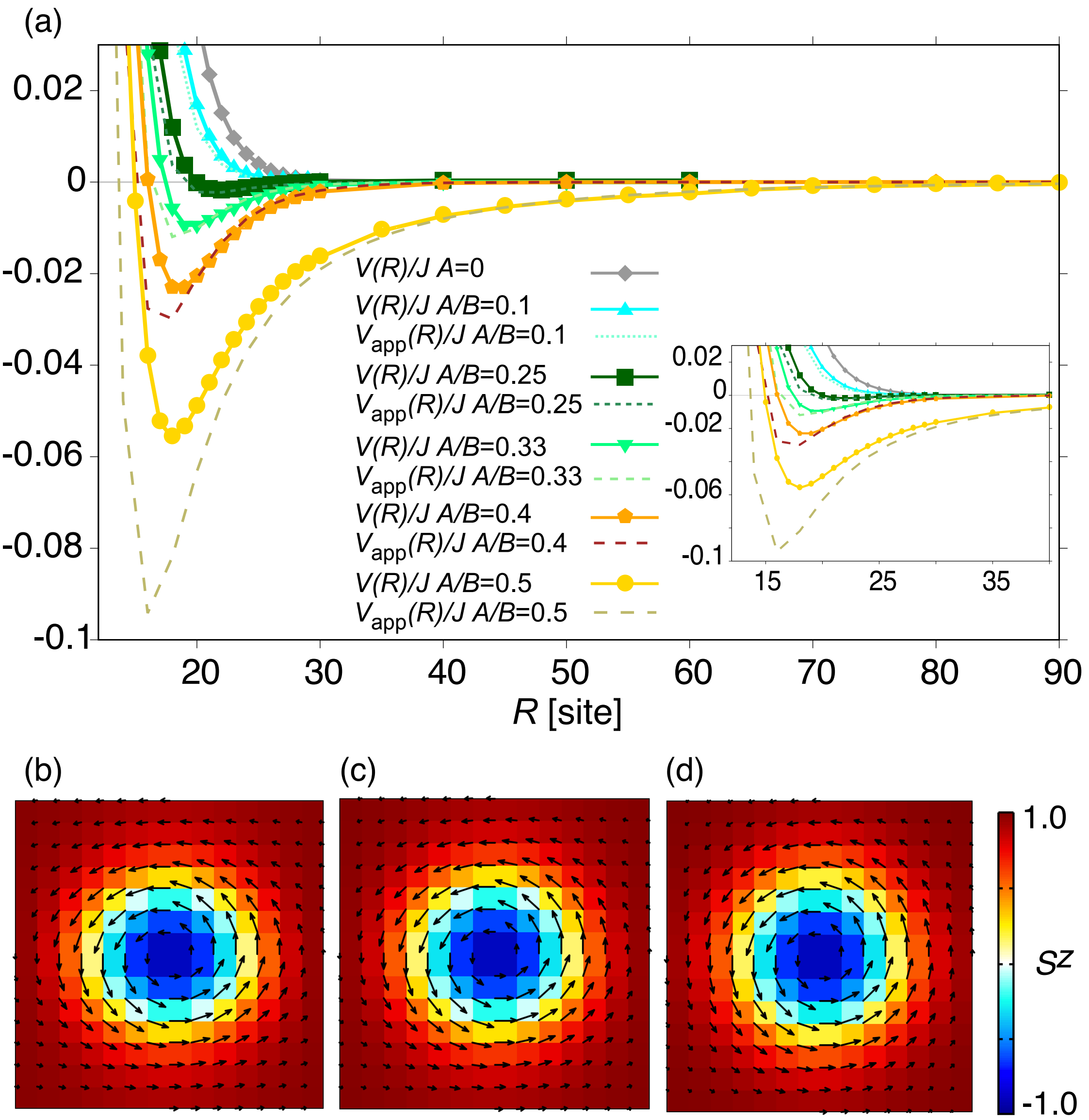

Fig.5.10 (a) Inter-skyrmion interaction $V(R)$ along the x direction with $BJ/D^2 = 0.75$ under the magneto-crystalline anisotropy for $0 \leq A/B \leq 0.5$, where the background spins are $\hat{\boldsymbol{t}} = \boldsymbol{e}_z$. Shown are the numerically obtained one $V(R)$ and the approximate one $V_{\text{app}}(R)$ for each case. (inset) Magnified view of the potential up to $R = 40$ sites. (b)-(d) Stable single-skyrmion shape when (b) $A/B = 0.5$, (c) 0.4, and (d) 0.0 and at $BJ/D^2 = 0.75$, obtained numerically. The details of the figures are the same as that in Fig. 5.9. Although the distortion of the skyrmion in (b)-(d) is smaller compared with that in Figs. 5.9(a) and (b), it has a significant effect on $V(R)$, as shown in (a).

Stronger B favors the smaller skyrmions, but the depth of the potential is almost the same regardless of the exact value of B.

The strong attractive interaction is thanks to the formation of a magnetic domain between the two skyrmions. Differently from the in-plane magnetic field case, which is discussed in Sec. 5.5, there are two energetically degenerate uniform states $\hat{\boldsymbol{t}}_{\pm}$ in this case. Thus, a small magnetic domain of $\boldsymbol{S}_{\boldsymbol{r}} = \hat{\boldsymbol{t}}_{-}$ can be formed between two skyrmions, when two skyrmions are placed in a FM state $\boldsymbol{S}_{\boldsymbol{r}} = \hat{\boldsymbol{t}}_{+}$. In Figs. 5.11(d)–(f), we plot the spin configuration of two such skyrmions for $BJ/D^2 = 1.0$ and $A/B = 1.0$. The region of $S^x_{\boldsymbol{r}} < 0$ is circled by the domain wall of $S^z_{\boldsymbol{r}} = 1$, which tightly bounds the two skyrmions. Also, the two skyrmions are embedded on the domain wall. The strong attraction suggests that the bound-state will be robust against external diffractions such as thermal fluctuations.

In Fig. 5.12, we plot the relative angle dependence of the interaction, plotted as a function of $\boldsymbol{R} = (X, Y)$ for $A/B = 1.0$ and $BJ/D^2 = 1.0$. Attractive interaction is found when the angle between the two skyrmions is less than $\sim 45°$ and otherwise repulsive. We note that qualitatively the same result of $V(\boldsymbol{R})$, Fig. 5.12, is obtained regardless of the exact value of A/B.

5.7 Elongated SkX and phase diagram in the presence of the attraction

We have investigated the inter-skyrmion potential in anisotropic geometries. Next, we discuss the ground-state lattice structures induced by the anisotropic attractive interaction, focusing on the case with the magnetic anisotropy which stabilizes the magnetic domains between two skyrmions when $A/B > 0.5$.

In Table 5.2, we summarize the ground-state phase diagram depending on B and A/B. This is obtained by the Monte Carlo (MC) simulations [see Sec. 5.4.3 in detail]. Regardless of the formation of the magnetic domain, $A/B \leq 0.5$ or $A/B > 0.5$, there are two critical magnetic fields B_{cr1} and B_{cr2}. The uniform FM phase, a single domain, appears at $B \geq B_{\text{cr2}}$, a SkX structure is obtained at $B_{\text{cr1}} \leq B < B_{\text{cr2}}$, and a spin helix state emerges at $B < B_{\text{cr1}}$. When $A/B \leq 0.5$, the FM phase points to the z axis [see Region (i) in Table 5.2]. By decreasing the magnetic field B below B_{cr2} with keeping A/B as the same value, an elongated triangular SkX along the y direction appears [see Region (ii)]. This distortion along the y direction is attributed to the anisotropic property of the interaction, as shown in Fig. 5.12: The interval of the skyrmions in the x direction is smaller than that in the y direction since the attractive interaction favors the smaller distance along the x axis. Further lowering B below B_{cr1} stabilizes a helical spin configuration [see Region (iii)]. On the other hand when $A/B > 0.5$, the FM state is composed of the tilted spins $S^z \neq 1$ due to the combined effect of the magneto-crystalline anisotropy and the Zeeman energy. When the magnetic field is high enough, the system prefers the single domain structure of the preferred directions $\hat{\boldsymbol{t}}_\pm$ [Region (iv)], since making the domain wall is energetically refused. The lower magnetic field than B_{cr2} [see Region (v)] prefers an elongated triangular lattice along the y axis, similar to the case of Region (ii). However, unlike Region (ii), the background of the lattice is composed of the magnetic domains of $\boldsymbol{S} = \hat{\boldsymbol{t}}_\pm$. This results in that skyrmions line up along the domain walls [see Fig. 5.14(c)]. In this Region, the domain walls are favored in terms of accompanying skyrmions with them.

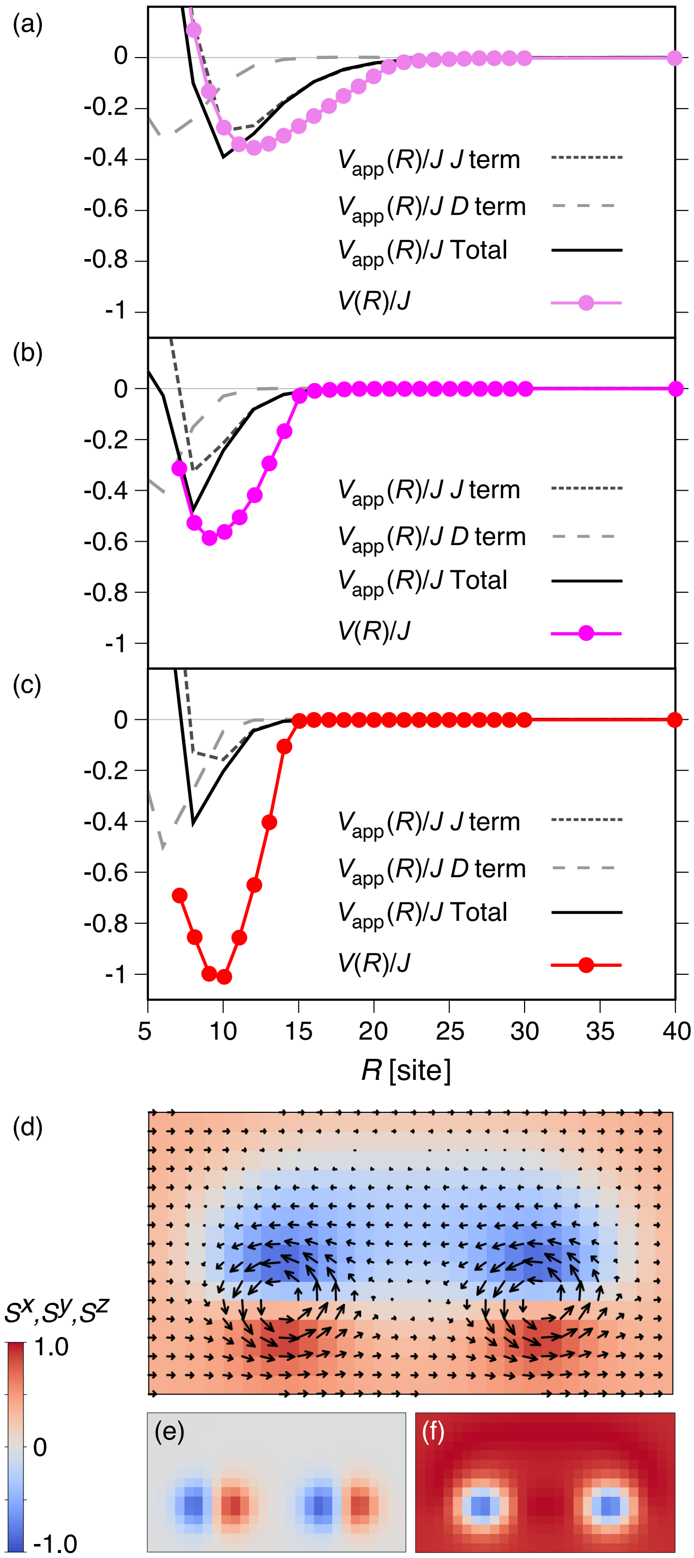

Fig.5.11 (a)-(c) Interaction potential $V(R)$ between two aligned skyrmions along the x axis in a magnetic field of strength $BJ/D^2 = 1.0$ and magneto-crystalline constant (a) $A/B = 0.67$, (b) 1.0, and (c) 2.0, where the background spins are tilted from $\boldsymbol{e}_z$ in the z-x plane. Numerically obtained interaction $V(R)$, the approximate potential $V_{\rm app}(R)$, and the two contributions from the J and the D terms in Eq. (5.25) are shown. (d)-(f) Magnetization configurations of a double-skyrmion state with $BJ/D^2 = 1.0$ and $A/B = 1.0$ at a fixed relative position $\boldsymbol{R} = R\boldsymbol{e}_x$ with $R = 14$, and the color plots indicate (d) $S^x_{\boldsymbol{r}}$, (e) $S^y_{\boldsymbol{r}}$, and (f) $S^z_{\boldsymbol{r}}$. A magnetic domain with $\boldsymbol{S}^x_{\boldsymbol{r}} < 0$ is formed between two skyrmions. They are surrounded by the domain wall, $\boldsymbol{S}^z_{\boldsymbol{r}} = 1$, and give rise to the strong attractive potential as shown in (a)-(c). Reproduced from [21]. Copyright 2021, American Physical Society.

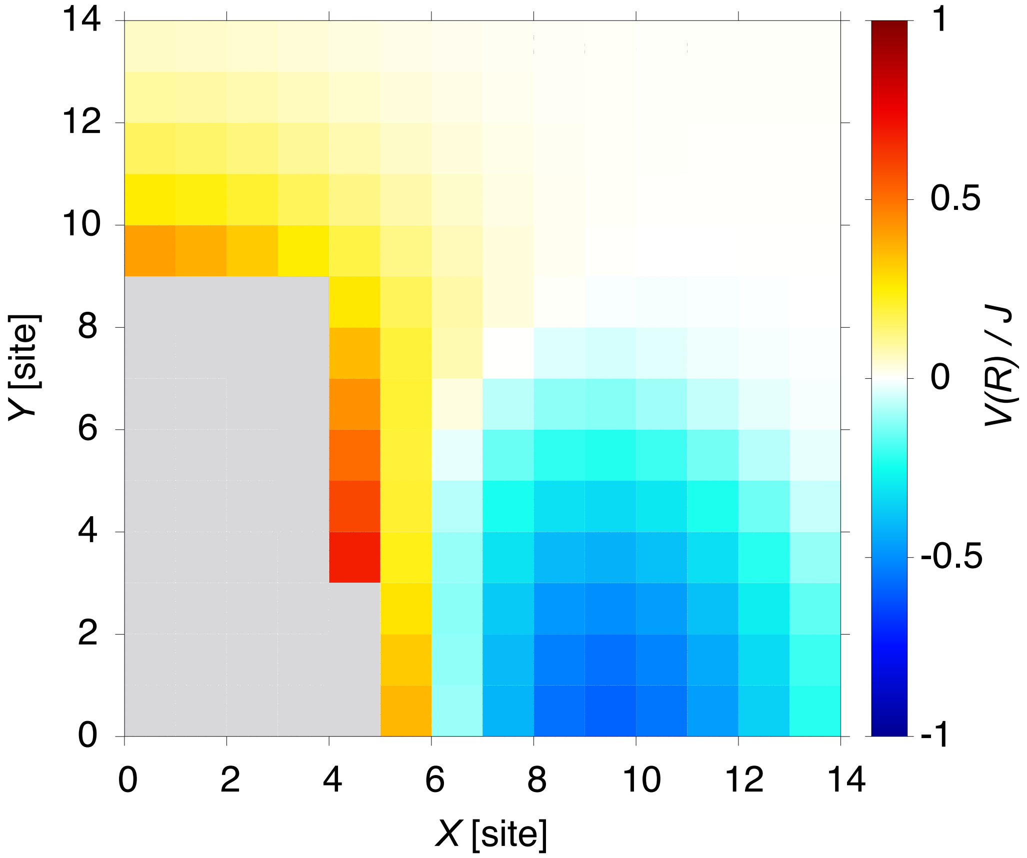

Fig.5.12 Inter-skyrmion potential $V(\boldsymbol{R})$ for deformed skyrmions along x at relative position $\boldsymbol{R} = (X, Y)$. The magnetic anisotropy constant is $A/B = 1.0$ and the external magnetic field is at $BJ/D^2 = 1.0$. No matter A/B is below or above 0.5, the angular dependence is almost the same. Reproduced from [21]. Copyright 2021, American Physical Society.

Specifically, the topological object which appears in Region (v) is a bimeron, not a skyrmion [22]. Here, a bimeron is a pair of merons and has the same topological charge as a skyrmion. It is the boundary condition surrounding the object that differs between a skyrmion and a meron: The magnetization around a skyrmion is pointing to the same direction, whereas that around a meron has a finite winding number $\pi_1(S^1)$ [147]. In the system in consideration, a skyrmion lattice continuously changes to a bimeron lattice, as we increase A/B and $\hat{\boldsymbol{t}}$ tilts from the z axis. For convenience, we express both of them as skyrmion in the thesis.

The critical magnetic fields B_{cr1} and B_{cr2}, which appear in Table 5.2, depend on A/B. We find that B_{cr1} is almost insensitive to A/B and is $\sim 0.3D^2/J$, while B_{cr2} strongly depends on the values of A/B. The behavior of B_{cr2} can be seen from the A/B vs. the single skyrmion excitation energy. If there was only repulsive interaction, B_{cr2} is determined as the magnetic field at which the single skyrmion excitation energy (the energy to create a single skyrmion) in the FM state becomes zero: This is because the inter-skyrmion interaction plays an important role only when the two skyrmions are close enough; The skyrmion lattice becomes exactly the ground state once the excitation energy becomes negative in this case. In Fig. 5.13, the

A/B B	$0 < A/B \leq 0.5$	$0.5 < A/B$
$B_{\mathrm{cr2}} \leq B$	(i) Single Domain ($S_z = 1$)	(iv) Tilted Single Domain ($S_z \neq 1$ and $S_x \neq 0$)
$B_{\mathrm{cr1}} \leq B < B_{\mathrm{cr2}}$	(ii) Elongated Triangular SkX	(v) Elongated Triangular SkX with Magnetic Domains
$B < B_{\mathrm{cr1}}$	(iii) Helix	

Table 5.2 Ground-state spin configurations obtained by the MC in a magneto-crystalline anisotropy A and an magnetic field B points to the z axis. The value of critical magnetic fields B_{cr1} and B_{cr2} depend on A/B. The single domain phases at large magnetic field regions, (i) and (iv), mean the FM phase. For a detailed explanation of the phases, see the text.

single-skyrmion excitation energy $\Delta E \equiv E_{\mathrm{1sk}} - E_{\mathrm{ferro}}$ is shown as a function of the external magnetic field BJ/D^2 for various A/B. The strong dependence on A/B of the zero point of ΔE is consistent with that of B_{cr2} dependence. We note that, in the present case, the attractive interaction shifts the phase boundary.

To study the phase boundary of the FM – SkX, we use the LLG equation to calculate the energy of the SkX state in the following way. We prepare a unit cell of size $2dx \times 2dy$ and place two skyrmions at $(dx/2, dy/2)$ and $(3dx/2, 3dy/2)$ in such a way that a periodic arrangement of the system reproduces the elongated triangular lattice found in the MC simulation. After relaxing the spin structure with the LLG equation, we calculate the energy per spin of the stationary state. The optimal skyrmion interval, dx and dy, are that minimize the one spin energy E_{1spin}. In Fig. 5.14(a), we show E_{1spin} as a function of (dx, dy) with $A/B = 1.0$ and $BJ/D^2 = 0.625$ (a-1), 0.65 (a-2), 0.66 (a-3), and 0.67 (a-4). Please note that the energy is with respect to that of the FM state, $\boldsymbol{S} = \hat{\boldsymbol{t}}_+$. Given that the energy minimum exists and the energy is negative in Figs. 5.14(a-1)-(a-3) clearly demonstrates that the SkX is the ground state at the corresponding magnetic fields. The single-skyrmion excitation energy ΔE with $A/B = 1.0$ crosses zero when $BJ/D^2 = 0.625$ (Fig. 5.13), meaning that the SkX phase at $BJ/D^2 > 0.625$ is due to the skyrmion condensation induced by the attraction. Increasing the magnetic field B enlarges the domain width in the y direction, and the domain size eventually becomes comparable to the system size. This is nothing but the phase transition to the FM phase. There is no energy minimum where $10 \leq dy \leq 40$, as shown in Fig. 5.14(a-4). This indicates that the phase boundary is at $BJ/D^2 \sim 0.66$.

The distribution of S^x of the optimal lattice are shown in Figs. 5.14(b-1)-(b-3), which are obtained from Figs. 5.14(a-1)-(a-3), respectively. It is visible that the magnetic domains of $S^x > 0$ and $S^x < 0$ (which corresponds to the domains of $\boldsymbol{S} = \hat{\boldsymbol{t}}_+$ and $\hat{\boldsymbol{t}}_-$, respectively) alternately align in the y direction. Due to the sign of the DM interaction (which favors counter crock-wise winding of spins in x-y plane in this model), the spins above (below) the domain wall has $S^x > 0$ ($S^x < 0$). Therefore, skyrmions can only emerge on the domain walls where S^x becomes the same sign as the skyrmion structure, and they cannot appear on the other ones. The inter-skyrmion energy between the two skyrmions in the y direction, over the domain wall, is

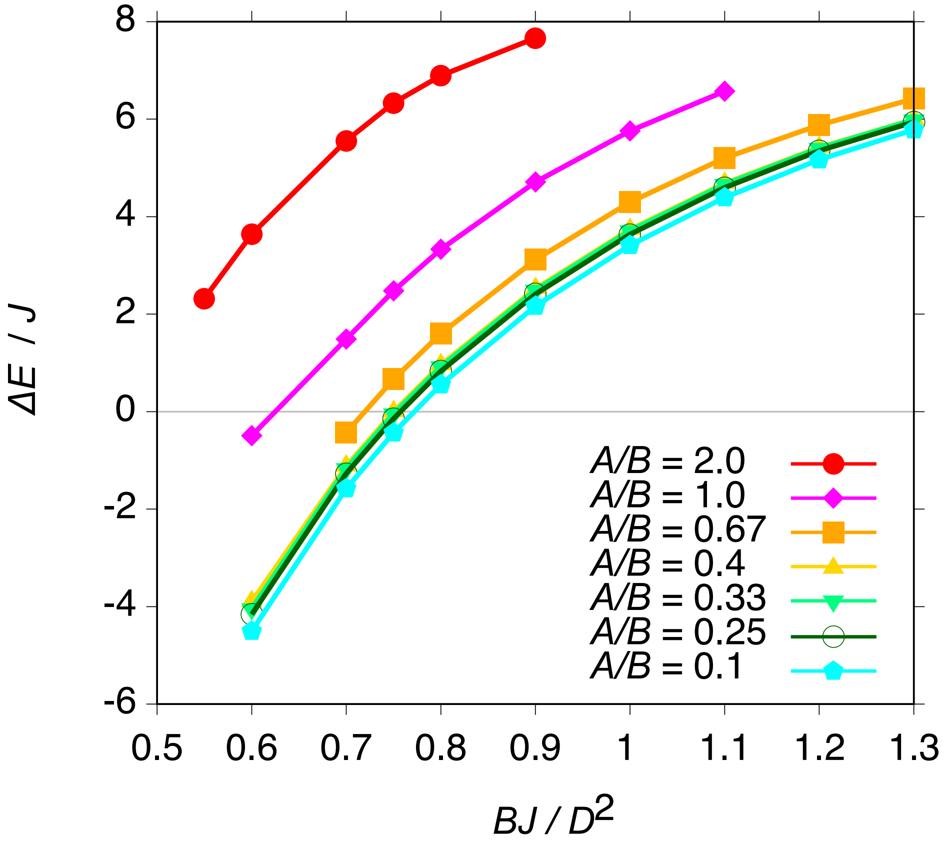

Fig.5.13 Single skyrmion excitation energy, $\Delta E \equiv E_{\mathrm{1sk}} - E_{\mathrm{ferro}}$, vs. BJ/D^2 for various A/B. Reproduced from [21]. Copyright 2021, American Physical Society.

negligible; This is because the resulted energies for the skyrmions in the optimized SkX are almost the same as those shown in Fig. 5.14(a).

In Fig. 5.14(a-4), we can find an optimal dx when we fix dy. This means that if several skyrmions are excited, they align along the x axis with the spacing dx. We indeed find 1D skyrmion chains as a metastable state from the MC simulation, shown in Fig. 5.14(c).

Finally, in Fig. 5.15(a), we mention the detailed ground-state phase diagram with $A/B = 1.0$ near $B = B_{\mathrm{cr2}}$. Figures 5.15 (b) and (c) show the interaction potential $V(R)$ with $BJ/D^2 = 1.0$, same as that in Fig. 5.11(b), and a zoom up of the single-skyrmion energy ΔE, same as that shown in Fig. 5.13, respectively. The attractive interaction is $\sim 0.6J$ at the optimal distance, as Fig. 5.15(b) shows. The SkX phase is thus stabilized when $\Delta E \sim 0.6J$, the magnetization of which corresponds to $BJ/D^2 \lesssim 0.66$ as shown in Fig. 5.15(c). Interestingly, this estimation coincides well with the numerically obtained result in Fig. 5.14. This indicates that the SkX phase in the region is due to the energy gain from exciting the skyrmions, further confirmed from the fact that $\Delta E < 0$ for $BJ/D^2 < 0.625$ [see Fig. 5.15(a)]. Whereas, the SkX phase with $0.625 \leq BJ/D^2 \leq 0.66$ is attributed to the attractive interaction. The width along the magnetic field δB in the region is almost the same

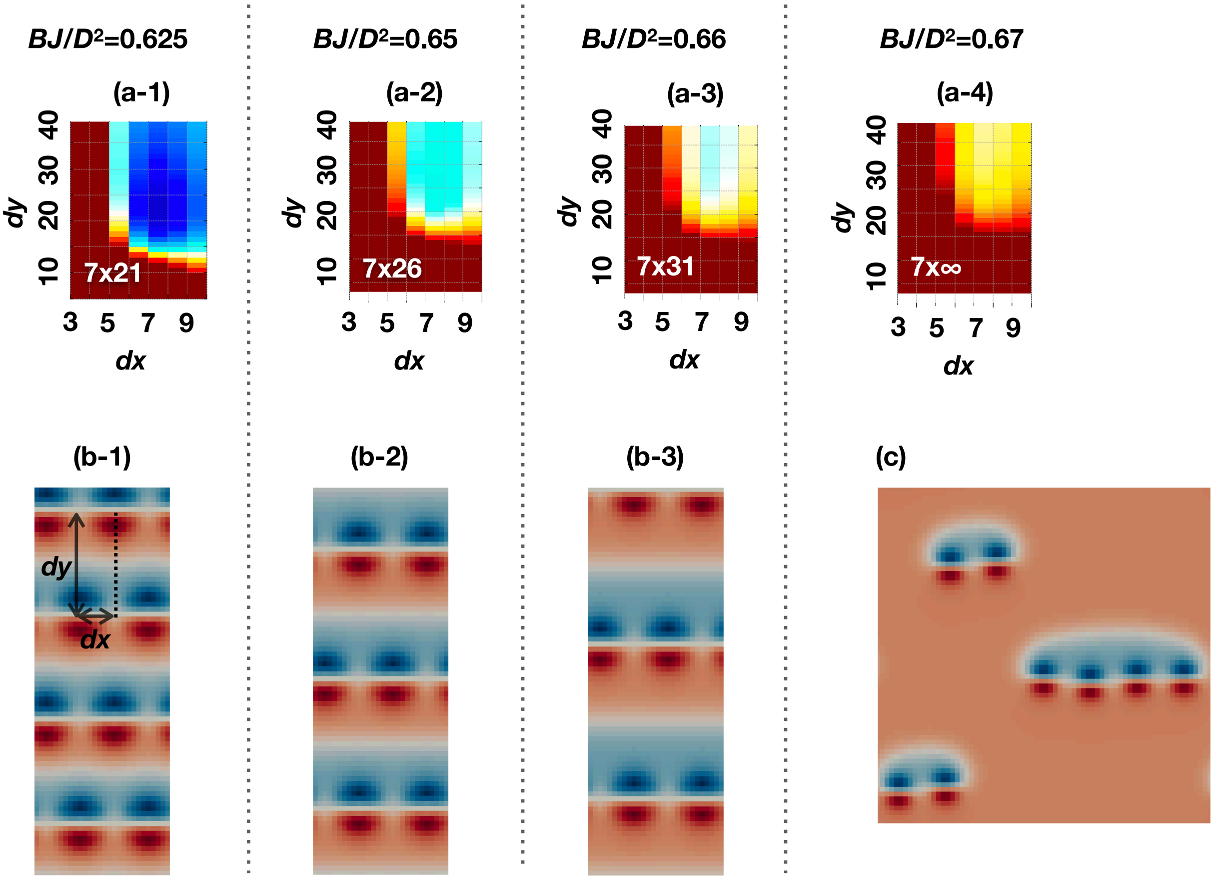

Fig.5.14 (a) One spin energy E_{1spin} of SkX obtained from a unit cell of size $2dx \times 2dy$ with the periodic boundaries. There are two skyrmions in it with (a-1) $BJ/D^2 = 0.625$, (a-2) 0.65, (a-3) 0.66, and (a-4) 0.67. The white letters indicate the optimal lattice spacing, dx and dy correspond to the energy minimum. No minimum is found in (a-4). (b) Real space image of optimal SkX obtained in (a). The distributions of S^x are shown. (c) Plot of S^x with $BJ/D^2 = 1.0$ found in the MC simulations. This is an excited state. Reproduced from [21]. Copyright 2021, American Physical Society.

as the depth of the potential. When the magnetic field exceeds $BJ/D^2 > 0.66$, the ground state is replaced by the FM phase, which can host a 1D skyrmion chain as an excited state [see Fig. 5.14(c)].

We note that when $A/B \leq 0.5$, we find phase boundary qualitatively the same. However, because of the small inter-skyrmion interaction for $A/B < 0.5$, δB is much narrower. We have confirmed that the in-plane magnetic field also gives rise to the similar ground-state phase diagram as that of $A/B \leq 0.5$; It includes the SkX phase induced by the attractive interaction and meta stable 1D skyrmion chain.

5.8 Tunable attraction by means of the in-plane magnetic field

We consider what happens when both effects, the in-plane magnetic field and the magneto-crystalline anisotropy in a (011) thin film, are combined. Please note that the magnetic anisotropy in the section is

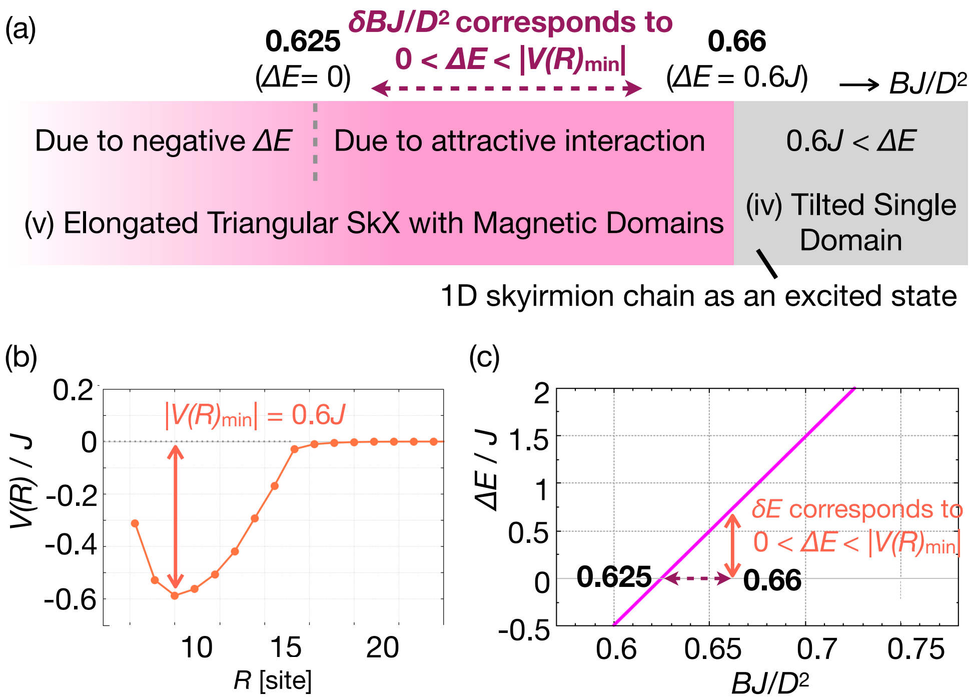

Fig.5.15 (a) Detailed phase diagram near the second critical magnetic field B_{cr2} with $A/B = 1.0$. In terms of the origin of the SkX, the phase can be separated into two regions: One region is attributed to the negative skyrmion excitation energy ($BJ/D^2 < 0.625$), and the other is attributed to the large attractive interaction ($0.625 \leq BJ/D^2 < 0.66$). Above $B_{\mathrm{cr2}}J/D^2 = 0.66$, skyrmions appear as excitations and line up in a 1D chain due to the attractive interaction in the x direction. (b) Magnified view of the interaction $V(R)$ replotted the one in Fig. 5.11(b); The potential depth is $|V(R)_{\mathrm{min}}| \sim 0.6J$. (c) Magnified view of Fig. 5.13, the single-skyrmion excitation energy ΔE vs. BJ/D^2 with $A/B = 1.0$. Solid arrow denotes $\delta E = |V(R)_{\mathrm{min}}|$ and dotted arrow indicates the corresponding δB, which determines the width of the SkX phase induced by the attraction. Reproduced from [21]. Copyright 2021, American Physical Society.

the same as the A term. The anisotropy potential reads

$$\begin{aligned} U_{\mathrm{iii}}(\boldsymbol{S_r}) = &- B(S^z_{\boldsymbol{r}} \cos\phi + S^x_{\boldsymbol{r}} \sin\phi) \\ &+ A\left[(S^x_{\boldsymbol{r}})^4 + \frac{(S^y_{\boldsymbol{r}} + S^z_{\boldsymbol{r}})^4}{4} + \frac{(-S^y_{\boldsymbol{r}} + S^z_{\boldsymbol{r}})^4}{4}\right], \end{aligned} \tag{5.38}$$

where the stable FM state can be expressed by the same form as Eq. (5.36). However, in this case the in-plan field lifts the degeneracy of the two easy-axes $\pm\theta$ shown in Fig. 5.8. In Fig. 5.16(a) we show the preferred angle θ in this case and metastable solutions $-\theta$ for various tilting angle for magnetic field ϕ. Notably, the metastable solution ($-\theta$) disappears when A/B becomes small. It is only if the metastable solution $\hat{\boldsymbol{t}}_-$ exists that the two skyrmions strongly interact by forming a magnetic domain $\hat{\boldsymbol{t}}_-$, when two skyrmions are embedded in the uniform background $\boldsymbol{S_r} = \hat{\boldsymbol{t}}_+$.

We find the drastic change of the strength of the attraction $V(\boldsymbol{R} = R\boldsymbol{e}_x)$, induced by the disappearance of the metastable magnetic domain, shown in Fig. 5.16(b). $V(\boldsymbol{R} = R\boldsymbol{e}_x)$ for different ϕ, $\phi = 17°$ and $30°$ with $A/B = 2.0$, are shown in Fig. 5.16(b). Answering the appearance of the metastable domain solution, the interaction has a deep (shallow) dip with $\phi = 17^\circ$ (30°). The inset in Fig. 5.16(b) displays that it is due to the formation of the domain that the large attractive interaction is induced. This is seen from the fact that the approximate interaction $V_{\mathrm{app}}(R)$ doesn't reproduce $V(R)$.

Let's compare the potential depth with that of Fig. 5.11(c). The shallower potential for $\phi = 17^\circ$ is because of larger anisotropy energy of $\hat{\boldsymbol{t}}_-$, appearing between two skyrmions, than that of the background spins. That is, $U_{\mathrm{iii}}(\hat{\boldsymbol{t}}_-) > U_{\mathrm{iii}}(\hat{\boldsymbol{t}}_+)$, while they are the same for $\phi = 0$. The shallower potential for $\phi = 30^\circ$, on the other hand, is due to the change of the skyrmion deformation; Under an in-plane field tilted to the x axis, the $S_x < 0$ ($S_x > 0$) component shrinks (expands) than the $\phi = 0$ case, which causes smaller attraction [see Fig. 5.5(b)].

This deformation also affects the ϕ dependence of the interaction potential. Figure 5.17 shows the interaction for various ϕ with keeping $A/B = 0.5$. This value, $A/B = 0.5$, means that no domain is formed between two skyrmions. As we increase ϕ, the attractive potential first gets larger and then becomes smaller. This behavior is very different from that of $A = 0$ case [see Fig. 5.6], where the potential well monotonically becomes deeper as we increase ϕ. The inset convinces that the attraction comes mainly from the J term, the skyrmion distortion. We note that the attraction is almost the same regardless of the value of B.

5.9 Attractive interactions with preserved C_4 symmetry

So far, we have focused on the (011) thin film since it breaks the C_4 symmetry in spin space. In this section, we treat a (001) thin film instead to see how the above results, especially in the absence of the in-plane magnetic field, are modified. In this case, the C_4 symmetry is preserved and the anisotropy potential is given by $A\left[(S^x_{\boldsymbol{r}})^4 + (S^y_{\boldsymbol{r}})^4 + (S^z_{\boldsymbol{r}})^4\right]$. It has eight easy-axes along $\langle 111 \rangle$ when $A > 0$ and six easy-axes along $\langle 100 \rangle$ when $A < 0$. For $A < 0$, since the external magnetic field in the z direction resolves the degeneracy of the easy axes and obviously prefers [001]. Thus, no domain is formed in this case. Whereas in case $A > 0$, the spins in the system prefer a direction between the z axis and $\langle 111 \rangle$ direction, in a Zeeman field along the z axis. We denote the angle between the thin film plane and the z axis as θ and calculate the optimal θ by minimizing the single domain energy, similarly to the (011) film case. In Fig. 5.18(a), we show θ vs. A/B. As you see in the graph, $A/B > 0.25$ is the condition for the formation of domains. This suggests the strong inter-skyrmion attraction may be found when $A/B > 0.25$.

We plot the inter-skyrmion interaction $V(\boldsymbol{R} = R\boldsymbol{e}_x)$ in Fig. 5.18(b) under an out-of-plane ($A/B = 0.2$) and tilted ($A/B = 2.0$) background FM spins. The interaction when $A/B = 0.2$ is always positive. The reason for this is that the shape of a single-skyrmion is almost circular due to the preservation of the C_4 symmetry in the spin space. On the other hand, when $A/B = 2.0$, the interaction is large attraction. This is attributed to the domain formation between the two skyrmions, same as the case of $A/B > 0.5$ in a (011) film. The smaller $|V(r)_{\mathrm{min}}|$ compared with Fig. 5.11(c) is again because of the C_4 symmetry, since the distortion of the

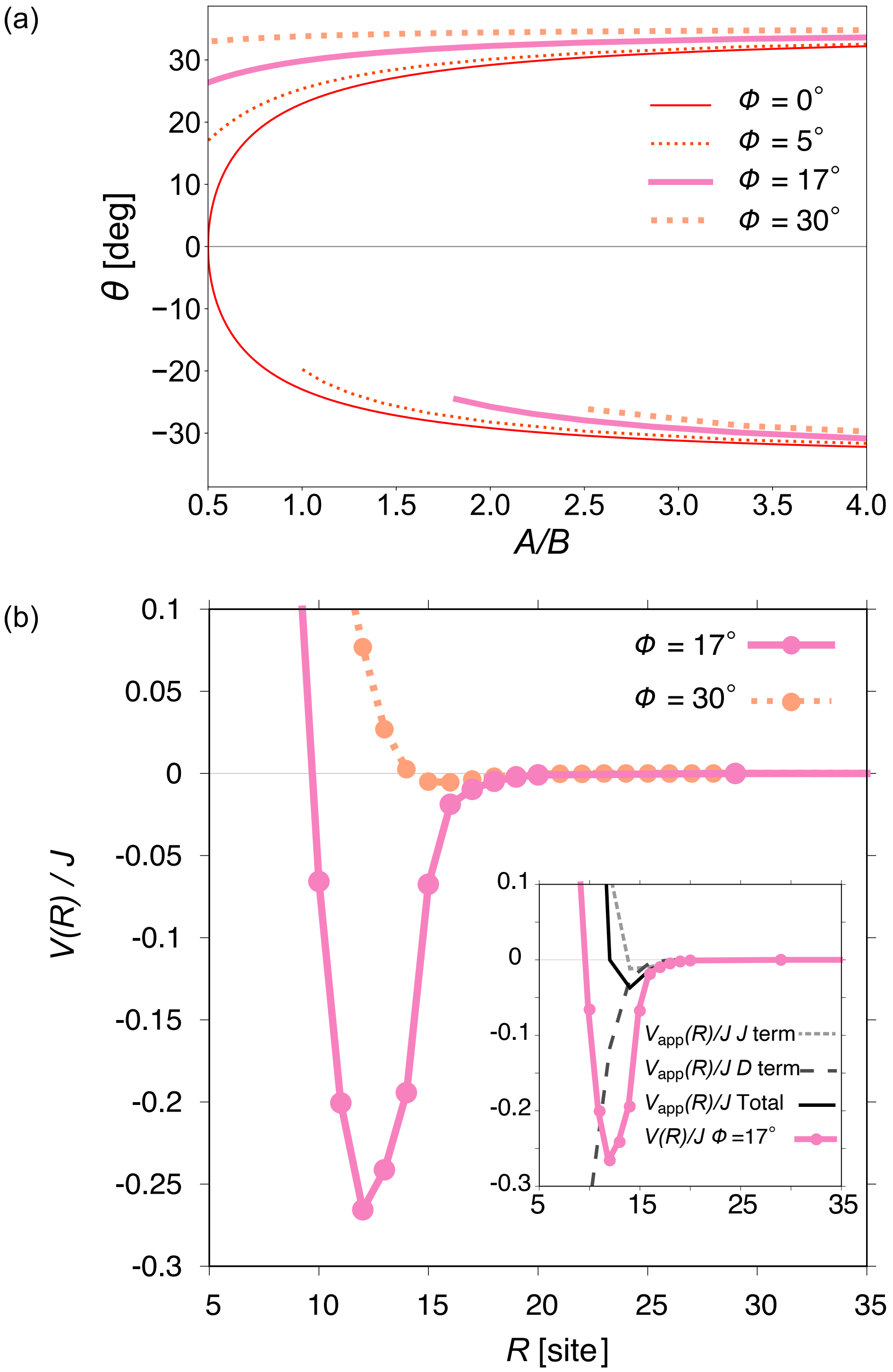

Fig.5.16 (a) Preferred angle θ of a FM state under a tilted magnetic field to the x axis and the magnetocrystalline anisotropy $A > 0$. A/B dependence of stable solution, $\theta > 0$, and metastable one, $\theta < 0$, are shown. We note that θ and ϕ denote the directions of the background magnetizations and the tilted external fields in the x-z plane. The metastable solution vanishes below a certain value of A/B. (b) Skyrmion-pair potential $V(R)$ aligned along the x axis when $BJ/D^2 = 0.5$, $A/B = 2.0$, and $\phi = 17^\circ$ and 30°. In both cases, when $\phi = 17^\circ$ and 30°, the background spins $\hat{\boldsymbol{t}}$ are tilted. Since the metastable solution exists only when $\phi = 17^\circ$, the large attractive potential is found in the parameter. Whereas, for $\phi = 30^\circ$, the attractive potential is found but quite small because of the absence of the domain of the $\theta < 0$. Inset replots the potential with $\phi = 17^\circ$ in the main panel, the approximate one $V_{\text{app}}(R)$, and the J term and D terms in Eq. (5.25). Reproduced from [21]. Copyright 2021, American Physical Society.

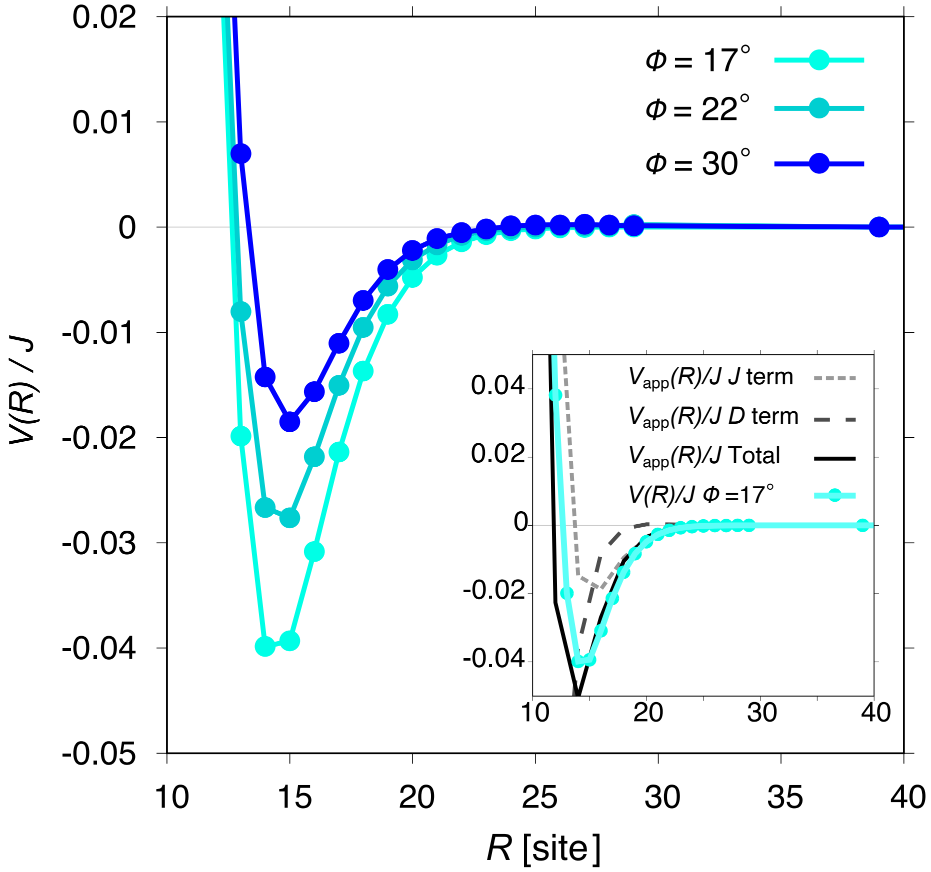

Fig.5.17 Pair potential $V(R)$ between two skyrmions lined up in the x direction with $A/B = 0.5$, $BJ/D^2 = 0.75$ and $\phi = 17°, 22°$, and $30°$. Inset shows the comparison of the data at $\phi = 17°$ with the approximate potential $V_{\text{app}}(R)$, and the J and D terms in Eq. (5.25), which contributes to the interaction.

skyrmion is smaller. This is seen from the inset of Fig. 5.18(b), where we show the approximate expression $V_{\text{app}}(Re_x)$ and the contributions from both the J and D terms. Since the J term contribution doesn't obtain the attraction, we conclude that the deformation of the skyrmion does not enhance the attraction.

The relative position dependence of the interaction is plotted in Fig. 5.19, which clearly shows the C_4 symmetry. Although the maximum attractive interaction is a bit smaller than that of a (011) film, the interesting point is that the attraction can be found in all the relative directions, unlike the (011) film case. There are 4 kinds of magnetic domains in the system (i.e., 4 different directions are found as solutions of the stable uniform state), and the magnetic domain is formed between two skyrmions along the x or the y axis.

We mention the ground-state phase diagram. There are two main differences from that of a (011) film case. Firstly, the SkX phase stabilized by the attraction appears only when $A/B > 0.25$. Secondly, due to the C_4 symmetry, a square lattice of skyrmions becomes stable in the intermediate strength of the magnetic field, and the four energetically degenerate magnetic domains align alternatively.

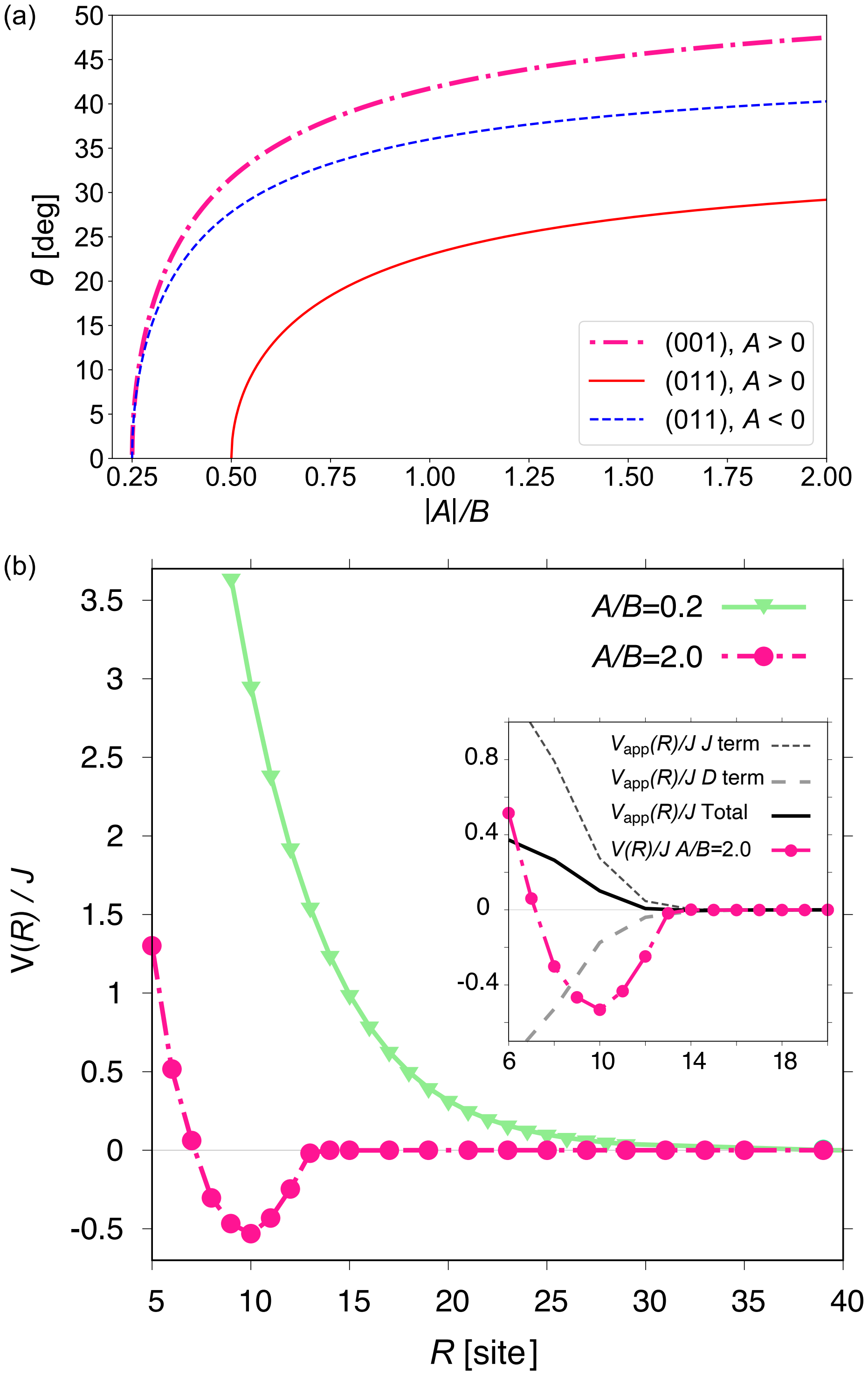

Fig.5.18 (a) $|A|/B$ dependence of favorable angle θ from the z direction of a FM spins in a (001) film. We replot the ones for (011) film [see Fig. 5.8] as a guide for the eye. When $A < 0$, the spins are parallel to the z direction regardless of the value of $|A|/B$, while the tilted spins, along the [110] direction from $\boldsymbol{e}_z$, are preferred when the magnetic anisotropy dominates the Zeeman field at $A/B > 0.25$. (b) Pair interaction potentials $V(R)$ for the skyrmions along the x axis with a magnetic field $BJ/D^2 = 0.75$ and the magneto-crystalline anisotropy $A/B = 2.0$ and 0.2. Inset displays the $V(R)$ with $A/B = 2.0$ in the main panel, the approximate potential at a large distance $V_{\text{app}}(R)$, and the two contributions from the J and the D terms. Reproduced from [21]. Copyright 2021, American Physical Society.

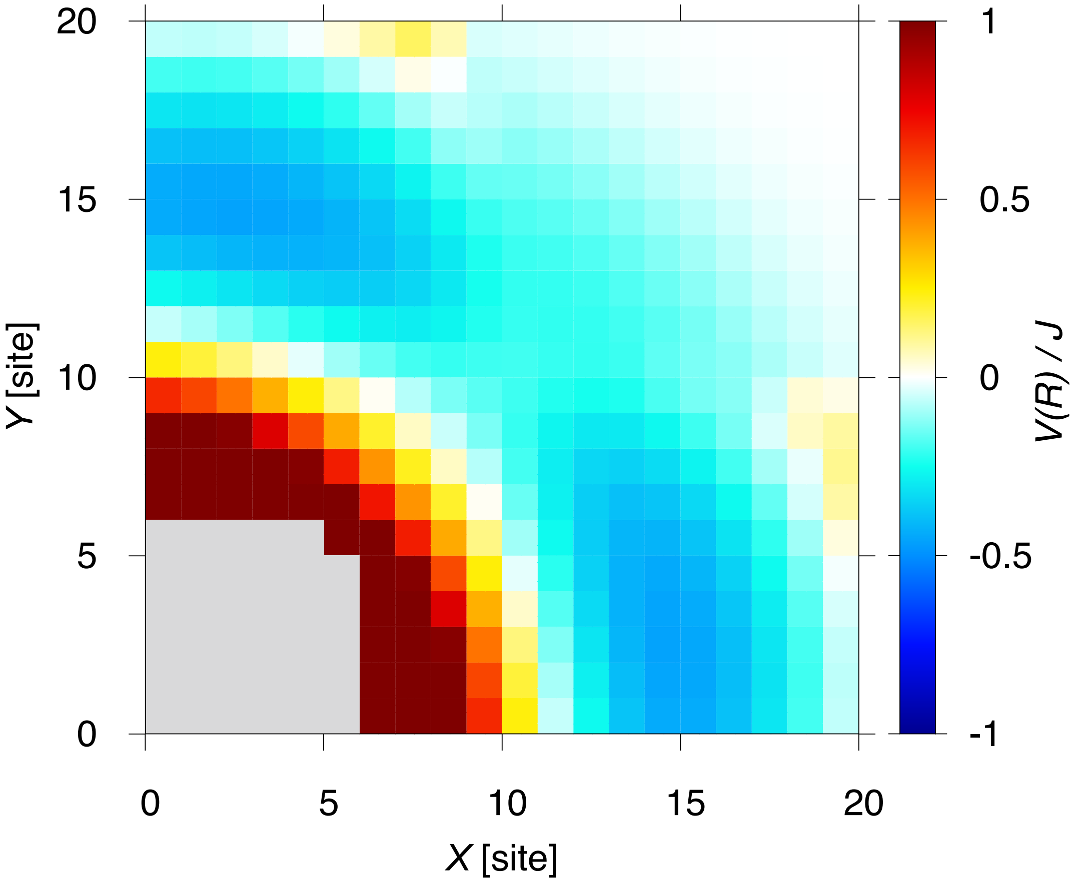

Fig.5.19 Relative position $\boldsymbol{R} = (X, Y)$ dependence of the inter-skyrmion interaction $V(\boldsymbol{R})$ on a (001) thin film. The magneto-crystalline anisotropy is $A/B = 1.0$ and the magnetic field is $BJ/D^2 = 0.75$. The potential $V(\boldsymbol{R})$ reflects the fact that the C_4 symmetry is preserved in the system. Reproduced from [21]. Copyright 2021, American Physical Society.

5.10 Complementary issues

5.10.1 Actual values of the magneto-crystalline anisotropy coefficient A in real materials

Our calculations requires $|A|/B_{\mathrm{cr2}} \geq 0.5$ to realize the large attraction and the domain wall skyrmions. The reported values of the ratio in real materials are $|A|/B_{\mathrm{cr2}} \sim 0.00364$, $|A|/B_{\mathrm{cr2}} \sim 0.385$, and $|A|/B_{\mathrm{cr2}} \sim 1.59$ in a $\mathrm{Cu_2OSeO_3}$ thin film at 5 K [107, 148, 149], in a $\mathrm{Fe_{0.7}Co_{0.3}Si}$ thin film at 5 K [150, 151], and in a $\mathrm{Co_{8.5}Zn_{7.5}Mn_4}$ thin film at 330 K [103, 22], respectively. In the last case, $\mathrm{Co_{8.5}Zn_{7.5}Mn_4}$, the domain wall skyrmions (or bimerons) certainly appears in a very thin film with ~ 50 nm thick.

5.10.2 Bound states at finite temperature

We comment on the relevance of the pair interaction obtained at 0 K to finite temperature. The large binding energy, $|V(\boldsymbol{R})_{\text{min}}|$, as large as J, is of the order of the energy of one skyrmion: Assuming a single-skyrmion embedded in a uniform magnetizations, the amount of the J and D terms [see Eq. (5.8)] is evaluated to be $\pi J/2$ by using $|\boldsymbol{\nabla}\boldsymbol{n}|^2 \sim 1/R_{\text{sk}}^2$ and $\boldsymbol{\nabla} \times \boldsymbol{n} \sim -1/R_{\text{sk}}$ where we consider only inside of the area πR_{sk}^2 at $R_{\text{sk}} \sim Ja/D$. Although the energy per spin is very small because of many spins involved in a skyrmion. Given that skyrmions are in fact observed in large thermal fluctuations at room temperature, however, the skyrmion-bound states which possess comparable binding energies might be also observable in a similar temperature.

5.10.3 Attractive interactions in the 3D cone phase

We also comment on the inter-skyrmion interactions in the 3D configuration, by applying our model to a 2D cross-section. Experimentally, the attractive inter-skyrmion interaction of skyrmions in the 3D cone phase is reported [17, 18]. We think that this can also be explained in our framework; The skyrmion tube structure has a tilted magnetization in the background. This is a similar situation to the tilted magnetic field case where skyrmions are not circularly symmetric anymore. Applying our result, the relative angle dependence of the sign of the interaction, we find that the stacking of the 2D planes results in an attractive interaction on average.

5.10.4 Effect of the dipole-dipole interaction

In the above calculations, we ignored the dipole-dipole interaction (DDI). Even when $A = 0$, DDI enlarges the size of the skyrmions and shifts the phase boundary of the SkX and FM states. When $A \neq 0$, it enhances the deformation of the skyrmion shape and quantitatively modifies the skyrmion-pair potential. Leaving the detailed study of this as future work, we have numerically found that the results of the thesis are the same even with the DDI. In the following, we show numerical data.

The DDI Hamiltonian reads

$$H_{\text{DDI}} = g_{\text{dd}} \sum_{\boldsymbol{r}_1, \boldsymbol{r}_2} \frac{\boldsymbol{S}_{\boldsymbol{r}_1} \cdot \boldsymbol{S}_{\boldsymbol{r}_2} - 3(\boldsymbol{S}_{\boldsymbol{r}_1} \cdot \hat{\boldsymbol{r}}_{12})(\boldsymbol{S}_{\boldsymbol{r}_1} \cdot \hat{\boldsymbol{r}}_{12})}{|\boldsymbol{r}_1 - \boldsymbol{r}_2|^3}, \tag{5.39}$$

where $g_{\text{dd}} = \mu_0 \mathcal{M}^2/(4\pi)$, μ_0 is the vacuum permeability, $\mathcal{M}$ denotes the magnitude of the magnetic moments, and we define $\hat{\boldsymbol{r}}_{12} \equiv (\boldsymbol{r}_1 - \boldsymbol{r}_2)/|\boldsymbol{r}_1 - \boldsymbol{r}_2|$.

In Fig. 5.20(a), we show the comparison of the interaction $V(R)$ with and without H_{DDI}, when $A = \phi = 0$. The $V(R)$ is isotropic repulsion for both cases. In the calculation, $g_{\text{dd}}/a^3 = 0.00439J$ is used in such a way that the skyrmion size is visibly changed. One can see that the skyrmion size is indeed increased from the shift of $V(R)$ with DDI to the right in Fig. 5.20(a). The H_{DDI} only enlarges the skyrmion. The inset of Fig. 5.20(a) compares $V(R)$ and $V_{\mathrm{app}}(R)$ with H_{DDI}, demonstrating that the dipole interaction commits to $V(R)$ only via the J term in Eq. (5.25).

On the other hand, when skyrmion is in the tilted background magnetization, the DDI non-trivially modifies the inter-skyrmion potential. Figure 5.20(b) displays $V(R\boldsymbol{e}_x)$ with $A/B = 1.0$ and $\phi = 0$ in the presence and absence of the DDI, where the same g_{dd} as Fig. 5.20(a) is used. Notably, as for the $A \neq 0$, H_{DDI} enhances the attraction. Furthermore, due to its long-range nature, the DDI may also modify the approximate interaction potential, Eq. (5.19). We also plot the $V_{\mathrm{app}}(R)$ in Fig. 5.20(b) with or without the DDI, from which one can see that the $V_{\mathrm{app}}(R)$, especially with the DDI case, does not reproduces the pair-potential even at a large distance. In Fig. 5.20(c), we compare $V(R)$ with the DDI at $g_{\mathrm{dd}}/a^3 = 0.00439J$ (replotted) and larger one $g_{\mathrm{dd}}/a^3 = 0.0196J$. It follows that the larger DDI not only deepens the attraction but also makes the potential more long-ranged. Although the larger DDI hardly changes the qualitative spin profile in the real space, as the Fig. 5.20(d) shows, H_{DDI} modifies the configuration as if the A term is enlarged; It prefers the in-plane magnetization.

5.11 Conclusion

In conclusion, we studied inter-skyrmion interactions and (meta)stable spin states in 2D chiral magnets on a (011) thin film. The film is assumed to be under a (tilted) magnetic field and/or the magnetocrystalline anisotropy. We find the approximate expression of the interaction $V_{\mathrm{app}}(R)$ at a large distance, using a single skyrmion configuration. $V_{\mathrm{app}}(R)$ can predict that the deformation of a skyrmion shape may lead to the sign change of the inter-skyrmion interaction. Numerical calculations back up the exhibition of the attractive interaction in an anisotropic geometry; When $A = 0$ or $\phi = 0$ and $A/B \leq 0.5$, $V(R)$ is a weak attraction in a certain direction and consistent with $V_{\mathrm{app}}(R)$. However, under the sufficiently large magnetocrystalline anisotropy ($\phi = 0$ and $A/B > 0.5$), the attractive interaction becomes much larger than that predicted by $V_{\mathrm{app}}(R)$. The giant attractive interaction, $\sim J$, is due to the magnetic domain formation between the two interacting skyrmions. Notably, the magnitude of the attraction can be controlled by the direction of the in-plane magnetic field by two orders of magnitude. The possible high controllability of the interactions, demonstrated here, may pave the way to utilize skyrmions as an information carrier.

In the vicinity of the SkX-FM phase boundary, the inter-skyrmion attraction stabilizes the distorted SkX as a ground state. It accompanies the magnetic domain wall in the background of the skyrmions. The strong attraction also enhances the upper critical magnetic field of the SkX in the phase diagram. We also find the 1D alignments of bound skyrmions as an excitation in the FM state.

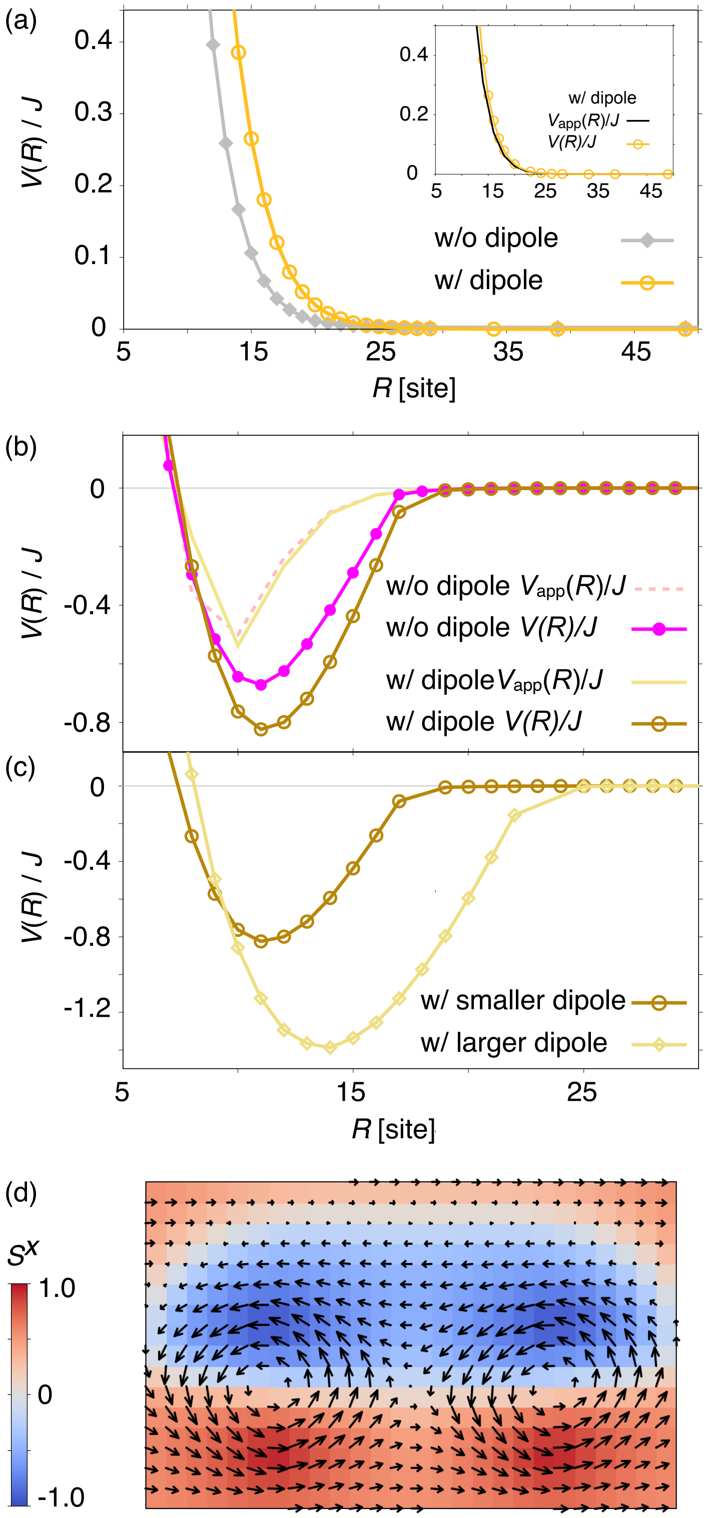

Fig.5.20 (a) Interaction potential $V(R)$ with or without the H_{DDI} at $A/B = 0.0$ and $g_{\mathrm{dd}}/a^3 = 0.00439J$. The inset shows $V(R)$ with H_{DDI} in the main panel and the approximate potential $V_{\mathrm{app}}(R)$. The relative position of the two skyrmions is $\boldsymbol{R} = R\boldsymbol{e}_x$ with $\phi = 0$ and $BJ/D^2 = 0.9$. (b) $V(R)$ with or without the H_{DDI} at $A/B = 1.0$ and $g_{\mathrm{dd}}/a^3 = 0.00439J$. Other parameters are the same as that in (a). Approximate potentials $V_{\mathrm{app}}(R)$ in the presence/ absence of the DDI are also shown in the same panel. (c) Interaction potential $V(R)$ with the H_{DDI} at $A/B = 1.0$ and $g_{\mathrm{dd}}/a^3 = 0.00439J$ (replotted) or $0.0196J$. Other parameters are the same as that in (a). (d) Magnetization configuration of a bound two skyrmions at a relative distance $R = 14$ in (c) with the larger DDI, with $g_{\mathrm{dd}}/a^3 = 0.0196J$. The color plots denote $S^x_{\boldsymbol{r}}$ and the black arrows show the in-plane (x-y plane) spin vector components.

Chapter 6

Conclusion

In the doctoral study, we investigated magnetically ordered spin configurations using atomistic spin dynamics simulations. Especially, we focused on spin states in amorphous and chiral magnets, which are capable of spintronics applications.

In terms of the spin dynamics simulations in amorphous ferromagnets $\mathrm{Co_4P}$, we demonstrated a model which combine RMC and ASD methods, to calculate the magnetic excitation spectra. It enables accurate calculation by reproducing realistic atomic structure and including magnon interactions up to all orders. Using the model, we have found that $\mathrm{Co_4P}$ has magnons which follow the Bloch's law, consistent with experiments and similar to that in crystal ferromagnets. There are two parabolas in the magnetic excitation spectrum. First dip is centered at $Q \sim 0$ and second one is at $Q \sim 3$ Å^{-1}. The second dip, conventionally called "roton-like feature", may be interpreted in terms of the magnon Umklapp scattering. This may be caused by the residual ordering in the re-created amorphous structure. The energy spectrum of $\mathrm{Co_4P}$ looks very similar to that of FCC Co up to the first Brillouin Zone. However, unlike crystals it is not periodic and second dip is not repeated at higher wavenumbers. We found that energy spectrum in QCA correctly predicts the spectra at $Q \sim 0$ and at high frequency region. The method for investigating the magnetic properties of amorphous magnets can be applied to other magnetism, such as antiferromagnets and spin glasses. It can also be extended to study the spin transport properties, i.e. using the Kubo formula [152], and may pave the way to utilize amorphous magnets as magnetic devices in the field of spintronics.

In terms of the anisotropic magnetic skyrmions in chiral magnets, we found the analytic expression of approximated inter-skyrmion interaction at a large distance from a single skyrmion configuration. Two mechanisms of inducing the attractive interactions are revealed: a small deformation of skyrmion shape or formation of magnetic domain between two skyrmions. The latter induces small attractions and latter causes large attractions. The large attraction in the latter case affects the ground state SkX and elongated triangular bimeron lattice appears with magnetic domains in the background. Due to the large attraction, there is an area in the phase diagram where the SkX is sustained by the attractive interaction. In addition, we found the attraction can be tuned in the range over double-digit by the in-plane magnetic field.

In this study, we have focused on 2D systems and ignored inter-layer interactions, i.e., in bilayer and multilayer systems. This interaction does not contain the spacial derivatives and does not change Eq. (5.19); We believe that the qualitative behavior of the skyrmion-skyrmion interaction is unchanged and leave the quantitative investigation as future work. The extension of the model to the multilayer systems may find a way of controlling the skyrmion qubits [153, 154, 155]. Similarly, time-dependent modulation of skyrmion shape, caused by the thermal fluctuations, etc., is also expected to adjust the skyrmion-skyrmion interaction. The result of the work would be a guiding principle for controlling the effective skyrmion pair potential.

Appendix

A Validation of the simulation at small wavenumber region

We note how our energy spectrum using JAMS (the name of our program), $\epsilon^{\mathrm{JAMS}}(Q)$, is quantitatively related to the QCA spectrum, $\epsilon^{\mathrm{QCA}}(Q)$,

$$\epsilon^{\mathrm{QCA}}(\boldsymbol{Q}) = 2SN/V \int d\boldsymbol{r}_{ij} J(r_{ij}) g(r_{ij})(1 - e^{i\boldsymbol{Q}\boldsymbol{r}_{ij}}), \tag{A.1}$$

where we include the original coefficients introduced by Kaneyoshi; Since the integrand is isotropic (meaning we can integrate over angular variables), Eq. (A.1) is rewritten as

$$\epsilon^{\mathrm{QCA}}(Q) = \mathscr{K} \int dr_{ij}\, r_{ij}^2 \frac{J(r_{ij})}{J_0} g(r_{ij}) \left(1 - \frac{\sin Q r_{ij}}{Q r_{ij}}\right), \tag{A.2}$$

where $\mathscr{K} \equiv 8S\pi\rho_{\mathrm{Co}}J_0$. Note that Eq. (A.1) can be exact in the case of lattice if we rewrite $J(r_{ij}) \to J(\boldsymbol{r}_{ij})$ and $g(r_{ij}) \to g(\boldsymbol{r}_{ij})$.

Let us confirm that our spectra $\epsilon^{\mathrm{JAMS}}(Q)$ obtains quantitatively equivalent dispersion relation to Eq. (A.2), by inserting specific values: $J_0 = 2.8 \times 10^{-21}$ [J] =17.478 [meV], $\rho_{\mathrm{Co}} = 0.8\rho = 0.0536$, $S = 1$.

$$\epsilon^{\mathrm{QCA}}(Q)[\mathrm{meV}] = 23.544 \int dr_{ij}\, r_{ij}^2 \frac{J(r_{ij})}{J_0} \times g(r_{ij}) \left(1 - \frac{\sin Q r_{ij}}{Q r_{ij}}\right). \tag{A.3}$$

In the limit of $Q \to 0$, Eq. (A.3) is approximated to

$$\epsilon^{\mathrm{QCA}}(Q)[\mathrm{meV}] = 5.83 \int dr_{ij} \frac{J(r_{ij})}{J_0} n(r_{ij})(Q r_{ij})^2. \tag{A.4}$$

where we used the relation $n(r) = 4\pi\rho_{\mathrm{Co}} r^2 g(r)$.

To be specific, we consider FCC lattice: $n(r) = z^{\rm 1st}_{\rm FCC}\delta(r - r_{\rm n.n.}) + ...)$ and $J(r_{ij}) = J_0\Theta(r_{\rm n.n.} - r)$;

$$\begin{aligned}\epsilon^{\rm QCA}(Q)[{\rm meV}] &= 5.83\int_0^{r_{\rm n.n.}} dr_{ij}\ z^{\rm 1st}_{\rm FCC}\delta(r - r_{\rm n.n.})(Qr_{ij})^2 \\ &= 5.83\ \times z^{\rm 1st}_{\rm FCC}\ r^2_{\rm n.n.} \times Q^2. \end{aligned} \tag{A.5}$$

Inserting $z^{\rm 1st}_{\rm FCC} = 12$ and $r_{\rm n.n.} = \frac{a_{\rm FCC}}{\sqrt{2}}$ gives

$$\epsilon^{\rm QCA}(Q)[{\rm meV}] = 49.5\ \times a_{\rm FCC} \times\ Q^2. \tag{A.6}$$

In our program, $\epsilon(\boldsymbol{Q})^{\rm JAMS}$ is defined as

$$\epsilon^{\rm JAMS}[{\rm meV}](\boldsymbol{Q}) = \frac{\hbar\gamma_e J_0}{\mu N}\sum_{ij}\frac{J(r_{ij})}{J_0}z_{ij_{\rm JAMS}}(1 - e^{i\boldsymbol{Q}\boldsymbol{r}_{ij}}), \tag{A.7}$$

By inserting values $\gamma_e = 1.76 \times 10^{11}[{\rm s}^{-1}{\rm T}^{-1}]$, $J_0 = 2.8 \times 10^{-21}[{\rm J}]$, $\mu = 1.0\mu_B = 9.27 \times 10^{-24}[{\rm JT}^{-1}]$,

$$\epsilon^{\rm JAMS}[{\rm meV}](\boldsymbol{Q}) = \frac{34.84}{N}\sum_{ij}\frac{J(r_{ij})}{J_0}z_{ij_{\rm JAMS}}(1 - e^{i\boldsymbol{Q}\boldsymbol{r}_{ij}}). \tag{A.8}$$

Note that the transformation coefficient from [J] to [meV] is 6.242×10^{21}. Above equation can be rewritten as

$$\epsilon^{\rm JAMS}[{\rm meV}](Q) = \frac{34.84}{N}\sum_{ij}\frac{J(r_{ij})}{J_0}z'_{ij_{\rm JAMS}}(1 - {\rm cos}Qr^{\perp}_{ij}), \tag{A.9}$$

where $r^{\perp}_{ij}$ is the vertical component to $\boldsymbol{Q}$ and $z'_{ij_{\rm JAMS}}$ is the number of interacting spins under specific $J(r_{ij})$.

In the limit of $Q \to 0$, Eq. (A.9) is approximated to

$$\epsilon^{\rm JAMS}[{\rm meV}](Q) = \frac{17.42}{N}\left[\sum_{ij}\frac{J(r_{ij})}{J_0}z'_{ij_{\rm JAMS}}(r^{\perp}_{ij})^2\right]\ Q^2. \tag{A.10}$$

In the case of FCC lattice: $J(r_{ij}) = J_0\Theta(r_{\rm n.n.} - r)$,

$$\epsilon^{\rm JAMS}[{\rm meV}](Q) = 17.42 \times z'_{n.n._{\rm JAMS}}(r^{\perp}_{n.n.})^2 \times\ Q^2. \tag{A.11}$$

Using the relations,

$$z'_{n.n._{\rm JAMS}} = \frac{2}{3}z^{\rm 1st}_{\rm FCC}, \tag{A.12}$$

$$r^{\perp}_{n.n._{\rm JAMS}} = \frac{1}{\sqrt{2}}r_{n.n.}, \tag{A.13}$$

it follows that

$$\epsilon^{\mathrm{JAMS}}[\mathrm{meV}](Q) = 5.81 \times z^{\mathrm{1st}}_{\mathrm{FCC}}(r_{n.n.})^2 \times \, Q^2. \tag{A.14}$$

We can clearly see that Eq. (A.6) and Eq. (A.14) have almost the same coefficient before Q^2.

B Derivation of the amorphous neutron scattering cross-section

Following a book [94], we derive suitable expression of cross-section for (polarized neutron beam's) magnetic inelastic scattering, which can also be used in amorphous magnetic systems.

B.1 Elastic scattering

There are several good reasons why thermal neutrons are widely used in the field of condensed matter physics; Firstly, they have comparable wavelength to the space between nuclei in crystals.c Secondly, the energy is of the same order as the excitations in solids, liquids, and gases. Thirdly, they are neutral particles and have magnetic moments.

Let us derive the general expression for the neutron cross-section. Let $\Psi_{\boldsymbol{Q}}$ be the initial state of a neutron, and $\Psi_{\boldsymbol{Q'}}$ be the final (scattered) state of a neutron. If the incident flux (number of the neutrons per unit area & per unit time) is N_{in}, then the scattered neutrons into the solid angle $d\Omega = \sin\theta d\theta d\phi$ per unit time is

$$N_{\mathrm{in}} \frac{d\Theta}{d\Omega} d\Omega, \tag{B.1}$$

where $\frac{d\Theta}{d\Omega}$ is the differential cross section. In order to calculate $\frac{d\Theta}{d\Omega}$ in the case of elastic scattering, the transition probability from $\Psi_{\boldsymbol{Q}}$ to $\Psi_{\boldsymbol{Q'}}$ is necessary. This probably is given by Fermi's Golden rule

$$W_{Q\to Q'} = \frac{2\pi}{\hbar} \left| \int d\boldsymbol{r} \Psi^*_{\boldsymbol{Q'}} \hat{V} \Psi_{\boldsymbol{Q}} \right|^2 \rho_{\boldsymbol{Q'}}(E), \tag{B.2}$$

where $\hat{V}$ is the potential which causes the transition, and $\rho_{\boldsymbol{Q'}}(E)$ is the DOS of final states per unit range of energy. We assume that the system is consist of free electrons, meaning

$$\Psi_{\boldsymbol{Q}} = \frac{1}{L^{3/2}} \exp(i\boldsymbol{Q}\cdot\boldsymbol{r}), \tag{B.3}$$

$$\rho_{\boldsymbol{Q'}}(E) = \left(\frac{L}{2\pi}\right)^3 \frac{d\boldsymbol{Q}}{dE} = \left(\frac{L}{2\pi}\right)^3 \frac{mQ}{\hbar^2} d\Omega. \tag{B.4}$$

Here we used $d\boldsymbol{Q} = Q^2 d\Omega dk$ and $E = \frac{\hbar^2 Q^2}{2m}$, and assumed the volume of the system is L^3. The incident flux is

$$\text{(velocity of incident neutron flux)}/L^3 = \frac{\hbar Q}{mL^3}. \tag{B.5}$$

From (B.2), (B.4), and (B.5),

$$d\Theta = W_{Q\to Q'}/\text{(incident flux)} \tag{B.6}$$

$$= L^6\left(\frac{m}{2\pi\hbar^2}\right)^2\left|\int d\boldsymbol{r}\Psi^*_{\boldsymbol{Q'}}\hat{V}\Psi_{\boldsymbol{Q}}\right|^2 d\Omega \tag{B.7}$$

$$\equiv \left(\frac{m}{2\pi\hbar^2}\right)^2 |\langle\boldsymbol{Q'}|\,\hat{V}\,|\boldsymbol{Q}\rangle|^2 d\Omega \tag{B.8}$$

The scattering amplitude $F(\boldsymbol{Q},\boldsymbol{Q'})$ is defined as

$$\frac{d\Theta}{d\Omega} = |F(\boldsymbol{Q},\boldsymbol{Q'})|^2. \tag{B.9}$$

From Eq. (B.8), we can take

$$F(\boldsymbol{Q},\boldsymbol{Q'}) = -\frac{m}{2\pi\hbar^2}\langle\boldsymbol{Q'}|\,\hat{V}\,|\boldsymbol{Q}\rangle\,. \tag{B.10}$$

B.2 Inelastic scattering

In this case, the initial and final change by an energy difference. Let's say they are $|\lambda\rangle$ and $|\lambda'\rangle$ respectively, having energies E_λ and $E_{\lambda'}$. The cross-section becomes

$$\frac{d\Theta}{d\Omega}_{\boldsymbol{Q},\lambda\to\boldsymbol{Q'},\lambda'} = \frac{Q'}{Q}\left(\frac{m}{2\pi\hbar^2}\right)^2 |\langle\boldsymbol{Q'}\lambda'|\,\hat{V}\,|\boldsymbol{Q}\lambda\rangle|^2. \tag{B.11}$$

They should conserve the energy

$$\frac{\hbar^2Q^2}{2m} + E_\lambda = \frac{\hbar^2Q'^2}{2m} + E_{\lambda'}. \tag{B.12}$$

Building the condition into the cross-section to define a "partial differential cross-section" as

$$\frac{d^2\Theta}{d\Omega dE'}_{\boldsymbol{Q},\lambda\to\boldsymbol{Q'},\lambda'} = \frac{Q'}{Q}\left(\frac{m}{2\pi\hbar^2}\right)^2 |\langle\boldsymbol{Q'}\lambda'|\,\hat{V}\,|\boldsymbol{Q}\lambda\rangle|^2\delta(\hbar\omega + E_\lambda - E_{\lambda'}), \tag{B.13}$$

where $E' \equiv E_{\lambda'}$ and

$$\hbar\omega = \frac{\hbar^2}{2m}(Q^2 - Q'^2) = E_\lambda - E_{\lambda'}. \tag{B.14}$$

We have to sum Eq. (B.13) over all possible final states of the targets $|\lambda'\rangle$, and average it over all the possible initial states. Initial states occur with probabilities p_λ, and we also take into account the spin states of neutrons (denoted by $\Theta,\ \Theta'$). The master formula is

$$\frac{d^2\Theta}{d\Omega dE'} = \frac{Q'}{Q}\left(\frac{m}{2\pi\hbar^2}\right)^2 \sum_{\lambda,\Theta} p_\lambda p_\Theta \sum_{\lambda',\Theta'} |\langle \boldsymbol{Q'}\Theta'\lambda'|\,\hat{V}\,|\boldsymbol{Q}\Theta\lambda\rangle|^2 \delta(\hbar\omega + E_\lambda - E_{\lambda'}). \tag{B.15}$$

Note that above equation is the first Born approximation to the cross-section (Eq. (B.2) is derived from perturbation theory).

B.3 Coherent and incoherent scattering

From experimental results, nucleon-nucleon interaction is a very short range ($\sim 10^{-4}$Å), which is much less than the thermal neutrons' wavelength (~ 1Å). So the scattering is isotropic, containing only s-wave. The scattering can be characterized by one parameter: scattering length ξ (complex). For now, we assume that the target is single spinless isotope with having a scattering length ξ.

It is only $\hat{V}(\boldsymbol{r}) \propto \delta(\boldsymbol{r})$ which gives isotropic scattering when we use the Born approximation (cf. Fermi 1936). If the nucleus is at position $\boldsymbol{R}$, the Fermi pseudo potential is

$$\hat{V}(\boldsymbol{r}) = \frac{2\pi\hbar^2}{m}\xi\delta(\boldsymbol{r} - \boldsymbol{R}). \tag{B.16}$$

Note that above equation is just a formal artifice. Substituting above Eq. into Eq. (B.10), the scattering amplitude is given by (we take $\boldsymbol{R} = \boldsymbol{0}$)

$$\begin{aligned} F &= -\frac{m}{2\pi\hbar^2}\frac{2\pi\hbar^2}{m}\xi \int d\boldsymbol{r}\exp(-i\boldsymbol{Q'}\cdot\boldsymbol{r})\delta(\boldsymbol{r})\exp(i\boldsymbol{Q}\cdot\boldsymbol{r}) \\ &= -\xi. \end{aligned} \tag{B.17}$$

Giving rise to

$$\frac{d\Theta}{d\Omega} = |\xi|^2 \text{ and } \Theta_\xi = 4\pi|\xi|^2, \tag{B.18}$$

where Θ_ξ is the total cross-section.

Next, let's consider a scattering from an array of N_{in} nuclei, which are rigidly bound at site $\boldsymbol{R_l}$. We remove the restriction that a target is single spinless isotope. The each scattering length is denoted as ξ_l. The interaction potential is

$$\hat{V}(\boldsymbol{r}) = \frac{2\pi\hbar^2}{m}\sum_l \xi_l \delta(\boldsymbol{r} - \boldsymbol{R_l}). \tag{B.19}$$

The cross-section is

$$\frac{d^2\Theta}{d\Omega dE'} = \frac{Q'}{Q}\left(\frac{m}{2\pi\hbar^2}\right)^2 \sum_{\lambda,\Theta} p_\lambda p_\Theta \sum_{\lambda',\Theta'} |\langle\Theta'\lambda'| \exp(i(\boldsymbol{Q} - \boldsymbol{Q'}) \cdot \boldsymbol{R}_l) |\Theta\lambda\rangle|^2 \delta(\hbar\omega + E_\lambda - E_{\lambda'}), \tag{B.20}$$

since $\langle \boldsymbol{Q'}| \hat{V} |\boldsymbol{Q}\rangle$ is now

$$\begin{aligned}\langle \boldsymbol{Q'}| \hat{V} |\boldsymbol{Q}\rangle &= \frac{2\pi\hbar^2}{m}\sum_l \xi_l \int d\boldsymbol{r}\exp(-i\boldsymbol{Q'}\cdot\boldsymbol{r})\delta(\boldsymbol{r} - \boldsymbol{R_l})\exp(i\boldsymbol{Q}\cdot\boldsymbol{r}) \\ &= \frac{2\pi\hbar^2}{m}\sum_l \xi_l \exp(i(\boldsymbol{Q} - \boldsymbol{Q'})\cdot\boldsymbol{R}_l).\end{aligned} \tag{B.21}$$

In the case of crystal, the energy can be approximated that it is independent both of isotope distribution and the states of nuclear spins, which are the only states the quantum numbers λ, λ' refer to. So the scattering is elastic, and the cross-section is reduces to

$$\frac{d\Theta}{d\Omega} = \sum_{\lambda,\Theta} p_\lambda p_\Theta \sum_{l,l'} \exp\left\{i(\boldsymbol{Q} - \boldsymbol{Q'})\cdot(\boldsymbol{R}_l - \boldsymbol{R}_{l'})\right\} \langle\Theta\lambda| \xi^*_{l'}\xi_l |\Theta\lambda\rangle . \tag{B.22}$$

Expressing

$$\overline{\xi^*_{l'}\xi_l} = \sum_\lambda p_\lambda \langle\lambda| \xi^*_{l'}\xi_l |\lambda\rangle \tag{B.23}$$

is convenient. Using the expression and $\sum_\Theta p_\Theta = 1$, Eq. (B.22) is now

$$\frac{d\Theta}{d\Omega} = \sum_{l,l'} \exp\left\{i(\boldsymbol{Q} - \boldsymbol{Q'})\cdot(\boldsymbol{R}_l - \boldsymbol{R}_{l'})\right\} \overline{\xi^*_{l'}\xi_l}. \tag{B.24}$$

Since ξ_l and ξ_l' are not correlated,

$$\overline{\xi_{l'}^{*}\xi_l} = \overline{\xi_{l'}^{*}}\,\overline{\xi_l} = |\bar{\xi}|^2 \text{ (if } l \neq l'), \tag{B.25}$$

$$\overline{\xi_{l'}^{*}\xi_l} = \overline{|\xi_l|^2} = \overline{|\xi|^2} \text{ (if } l = l'), \tag{B.26}$$

$$\tag{B.27}$$

so in general

$$\overline{\xi_{l'}^{*}\xi_l} = |\bar{\xi}|^2 + \delta_{l,l'}(\overline{|\xi|^2} - |\bar{\xi}|^2). \tag{B.28}$$

We can substitute above equation into Eq. (B.24), to obtain

$$\begin{aligned} \frac{d\Theta}{d\Omega} &= \sum_{l,l'} \exp\left\{i(\boldsymbol{Q} - \boldsymbol{Q'}) \cdot (\boldsymbol{R}_l - \boldsymbol{R}_{l'})\right\} [|\bar{\xi}|^2 + \delta_{l,l'}(\overline{|\xi|^2} - |\bar{\xi}|^2)], \\ &= \left(\frac{d\Theta}{d\Omega}\right)_{\text{coh}} + \left(\frac{d\Theta}{d\Omega}\right)_{\text{incoh}}, \\ &= |\bar{\xi}|^2 \left|\sum_l \exp(i(\boldsymbol{Q} - \boldsymbol{Q'}) \cdot \boldsymbol{R}_l)\right|^2 + [N_{\text{in}}\overline{|\xi - \bar{\xi}|^2}]. \end{aligned} \tag{B.29}$$

Physical meaning of the coherent and incoherent scattering are follows; The "mean scattering potential" is the only component which affects on the interference, thus coherent potential is proportional to $\bar{\xi}$ (average over all different scattering lengths ξ). Whereas the deviations from the mean potential distribute randomly, and they cannot interfere, thus the incoherent potential is proportional to $\overline{|\xi - \bar{\xi}|^2}$ (mean-square of the deviation).

B.4 Scattering by magnetic interactions

We first review the cross-sections for scattering by unpaired electrons. We handle two cases (a) when the unpaired electrons' wave functions are localized and (b) when the itinerant behaviors are allowed. The Hamiltonian in the case of single neutron with magnetic moment μ and mass M in magnetic field $\boldsymbol{B}$ and electric field $\boldsymbol{E}$ is (up to the order of $1/m^2$)

$$\mathcal{H} = \frac{\hat{\boldsymbol{p}^2}}{2M} - \hat{\boldsymbol{\mu}} \cdot \hat{\boldsymbol{B}} - \frac{1}{mc}\hat{\boldsymbol{\mu}} \cdot (\hat{\boldsymbol{E}} \times \hat{\boldsymbol{p}}) - \frac{\hbar\mu}{2mc}\boldsymbol{\nabla} \cdot \hat{\boldsymbol{E}}, \tag{B.30}$$

where the second term is the only magnetic interaction among the four (the first term is the kinetic energy, the third term is the third and fourth terms is important when we consider polarized neutrons).

Let's focus on the interaction with magnetic field arising from the unpaired electrons in crystals. Rewriting the second term

$$-\hat{\boldsymbol{\mu}}\cdot\hat{\boldsymbol{B}} = -\gamma_n\mu_N\hat{\boldsymbol{\Theta}}\cdot\hat{\boldsymbol{B}} \quad (\gamma_n = -1.91), \tag{B.31}$$

$\boldsymbol{B}$ due to a moving single electron (with spin $\boldsymbol{s}$, mass m_e, and velocity $\boldsymbol{\mathcal{V}}_e$) is

$$\boldsymbol{B} = \mathrm{rot}\left(\frac{\boldsymbol{s}\times\boldsymbol{R}}{|\boldsymbol{R}|^3}\right) - \frac{e}{c}\frac{\boldsymbol{\mathcal{V}}_e\times\boldsymbol{R}}{|\boldsymbol{R}|^3}, \tag{B.32}$$

due to Biot - Savart law. Here we assumed that $v_e << c$, where the origin of $\boldsymbol{R}$ is where the electron is. The second term is now

$$-\hat{\boldsymbol{\mu}}\cdot\hat{\boldsymbol{B}} = \gamma_e\mu_N\left\{2\mu_B\hat{\boldsymbol{\Theta}}\cdot\mathrm{rot}\left(\frac{\hat{\boldsymbol{s}}\times\boldsymbol{R}}{|\boldsymbol{R}|^3}\right) - \frac{e}{2m_e c}\left(\hat{\boldsymbol{p}}_e\cdot\frac{\hat{\boldsymbol{\Theta}}\times\boldsymbol{R}}{|\boldsymbol{R}|^3} + \frac{\hat{\boldsymbol{\Theta}}\times\boldsymbol{R}}{|\boldsymbol{R}|^3}\cdot\hat{\boldsymbol{p}}_e\right)\right\}, \tag{B.33}$$

where the second term is due to the operator nature of $\hat{\boldsymbol{p}}_e \equiv m\boldsymbol{\mathcal{V}}_e$ (This means that $-\hat{\boldsymbol{\mu}}\cdot\hat{\boldsymbol{B}}$ was chosen to satisfy $\mathcal{H} = \mathcal{H}^\dagger$). The first term is classically dipole-dipole interaction and the second term is due to the electron's motion. Substituting above equation into Eq. (B.13) gives the cross-section in this case as

$$\begin{aligned}\frac{d^2\Theta}{d\Omega dE'} = &\left(\frac{m}{2\pi\hbar^2}\right)^2(2\gamma_e\mu_N\mu_B)^2\sum_{\lambda\lambda'\Theta}\frac{Q'}{Q}p_\lambda p_\Theta\delta(\hbar\omega + E_\lambda - E_{\lambda'}) \\ &\times\left|\langle\boldsymbol{Q'}\lambda'\Theta'|\sum_i\hat{\boldsymbol{\Theta}}\cdot\mathrm{rot}\left(\frac{\hat{\boldsymbol{s}}_i\times\boldsymbol{R}}{|\boldsymbol{R}|^3}\right) - \frac{1}{2\hbar}\left(\hat{\boldsymbol{p}}_i\cdot\frac{\hat{\boldsymbol{\Theta}}\times\boldsymbol{R}}{|\boldsymbol{R}|^3} + \frac{\hat{\boldsymbol{\Theta}}\times\boldsymbol{R}}{|\boldsymbol{R}|^3}\cdot\hat{\boldsymbol{p}}_i\right)|\boldsymbol{Q}\lambda\Theta\rangle\right|^2.\end{aligned} \tag{B.34}$$

The matrix elements $\langle\boldsymbol{Q'}|\sum_i\hat{\boldsymbol{\Theta}}\cdot\mathrm{rot}\left(\frac{\hat{\boldsymbol{s}}_i\times\boldsymbol{R}}{|\boldsymbol{R}|^3}\right) - \frac{1}{2\hbar}\left(\hat{\boldsymbol{p}}_i\cdot\frac{\hat{\boldsymbol{\Theta}}\times\boldsymbol{R}}{|\boldsymbol{R}|^3} + \frac{\hat{\boldsymbol{\Theta}}\times\boldsymbol{R}}{|\boldsymbol{R}|^3}\cdot\hat{\boldsymbol{p}}_i\right)|\boldsymbol{Q}\rangle$ can be calculated by utilizing the relations

$$\begin{aligned}\mathrm{rot}\left(\frac{\hat{\boldsymbol{s}}_i\times\boldsymbol{R}}{|\boldsymbol{R}|^3}\right) &= -\mathrm{rot}\left(\hat{\boldsymbol{s}}_i\times\boldsymbol{\nabla}\left(\frac{1}{|\boldsymbol{R}|}\right)\right) \\ &= -\boldsymbol{\nabla}\times(\hat{\boldsymbol{s}}_i\times\boldsymbol{\nabla})\left(\frac{1}{|\boldsymbol{R}|}\right) \\ &= -\frac{1}{2\pi^2}\int d\boldsymbol{q}\frac{1}{q^2}\left\{\boldsymbol{q}\times(\hat{\boldsymbol{s}}_i\times\boldsymbol{q})\right\}e^{i\boldsymbol{q}\cdot\boldsymbol{R}},\end{aligned} \tag{B.35}$$

as

$$\langle\boldsymbol{Q'}|\hat{\boldsymbol{\Theta}}\cdot\mathrm{rot}\left(\frac{\hat{\boldsymbol{s}}_i\times\boldsymbol{R}}{|\boldsymbol{R}|^3}\right)|\boldsymbol{Q}\rangle = 4\pi\mathrm{exp}(i\boldsymbol{\kappa}\cdot\boldsymbol{r}_i)\hat{\boldsymbol{\Theta}}\cdot\left\{\tilde{\boldsymbol{\kappa}}\times(\hat{\boldsymbol{s}}_i\times\tilde{\boldsymbol{\kappa}})\right\}, \tag{B.36}$$

$$\langle\boldsymbol{Q'}|\hat{\boldsymbol{p}}_i\cdot\frac{\hat{\boldsymbol{\Theta}}\times\boldsymbol{R}}{|\boldsymbol{R}|^3}|\boldsymbol{Q}\rangle = -\frac{4\pi i}{|\boldsymbol{\kappa}|}\mathrm{exp}(i\boldsymbol{\kappa}\cdot\boldsymbol{r}_i)\hat{\boldsymbol{\Theta}}\cdot(\tilde{\boldsymbol{\kappa}}\times\hat{\boldsymbol{p}}_i), \tag{B.37}$$

where $\boldsymbol{\kappa} \equiv (\boldsymbol{Q} - \boldsymbol{Q'})$ and $\tilde{\boldsymbol{\kappa}} \equiv \boldsymbol{\kappa}/|\boldsymbol{\kappa}|$, and $\boldsymbol{r}_i$ is the position of the i-th electron. Here we used the relation

$\boldsymbol{r} \equiv \boldsymbol{r}_i + \boldsymbol{R}$.

Since $\exp(i\boldsymbol{\kappa}\cdot\boldsymbol{r}_i)$ commutes with $\tilde{\boldsymbol{\kappa}} \times \hat{\boldsymbol{p}}_i$, we can rewrite the cross-section as

$$\frac{d^2\Theta}{d\Omega dE'} = \left(\frac{m}{2\pi\hbar^2}\right)^2 (8\pi\gamma_e\mu_N\mu_B)^2 \sum_{\lambda\lambda'\Theta} \frac{Q'}{Q} p_\lambda p_\Theta |\left\langle\lambda\Theta\right| \hat{\boldsymbol{\Theta}}\cdot\hat{\boldsymbol{Q}}_\perp \left|\lambda'\Theta'\right\rangle|^2 \times \delta(\hbar\omega + E_\lambda - E_{\lambda'}), \tag{B.38}$$

where we defined $\hat{\boldsymbol{Q}}_\perp$ as

$$\hat{\boldsymbol{Q}}_\perp \equiv \sum_i \exp(i\boldsymbol{\kappa}\cdot\boldsymbol{r}_i) \left\{ \tilde{\boldsymbol{\kappa}} \times \hat{\boldsymbol{s}}_i \times \tilde{\boldsymbol{\kappa}} - \frac{i}{\hbar|\boldsymbol{\kappa}|}(\tilde{\boldsymbol{\kappa}} \times \hat{\boldsymbol{p}}_i) \right\}. \tag{B.39}$$

If we focus on unpolarized neutron scatterings,

$$\sum_\Theta p_\Theta \left\langle\Theta\right| \hat{\Theta}_a \hat{\Theta}_b \left|\Theta\right\rangle = \delta_{a,\,b}, \tag{B.40}$$

where $a,\ b$ are x, y, z components. Using $\frac{m}{2\pi\hbar^2}\cdot 8\pi\gamma_e\mu_N\mu_B = \frac{\gamma_e e^2}{m_e c^2}$ $(\mu_N = \frac{e\hbar}{2m_p c})$, we have finally

$$\begin{aligned} \frac{d^2\Theta}{d\Omega dE'} &= \left(\frac{\gamma_e e^2}{m_e c^2}\right)^2 \sum_{\lambda\lambda'} \frac{Q'}{Q} p_\lambda |\left\langle\lambda\right| \hat{\boldsymbol{Q}}_\perp \left|\lambda'\right\rangle|^2 \times \delta(\hbar\omega + E_\lambda - E_{\lambda'}) \\ &\equiv \left(\frac{\gamma_e e^2}{m_e c^2}\right)^2 \frac{Q'}{Q} \sum_{a,b} (\delta_{a,b} - \tilde{\kappa}_a\tilde{\kappa}_b) \sum_{\lambda,\lambda'} p_\lambda \left\langle\lambda\right| \hat{Q}_a^\dagger \left|\lambda'\right\rangle \left\langle\lambda'\right| \hat{Q}_b \left|\lambda\right\rangle, \end{aligned} \tag{B.41}$$

where $\hat{\boldsymbol{Q}}_\perp = \tilde{\boldsymbol{\kappa}} \times (\hat{\boldsymbol{Q}} \times \tilde{\boldsymbol{\kappa}})$ and $\hat{\boldsymbol{Q}}_\perp^\dagger \cdot \hat{\boldsymbol{Q}}_\perp = \sum_{a,b}(\delta_{a,b} - \tilde{\kappa}_a\tilde{\kappa}_b)\hat{Q}_a^\dagger\hat{Q}_b$ were used.

In many cases, the orbital moment is quenched or zero. In this case, $\hat{\boldsymbol{Q}}$ is simplified to

$$\hat{\boldsymbol{Q}} = \sum_i \exp(i\boldsymbol{\kappa}\cdot\boldsymbol{r}_i)\hat{\boldsymbol{s}}_i. \tag{B.42}$$

In the case of crystal, all sites are identical, so they can be specified by a vector $\boldsymbol{R}_{ld} \equiv \boldsymbol{l} + \boldsymbol{d}$, where $\boldsymbol{l}$ is the position of unit cell (lattice vector) and $\boldsymbol{d}$ is the position of atoms in the unitcell. This allows us to rewrite Eq. (B.42) as

$$\hat{\boldsymbol{Q}} = \sum_{l,d} \exp(i\boldsymbol{\kappa}\cdot\boldsymbol{R}_{ld}) \sum_{\nu(d)} \exp(i\boldsymbol{\kappa}\cdot\boldsymbol{r}_\nu)\hat{\boldsymbol{s}}_i. \tag{B.43}$$

In the ground state, the spins will be coupled together to obtain total spins $\hat{\boldsymbol{S}}_{ld}$. This is the only vector in $\hat{\boldsymbol{Q}}$, so it must be proportional to $\hat{\boldsymbol{S}}_{ld}$ (Wigner-Eckart theorem). We can rewrite $\langle\lambda'|\,\hat{\boldsymbol{Q}}\,|\lambda\rangle$ in Eq. (B.41) as

$$\langle\lambda'|\,\hat{\boldsymbol{Q}}\,|\lambda\rangle = \sum_{l,d} \exp(i\boldsymbol{\kappa}\cdot\boldsymbol{R}_{ld})F_d(\boldsymbol{\kappa})\,\langle\lambda'|\,\hat{\boldsymbol{S}}_{ld}\,|\lambda\rangle\,, \tag{B.44}$$

where $F_d(\boldsymbol{\kappa})$ is the Fourier transformation of (normalized) spin density which is associated with the d-th site ion, called form factor. Inserting above equation into Eq. (B.41) gives the partial differential cross-section due to the scattering with only spin angular momentum as

$$\begin{aligned}\frac{d^2\Theta}{d\Omega dE'} = {} & \left(\frac{\gamma_e e^2}{m_e c^2}\right)^2 \frac{Q'}{Q}\sum_{a,b}(\delta_{a,b}-\tilde{\kappa}_a\tilde{\kappa}_b)\sum_{\lambda,\lambda'}p_\lambda\sum_{l,d}\sum_{l',d'}F_d^*(\boldsymbol{\kappa})F_{d'}(\boldsymbol{\kappa})\mathrm{exp}\left\{i\boldsymbol{\kappa}\cdot(\boldsymbol{R}_{l'd'}-\boldsymbol{R}_{ld})\right\}\\ & \times\langle\lambda|\,\hat{S}^a_{ld}\,|\lambda'\rangle\,\langle\lambda'|\,\hat{S}^b_{l'd'}\,|\lambda\rangle\,\delta(\hbar\omega+E_\lambda-E_{\lambda'}).\end{aligned} \tag{B.45}$$

If we want to take the orbital momentum into account, the cross-section becomes

$$\begin{aligned}\frac{d^2\Theta}{d\Omega dE'} = {} & \left(\frac{\gamma_e e^2}{m_e c^2}\right)^2 \left\{\frac{1}{2}gF(\boldsymbol{\kappa})\right\}^2 \frac{Q'}{Q}\sum_{a,b}(\delta_{a,b}-\tilde{\kappa}_a\tilde{\kappa}_b)\sum_{\lambda,\lambda'}p_\lambda\sum_{l,d}\sum_{l',d'}\mathrm{exp}\left\{i\boldsymbol{\kappa}\cdot(\boldsymbol{R}_{l'd'}-\boldsymbol{R}_{ld})\right\}\\ & \times\langle\lambda|\,\hat{S}^a_{ld}\,|\lambda'\rangle\,\langle\lambda'|\,\hat{S}^b_{l'd'}\,|\lambda\rangle\,\delta(\hbar\omega+E_\lambda-E_{\lambda'}).\end{aligned} \tag{B.46}$$

where $F(\boldsymbol{\kappa}) = j_0\frac{g_S}{g} + (j_0+j_2)(\frac{g-g_S}{g})$ ($j_0,\ j_2$ are spherical Bessel functions of order 0, 2, and $g\mu_B S$ is the total magnetic moment of each ion). Note that here we assumed the wave functions of the unpaired electrons have much smaller momentum than $|\boldsymbol{\kappa}|$ (dipole approximation).

B.5 Elastic magnetic scattering

The elastic scattering due to magnetic interactions are used in two ways. (a) Determinate magnetic structures such as directions and positions of the spins, and (b) get the information on magnetic form factors which reflects the properties of the unpaired spins.

In the case of scatterings due to purely magnetic interactions, the starting point is Eq. (B.46). Elastic scattering requires $E_\lambda = E_{\lambda'}$, so

$$\frac{d\Theta}{d\Omega} = \left(\frac{\gamma_e e^2}{m_e c^2}\right)^2 \left\{\frac{1}{2}gF(\boldsymbol{\kappa})\right\}^2 \frac{Q'}{Q}\sum_{a,b}(\delta_{a,b}-\tilde{\kappa}_a\tilde{\kappa}_b)\sum_{\lambda}p_\lambda\sum_{l}\sum_{l'}\mathrm{exp}\left\{i\boldsymbol{\kappa}\cdot(\boldsymbol{R}_{l'}-\boldsymbol{R}_{l})\right\}\langle\lambda|\,\hat{S}^a_l\,|\lambda\rangle\,\langle\lambda|\,\hat{S}^b_{l'}\,|\lambda\rangle\,. \tag{B.47}$$

Note that we assume the system is Bravais lattice and choose the quantization axis to be parallel to the mean direction of all the spins (such as z axis, so that the density matrix is diagonal).

We want to estimate $\sum_\lambda p_\lambda\,\langle\lambda|\,\hat{S}^a_l\,|\lambda\rangle\,\langle\lambda|\,\hat{S}^b_{l'}\,|\lambda\rangle$. This is different from $\langle\hat{S}^a\hat{S}^b\rangle$. In the case of ferromagnet, we can choose the states $|\lambda\rangle$ to be independent of the positions of spins $\boldsymbol{R}_l$. Under this condition,

$$\langle\lambda|\,\hat{S}^a_l\,|\lambda\rangle = \frac{1}{N_{\text{in}}}\langle\lambda|\,\hat{S}^a_{\text{total}}\,|\lambda\rangle = \frac{1}{N_{\text{in}}}\delta_{a,z}\,\langle\lambda|\,\hat{S}^z_{\text{total}}\,|\lambda\rangle\,, \tag{B.48}$$

obviously $\hat{S}^z_{\text{total}} \equiv \sum_l \hat{S}^z_l$.

B.6 Correlation functions in magnetic scattering

In the localized model, we found Eq. (B.46) is the cross-section due to the magnetic scatterings in crystal. The orbital motion of the spins are taken into account under dipole approximation. To rewrite Eq. (B.46) using a correlation function, we use delta function of the integral representation as

$$\begin{aligned}
&\sum_{\lambda,\lambda'} p_\lambda\,\langle\lambda|\exp(-i\boldsymbol{\kappa}\cdot\boldsymbol{R}_{ld})\hat{S}^a_{ld}\,|\lambda'\rangle\,\langle\lambda'|\exp(-i\boldsymbol{\kappa}\cdot\boldsymbol{R}_{l'd'})\hat{S}^b_{l'd'}\,|\lambda\rangle\,\delta(\hbar\omega+E_\lambda-E_{\lambda'})\\
&\quad=\sum_{\lambda,\lambda'} p_\lambda\frac{1}{2\pi\hbar}\int_{-\infty}^{\infty} dt\,\exp(-i\omega t)\,\langle\lambda|\exp(-i\boldsymbol{\kappa}\cdot\boldsymbol{R}_{ld})\hat{S}^a_{ld}\,|\lambda'\rangle\\
&\quad\times\langle\lambda'|\exp(i\hat{\mathcal{H}}t/\hbar)\exp(-i\boldsymbol{\kappa}\cdot\boldsymbol{R}_{l'd'})\exp(-i\hat{\mathcal{H}}t/\hbar+i\hat{\mathcal{H}}t/\hbar)\hat{S}^b_{l'd'}\exp(-i\hat{\mathcal{H}}t/\hbar)\,|\lambda\rangle\\
&\quad=\frac{1}{2\pi\hbar}\int_{-\infty}^{\infty} dt\,\exp(-i\omega t)\langle\exp(-i\boldsymbol{\kappa}\cdot\hat{\boldsymbol{R}}_{ld}(0))\hat{S}^a_{ld}(0)\exp(-i\boldsymbol{\kappa}\cdot\hat{\boldsymbol{R}}_{l'd'}(t))\hat{S}^b_{l'd'}(t)\rangle.
\end{aligned}\tag{B.49}$$

Here we used $\exp(i\boldsymbol{\kappa}\cdot\hat{\boldsymbol{R}}(t)) = \exp(i\mathcal{H}t/\hbar)\exp(i\boldsymbol{\kappa}\cdot\boldsymbol{R})\exp(-i\mathcal{H}t/\hbar)$. The above equation can be rewritten

$$\begin{aligned}
&=\frac{1}{2\pi\hbar}\int_{-\infty}^{\infty} dt\,\exp(-i\omega t)\left\langle\exp(-i\boldsymbol{\kappa}\cdot\hat{\boldsymbol{R}}_{ld}(0))\hat{S}^a_{ld}(0)\int d\boldsymbol{r}'\exp(i\boldsymbol{\kappa}\cdot\boldsymbol{r}')\delta(\boldsymbol{r}'-\hat{\boldsymbol{R}}_{l'd'}(t))\hat{S}^b_{l'd'}(t)\right\rangle\\
&=\frac{1}{2\pi\hbar}\int_{-\infty}^{\infty} dt\,\exp(-i\omega t)\left\langle\int d\boldsymbol{r}\,\exp(i\boldsymbol{\kappa}\cdot\boldsymbol{r})\delta(\boldsymbol{r}-\hat{\boldsymbol{R}}_{ld}(0))\hat{S}^a_{ld}(0)\int d\boldsymbol{r}'\exp(i\boldsymbol{\kappa}\cdot\boldsymbol{r}')\delta(\boldsymbol{r}'-\hat{\boldsymbol{R}}_{l'd'}(t))\hat{S}^b_{l'd'}(t)\right\rangle\\
&=\frac{1}{2\pi\hbar}\int_{-\infty}^{\infty} dt\,\exp(-i\omega t)\left\langle\int d\boldsymbol{r}\,\exp(i\boldsymbol{\kappa}\cdot\boldsymbol{r})\delta(\boldsymbol{r}+\hat{\boldsymbol{R}}_{ld}(0))\hat{S}^a_{ld}(0)\int d\boldsymbol{r}'\exp(i\boldsymbol{\kappa}\cdot\boldsymbol{r}')\delta(\boldsymbol{r}'-\hat{\boldsymbol{R}}_{l'd'}(t))\hat{S}^b_{l'd'}(t)\right\rangle\\
&=\frac{1}{2\pi\hbar}\int_{-\infty}^{\infty} dt\,\int d\boldsymbol{r}\,\exp(i\boldsymbol{\kappa}\cdot\boldsymbol{r}-i\omega t)\int d\boldsymbol{r}'\left\langle\delta(\boldsymbol{r}+\hat{\boldsymbol{R}}_{ld}(0)-\boldsymbol{r}')\hat{S}^a_{ld}(0)\delta(\boldsymbol{r}'-\hat{\boldsymbol{R}}_{l'd'}(t))\hat{S}^b_{l'd'}(t)\right\rangle.
\end{aligned}\tag{B.50}$$

Hence the partial differential cross-section Eq. (B.46) can be rewritten as

$$\begin{aligned}
\frac{d^2\Theta}{d\Omega dE'} &= \left(\frac{\gamma_e e^2}{m_e c^2}\right)^2\left\{\frac{1}{2}gF(\boldsymbol{\kappa})\right\}^2\frac{Q'}{Q}\sum_{a,b}(\delta_{a,b}-\tilde{\kappa}_a\tilde{\kappa}_b)\\
&\quad\times\frac{N_{\text{in}}}{2\pi\hbar}\int_{-\infty}^{\infty} dt\,\int d\boldsymbol{r}\,\exp(i\boldsymbol{\kappa}\cdot\boldsymbol{r}-i\omega t)\Gamma_{ab}(\boldsymbol{r},t),
\end{aligned}\tag{B.51}$$

where N_{in} is the total number of unit cells, and

$$\Gamma_{ab}(\boldsymbol{r},t) \equiv \frac{1}{N_{\text{in}}}\sum_{l,d}\sum_{l',d'}\int d\boldsymbol{r}'\left\langle\delta(\boldsymbol{r}+\hat{\boldsymbol{R}}_{ld}(0)-\boldsymbol{r}')\hat{S}^a_{ld}(0)\delta(\boldsymbol{r}'-\hat{\boldsymbol{R}}_{l'd'}(t))\hat{S}^b_{l'd'}(t)\right\rangle. \tag{B.52}$$

To a good approximation, it is known that the motion of ions are independent of the direction of spins (since the spin dependent force is small). So $\Gamma_{ab}(\boldsymbol{r},t)$ becomes

$$\Gamma_{ab}(\boldsymbol{r},t) \equiv \frac{1}{N_{\text{in}}} \sum_{l,d}\sum_{l',d'} \langle \hat{S}^a_{ld}(0)\hat{S}^b_{l'd'}(t)\rangle \int d\boldsymbol{r}' \left\langle \delta(\boldsymbol{r}+\hat{\boldsymbol{R}}_{ld}(0)-\boldsymbol{r}')\delta(\boldsymbol{r}'-\hat{\boldsymbol{R}}_{l'd'}(t))\right\rangle . \tag{B.53}$$

In the case of the system is a Bravais lattice,

$$\Gamma_{ab}(\boldsymbol{r},t) = \sum_{l} \gamma_{ab}(l,t)\mathfrak{G}_l(\boldsymbol{r},t) \tag{B.54}$$

$$\gamma_{ab}(l,t) = \frac{1}{N_{\text{in}}} \sum_{m} \langle \hat{S}^a_{m}(0)\hat{S}^b_{m+l}(t)\rangle = \gamma_{ab}(l,\infty) + \gamma'_{ab}(l,t) \tag{B.55}$$

$$\begin{aligned}\mathfrak{G}_l(\boldsymbol{r},t) &= \int d\boldsymbol{r}' \left\langle \delta(\boldsymbol{r}+\hat{\boldsymbol{R}}_{0}(0)-\boldsymbol{r}')\delta(\boldsymbol{r}'-\hat{\boldsymbol{R}}_{l}(t))\right\rangle \\ &= \mathfrak{G}_l(\boldsymbol{r},\infty) + \mathfrak{G}'_l(\boldsymbol{r},t).\end{aligned} \tag{B.56}$$

In the above equation, $\mathfrak{G}_l(\boldsymbol{r},\infty)$ and $\gamma_{ab}(\boldsymbol{r},\infty)$ mean the limit of $t \to \infty$. In this limit, the correlations between the two terms of the right hand side of Eq. (B.55) and (B.56) disappear. This vanishes the time dependence of both functions. Also, in the case of liquid, the density is uniform (let's say ρ) in the system. So $\mathfrak{G}_l(\boldsymbol{r},\infty) = \rho$ and $\mathfrak{G}^s_l(\boldsymbol{r},\infty) = 0$ ("$\mathfrak{G}^s$" means the self correlation). So $\Gamma_{ab}(\boldsymbol{r},t)$ becomes

$$\Gamma_{ab}(\boldsymbol{r},t) = \sum_{l} \gamma_{ab}(l,\infty)\mathfrak{G}_l(\boldsymbol{r},\infty) + \sum_{l} \gamma_{ab}(l,\infty)\mathfrak{G}_l(\boldsymbol{r},t) + \sum_{l} \gamma_{ab}(l,t)\mathfrak{G}_l(\boldsymbol{r},\infty) + \sum_{l} \gamma_{ab}(l,t)\mathfrak{G}_l(\boldsymbol{r},t). \tag{B.57}$$

The first term is the elastic magnetic scattering, the second term is elastic magnetic scattering and inelastic vibrational (phonon) scattering (called "magnetovibrational scattering"), the third term is inelastic magnetic scattering, and the last term is inelastic scatterings due to both spin and phonon systems.

B.7 scattering from phonons

To evaluate $\mathfrak{G}_l(\boldsymbol{r},\infty)$ in Eq. (B.57), let us treat scatterings from phonons. We consider calculating the cross-sections when the configuration of nuclei can deviate from the equilibrium one. The system is assumed to be periodic. Initially, we will focus on the case that the displacements are up to quadratic terms, which is called harmonic approximation, giving rise to a non-interacting phonons. Let us say that $u(\boldsymbol{R}_l)$ is the deviation from lattice, which is assumed to be a Bravais lattice. The potential energy U of the system is the lowest when all the deviations $u(\boldsymbol{R}_l)$ are zero. Expanding U around the potential in equilibrium U_0, in a series gives

$$U - U_0 = \frac{1}{2} \sum_{a,l} \sum_{b,l'} u_a(R_l) A_{ab}(l,l') u_b(R_{l'}) + (\text{higher order}), \tag{B.58}$$

where $A_{ab}(l,l')$ is the second-order differential coefficient. This satisfies

$$A_{ab}(l,l') = A_{ba}(l',l) = A_{ab}(l-l') = A_{ba}(l,l'), \tag{B.59}$$

since all the atoms are symmetric if it's a crystal. In this case the equation of motion reads

$$M\ddot{u}_a(R_l) = -\sum_{b,l'} A_{ab}(l,l') u_b(l'). \tag{B.60}$$

The right hand side of above equation should vanish when all the nuclei moves to the same direction at the same time (by identical amount). So $\sum_{l'} A_{ab}(l,l') = 0$. Assuming that the time dependence is $\exp(-i\omega_0 t)$,the EOM becomes

$$M\omega_0^2 u_a(R_l) = \sum_{b,l'} A_{ab}(l,l') u_b(l'). \tag{B.61}$$

Using the lattice's translational symmetry, we can assume

$$u_a(R_l) = \frac{\Theta_a}{\sqrt{M}} \exp(i\boldsymbol{q} \cdot \boldsymbol{R}_l). \tag{B.62}$$

Now the EOM can be written as

$$\begin{aligned} M\omega_0^2 \Theta_a &= \exp(-i\boldsymbol{q} \cdot \boldsymbol{R}_l) \sum_{b,l'} A_{ab}(l,l') \exp(i\boldsymbol{q} \cdot \boldsymbol{R}_{l'}) \Theta_b \\ &= \sum_{b,l} A_{ab}(l) \exp(-i\boldsymbol{q} \cdot \boldsymbol{R}_l) \Theta_b. \end{aligned} \tag{B.63}$$

Corresponding to three values of a, there are three corresponding solutions of ω_0^2. Let's express this fact by denoting $\omega_j(\boldsymbol{q})$, where index j takes three values. The EOM is now

$$\omega_j^2(\boldsymbol{q}) \Theta_a^j(\boldsymbol{q}) = \sum_b \mathcal{A}_{ab}(\boldsymbol{q}) \Theta_b^j(\boldsymbol{q}), \tag{B.64}$$

$$\mathcal{A}_{ab}(\boldsymbol{q}) = \frac{1}{M} \sum_l A_{ab}(l) \exp(-i\boldsymbol{q} \cdot \boldsymbol{R}_l). \tag{B.65}$$

The latter of above equation tells that

$$\mathcal{A}^*_{ab}(\boldsymbol{q}) = \mathcal{A}_{ab}(-\boldsymbol{q}). \tag{B.66}$$

If all the sites are the center of symmetry, such as a Bravais lattice case,

$$\mathcal{A}^*_{ab}(\boldsymbol{q}) = \mathcal{A}_{ab}(\boldsymbol{q}). \tag{B.67}$$

We assume $\Theta^{*j}_a(\boldsymbol{q}) = \Theta^j_a(-\boldsymbol{q})$ by ignoring the arbitrary phase factor. Also we can choose

$$\sum_j \Theta^{*j}_a(\boldsymbol{q})\Theta^j_b(\boldsymbol{q}) = \delta_{a,b}, \tag{B.68}$$

$$\sum_a \Theta^{*j}_a(\boldsymbol{q})\Theta^{j'}_a(\boldsymbol{q}) = \delta_{j,j'}. \tag{B.69}$$

By analogy with position operator $\hat{x} = \sqrt{\frac{\hbar}{2M\omega_0}}(a + a^\dagger)$ and momentum operator $\hat{p} = -i\sqrt{\frac{\hbar\omega_0 M}{2}}(a - a^\dagger)$, we define $\hat{a}_a(l)$ and $\hat{a}^\dagger_a(l)$ via the transformations

$$\hat{a}_a(l) = \frac{1}{\sqrt{N_{\text{in}}}} \sum_{j,\boldsymbol{q}} \Theta^j_a(\boldsymbol{q})\text{exp}(i\boldsymbol{q}\cdot\boldsymbol{l})\hat{a}_j(\boldsymbol{q}), \tag{B.70}$$

$$\hat{a}^\dagger_a(l) = \frac{1}{\sqrt{N_{\text{in}}}} \sum_{j,\boldsymbol{q}} \Theta^{*j}_a(\boldsymbol{q})\text{exp}(-i\boldsymbol{q}\cdot\boldsymbol{l})\hat{a}^\dagger_j(\boldsymbol{q}). \tag{B.71}$$

Thus we get

$$\hat{u}_a(l) = \sum_{j,\boldsymbol{q}} \sqrt{\frac{\hbar}{2N_{\text{in}}M\omega_j(\boldsymbol{q})}} \left\{ \Theta^j_a(\boldsymbol{q})\text{exp}(i\boldsymbol{q}\cdot\boldsymbol{l})\hat{a}_j(\boldsymbol{q}) + \Theta^{*j}_a(\boldsymbol{q})\text{exp}(-i\boldsymbol{q}\cdot\boldsymbol{l})\hat{a}^\dagger_j(\boldsymbol{q}) \right\}. \tag{B.72}$$

Let's calculate the cross sections for coherent and incoherent scatterings from phonons. The scatterings are due to vibrations under harmonic potentials. In the case of Bravais lattice, from Eq. (B.29),

$$\left(\frac{d\Theta}{d\Omega}\right)^{\text{el}}_{\text{coh}} = \frac{\Theta_c}{4\pi}\left| \int d\boldsymbol{r}\ \text{exp}(i\boldsymbol{\kappa}\cdot\boldsymbol{r})\langle\hat{\mathfrak{p}}(\boldsymbol{r})\rangle \right|^2. \tag{B.73}$$

Here $\Theta_c = 4\pi|\bar{\xi}|^2$. In this case,

$$\begin{aligned} \langle\hat{\mathfrak{p}}(\boldsymbol{r})\rangle &= \sum_l \langle\delta(\boldsymbol{r} - \boldsymbol{R}_l(0) - \hat{\boldsymbol{u}}(R_l))\rangle \\ &= \left(\frac{1}{2\pi}\right)^3 \int d\boldsymbol{Q}\ \sum_l \text{exp}(i\boldsymbol{Q}\cdot(\boldsymbol{r} - \boldsymbol{R}_l))\langle\text{exp}(-i\boldsymbol{Q}\cdot\hat{\boldsymbol{u}}(R_l))\rangle. \end{aligned} \tag{B.74}$$

Using the relation $\langle \exp\hat{Q} \rangle = \exp\left\{\frac{1}{2}\langle \hat{Q}^2 \rangle\right\}, Q =$ (linear combination of operators a and $a^\dagger$),

$$\langle \exp(-i\boldsymbol{Q}\cdot\hat{\boldsymbol{u}}(R_l))\rangle = \exp(-\frac{1}{2}\langle\{\boldsymbol{Q}\cdot\hat{\boldsymbol{u}}(R_l)\}^2\rangle) \tag{B.75}$$

and the expansion with $\hat{a}_j(\boldsymbol{q})$ (Eq. (B.72)),

$$\langle\{\boldsymbol{Q}\cdot\hat{\boldsymbol{u}}(R_l)\}^2\rangle = \frac{\hbar}{2N_{\text{in}}M}\sum_{j,\boldsymbol{q}}\frac{|\boldsymbol{Q}\cdot\boldsymbol{\Theta}^j(\boldsymbol{q})|^2}{\omega_j(\boldsymbol{q})}\{2n_j(\boldsymbol{q})+1\}\,, \tag{B.76}$$

where $n_j(\boldsymbol{q}) = \langle \hat{a}_j^\dagger(\boldsymbol{q})\hat{a}_j(\boldsymbol{q})\rangle$. Thus the Debye-Waller factor $\mathrm{e}^{-\mathfrak{W}(\boldsymbol{Q})}$ is

$$\mathrm{e}^{-\mathfrak{W}(\boldsymbol{Q})} \equiv \langle \mathrm{e}^{-i\boldsymbol{Q}\hat{\boldsymbol{u}}(R_l))}\rangle = \exp\left[-\frac{\hbar}{4N_{\text{in}}M}\sum_{j,\boldsymbol{q}}\frac{|\boldsymbol{Q}\cdot\boldsymbol{\Theta}^j(\boldsymbol{q})|^2}{\omega_j(\boldsymbol{q})}\{2n_j(\boldsymbol{q})+1\}\right] \tag{B.77}$$

Substituting above equation into Eq. (B.73), it follows that

$$\int d\boldsymbol{r}\,\exp(i\boldsymbol{\kappa}\cdot\boldsymbol{r})\langle\hat{\mathfrak{p}}(\boldsymbol{r})\rangle = \sum_l \exp(i\boldsymbol{\kappa}\cdot\boldsymbol{R}_l)\exp\left\{-\mathfrak{W}(\boldsymbol{\kappa})\right\}, \tag{B.78}$$

$$\left(\frac{d\Theta}{d\Omega}\right)^{\text{el}}_{\text{coh}} = \frac{N_{\text{in}}\Theta_c}{4\pi}\frac{(2\pi)^3}{V}\sum_{\boldsymbol{\tau}}\delta(\boldsymbol{\kappa}-\boldsymbol{\tau})\exp(-2\mathfrak{W}(\boldsymbol{\kappa})). \tag{B.79}$$

From Eq. (B.29), the cross-section due to incoherent elastic scattering is

$$\begin{aligned}\left(\frac{d\Theta}{d\Omega}\right)^{\text{el}}_{\text{incoh}} &= \frac{N_{\text{in}}\Theta_i}{4\pi}\sum_l\langle\exp(-i\boldsymbol{\kappa}\cdot\hat{\boldsymbol{R}}_l(0))\rangle\langle\exp(i\boldsymbol{\kappa}\cdot\hat{\boldsymbol{R}}_l(0))\rangle \\ &= \frac{N_{\text{in}}\Theta_i}{4\pi}\exp(-2\mathfrak{W}(\boldsymbol{\kappa})).\end{aligned} \tag{B.80}$$

In the case of inelastic coherent scattering,

$$\left(\frac{d\Theta}{d\Omega}\right)^{\text{inel}}_{\text{coh}} = \frac{N_{\text{in}}\Theta_c}{4\pi}\frac{Q'}{Q}\frac{1}{2\pi\hbar}\int dt\,\exp(i\omega t)\int d\boldsymbol{r}\exp(i\boldsymbol{\kappa}\cdot\boldsymbol{r})\mathfrak{G}'(\boldsymbol{r},t) \tag{B.81}$$

$$\mathfrak{G}'(\boldsymbol{r},t) = \mathfrak{G}(\boldsymbol{r},t) - \mathfrak{G}(\boldsymbol{r},\infty) \tag{B.82}$$

$$\mathfrak{G}(\boldsymbol{r},t) = \frac{1}{N_{\text{in}}(2\pi)^3}\sum_{l,l'}\int d\boldsymbol{Q}\exp(-i\boldsymbol{Q}\cdot\boldsymbol{r})\langle\exp(-i\boldsymbol{Q}\cdot\hat{\boldsymbol{R}}_l(0))\exp(i\boldsymbol{Q}\cdot\hat{\boldsymbol{R}}_{l'}(t))\rangle \tag{B.83}$$

$$\begin{aligned}\mathfrak{G}(\boldsymbol{r},\infty) &= \frac{1}{N_{\text{in}}(2\pi)^3}\sum_{l,l'}\int d\boldsymbol{Q}\exp(-i\boldsymbol{Q}\cdot\boldsymbol{r})\langle\exp(-i\boldsymbol{Q}\cdot\hat{\boldsymbol{R}}_l(0))\rangle\langle\exp(i\boldsymbol{Q}\cdot\hat{\boldsymbol{R}}_{l'}(0))\rangle \\ &= \frac{1}{N_{\text{in}}(2\pi)^3}\sum_{l,l'}\int d\boldsymbol{Q}\exp(-i\boldsymbol{Q}\cdot\boldsymbol{r})\langle\exp(-i\boldsymbol{Q}\cdot(\boldsymbol{R}_l-\boldsymbol{R}_{l'}))\exp(-2\mathfrak{W}(\boldsymbol{Q}))\end{aligned} \tag{B.84}$$

In the case of Bravais lattice, we can rewrite $\langle \exp(-i\boldsymbol{Q}\cdot\hat{\boldsymbol{R}}_l(0))\exp(i\boldsymbol{Q}\cdot\hat{\boldsymbol{R}}_{l'}(t))\rangle$ as

$$\begin{aligned}\langle \exp(-i\boldsymbol{Q}\cdot\hat{\boldsymbol{R}}_l(0))\exp(i\boldsymbol{Q}\cdot\hat{\boldsymbol{R}}_{l'}(t))\rangle &= \exp(-i\boldsymbol{Q}\cdot(\boldsymbol{R}_l-\boldsymbol{R}_{l'}))\langle\exp(-i\boldsymbol{Q}\cdot\hat{\boldsymbol{u}}(l,0))\exp(i\boldsymbol{Q}\cdot\hat{\boldsymbol{u}}(l',t))\rangle\\ &= \exp(-2\mathfrak{W}(\boldsymbol{Q}))\exp(\langle\boldsymbol{Q}\cdot\hat{\boldsymbol{u}}(l,0)\boldsymbol{Q}\cdot\hat{\boldsymbol{u}}(l',t)\rangle),\end{aligned} \tag{B.85}$$

since

$$\langle \exp\hat{A}\exp\hat{B}\rangle = \exp\left\{\frac{1}{2}[\hat{A},\hat{B}]\right\}\langle\exp(\hat{A}+\hat{B})\rangle, \tag{B.86}$$

where $\hat{A}=-i\boldsymbol{Q}\cdot\hat{\boldsymbol{u}}(l,0),\ \hat{B}=i\boldsymbol{Q}\cdot\hat{\boldsymbol{u}}(l',t)$), and

$$\langle\exp(\hat{A}+\hat{B})\rangle = \exp\left\{\frac{1}{2}\langle(\hat{A}+\hat{B})^2\rangle\right\}. \tag{B.87}$$

So the cross-section is

$$\left(\frac{d\Theta}{d\Omega}\right)^{\text{inel}}_{\text{coh}} = \frac{\Theta_c}{4\pi}\frac{Q'}{Q}\frac{1}{2\pi\hbar}\int dt\,\exp(-i\omega t)\exp(-2\mathfrak{W}(\boldsymbol{\kappa}))\sum_{l,l'}\exp\left\{-i\boldsymbol{\kappa}\cdot(\boldsymbol{R}_l-\boldsymbol{R}_{l'})\right\}\left[\exp(\langle\boldsymbol{\kappa}\cdot\hat{\boldsymbol{u}}(l,0)\boldsymbol{\kappa}\cdot\hat{\boldsymbol{u}}(l',t)\rangle)-1\right]. \tag{B.88}$$

For inelastic incoherent scattering, $l=l'$,

$$\left(\frac{d\Theta}{d\Omega}\right)^{\text{inel}}_{\text{coh}} = \frac{\Theta_c}{4\pi}\frac{Q'}{Q}\frac{1}{2\pi\hbar}\int dt\,\exp(-i\omega t)\exp(-2\mathfrak{W}(\boldsymbol{\kappa}))\sum_{l}[\exp(\langle\boldsymbol{\kappa}\cdot\hat{\boldsymbol{u}}(l,0)\boldsymbol{\kappa}\cdot\hat{\boldsymbol{u}}(l,t)\rangle)-1]. \tag{B.89}$$

B.8 Correlation functions in magnetic scattering -again-

Let us return to evaluate $\mathfrak{G}_l(\boldsymbol{r},\infty)$ in Eq. (B.57). Using Eq. (B.77),

$$\mathfrak{G}_l(\boldsymbol{r},\infty) = \left(\frac{1}{2\pi}\right)^3\int d\boldsymbol{q}\,\exp\left\{i\boldsymbol{q}\cdot(\boldsymbol{r}-\boldsymbol{R}_l)\right\}\exp(-2\mathfrak{W}(\boldsymbol{q})). \tag{B.90}$$

Using the result into Eq. (B.57), the cross-sections corresponding each term are given by

$$\left(\frac{d\Theta}{d\Omega}\right)_{\mathrm{m:el,ph:el}} = \left(\frac{\gamma_e e^2}{m_e c^2}\right)^2 \left\{\frac{1}{2} g F(\boldsymbol{\kappa})\right\}^2 \sum_{a,b}(\delta_{ab} - \tilde{\kappa}_a\tilde{\kappa}_b) N_{\mathrm{in}} \sum_{l} \exp(-i\boldsymbol{\kappa}\cdot\boldsymbol{R}_l)\exp(-2\mathfrak{W}(\boldsymbol{\kappa}))\gamma_{ab}(l,\infty) \tag{B.91}$$

$$\begin{aligned}\left(\frac{d\Theta}{d\Omega}\right)_{\mathrm{m:el,ph:inel}} &= \left(\frac{\gamma_e e^2}{m_e c^2}\right)^2 \left\{\frac{1}{2} g F(\boldsymbol{\kappa})\right\}^2 \frac{Q'}{Q} \sum_{a,b}(\delta_{ab} - \tilde{\kappa}_a\tilde{\kappa}_b) N_{\mathrm{in}} \sum_{l,l'} \exp(-i\boldsymbol{\kappa}\cdot(\boldsymbol{R}_l - \boldsymbol{R}_{l'})\exp(-2\mathfrak{W}(\boldsymbol{\kappa})) \\ &\times \frac{1}{2\pi\hbar}\int dt\, \exp(-i\omega t)\left\{\exp\langle\boldsymbol{\kappa}\cdot\hat{\boldsymbol{u}}(l,0)\boldsymbol{\kappa}\cdot\hat{\boldsymbol{u}}(l',t)\rangle - 1\right\}\gamma_{ab}(l'-l,\infty)\end{aligned} \tag{B.92}$$

$$\begin{aligned}\left(\frac{d\Theta}{d\Omega}\right)_{\mathrm{m:inel,ph:el}} &= \left(\frac{\gamma_e e^2}{m_e c^2}\right)^2 \left\{\frac{1}{2} g F(\boldsymbol{\kappa})\right\}^2 \frac{Q'}{Q} \sum_{a,b}(\delta_{ab} - \tilde{\kappa}_a\tilde{\kappa}_b) N_{\mathrm{in}} \sum_{l} \exp(-i\boldsymbol{\kappa}\cdot\boldsymbol{R}_l)\exp(-2\mathfrak{W}(\boldsymbol{\kappa})) \\ &\times \frac{1}{2\pi\hbar}\int dt\, \exp(-i\omega t)\gamma'_{ab}(l,t)\end{aligned} \tag{B.93}$$

$$\begin{aligned}\left(\frac{d\Theta}{d\Omega}\right)_{\mathrm{m:inel,ph:inel}} &= \left(\frac{\gamma_e e^2}{m_e c^2}\right)^2 \left\{\frac{1}{2} g F(\boldsymbol{\kappa})\right\}^2 \frac{Q'}{Q} \sum_{a,b}(\delta_{ab} - \tilde{\kappa}_a\tilde{\kappa}_b) N_{\mathrm{in}} \sum_{l,l'} \exp(-i\boldsymbol{\kappa}\cdot(\boldsymbol{R}_l - \boldsymbol{R}_{l'}))\exp(-2\mathfrak{W}(\boldsymbol{\kappa})) \\ &\times \frac{1}{2\pi\hbar}\int dt\, \exp(-i\omega t)\left\{\exp\langle\boldsymbol{\kappa}\cdot\hat{\boldsymbol{u}}(l,0)\boldsymbol{\kappa}\cdot\hat{\boldsymbol{u}}(l',t)\rangle - 1\right\}\gamma'_{ab}(l'-l,t)\end{aligned} \tag{B.94}$$

B.9 Relaxation functions and generalized susceptibilities in the localized model

Relaxation function is a response function when the external force forms a step function. This time we treat localized model and Bravais lattice. Let's express γ_{ab} using spin operators $\hat{S}^a_{\boldsymbol{q}}$,

$$\hat{S}^a_{\boldsymbol{q}} = \sum_l \exp(-i\boldsymbol{q}\cdot\boldsymbol{R}_l)\hat{S}^a_l, \tag{B.95}$$

$$\hat{S}^a_l = \frac{1}{N_{\mathrm{in}}}\sum_{\boldsymbol{q}} \exp(i\boldsymbol{q}\cdot\boldsymbol{R}_l)\hat{S}^a_{\boldsymbol{q}}. \tag{B.96}$$

Thus

$$\begin{aligned}\sum_l \exp(i\boldsymbol{\kappa}\cdot\boldsymbol{R}_l)\gamma_{ab}(l,t) &= \frac{1}{N_{\mathrm{in}}}\sum_{l,m}\exp(i\boldsymbol{\kappa}\cdot\boldsymbol{R}_l)\langle\hat{S}^a_m(0)\hat{S}^b_{m+l}(t)\rangle \\ &= \frac{1}{N_{\mathrm{in}}}\sum_{l,m}\exp(i\boldsymbol{\kappa}\cdot\boldsymbol{R}_l)\left\langle\frac{1}{N_{\mathrm{in}}}\sum_{\boldsymbol{q}_1}\exp(i\boldsymbol{q}_1\cdot\boldsymbol{R}_m)\hat{S}^a_{\boldsymbol{q}_1}(0)\frac{1}{N_{\mathrm{in}}}\sum_{\boldsymbol{q}_2}\exp(i\boldsymbol{q}_2\cdot\boldsymbol{R}_{m+l})\hat{S}^b_{\boldsymbol{q}_2}(t)\right\rangle \\ &= \frac{1}{N_{\mathrm{in}}}\sum_{\boldsymbol{q}_1,\boldsymbol{q}_2}\left\langle\frac{1}{N_{\mathrm{in}}}\sum_{m}\exp(i(\boldsymbol{q}_1+\boldsymbol{q}_2)\cdot\boldsymbol{R}_m)\hat{S}^a_{\boldsymbol{q}_1}(0)\frac{1}{N_{\mathrm{in}}}\sum_{l}\exp(i(\boldsymbol{\kappa}+\boldsymbol{q}_2)\cdot\boldsymbol{R}_l)\hat{S}^b_{\boldsymbol{q}_2}(t)\right\rangle \\ &= \frac{1}{N_{\mathrm{in}}}\sum_{\boldsymbol{q}_1,\boldsymbol{q}_2}\left\langle\delta_{\boldsymbol{q}_1,-\boldsymbol{q}_2}\hat{S}^a_{\boldsymbol{q}_1}(0)\delta_{\boldsymbol{\kappa},-\boldsymbol{q}_2}\hat{S}^b_{\boldsymbol{q}_2}(t)\right\rangle \\ &= \frac{1}{N_{\mathrm{in}}}\left\langle\hat{S}^a_{\boldsymbol{\kappa}}(0)\hat{S}^b_{-\boldsymbol{\kappa}}(t)\right\rangle,\end{aligned} \tag{B.97}$$

where we used the relation $\boldsymbol{R}_{m+l} = \boldsymbol{R}_l + \boldsymbol{R}_m$. Summing up Eq. (B.91) and Eq. (B.93) (total cross-section in terms of magnetic scattering) reads

$$\begin{aligned}\left(\frac{d^2\Theta}{d\Omega dE'}\right) &= \left(\frac{\gamma_e e^2}{m_e c^2}\right)^2 \left\{\frac{1}{2}gF(\boldsymbol{\kappa})\right\}^2 \frac{Q'}{Q}\sum_{a,b}(\delta_{ab} - \tilde{\kappa}_a\tilde{\kappa}_b)N_{\text{in}}\sum_l \exp(-i\boldsymbol{\kappa}\cdot\boldsymbol{R}_l)\exp(-2\mathfrak{W}(\boldsymbol{\kappa})) \\ &\quad\times \frac{1}{2\pi\hbar}\int dt\,\exp(-i\omega t)[\gamma'_{ab}(l,t) + \gamma_{ab}(l,\infty)] \\ &= \left(\frac{\gamma_e e^2}{m_e c^2}\right)^2 \left\{\frac{1}{2}gF(\boldsymbol{\kappa})\right\}^2 \frac{Q'}{Q}\sum_{a,b}(\delta_{ab} - \tilde{\kappa}_a\tilde{\kappa}_b)\exp(-2\mathfrak{W}(\boldsymbol{\kappa}))\frac{1}{2\pi\hbar}\int dt\,\exp(-i\omega t)\left\langle \hat{S}^a_{\boldsymbol{\kappa}}(0)\hat{S}^b_{-\boldsymbol{\kappa}}(t)\right\rangle\end{aligned} \tag{B.98}$$

The above equation satisfies the detailed balance condition,

$$\left(\frac{d^2\Theta}{d\Omega dE'}\right)_{\boldsymbol{\kappa},\omega} = \exp(\hbar\omega\xi)\left(\frac{d^2\Theta}{d\Omega dE'}\right)_{-\boldsymbol{\kappa},-\omega}. \tag{B.99}$$

The above equation shows that

$$\mathrm{e}^{-\xi E_\lambda}\left(\frac{d^2\Theta}{d\Omega dE'}\right)_{\boldsymbol{\kappa},\omega} = \mathrm{e}^{-\xi E_{\lambda'}}\left(\frac{d^2\Theta}{d\Omega dE'}\right)_{-\boldsymbol{\kappa},-\omega}. \tag{B.100}$$

We assumed the neutrons' population of energy E obeys Boltzmann distribution.

If we assume that the external magnetic field is weak enough to use the linear response theory, we can express the cross-section Eq. (B.98) using Green function of spins, $\mathfrak{G}^{ab}_{\boldsymbol{\kappa}}(t) - i\theta(t)\langle[\hat{S}^a_{\boldsymbol{\kappa}}(t), \hat{S}^b_{-\boldsymbol{\kappa}}(0)]\rangle$ as

$$\left(\frac{d^2\Theta}{d\Omega dE'}\right) = \frac{-\hbar}{2}\left(\frac{\gamma_e e^2}{m_e c^2}\right)^2 \left\{\frac{1}{2}gF(\boldsymbol{\kappa})\right\}^2 \frac{Q'}{Q}\exp(-2\mathfrak{W}(\boldsymbol{\kappa}))\frac{\exp(\hbar\omega\xi)}{\exp(\hbar\omega\xi) - 1}\sum_{a,b}(\delta_{ab} - \tilde{\kappa}_a\tilde{\kappa}_b)\mathrm{Im}\left\{\mathfrak{G}^{ab}_{\boldsymbol{\kappa}}(\omega)\right\} \tag{B.101}$$

The above equation is quite general.

B.10 Polarization Analysis

We haven't taken into account the spin states of the neutrons, though it is important to specify the state of them. In order to understand how the polarization affects the cross-section, we have to know:

1. the relation between polarization of incident neutrons and the cross-section, and
2. the relation between polarization of scattered neutrons and the target system's properties.

In short, we will see that the cross-section of polarized neutrons are independent of polarization when there is no preferred axis in the scattering process (target system) itself. However, when the target system has preferred orientation such as ferromagnets, the new term appears due to the interplay of nuclear and magnetic scatterings in the case of elastic cross-sections. The polarization will be created due to inelastic magnetic scattering, the direction of which depends on whether the elementary excitation is created of annihilated in the scattering process.

Let's define the polarization of a beam of neutrons as

$$\mathfrak{P} \equiv 2\langle\hat{\boldsymbol{s}}\rangle = \left\langle \hat{\boldsymbol{\Upsilon}} \right\rangle, \tag{B.102}$$

where $\hat{\Upsilon}^a$ are Pauli matrices. When we focus on single neutron which is fully polarized, the density matrix $\hat{\varrho}$ can be expressed via Pauli matrices as

$$\hat{\varrho} = \frac{1}{2}\left(\boldsymbol{I} + \mathfrak{P}\cdot\hat{\boldsymbol{\Upsilon}}\right), \tag{B.103}$$

where

$$\mathfrak{P}_x = 2\mathrm{Re}(\varrho^*_{\uparrow\downarrow}),\ \ \mathfrak{P}_y = 2\mathrm{Im}(\varrho^*_{\uparrow\downarrow}),\ \ \mathfrak{P}_z = \varrho_{\uparrow\uparrow} - \varrho_{\downarrow\downarrow}. \tag{B.104}$$

When it comes to a beam of neutrons, the polarization of the beam should be defined by averaging over all the polarization of single neutron as

$$\mathfrak{P} = \frac{1}{N_{\text{in}}}\sum_j \mathfrak{P}_j. \tag{B.105}$$

From Eq. (B.15), the partial differential cross-section is given by

$$\frac{d^2\Theta}{d\Omega dE'} = \frac{Q'}{Q}\left(\frac{m}{2\pi\hbar^2}\right)^2 \sum_{\lambda,\Theta} p_\lambda p_\Theta \sum_{\lambda',\Theta'} |\langle\Theta'\lambda'|\,\hat{V}(\boldsymbol{\kappa})\,|\Theta\lambda\rangle\,|^2 \delta(\hbar\omega + E_\lambda - E_{\lambda'}), \tag{B.106}$$

where $\hat{V}(\boldsymbol{\kappa})$ is the Fourier transformation of the potential $\hat{V}$ between the injected neutron and the targets.

In the case of nuclear scattering from nuclei,

$$\hat{V}_N(\boldsymbol{\kappa}) = \frac{2\pi\hbar^2}{m}\sum_{l,d}\exp(i\boldsymbol{\kappa}\cdot\boldsymbol{R}_{ld})\hat{\xi}_{ld}, \tag{B.107}$$

$$\hat{\xi}_{ld} = A_{ld} + \frac{1}{2}B_{ld}\hat{\boldsymbol{\Theta}}\cdot\hat{\boldsymbol{l}}_{ld}, \tag{B.108}$$

where $\hat{\xi}_{ld}$ is a scattering amplitude operator (this operator reproduces the same properties of the scattering length ξ_l in Eq. (B.16)) and $\hat{\boldsymbol{l}}_{ld}$ is the angular momentum of the nucleus at site $\boldsymbol{R}_{ld}$.

In the case of magnetic scattering from unpaired electrons (cf. Eq. (B.38)),

$$\hat{V}_M(\boldsymbol{\kappa}) = \left(\frac{2\pi\hbar^2}{m}\right)\left(\frac{\gamma_e e^2}{m_e c^2}\right)\hat{\boldsymbol{\Theta}}\cdot\sum_i \exp(i\boldsymbol{\kappa}\cdot\boldsymbol{r}_i)\left\{\tilde{\boldsymbol{\kappa}}\times\hat{\boldsymbol{s}}_i\times\hat{\boldsymbol{\kappa}} - \frac{i}{\hbar|\boldsymbol{\kappa}|}(\tilde{\boldsymbol{\kappa}}\times\hat{\boldsymbol{p}}_i)\right\}. \tag{B.109}$$

Above two potentials both have the same form

$$\hat{\mathcal{V}} = \hat{\xi} + \hat{\boldsymbol{\mathfrak{a}}}\cdot\hat{\boldsymbol{\Theta}}, \tag{B.110}$$

where $\hat{\xi}$ and $\hat{\boldsymbol{\mathfrak{a}}}$ reflect the properties of target system. So all we have to do is to study the modification of the general form of potential Eq. (B.110) due to the polarization.

Let's consider a part of cross-section Eq. (B.106) which depends on the neutron spins $\hat{\boldsymbol{\Theta}}$

$$\sum_{\Theta,\Theta'} p_\Theta \langle\Theta|\,\hat{\mathcal{V}}^\dagger\,|\Theta'\rangle\,\langle\Theta'|\,\hat{\mathcal{V}}\,|\Theta\rangle\,. \tag{B.111}$$

If there is no correlation in phase between the states $|\Theta\rangle$ (meaning that the density matrix with respect to Θ is diagonal), the above equation can be reduced to

$$\sum_{\Theta} p_\Theta \langle\Theta|\,\hat{\mathcal{V}}^\dagger\hat{\mathcal{V}}\,|\Theta\rangle\,. \tag{B.112}$$

Using $p_\Theta = \langle\Theta|\,\hat{\rho}\,|\Theta\rangle$ and $\langle\Theta'|\,\hat{\rho}\,|\Theta\rangle = \delta_{\Theta,\Theta'}\langle\Theta|\,\hat{\rho}\,|\Theta\rangle$, Eq. (B.111) can be rewritten as

$$\sum_{\Theta,\Theta'} p_\Theta \langle\Theta|\,\hat{\mathcal{V}}^\dagger\,|\Theta'\rangle\,\langle\Theta'|\,\hat{\mathcal{V}}\,|\Theta\rangle = \sum_{\Theta}\langle\Theta|\,\hat{\mathcal{V}}^\dagger\hat{\mathcal{V}}\hat{\rho}\,|\Theta\rangle = \mathrm{Tr}\;\hat{\rho}\hat{\mathcal{V}}^\dagger\hat{\mathcal{V}}. \tag{B.113}$$

The cross-section Eq. (B.106) is now

$$\frac{d^2\Theta}{d\Omega dE'} = \frac{Q'}{Q}\left(\frac{m}{2\pi\hbar^2}\right)^2\sum_{\lambda,\lambda'} p_\lambda \mathrm{Tr}\hat{\rho}|\,\langle\lambda'|\,\hat{V}(\boldsymbol{\kappa})\,|\lambda\rangle\,|^2\delta(\hbar\omega + E_\lambda - E_{\lambda'}). \tag{B.114}$$

Next, let us consider the polarization of the scattered neutrons $\boldsymbol{\mathfrak{P}}'$. This represents the transfer of spins in the incident neutron beam (defined by $\boldsymbol{\mathfrak{P}}$), associated with the interaction potential $\mathcal{V}$. Thus

$$\boldsymbol{\mathfrak{P}}' = \frac{\mathrm{Tr}\;\hat{\rho}\hat{\mathcal{V}}^\dagger\hat{\boldsymbol{\Theta}}\hat{\mathcal{V}}}{\mathrm{Tr}\;\hat{\rho}\hat{\mathcal{V}}^\dagger\hat{\mathcal{V}}} \tag{B.115}$$

Note that the normalization Tr $\hat{\rho}\hat{\mathcal{V}}^\dagger\hat{\mathcal{V}}$ was chosen so that $|\boldsymbol{\mathfrak{P}}'| = 1$.

So $\boldsymbol{\mathfrak{P}}'\left(\frac{d^2\Theta}{d\Omega dE'}\right)$ (full scattered polarization) becomes

$$\boldsymbol{\mathfrak{P}}'\left(\frac{d^2\Theta}{d\Omega dE'}\right) = \frac{Q'}{Q}\left(\frac{m}{2\pi\hbar^2}\right)^2 \sum_{\lambda,\lambda'} p_\lambda \mathrm{Tr}\hat{\rho}\,\langle\lambda|\,\hat{V}(\boldsymbol{\kappa})\,|\lambda'\rangle\,\hat{\boldsymbol{\Theta}}\,\langle\lambda'|\,\hat{V}(\boldsymbol{\kappa})\,|\lambda\rangle\,\delta(\hbar\omega + E_\lambda - E_{\lambda'}). \tag{B.116}$$

Using the general form of the potential $\hat{\mathcal{V}}$, Eq. (B.110),

$$\begin{aligned} \mathrm{Tr}\;\hat{\rho}\hat{\mathcal{V}}^\dagger\hat{\mathcal{V}} &= \frac{1}{2}\mathrm{Tr}\;(\boldsymbol{I} + \boldsymbol{\mathfrak{P}}\cdot\hat{\boldsymbol{\Theta}})(\hat{\xi}^\dagger + \hat{\boldsymbol{\mathfrak{a}}}^\dagger\cdot\hat{\boldsymbol{\Theta}})(\hat{\xi} + \hat{\boldsymbol{\mathfrak{a}}}\cdot\hat{\boldsymbol{\Theta}}) \\ &= \hat{\boldsymbol{\mathfrak{a}}}^\dagger\hat{\boldsymbol{\mathfrak{a}}} + \hat{\xi}^\dagger\hat{\xi} + \hat{\xi}^\dagger\hat{\boldsymbol{\mathfrak{a}}}\cdot\boldsymbol{\mathfrak{P}} + (\hat{\boldsymbol{\mathfrak{a}}}^\dagger\cdot\boldsymbol{\mathfrak{P}})\hat{\xi} + i\boldsymbol{\mathfrak{P}}\cdot(\hat{\boldsymbol{\mathfrak{a}}}^\dagger\times\hat{\boldsymbol{\mathfrak{a}}}), \end{aligned} \tag{B.117}$$

where we used Eq. (B.103). For Tr $\hat{\rho}\hat{\mathcal{V}}^\dagger\hat{\boldsymbol{\Theta}}\hat{\mathcal{V}}$, we have

$$\begin{aligned} \mathrm{Tr}\;\hat{\rho}\hat{\mathcal{V}}^\dagger\hat{\boldsymbol{\Theta}}\hat{\mathcal{V}} = {} & \hat{\xi}^\dagger\hat{\boldsymbol{\mathfrak{a}}} + \hat{\boldsymbol{\mathfrak{a}}}^\dagger\hat{\xi} + \hat{\xi}^\dagger\hat{\xi}\boldsymbol{\mathfrak{P}} + \hat{\boldsymbol{\mathfrak{a}}}^\dagger(\hat{\boldsymbol{\mathfrak{a}}}\cdot\boldsymbol{\mathfrak{P}}) + (\hat{\boldsymbol{\mathfrak{a}}}^\dagger\cdot\boldsymbol{\mathfrak{P}})\hat{\boldsymbol{\mathfrak{a}}} \\ & - \boldsymbol{\mathfrak{P}}\cdot(\hat{\boldsymbol{\mathfrak{a}}}^\dagger\cdot\hat{\boldsymbol{\mathfrak{a}}}) - i\hat{\boldsymbol{\mathfrak{a}}}^\dagger\times\hat{\boldsymbol{\mathfrak{a}}} + i\hat{\xi}^\dagger(\hat{\boldsymbol{\mathfrak{a}}}\times\boldsymbol{\mathfrak{P}}) + i(\boldsymbol{\mathfrak{P}}\times\hat{\boldsymbol{\mathfrak{a}}}^\dagger)\hat{\xi}, \end{aligned} \tag{B.118}$$

where we used the identities:

$$\hat{\Theta}^a\hat{\Theta}^b = \delta_{a,b}I + i\epsilon_{ab\gamma_e}\hat{\Theta}^\gamma_e \tag{B.119}$$

$$\mathrm{Tr}\;\hat{\Theta}^a\hat{\Theta}^b = 2\delta_{ab}I \tag{B.120}$$

$$\mathrm{Tr}\;\hat{\Theta}^a\hat{\Theta}^b\hat{\Theta}^\gamma_e = i\epsilon_{ab\gamma'_e}\mathrm{Tr}\;\hat{\Theta}^{\gamma'_e}\hat{\Theta}^\gamma_e = 2i\epsilon_{ab\gamma_e} \tag{B.121}$$

$$\mathrm{Tr}\;\hat{\Theta}^a\hat{\Theta}^b\hat{\Theta}^\gamma_e\hat{\Theta}^\delta = 2(\delta_{ab}\delta_{\gamma_e\delta} - \delta_{a\gamma_e}\delta_{b\delta} + \delta_{a\delta}\delta_{b\gamma_e}) \tag{B.122}$$

Note that if we assume that the nuclei have randomly oriented spins, the term $(\hat{\boldsymbol{\mathfrak{a}}}^\dagger\times\hat{\boldsymbol{\mathfrak{a}}})$ should be purely magnetic scattering (since nuclear scattering vanishes if we use $[\hat{\Theta}^a, \hat{\Theta}^b] = 2i\epsilon_{ab\gamma_e}\Theta^\gamma_e$).

B.11 Inelastic magnetic scattering

Let's focus on inelastic magnetic scattering, since this is the case we want to treat. We can utilize the general form Eq. (B.117) and Eq. (B.118) to calculate cross-section and the polarization of scattered neutrons. In this case, $\hat{\xi} = 0$ and $\hat{\boldsymbol{\mathfrak{a}}}$ is

$$\hat{\boldsymbol{\mathfrak{a}}} = \left(\frac{2\pi\hbar^2}{m}\right)\left(\frac{\gamma_e e^2}{m_e c^2}\right)\left\{\frac{1}{2}gF(\boldsymbol{\kappa})\right\}\sum_{l,d}\exp\left(i\boldsymbol{\kappa}\cdot\boldsymbol{R}_{ld}\right)\{\tilde{\boldsymbol{\kappa}}\times(\hat{\boldsymbol{S}}_{ld}\times\tilde{\boldsymbol{\kappa}})\}. \tag{B.123}$$

We used Eq. (B.46), and included the orbital momentum contribution under the dipole approximation. Using $\hat{\xi} = 0$ in Eq. (B.117), the cross-section becomes

$$\frac{d^2\Theta}{d\Omega dE'} = \left(\frac{m}{2\pi\hbar^2}\right)^2 \frac{Q'}{Q} \sum_{\lambda,\lambda'} p_\lambda \left\{ \langle\lambda| \hat{\boldsymbol{\mathfrak{a}}}^\dagger |\lambda'\rangle \langle\lambda'| \hat{\boldsymbol{\mathfrak{a}}} |\lambda\rangle + i\boldsymbol{\mathfrak{P}} \cdot \langle\lambda| \hat{\boldsymbol{\mathfrak{a}}}^\dagger |\lambda'\rangle \times \langle\lambda'| \hat{\boldsymbol{\mathfrak{a}}} |\lambda\rangle \right\} \delta(\hbar\omega + E_\lambda - E_{\lambda'}). \tag{B.124}$$

For the polarization of $\boldsymbol{Q}'$, scattering beam, is

$$\begin{aligned} \boldsymbol{\mathfrak{P}}' \left(\frac{d^2\Theta}{d\Omega dE'}\right) = \left(\frac{m}{2\pi\hbar^2}\right)^2 \frac{Q'}{Q} \sum_{\lambda,\lambda'} p_\lambda & \left\{ \langle\lambda| \hat{\boldsymbol{\mathfrak{a}}}^\dagger |\lambda'\rangle \langle\lambda'| \hat{\boldsymbol{\mathfrak{a}}} \cdot \boldsymbol{\mathfrak{P}} |\lambda\rangle + \langle\lambda| \hat{\boldsymbol{\mathfrak{a}}}^\dagger \cdot \boldsymbol{\mathfrak{P}} |\lambda'\rangle \langle\lambda'| \hat{\boldsymbol{\mathfrak{a}}} |\lambda\rangle \right. \\ & \left. - \boldsymbol{\mathfrak{P}} \langle\lambda| \hat{\boldsymbol{\mathfrak{a}}}^\dagger |\lambda'\rangle \langle\lambda'| \hat{\boldsymbol{\mathfrak{a}}} |\lambda\rangle - i \langle\lambda| \hat{\boldsymbol{\mathfrak{a}}}^\dagger |\lambda'\rangle \times \langle\lambda'| \hat{\boldsymbol{\mathfrak{a}}} |\lambda\rangle \right\} \delta(\hbar\omega + E_\lambda - E_{\lambda'}). \end{aligned} \tag{B.125}$$

Finally, let's express above equations in terms of correlation functions. We choose the simplest term to examine how it changes due to the incident beam's polarization. We focus on the term

$$\left(\frac{m}{2\pi\hbar^2}\right)^2 \frac{Q'}{Q} \sum_{\lambda,\lambda'} p_\lambda \left\{ \langle\lambda| \hat{\boldsymbol{\mathfrak{a}}}^\dagger |\lambda'\rangle \langle\lambda'| \hat{\boldsymbol{\mathfrak{a}}} |\lambda\rangle \right\} \delta(\hbar\omega + E_\lambda - E_{\lambda'}). \tag{B.126}$$

Inserting Eq. (B.123) into above equation and assuming $p_\lambda = \exp(-bE_\lambda)/\mathrm{Tr}\,\exp(-b\mathcal{H})$ (Boltzmann distribution),

$$\begin{aligned} \text{Eq. (B.126)} = & \left(\frac{\gamma_e e^2}{m_e c^2}\right)^2 \left\{\frac{1}{2} g F(\boldsymbol{\kappa})\right\}^2 \left(\frac{1}{\mathrm{Tr}\,\exp(-b\mathcal{H})}\right) \frac{Q'}{Q} \sum_{\lambda,\lambda'} \exp(-bE_\lambda) \sum_{l,d} \sum_{l',d'} \exp\left\{i\boldsymbol{\kappa} \cdot (\boldsymbol{R}_{l'd'} - \boldsymbol{R}_{ld})\right\} \\ & \times \langle\lambda| \tilde{\boldsymbol{\kappa}} \times (\hat{\boldsymbol{S}}_{ld} \times \tilde{\boldsymbol{\kappa}}) |\lambda'\rangle \langle\lambda'| \tilde{\boldsymbol{\kappa}} \times (\hat{\boldsymbol{S}}_{l'd'} \times \tilde{\boldsymbol{\kappa}}) |\lambda\rangle\, \delta(\hbar\omega + E_\lambda - E_{\lambda'}) \\ = & \left(\frac{\gamma_e e^2}{m_e c^2}\right)^2 \left\{\frac{1}{2} g F(\boldsymbol{\kappa})\right\}^2 \left(\frac{1}{\mathrm{Tr}\,\exp(-b\mathcal{H})}\right) \frac{Q'}{Q} \sum_{\lambda,\lambda'} \exp(-bE_\lambda) \sum_{l,d} \sum_{l',d'} \exp\left\{i\boldsymbol{\kappa} \cdot (\boldsymbol{R}_{l'd'} - \boldsymbol{R}_{ld})\right\} \\ & \times \langle\lambda| \tilde{\boldsymbol{\kappa}} \times (\hat{\boldsymbol{S}}_{ld} \times \tilde{\boldsymbol{\kappa}}) |\lambda'\rangle \langle\lambda'| \tilde{\boldsymbol{\kappa}} \times (\hat{\boldsymbol{S}}_{l'd'} \times \tilde{\boldsymbol{\kappa}}) |\lambda\rangle \frac{1}{2\pi} \int_{-\infty}^{\infty} dt \exp(-i\hbar\omega t - iE_\lambda t + iE_{\lambda'} t). \end{aligned} \tag{B.127}$$

Using $\hat{S}_{l'd'}(t) = \exp(i\hat{\mathcal{H}}t/\hbar)\hat{S}_{l'd'} \exp(-i\hat{\mathcal{H}}t/\hbar)$ and $\hat{\boldsymbol{S}}^{\perp}_{l'd'}(t) \equiv \tilde{\boldsymbol{\kappa}} \times (\hat{\boldsymbol{S}}_{l'd'}(t) \times \tilde{\boldsymbol{\kappa}})$,

$$\text{Eq. (B.127)} = \left(\frac{\gamma_e e^2}{m_e c^2}\right)^2 \left\{\frac{1}{2} g F(\boldsymbol{\kappa})\right\}^2 \frac{Q'}{Q} \sum_{l,d} \sum_{l',d'} \exp\left\{i\boldsymbol{\kappa} \cdot (\boldsymbol{R}_{l'd'} - \boldsymbol{R}_{ld})\right\} \frac{1}{2\pi\hbar} \int_{-\infty}^{\infty} dt \exp(-i\omega t) \langle \hat{\boldsymbol{S}}^{\perp}_{ld}(0) \hat{\boldsymbol{S}}^{\perp}_{l'd'}(t) \rangle. \tag{B.128}$$

Similarly, other terms can also be evaluated to get

$$
\begin{aligned}
\frac{d^2\Theta}{d\Omega dE'} &= \left(\frac{\gamma_e e^2}{m_e c^2}\right)^2 \left\{\frac{1}{2} g F(\boldsymbol{\kappa})\right\}^2 \frac{Q'}{Q} \sum_{l,d} \sum_{l',d'} \exp\left\{i\boldsymbol{\kappa}\cdot(\boldsymbol{R}_{l'd'} - \boldsymbol{R}_{ld})\right\} \\
&\quad \times \frac{1}{2\pi\hbar} \int_{-\infty}^{\infty} dt\, \exp(-i\omega t) \left\{ \langle \hat{\boldsymbol{S}}^{\perp}_{ld}(0) \cdot \hat{\boldsymbol{S}}^{\perp}_{l'd'}(t) \rangle + i\boldsymbol{\mathfrak{P}} \cdot \langle \hat{\boldsymbol{S}}^{\perp}_{ld}(0) \times \hat{\boldsymbol{S}}^{\perp}_{l'd'}(t) \rangle \right\}, \qquad \text{(B.129)} \\
\boldsymbol{\mathfrak{P}}' \left(\frac{d^2\Theta}{d\Omega dE'}\right) &= \left(\frac{\gamma_e e^2}{m_e c^2}\right)^2 \left\{\frac{1}{2} g F(\boldsymbol{\kappa})\right\}^2 \frac{Q'}{Q} \sum_{l,d} \sum_{l',d'} \exp\left\{i\boldsymbol{\kappa}\cdot(\boldsymbol{R}_{l'd'} - \boldsymbol{R}_{ld})\right\} \\
&\quad \times \frac{1}{2\pi\hbar} \int_{-\infty}^{\infty} dt\, \exp(-i\omega t) \Big\{ \langle \hat{\boldsymbol{S}}^{\perp}_{ld}(0) \{\boldsymbol{\mathfrak{P}} \cdot \hat{\boldsymbol{S}}^{\perp}_{l'd'}(t)\} \rangle + \langle \{\boldsymbol{\mathfrak{P}} \cdot \hat{\boldsymbol{S}}^{\perp}_{ld}(0)\} \hat{\boldsymbol{S}}^{\perp}_{l'd'}(t) \rangle \\
&\qquad - \boldsymbol{\mathfrak{P}} \langle \hat{\boldsymbol{S}}^{\perp}_{ld}(0) \hat{\boldsymbol{S}}^{\perp}_{l'd'}(t) \rangle - i \langle \hat{\boldsymbol{S}}^{\perp}_{ld}(0) \times \hat{\boldsymbol{S}}^{\perp}_{l'd'}(t) \rangle \Big\}. \qquad \text{(B.130)}
\end{aligned}
$$

Note that Eq. (B.130) is a vector, not a scalar.

Finally, in the case of the unpolarized neutron, the cross-section for amorphous magnets may be (from Eq. (B.98))

$$
\begin{aligned}
\frac{d^2\Theta}{d\Omega dE'} &= \left(\frac{\gamma_e e^2}{m_e c^2}\right)^2 \left\{\frac{1}{2} g F(\boldsymbol{\kappa})\right\}^2 \frac{Q'}{Q} \sum_{a,b} (\delta_{ab} - \tilde{\kappa}_a \tilde{\kappa}_b) \frac{1}{2\pi\hbar} \int dt\, \exp(-i\omega t) \\
&\quad \times \sum_{l,d} \sum_{l',d'} \exp(i\boldsymbol{\kappa}(\boldsymbol{R}_{ld} - \boldsymbol{R}_{l'd'})) \left\langle \hat{S}^a_{ld}(0) \hat{S}^b_{l'd'}(t) \right\rangle \int d\boldsymbol{r}' \left\langle \delta\{\boldsymbol{r} + \hat{\boldsymbol{R}}_{ld}(0) - \boldsymbol{r}'\} \delta\{\boldsymbol{r}' - \hat{\boldsymbol{R}}_{l'd'}(t)\} \right\rangle ,
\end{aligned}
\tag{B.131}
$$

where we assumed the motion of ions are independent of the direction of spins. If we don't assume this, then the Eq. (B.131) becomes (from Eq. (B.52))

$$
\begin{aligned}
\frac{d^2\Theta}{d\Omega dE'} &= \left(\frac{\gamma_e e^2}{m_e c^2}\right)^2 \left\{\frac{1}{2} g F(\boldsymbol{\kappa})\right\}^2 \frac{Q'}{Q} \sum_{a,b} (\delta_{ab} - \tilde{\kappa}_a \tilde{\kappa}_b) \\
&\quad \times \frac{1}{2\pi\hbar} \int dt\, \exp(-i\omega t) \sum_{l,d} \sum_{l',d'} \left\langle \exp(-i\boldsymbol{\kappa} \cdot \hat{\boldsymbol{R}}_{ld}(0)) \hat{S}^a_{ld}(0) \exp(i\boldsymbol{\kappa} \cdot \hat{\boldsymbol{R}}_{l'd'}(t)) \hat{S}^b_{l'd'}(t) \right\rangle .
\end{aligned}
\tag{B.132}
$$

Since we are assuming that the positions of atoms don't change while the simulation, $\hat{\boldsymbol{u}}(R_{ld})$ in Eq. (B.77) is 0. In other words, we may be able to ignore Debye-Waller factor, since the thermal fluctuation is already included in the LLG equation, and the positions of atoms are fixed. This simplifies Eq. (B.131) as

$$
\begin{aligned}
\frac{d^2\Theta}{d\Omega dE'} &= \left(\frac{\gamma_e e^2}{m_e c^2}\right)^2 \left\{\frac{1}{2} g F(\boldsymbol{\kappa})\right\}^2 \frac{Q'}{Q} \sum_{a,b} (\delta_{ab} - \tilde{\kappa}_a \tilde{\kappa}_b) \\
&\quad \times \frac{1}{2\pi\hbar} \int dt\, \exp(-i\omega t) \sum_{l,d} \sum_{l',d'} \exp(i\boldsymbol{\kappa}(\boldsymbol{R}_{ld} - \boldsymbol{R}_{l'd'})) \left\langle \hat{S}^a_{ld}(0) \hat{S}^b_{l'd'}(t) \right\rangle .
\end{aligned}
\tag{B.133}
$$

This means we don't consider nuclear scattering. In the above equation, contribution of elastic magnetic scattering is the limit $t \to \infty$. Otherwise, Eq. (B.133) is the cross-section for inelastic magnetic scattering of unpolarized neutron beam. In the case of the polarized neutron, Eq. (B.129) is the alternative result.

C Analytic expression of double-skyrmion state

We show how to combine two single-skyrmion states to obtain a two-skyrmion state. The stereo-graphic projection is defined as

$$p : \mathbb{C} \cup \infty \mapsto S^2, \tag{C.1}$$

where a complex number $u = u_1 + iu_2$ ($u_1, u_2 \in \mathbb{R}$) is mapped to a normalized three-dimensional vector:

$$p(u) = \left(\frac{2u_1}{1+|u|^2}, \frac{2u_2}{1+|u|^2}, \frac{1-|u|^2}{1+|u|^2} \right). \tag{C.2}$$

p denotes the projection which maps $u = 0$ to $|u| = \infty$ and $p(0) = (0, 0, 1)$ to $p(\infty) = (0, 0, -1)$. In addition, we introduce an orthogonal transformation $\mathcal{R}$ which is a rotation about $\boldsymbol{e}_z \times \hat{\boldsymbol{t}}$ by $\cos^{-1}(\boldsymbol{e}_z \cdot \hat{\boldsymbol{t}})$. Here $\mathcal{R}$ satisfies $\mathcal{R}(\boldsymbol{e}_z) = \hat{\boldsymbol{t}}$. Thus, the coupled operator $p_{\hat{\boldsymbol{t}}}(u) \equiv \mathcal{R}[p(u)]$ maps $u = 0$ to $p_{\hat{\boldsymbol{t}}}(0) = \hat{\boldsymbol{t}}$. The boundary condition regarding $u(\boldsymbol{r}) = p_{\hat{\boldsymbol{t}}}^{-1}[\boldsymbol{n}(\boldsymbol{r})]$ is given by $u(\infty) = 0$, for a skymion configurations $\boldsymbol{n}(\boldsymbol{r})$ that satisfies $\boldsymbol{n}(\infty) = \hat{\boldsymbol{t}}$.

Using the two single-skyrmion solutions $\boldsymbol{n}_u(\boldsymbol{r}) = p_{\hat{\boldsymbol{t}}}(u)$ and $\boldsymbol{n}_v(\boldsymbol{r}) = p_{\hat{\boldsymbol{t}}}(v)$ which have skyrmion charge densities $\rho_{\text{ch}}(\boldsymbol{r}) = \boldsymbol{n} \cdot (\partial_x \boldsymbol{n} \times \partial_y \boldsymbol{n})/(4\pi)$ near $\boldsymbol{r} = \boldsymbol{r}_u$ and $\boldsymbol{r}_v$, we can obtain a composite skyrmion states as

$$\boldsymbol{n}_w(\boldsymbol{r}) = p_{\hat{\boldsymbol{t}}}(w), \quad w = u + v. \tag{C.3}$$

Note that the total skyrmion chargeth is preserved in the procedure, with keeping the boundary condition: If $\boldsymbol{n}_u(\infty) = \boldsymbol{n}_v(\infty) = \hat{\boldsymbol{t}}$, i.e., $u(\infty) = v(\infty) = 0$, $\boldsymbol{n}_w(\infty)$ is given by $\boldsymbol{n}_w(\infty) = p_{\hat{\boldsymbol{t}}}(0+0) = \hat{\boldsymbol{t}}$. Eq. (C.3) stands for the composite skyrmion state, at sufficiently large distance $|\boldsymbol{r}_u - \boldsymbol{r}_v|$.

Next, we approximate $\boldsymbol{n}_w(\boldsymbol{r})$ in terms of $\boldsymbol{n}_{u,v}(\boldsymbol{r})$. In the following discussion, we assume $\hat{\boldsymbol{t}} = \boldsymbol{e}_z$ for simplicity. In the case of the general $\hat{\boldsymbol{t}}$, the result is given by applying the operation $\mathcal{R}$ to all $\boldsymbol{n}_u, \boldsymbol{n}_v$, and $\boldsymbol{n}_w$. When a unit vector $\boldsymbol{n}$ is almost the same as $\boldsymbol{n}_0$, we can expand $\boldsymbol{n}$ as

$$\boldsymbol{n} \simeq \boldsymbol{n}_0 + \boldsymbol{\epsilon} \times \boldsymbol{n}_0 + \frac{1}{2}\boldsymbol{\epsilon} \times (\boldsymbol{\epsilon} \times \boldsymbol{n}_0), \tag{C.4}$$

as a property of unit vector fields, where $\boldsymbol{\epsilon}$ is defined to be satisfy $\boldsymbol{\epsilon} \cdot \boldsymbol{n}_0 = 0$. Under the approximation of

Eq. (C.4), $\boldsymbol{n}$ satisfies the normalization condition up to the second order of $\boldsymbol{\epsilon}$:

$$|\boldsymbol{n}|^2 = 1 + o(\boldsymbol{\epsilon}^2). \tag{C.5}$$

Using the relation $\delta\boldsymbol{n} = \boldsymbol{\epsilon} \times \boldsymbol{n}_0$, $\boldsymbol{\epsilon}$ can be expressed as

$$\boldsymbol{\epsilon} = \hat{\boldsymbol{t}} \times \delta\boldsymbol{n}. \tag{C.6}$$

Also, if $\boldsymbol{n}_{a=u,v}(\boldsymbol{r})$ is far from the skyrmion core, $\boldsymbol{r} = \boldsymbol{r}_a$ is close to $\hat{\boldsymbol{t}}$. Thus it is expanded as

$$\boldsymbol{n}_a \simeq \hat{\boldsymbol{t}} + \boldsymbol{\epsilon}_a^0 \times \hat{\boldsymbol{t}} + \frac{1}{2}\boldsymbol{\epsilon}_a^0 \times \left(\boldsymbol{\epsilon}_a^0 \times \hat{\boldsymbol{t}}\right), \quad a = u, v \tag{C.7}$$

When $\hat{\boldsymbol{t}} = \boldsymbol{e}_z$, the expansion of Eq. (C.2) near $u = 0$ obtains

$$\delta\boldsymbol{n}_u = (2u_1, 2u_2, 0), \tag{C.8}$$

$$\boldsymbol{\epsilon}_u^0 = \hat{\boldsymbol{t}} \times \delta\boldsymbol{n}_u = (-2u_2, 2u_1, 0). \tag{C.9}$$

Similarly, we find $\delta\boldsymbol{n}_v = (2v_1, 2v_2, 0)$ and $\boldsymbol{\epsilon}_v^0 = \hat{\boldsymbol{t}} \times \delta\boldsymbol{n}_v = (-2v_2, 2v_1, 0)$.

The combined configuration $\boldsymbol{n}_w$ is now found to be approximated as follows, due to the above equations. When $|\boldsymbol{r}_u - \boldsymbol{r}_v|$ is sufficiently large, $v = p^{-1}(\boldsymbol{n}_v)$ follows $|v| \ll 1$ near $\boldsymbol{r} = \boldsymbol{r}_u$. We can thus expand $\boldsymbol{n}_w$ in terms of the linear terms of v as

$$\begin{aligned}
\boldsymbol{n}_w =& p(u+v) \\
=& \left(\frac{2(u_1+v_1)}{1+|u+v|^2}, \frac{2(u_2+v_2)}{1+|u+v|^2}, \frac{1-|u+v|^2}{1+|u+v|^2}\right) \\
=& \boldsymbol{n}_u + \left(\frac{2v_1}{1+|u|^2}, \frac{2v_2}{1+|u|^2}, -\frac{2(u_1v_1+u_2v_2)}{1+|u|^2}\right) - \frac{2(u_1v_1+u_2v_2)}{1+|u|^2}\boldsymbol{n}_u + O(v^2) \\
=& \boldsymbol{n}_u + \frac{1}{2}\left[(1+n_{uz})\delta\boldsymbol{n}_v - (\boldsymbol{n}_u \cdot \delta\boldsymbol{n}_v)(\boldsymbol{e}_z + \boldsymbol{n}_u)\right] + O(v^2).
\end{aligned} \tag{C.10}$$

Applying Eq. (C.4), $\boldsymbol{n}_w$ up to the second order of v is obtained as

$$\boldsymbol{n}_w = \boldsymbol{n}_u + \boldsymbol{\epsilon}_v \times \boldsymbol{n}_u + \frac{1}{2}\boldsymbol{\epsilon}_v \times (\boldsymbol{\epsilon}_v \times \boldsymbol{n}_u) + O(v^3), \tag{C.11}$$

$$\boldsymbol{\epsilon}_v = \frac{1}{2}\boldsymbol{n}_u \times \left[(1 + \boldsymbol{n}_u \cdot \boldsymbol{e}_z)\delta\boldsymbol{n}_v - (\boldsymbol{n}_u \cdot \delta\boldsymbol{n}_v)\boldsymbol{e}_z\right]. \tag{C.12}$$

When $\hat{\boldsymbol{t}} \neq \boldsymbol{e}_z$, we use $\mathcal{R}$ for all vector fields and obtain Eq. (C.11) and

$$\boldsymbol{\epsilon}_v = \frac{1}{2}\boldsymbol{n}_u \times \left[(1 + \boldsymbol{n}_u \cdot \hat{\boldsymbol{t}})\delta\boldsymbol{n}_v - (\boldsymbol{n}_u \cdot \delta\boldsymbol{n}_v)\hat{\boldsymbol{t}}\right]. \tag{C.13}$$

We can also expand $\boldsymbol{n}_w$ around $\boldsymbol{r} = \boldsymbol{r}_v$ in the similar way as

$$\boldsymbol{n}_w = \boldsymbol{n}_v + \boldsymbol{\epsilon}_u \times \boldsymbol{n}_v + \frac{1}{2}\boldsymbol{\epsilon}_u \times (\boldsymbol{\epsilon}_u \times \boldsymbol{n}_v) + O(u^3), \tag{C.14}$$

$$\boldsymbol{\epsilon}_u = \frac{1}{2}\boldsymbol{n}_v \times \left[(1 + \boldsymbol{n}_v \cdot \hat{\boldsymbol{t}})\delta\boldsymbol{n}_u - (\boldsymbol{n}_v \cdot \delta\boldsymbol{n}_u)\hat{\boldsymbol{t}}\right]. \tag{C.15}$$

D Derivation of analytic approximation of the inter-skyrmion interaction

Firstly, given the energy functional (5.7), we derive the equation which is satisfied by a stationary solution. Suppose that we have $\boldsymbol{n}_0(\boldsymbol{r})$, a stationary solution and satisfies the boundary condition, $\boldsymbol{n}_0(\infty) = \hat{\boldsymbol{t}}$. Using Eq. (C.4), a spin state with a small fluctuation close to $\boldsymbol{n}_0(\boldsymbol{r})$ can be expressed as

$$\boldsymbol{n}(\boldsymbol{r}) \simeq \boldsymbol{n}_0(\boldsymbol{r}) + \boldsymbol{\epsilon}(\boldsymbol{r}) \times \boldsymbol{n}_0(\boldsymbol{r}), \tag{D.1}$$

up to the linear terms of $\boldsymbol{\epsilon}(\boldsymbol{r})$. The energy difference between the sates of $\boldsymbol{n}(\boldsymbol{r})$ and that of $\boldsymbol{n}_0(\boldsymbol{r})$ is

$$\begin{aligned}
&F[\boldsymbol{n}(\boldsymbol{r})] - F[\boldsymbol{n}_0(\boldsymbol{r})] \\
&\simeq \int \frac{d^2r}{a^2}\left[\frac{\partial f(\boldsymbol{n}_0)}{\partial \boldsymbol{n}} \cdot (\boldsymbol{\epsilon} \times \boldsymbol{n}_0) + \frac{\partial f(\boldsymbol{n}_0)}{\partial \partial_i \boldsymbol{n}} \cdot \partial_i(\boldsymbol{\epsilon} \times \boldsymbol{n}_0)\right] \\
&= \int \frac{d^2r}{a^2}\left[\frac{\partial f(\boldsymbol{n}_0)}{\partial \boldsymbol{n}} - \partial_i \frac{\partial f(\boldsymbol{n}_0)}{\partial \partial_i \boldsymbol{n}}\right] \cdot (\boldsymbol{\epsilon} \times \boldsymbol{n}_0) \\
&= \int \frac{d^2r}{a^2}\boldsymbol{\epsilon} \cdot \left\{\boldsymbol{n}_0 \times \left[\frac{\partial f(\boldsymbol{n}_0)}{\partial \boldsymbol{n}} - \partial_i \frac{\partial f(\boldsymbol{n}_0)}{\partial \partial_i \boldsymbol{n}}\right]\right\}.
\end{aligned} \tag{D.2}$$

Using above equation, the stationary solution $\boldsymbol{n}_0(\boldsymbol{r})$ satisfies

$$\boldsymbol{n}_0 \times \left[\frac{\partial f(\boldsymbol{n}_0)}{\partial \boldsymbol{n}} - \partial_i \frac{\partial f(\boldsymbol{n}_0)}{\partial \partial_i \boldsymbol{n}}\right] = 0, \tag{D.3}$$

which is equivalent to the LLG equation for stationary solutions, $d\boldsymbol{n}/dt = -\boldsymbol{n} \times \boldsymbol{B}_{\text{eff}} + \alpha\boldsymbol{n} \times d\boldsymbol{n}/dt$. Here, the effective magnetic field is

$$\boldsymbol{B}_{\text{eff}} = -\frac{\partial f(\boldsymbol{n})}{\partial \boldsymbol{n}} + \partial_i \frac{\partial f(\boldsymbol{n})}{\partial \partial_i \boldsymbol{n}}. \tag{D.4}$$

Finally, we consider the inter-skyrmion interaction of which is located at $\boldsymbol{r} = \pm\boldsymbol{R}/2$. We assume that a single-skyrmion solution placed at $\boldsymbol{r}=0$ is expressed as $\boldsymbol{n}_{\mathrm{1sk}}(\boldsymbol{r})$ and satisfies Eq. (D.3). The single-skyrmion state placed at $\boldsymbol{r}_u=\boldsymbol{R}/2$ is given by $\boldsymbol{n}_u(\boldsymbol{r})=\boldsymbol{n}_{\mathrm{1sk}}(\boldsymbol{r}-\boldsymbol{R}/2)$ and that placed at $\boldsymbol{r}_v=-\boldsymbol{R}/2$ is obtained as $\boldsymbol{n}_v(\boldsymbol{r})=\boldsymbol{n}_{\mathrm{1sk}}(\boldsymbol{r}+\boldsymbol{R}/2)$. Whereas the double-skyrmion state is approximately expressed as the composite skyrmion state derived in Sec. C: $\boldsymbol{n}_{\mathrm{2sk}}\simeq\boldsymbol{n}_w=p_{\hat{\boldsymbol{t}}}(p_{\hat{\boldsymbol{t}}}^{-1}(\boldsymbol{n}_u)+p_{\hat{\boldsymbol{t}}}^{-1}(\boldsymbol{n}_v))$.

Here we derive an approximate expression of Eq. (5.18) at large $|\boldsymbol{R}|$. The region of the integral can be divided into D_+ and D_-, which corresponds to the right and left sides of the integral path Γ in Fig. 5.4, respectively, and Eq. (5.18) is rewritten as

$$V_{\mathrm{int}}(\boldsymbol{R})=V_+(\boldsymbol{R})+V_-(\boldsymbol{R}), \tag{D.5}$$

$$V_\pm(\boldsymbol{R})\equiv\int_{D_\pm}\frac{d^2r}{a^2}[f(\boldsymbol{n}_{\mathrm{2sk}})-f(\boldsymbol{n}_u)-f(\boldsymbol{n}_v)+f(\hat{\boldsymbol{t}})]. \tag{D.6}$$

If $|\boldsymbol{R}|$ is much larger than the skyrmion size, we can respectively replace $\boldsymbol{n}_{\mathrm{2sk}}$ and $\boldsymbol{n}_v$ by the right-hand side of Eq. (C.11) and Eq. (C.7) in D_+. Further expanding the integrand up to the linear terms of $\boldsymbol{\epsilon}_v$ and $\boldsymbol{\epsilon}_v^0$ gives

$$\begin{aligned}
V_+(\boldsymbol{R})&\simeq\int_{D_+}\frac{d^2r}{a^2}\left[f\left(\boldsymbol{n}_u+\boldsymbol{\epsilon}_v\times\boldsymbol{n}_u+\frac{1}{2}\boldsymbol{\epsilon}_v\times(\boldsymbol{\epsilon}_v\times\boldsymbol{n}_u)\right)-f(\boldsymbol{n}_u)-f\left(\hat{\boldsymbol{t}}+\boldsymbol{\epsilon}_v^0\times\hat{\boldsymbol{t}}+\frac{1}{2}\boldsymbol{\epsilon}_v^0\times(\boldsymbol{\epsilon}_v^0\times\hat{\boldsymbol{t}})\right)+f(\hat{\boldsymbol{t}})\right]\\
&\simeq\int_{D_+}\frac{d^2r}{a^2}\left[\frac{\partial f(\boldsymbol{n}_u)}{\partial\boldsymbol{n}}\cdot(\boldsymbol{\epsilon}_v\times\boldsymbol{n}_u)+\frac{\partial f(\boldsymbol{n}_u)}{\partial\partial_i\boldsymbol{n}}\cdot\partial_i(\boldsymbol{\epsilon}_v\times\boldsymbol{n}_u)-\frac{\partial f(\hat{\boldsymbol{t}})}{\partial\boldsymbol{n}}\cdot(\boldsymbol{\epsilon}_v^0\times\hat{\boldsymbol{t}})-\frac{\partial f(\hat{\boldsymbol{t}})}{\partial\partial_i\boldsymbol{n}}\cdot\partial_i(\boldsymbol{\epsilon}_v^0\times\hat{\boldsymbol{t}})\right]\\
&=\int_{D_+}\frac{d^2r}{a^2}\partial_i\left[\frac{\partial f(\boldsymbol{n}_u)}{\partial\partial_i\boldsymbol{n}}\cdot(\boldsymbol{\epsilon}_v\times\boldsymbol{n}_u)-\frac{\partial f(\hat{\boldsymbol{t}})}{\partial\partial_i\boldsymbol{n}}\cdot(\boldsymbol{\epsilon}_v^0\times\hat{\boldsymbol{t}})\right]\\
&=\oint_{\partial D_+}\frac{d\ell_j}{a^2}\epsilon_{ij}\left[\frac{\partial f(\boldsymbol{n}_u)}{\partial\partial_i\boldsymbol{n}}\cdot(\boldsymbol{\epsilon}_v\times\boldsymbol{n}_u)-\frac{\partial f(\hat{\boldsymbol{t}})}{\partial\partial_i\boldsymbol{n}}\cdot(\boldsymbol{\epsilon}_v^0\times\hat{\boldsymbol{t}})\right],
\end{aligned} \tag{D.7}$$

where ϵ_{ij} denotes the Levi-Civita symbol in 2D, ∂D_+ stands for the boundary of the region D_+, and $d\boldsymbol{\ell}$ represents the vector integral element. From the second to the third lines, the relation that $\boldsymbol{n}_u(\boldsymbol{r})$ and $\hat{\boldsymbol{t}}$ satisfy Eq. (D.3) is used. From the third to the fourth lines, Green's theorem is used.

If the system is large enough, the integral along ∂D_+ becomes zero, except for the boundary between D_+ and D_-, due to the relations $\boldsymbol{n}_u\to\hat{\boldsymbol{t}}$ and $\boldsymbol{\epsilon}_v,\boldsymbol{\epsilon}_v^0\to\boldsymbol{0}$ as $\boldsymbol{r}\to\infty$. We thus obtain

$$V_+(\boldsymbol{R})\simeq\int_{-\Gamma}\frac{d\ell_j}{a^2}\epsilon_{ji}\left[\frac{\partial f(\boldsymbol{n}_u)}{\partial\partial_i\boldsymbol{n}}\cdot(\boldsymbol{\epsilon}_v\times\boldsymbol{n}_u)-\frac{\partial f(\hat{\boldsymbol{t}})}{\partial\partial_i\boldsymbol{n}}\cdot(\boldsymbol{\epsilon}_v^0\times\hat{\boldsymbol{t}})\right]. \tag{D.8}$$

Because $|\boldsymbol{R}|$ is so large, we can also expand $\boldsymbol{n}_u$ as $\boldsymbol{n}_u\simeq\hat{\boldsymbol{t}}+\delta\boldsymbol{n}_u$ on the boundary Γ to obtain

$$\frac{\partial f(\boldsymbol{n}_u)}{\partial\partial_i n_\alpha}\simeq\frac{\partial f(\hat{\boldsymbol{t}})}{\partial\partial_i n_\alpha}+\frac{\partial^2 f(\hat{\boldsymbol{t}})}{\partial(\partial_i n_\alpha)\partial n_\beta}\delta n_{u,\beta}+\frac{\partial^2 f(\hat{\boldsymbol{t}})}{\partial(\partial_i n_\alpha)\partial(\partial_j n_\beta)}\partial_j\delta n_{u,\beta}, \tag{D.9}$$

$$(\boldsymbol{\epsilon}_v\times\boldsymbol{n}_u)_\alpha\simeq\delta n_{v,\alpha}-(\delta\boldsymbol{n}_u\cdot\delta\boldsymbol{n}_v)\hat{t}_\alpha, \tag{D.10}$$

where Eq. (C.12) is used. By substituting the above equations into Eq. (D.8), we find

$$V_{+}(\boldsymbol{R}) \simeq \int_{\Gamma} \frac{d\ell_j}{a^2} \epsilon_{ji} \left[\frac{\partial f(\hat{\boldsymbol{t}})}{\partial \partial_i n_\alpha} (\delta \boldsymbol{n}_u \cdot \delta \boldsymbol{n}_v) t_\alpha - \frac{\partial^2 f(\hat{\boldsymbol{t}})}{\partial(\partial_i n_\alpha) \partial n_\beta} \delta n_{u,\beta} \delta n_{v,\alpha} - \frac{\partial^2 f(\hat{\boldsymbol{t}})}{\partial(\partial_i n_\alpha) \partial(\partial_k n_\beta)} (\partial_k \delta n_{u,\beta}) \delta n_{v,\alpha} \right]. \tag{D.11}$$

We note that the bi-linear terms of $\boldsymbol{\epsilon}_v$ and $\boldsymbol{\epsilon}_v^0$ ignored in Eq. (D.7) obtain the higher-order contributions of $\delta \boldsymbol{n}_{u,v}$ to $V_{+}(\boldsymbol{R})$, when $\boldsymbol{n}_{1\mathrm{sk}}$ rapidly converges to $\hat{\boldsymbol{t}}$. This is, for instance, the isotropic case under out-of-plane magnetic field, where $\delta \boldsymbol{n}_{1\mathrm{sk}}(\boldsymbol{r}) \propto e^{-\tilde{r}}/\sqrt{\tilde{r}}$ with $\tilde{r} = |\boldsymbol{r}|/\sqrt{B/Ja^2}$. To be more specific, the second-order terms' contributions to the second line of Eq. (D.7) are shown as

$$\begin{aligned} F_2 = \int_{D_+} \frac{d^2 r}{a^2} \Bigg\{ & \frac{\partial f(\boldsymbol{n}_u)}{\partial \boldsymbol{n}} \cdot \left[\frac{1}{2} \boldsymbol{\epsilon}_v \times (\boldsymbol{\epsilon}_v \times \boldsymbol{n}_u) \right] + \frac{\partial f(\boldsymbol{n}_u)}{\partial \partial_i \boldsymbol{n}} \cdot \partial_i \left[\frac{1}{2} \boldsymbol{\epsilon}_v \times (\boldsymbol{\epsilon}_v \times \boldsymbol{n}_u) \right] \\ & - \frac{\partial f(\hat{\boldsymbol{t}})}{\partial \boldsymbol{n}} \cdot \left[\frac{1}{2} \boldsymbol{\epsilon}_v^0 \times (\boldsymbol{\epsilon}_v^0 \times \hat{\boldsymbol{t}}) \right] - \frac{\partial f(\hat{\boldsymbol{t}})}{\partial \partial_i \boldsymbol{n}} \cdot \partial_i \left[\frac{1}{2} \boldsymbol{\epsilon}_v^0 \times (\boldsymbol{\epsilon}_v^0 \times \hat{\boldsymbol{t}}) \right] \\ & + \frac{\partial^2 f(\boldsymbol{n}_u)}{\partial n_\alpha \partial n_\beta} (\boldsymbol{\epsilon}_v \times \boldsymbol{n}_u)_\alpha (\boldsymbol{\epsilon}_v \times \boldsymbol{n}_u)_\beta - \frac{\partial^2 f(\hat{\boldsymbol{t}})}{\partial n_\alpha \partial n_\beta} (\boldsymbol{\epsilon}_v^0 \times \hat{\boldsymbol{t}})_\alpha (\boldsymbol{\epsilon}_v^0 \times \hat{\boldsymbol{t}})_\beta \\ & + 2 \frac{\partial^2 f(\boldsymbol{n}_u)}{\partial \partial_i n_\alpha \partial n_\beta} \left[\partial_i (\boldsymbol{\epsilon}_v \times \boldsymbol{n}_u)_\alpha \right] (\boldsymbol{\epsilon}_v \times \boldsymbol{n}_u)_\beta - 2 \frac{\partial^2 f(\hat{\boldsymbol{t}})}{\partial \partial_i n_\alpha \partial n_\beta} \left[\partial_i (\boldsymbol{\epsilon}_v^0 \times \hat{\boldsymbol{t}})_\alpha \right] (\boldsymbol{\epsilon}_v^0 \times \hat{\boldsymbol{t}})_\beta \\ & + \frac{\partial^2 f(\boldsymbol{n}_u)}{\partial \partial_i n_\alpha \partial \partial_j n_\beta} \left[\partial_i (\boldsymbol{\epsilon}_v \times \boldsymbol{n}_u)_\alpha \right] \left[\partial_j (\boldsymbol{\epsilon}_v \times \boldsymbol{n}_u)_\beta \right] - \frac{\partial^2 f(\hat{\boldsymbol{t}})}{\partial \partial_i n_\alpha \partial \partial_j n_\beta} \left[\partial_i (\boldsymbol{\epsilon}_v^0 \times \hat{\boldsymbol{t}})_\alpha \right] \left[\partial_j (\boldsymbol{\epsilon}_v^0 \times \hat{\boldsymbol{t}})_\beta \right] \Bigg\}. \end{aligned} \tag{D.12}$$

Using Eq. (D.3) and the Green's theorem, as the previous case, the first and the second lines becone line integrals along Γ, resulting in the third-order terms of $\delta \boldsymbol{n}$. On the other hand, the other lines cannot be rewritten as simple line integrals. When $\boldsymbol{\epsilon}_v$ and $\boldsymbol{\epsilon}_v^0$ rapidly vanish, however, the area integral of D_+ mostly comes from the boundary Γ, where $\boldsymbol{n}_u$ can be approximated as $\boldsymbol{n}_u \simeq \hat{\boldsymbol{t}} + \delta \boldsymbol{n}_u$. In this case, we can expand the derivatives of f in the vicinity of $\boldsymbol{n}_u \simeq \hat{\boldsymbol{t}}$ as in the case of Eq. (D.9), subtract each of the last three lines, obtain an additional component $\delta \boldsymbol{n}_u$. In this way, the contribution of F_2 to $V_{+}(\boldsymbol{R})$ is in the third-order of $\delta \boldsymbol{n}_{u,v}$ and hence can be ignored compared with the leading terms, Eq. (D.11).

Similarly, we obtain the approximation for $V_{-}(\boldsymbol{R})$, given by the right-hand side of Eq. (D.11) with $\Gamma \to -\Gamma$ and $\delta \boldsymbol{n}_u \leftrightarrow \delta \boldsymbol{n}_v$. To summarize, $V_{\mathrm{int}}(\boldsymbol{R})$ in Eq. (D.5) can be approximated by

$$V_{\mathrm{app}}(\boldsymbol{R}) = \int_{\Gamma} \frac{d\ell_j}{a^2} \epsilon_{ji} \left(A_{vu} - A_{uv} \right)_i , \tag{D.13}$$

$$(A_{uv})_i = \frac{\partial^2 f(\hat{\boldsymbol{t}})}{\partial n_\alpha \partial(\partial_i n_\beta)} \delta n_{u,\alpha} \delta n_{v,\beta} + \frac{\partial^2 f(\hat{\boldsymbol{t}})}{\partial(\partial_k n_\alpha) \partial(\partial_i n_\beta)} (\partial_k \delta n_{u,\alpha}) \delta n_{v,\beta}, \tag{D.14}$$

which are the same as Eqs. (5.26) and (5.20) with $u \to +$ and $v \to -$.

Acknowledgement

I'd take this opportunity to thank everyone who has supported me during my time as a student in laboratories. I would like to thank Prof. Eiji Saitoh and Dr. Yuki Shiomi for their research guidance on nonlinear spin waves as my undergraduate advisors. I would like to thank Prof. Gerrit E. W. Bauer for his research guidance on amorphous magnets as my official supervisor for my master's research. Dr. Joseph Barker gave me research guidance on amorphous magnetism and told me how to program as a practical supervisor for my master's research. Prof. Yuki Kawaguchi gave me research guidance on magnetic skyrmions as a practical supervisor for my doctoral research. Prof. Masaki Fujita kindly agreed to be official supervisor for my doctoral research after Prof. Bauer has retired. After the retirement of Prof. Bauer and the dismantling of the group in Tohoku university, I got the opportunity to spend my doctoral course at Nagoya University as a research student while affiliated in Tohoku university. I would like to express my gratitude to the administrative staff of both Tohoku university and Nagoya university for making the necessary arrangements. Also, I am so grateful to all the members of Tanaka-Kawaguchi group in Nagoya University for accepting me as a student. I would also like to thank the lab secretaries, Ms. Yumiko Sato, Ms. Mika Terada, Ms. Yuki Konno, and Ms. Kaoru Kimura. Their support for my business trips, etc. and their concern for my daily life were delightful. I would like to thank friends of mine who are the same grade in the laboratories: Mr. Ryuichi Ito, Mr. Akihiro Ozawa, Mr. Masaki Takagaki, Mr. Daisuke Oshima, and Mr. Daijiro Takagi. As for the fruitful discussions, especially during master and doctoral course, I deeply appreciate Prof. Kentaro Nomura, Dr. Yasufumi Araki, Dr. Koji Kobayashi, Dr. Koji Sato, Dr. Weichao Yu, Dr. Yuya Ominato, Dr. Alejandro O. Leon, Dr. Kazuya Fujimoto, Dr. Shun Tamura, Dr. Sho Nakosai, Dr. Terumichi Ohashi, Mr. Wichmann R. Jan Erik, Mr. Akihiro Ozawa, Mr. Masaki Takagaki, Mr. Naohiro Ito, Mr. Yuya Kurebayashi, Mr. Daichi Saito, Mr. Sehoon Kim, Mr. Takuma Sato, Mr. Jin Watanabe, Mr. Hiroki Arisawa. I would also like to thank GP-Spin program and GP-Spin's secretaries, Ms. Junko Hori, Ms. Yuho Tashiro, Ms. Yumi Takahashi, Ms. Eiko Uzuyama and Ms. Miki Shoji. GP-Spin has given me opportunities for long-term overseas training twice and presenting at international conferences several times. I would like to thank all the members in Stoner lab. in the University of Leeds for accepting me as a visiting student. GP-Spin also gave me good chances to meet wonderful colleagues outside of my department. I would like to thank friends of mine who are the same grade in GP-Spin: Mr. Naohiro Ito, Mr. Daichi Saito, Mr. Yuta Yahagi, and Mr. Shogo Yamashita. We encouraged and supported each other. I would also like to thank all of my family (fathers, mothers, brother, grandparents, and husband). Thank you so much for keeping supporting me through good times and bad times.

I am also grateful to all of the following people who have shared the laboratories. All the members of Saitoh group that I belonged to when I was a fourth-year undergraduate: Prof. Kenichi Uchida, Dr. Saburo Takahashi, Dr. Ryo Iguchi, Dr. Tomohiko Niizeki, Dr. Yasuyuki Oikawa, Dr. Naoto Yokoi, Dr. Yusuke Hashimoto, Dr. Kazuya Harii, Dr. Rafael Ramos, Dr. Yong Jun Seo, Dr. Takashi Kikkawa, Dr. Daichi Hirobe, Dr. Shunsuke Daimon, Dr. Jana Lustikova, Dr. Yagmur Ahmet, Dr. Koichi Oyanagi, Dr. Tomosato Hioki, Dr. Maki Umeda, Dr. Yao Chen, Mr. Tomoki Watamura, Mr. Rei Tsuboi. All the members of Bauer group I belonged to as a master's student and involved during the doctoral coarse: Dr. Ryota Nakai, Dr. Mehrdad Elyasi, Mr. Hikaru Hashimoto, Mr. Haruki Kimura. All the members of Tanaka-Kawaguchi group I belonged to as a doctoral student: Prof. Yukio Tanaka, Dr. Keiji Yada, Dr. Shu Suzuki, Dr. Satoshi Ikegaya, Mr. Ryoi Ohashi, Mr. Yuya Imaeda, Mr. Kazuhiro Kurisawa, Mr. Yuhi Takabatake, Mr. Naoki Terao, Mr. Souma Yoshida, Mr. Eslam Ahmed, Mr. Shoma Kobae, Mr. Fumiya Kondo, Mr. Yuya Hiramatsu, Mr. Yuto Mizuno, Mr. Yuki Mori, Mr. Yasunori Ueno, Mr. Yusuke Koyama, Mr. Takashi Sakamori, Mr. Toma Yoneya. Thesis reviewers: Prof. G. E. W. Bauer, Prof. Y. Hirayama, Prof. N. Shibata, Prof. Y. Kawaguchi, and Prof. M. Fujita. Once again, I deeply appreciate you all and I wish you all the best.

List of Publications and Presentations

Peer-reviewed papers

- S. Watanabe, D. Hirobe, Y. Shiomi, R. Iguchi, S. Daimon, M. Kameda, S. Takahashi, and E. Saitoh, “Generation of megahertz-band spin currents using nonlinear spin pumping“, Sci. Rep. 7, 4576 (2017).

- M. Kameda (corresponding author), D. Hirobe, S. Daimon, Y. Shiomi, S. Takahashi, and E. Saitoh, “Microscopic formulation of nonlinear spin current induced by spin pumping“, J. Magn. Magn. Mater. 476, 459 (2019).

- M. Kameda (corresponding author), R. Koyama, T. Nakajima, and Y. Kawaguchi, “Controllable inter-skyrmion attractive interactions and resulting skyrmion-lattice structures in two-dimensional chiral magnets with in-plane anisotropy“, Phys. Rev. B 104, 174446 (2021).

- M. Kameda, G. E. W. Bauer, and J. Barker, submitted (arXiv:2201.06986).

Presentations at Conferences

- M. Kameda, J. Barker, and G. E. W. Bauer, “Numerical Study of Magnetic Excitations in Amorphous Ferromagnets”, Spin Mechanics 6, Sendai, Japan (February, 2019), poster presentation.

- M. Kameda, J. Barker, and G. E. W. Bauer, “Numerical Study of Magnetic Excitations in Amorphous Ferromagnets”, 平成30年度新学術領域ナノスピン変換年次報告会, Sendai, Japan (March, 2019), poster presentation.

- M. Kameda, G. E. W. Bauer, and J. Barker, “Numerical Study of Magnetic Excitations in Amorphous Ferromagnets”, Tohoku-Lorraine Conference 2019, Nancy, France (September, 2019), oral presentation.

- 亀田麻衣, 廣部大地, 大門俊介, 塩見雄毅, 高橋三郎, 齊藤英治, “非線形磁化ダイナミクスによるスピンポンプ・スピン流の微視的定式化”, 日本物理学会秋季大会, Gifu, Japan, (September, 2019), oral presentation.

- M. Kameda, G. E. W. Bauer, and J. Barker, “Numerical Study of Magnetic Excitations in Amorphous Ferromagnets”, Summit of Materials Science: SMS 2019 and Global Institute for Materials Research Tohoku: GIMRT User Meeting 2019, Sendai, Japan, (November, 2019), poster presentation.

- M. Kameda, G. E. W. Bauer, and J. Barker, “Numerical Study of Magnetic Excitations in Amorphous Ferromagnets”, International Conference on Topological Materials Science 2019, Kyoto, Japan (December, 2019), poster presentation.

- 亀田麻衣, 川口由紀, “結晶磁気異方性により歪んだ磁気スキルミオンとその格子構造”, 日本物理学会秋季大会, Online (September, 2020), oral presentation.

- (Peer reviewed) M. Kameda, Y. Kawaguchi, “Attractive inter-skyrmion couplings induced by distorted skyrmions”, Trends in MAGnetism 2020, online (September, 2021), oral presentation.

- 亀田麻衣, 川口由紀, “異方的2次元カイラル磁性体における歪んだ磁気スキルミオン間の引力相互作用”, 日本物理学会秋季大会 Online (September, 2021), oral presentation.

- (Peer reviewed) M. Kameda, Y. Kawaguchi, “Attractive inter-skyrmion couplings induced by distorted skyrmions”, EP2DS-24/MSS-20, online (October, 2021), poster presentation.

- M. Kameda, G. E. W. Bauer, and J. Barker, “アモルファス強磁性体 Co_4P における磁気励起の理論”, 日本物理学会第77回年次大会, Okayama (March, 2022), oral presentation (to be presented).

Presentations at Symposiums and Workshops

- M. Kameda, S. Watanabe, D. Hirobe, Y. Shiomi, R. Iguchi, S. Daimon, S. Takahashi, and E. Saitoh, "Megahertz signal in spin pumping caused by nonlinear interacting magnons", York-Tohoku summer school 2017, York, United Kingdom (July, 2017), oral presentation.

- M. Kameda, J. Barker, and G. E. W. Bauer, "Numerical Study of Amorphous Magnetic Materials: CoP alloy", Prospect of Future Spintronics 2017, Sendai, Japan (October, 2017), poster presentation.

- M. Kameda, J. Barker, and G. E. W. Bauer, "Searching for magnetic excitations in amorphous magnets", Kick-off Symposium for World Leading Research Centers, Sendai, Japan (February, 2018), poster presentation.

- M. Kameda, J. Barker, and G. E. W. Bauer, "Numerical Study of Magnetic Excitations in Amorphous Ferromagnets", student-organizing joint seminar, Sendai, Japan (March, 2019), oral presentation.

- M. Kameda, G. E. W. Bauer, and J. Barker, "Numerical Study of Magnetic Excitations in Amorphous Ferromagnets", Core-to-Core workshop on New-Concept Spintronic Device, York, United Kingdom (June, 2019), poster presentation.

- M. Kameda, G. E. W. Bauer, J. Barker, "Magnetic Excitations in Amorphous Ferromagnet CoP alloy", The 4th Int'l Symposium for the CRC for Spintronics, online (February, 2021), poster presentation.

- (Invited) M. Kameda, Y. Kawaguchi, "Attractive inter-skyrmion couplings induced by distorted skyrmions", The 5th Symposium for The Core Research Clusters for Materials Science and Spintronics, online (October, 2021), oral presentation.

- M. Kameda, Y. Kawaguchi, "Attractive inter-skyrmion couplings induced by distorted skyrmions", The 5th Symposium for the Core Research Clusters for Materials Science and Spintronics, online (October, 2021), poster presentation.

Awards and others

- M. Kameda, 特別研究員 DC1, 日本学術振興会 (2019 年度-2021 年度).

- M. Kameda, G. E. W. Bauer, and J. Barker, Poster preview award, International Conference on Topological Materials Science 2019, Kyoto, Japan (December, 2019).

- M. Kameda and Y. Kawaguchi, 日本物理学会 領域 3 学生優秀発表賞, 日本物理学会 2021 年秋季大会, オンライン (2021 年 9 月).

- M. Kameda and Y Kawaguchi, Best poster award, The 5th Symposium for the Core Research Clusters for Materials Science and Spintronics, online (October, 2021).

References

[1] Yaroslav Tserkovnyak, Arne Brataas, Gerrit E. W. Bauer, and Bertrand I. Halperin. Nonlocal magnetization dynamics in ferromagnetic heterostructures. *Rev. Mod. Phys.*, Vol. 77, pp. 1375–1421, Dec 2005.

[2] Devin Wesenberg, Tao Liu, Davor Balzar, Mingzhong Wu, and Barry L. Zink. Long-distance spin transport in a disordered magnetic insulator. *Nat. Phys.*, Vol. 13, pp. 987–993, 7 2017.

[3] Héctor Ochoa, Ricardo Zarzuela, and Yaroslav Tserkovnyak. Spin hydrodynamics in amorphous magnets. *Phys. Rev. B*, Vol. 98, p. 054424, Aug 2018.

[4] Juan M. Gomez-Perez, Koichi Oyanagi, Reimei Yahiro, Rafael Ramos, Luis E. Hueso, Eiji Saitoh, and Fèlix Casanova. Absence of evidence of spin transport through amorphous $\mathrm{Y_3Fe_5O_{12}}$. *Appl. Phys. Lett.*, Vol. 116, p. 032401, 1 2020.

[5] Liupeng Yang, Yaoyu Gu, Lina Chen, Kaiyuan Zhou, Qingwei Fu, Wenqiang Wang, Liyuan Li, Chunjie Yan, Haotian Li, Like Liang, Zishuang Li, Yong Pu, Youwei Du, and Ronghua Liu. Absence of spin transport in amorphous YIG evidenced by nonlocal spin transport experiments. *Phys. Rev. B*, Vol. 104, p. 144415, 10 2021.

[6] R. Alben. Spin waves in a model for an amorphous ferromagnet. *AIP Conf. Proc.*, Vol. 29, pp. 136–140, Apr 1976.

[7] L.M. Roth and V.A. Singh. Comment on spin wave excitations in amorphous ferromagnets. *Phys. Lett. A*, Vol. 59, No. 1, pp. 49–51, 1976.

[8] Takahito Kaneyoshi. Spin Waves in Amorphous Ferromagnets. *J. Phys. Soc. Jpn.*, Vol. 45, No. 6, pp. 1835–1841, 1978.

[9] H. A. Mook, N. Wakabayashi, and D. Pan. Magnetic excitations in the amorphous ferromagnet $\mathrm{co_4}$p. *Phys. Rev. Lett.*, Vol. 34, pp. 1029–1033, Apr 1975.

[10] M. Kameda, D. Hirobe, S. Daimon, Y. Shiomi, S. Takahashi, and E. Saitoh. Microscopic formulation of nonlinear spin current induced by spin pumping. *J. Magn. Magn. Mater.*, Vol. 476, pp. 459 – 463, 2019.

[11] Joseph Barker and Gerrit E. W. Bauer. Semiquantum thermodynamics of complex ferrimagnets. *Phys. Rev. B*, Vol. 100, p. 140401, 10 2019.

[12] G. Shirane, J. D. Axe, C. F. Majkrzak, and T. Mizoguchi. Magnetic excitations in amorphous ferromagnets. *Phys. Rev. B*, Vol. 26, pp. 2575–2583, 9 1982.

[13] Naoto Nagaosa and Yoshinori Tokura. Topological properties and dynamics of magnetic skyrmions. *Nat. Nanotechnol.*, Vol. 8, pp. 899–911, 12 2013.

[14] Shi-Zeng Lin, Charles Reichhardt, Cristian D. Batista, and Avadh Saxena. Particle model for skyrmions in metallic chiral magnets: Dynamics, pinning, and creep. *Phys. Rev. B*, Vol. 87, p. 214419, Jun 2013.

[15] Shi-Zeng Lin and Avadh Saxena. Noncircular skyrmion and its anisotropic response in thin films of chiral magnets under a tilted magnetic field. *Phys. Rev. B*, Vol. 92, p. 180401(R), 2015.

[16] A O Leonov, T L Monchesky, J C Loudon, and A N Bogdanov. Three-dimensional chiral skyrmions with attractive interparticle interactions. *J. Phys.: Condens. Matter*, Vol. 28, No. 35, p. 35LT01, jul 2016.

[17] J. C. Loudon, A. O. Leonov, A. N. Bogdanov, M. Ciomaga Hatnean, and G. Balakrishnan. Direct observation of attractive skyrmions and skyrmion clusters in the cubic helimagnet $\mathrm{Cu_2OSeO_3}$. *Phys. Rev. B*, Vol. 97, p. 134403, Apr 2018.

[18] Haifeng Du, Xuebing Zhao, Filipp N. Rybakov, Aleksandr B. Borisov, Shasha Wang, Jin Tang, Chiming Jin, Chao Wang, Wensheng Wei, Nikolai S. Kiselev, Yuheng Zhang, Renchao Che, Stefan Blügel, and Mingliang Tian. Interaction of Individual Skyrmions in a Nanostructured Cubic Chiral Magnet. *Phys. Rev. Lett.*, Vol. 120, p. 197203, May 2018.

[19] J.F. Sadoc and J. Dixmier. Structural investigation of amorphous CoP and NiP alloys by combined X-ray and neutron scattering. *Mater. Sci. Eng.*, Vol. 23, pp. 187–192, 5 1976.

[20] M. Kameda, G. E. W. Bauer, and J. Barker. *submitted (arXiv:2201.06986).*

[21] M. Kameda, R. Koyama, T. Nakajima, and Y. Kawaguchi. Controllable interskyrmion attractive interactions and resulting skyrmion-lattice structures in two-dimensional chiral magnets with in-plane anisotropy. *Phys. Rev. B*, Vol. 104, p. 174446, 2021.

[22] Tomoki Nagase, Yeong-Gi So, Hayata Yasui, Takafumi Ishida, Hiroyuki K. Yoshida, Yukio Tanaka, Koh Saitoh, Nobuyuki Ikarashi, Yuki Kawaguchi, Makoto Kuwahara, and Masahiro Nagao. Observation of domain wall bimerons in chiral magnets. *Nat. Commun.*, Vol. 12, p. 3490, 6 2021.

[23] M. N. Baibich, J. M. Broto, A. Fert, F. Nguyen Van Dau, F. Petroff, P. Etienne, G. Creuzet, A. Friederich, and J. Chazelas. Giant magnetoresistance of (001)fe/(001)cr magnetic superlattices. *Phys. Rev. Lett.*, Vol. 61, pp. 2472–2475, Nov 1988.

[24] G. Binasch, P. Grünberg, F. Saurenbach, and W. Zinn. Enhanced magnetoresistance in layered magnetic structures with antiferromagnetic interlayer exchange. *Phys. Rev. B*, Vol. 39, pp. 4828–4830, Mar 1989.

[25] M. Julliere. Tunneling between ferromagnetic films. *Phys. Lett. A*, Vol. 54, No. 3, pp. 225–226, 1975.

[26] M. I. Dyakonov and V. I. Perel. Current-induced spin orientation of electrons in semiconductors. *Phys. Lett. A*, Vol. 35, No. 6, pp. 459–460, 1971.

[27] S. Murakami. Dissipationless Quantum Spin Current at Room Temperature. *Science*, Vol. 301, pp. 1348–1351, 9 2003.

[28] Jairo Sinova, Dimitrie Culcer, Q. Niu, N. A. Sinitsyn, T. Jungwirth, and A. H. MacDonald. Universal intrinsic spin hall effect. *Phys. Rev. Lett.*, Vol. 92, p. 126603, Mar 2004.

[29] E. Saitoh, M. Ueda, H. Miyajima, and G. Tatara. Conversion of spin current into charge current at room temperature: Inverse spin-Hall effect. *Appl. Phys. Lett.*, Vol. 88, p. 182509, 5 2006.

[30] S. O. Valenzuela and M. Tinkham. Direct electronic measurement of the spin Hall effect. *Nature*, Vol. 442, pp. 176–179, 7 2006.

[31] Akihito Takeuchi and Gen Tatara. Charge and spin currents generated by dynamical spins. *Journal of the Physical Society of Japan*, Vol. 77, No. 7, p. 074701, 2008.

[32] K. Ando, M. Morikawa, T. Trypiniotis, Y. Fujikawa, C. H. W. Barnes, and E. Saitoh. Photoinduced inverse spin-Hall effect: Conversion of light-polarization information into electric voltage. *Appl. Phys. Lett.*, Vol. 96, p. 082502, 2 2010.

[33] K. Uchida, S. Takahashi, K. Harii, J. Ieda, W. Koshibae, K. Ando, S. Maekawa, and E. Saitoh. Observation of the spin Seebeck effect. *Nature*, Vol. 455, pp. 778–781, 10 2008.

[34] Ken-ichi Uchida, Hiroto Adachi, Takeru Ota, Hiroyasu Nakayama, Sadamichi Maekawa, and Eiji Saitoh. Observation of longitudinal spin-Seebeck effect in magnetic insulators. *Appl. Phys. Lett.*, Vol. 97, p. 172505, 10 2010.

[35] Jiang Xiao, Gerrit E. W. Bauer, Ken-chi Uchida, Eiji Saitoh, and Sadamichi Maekawa. Theory of magnon-driven spin seebeck effect. *Phys. Rev. B*, Vol. 81, p. 214418, Jun 2010.

[36] C. M. Jaworski, J. Yang, S. Mack, D. D. Awschalom, J. P. Heremans, and R. C. Myers. Observation of the spin-Seebeck effect in a ferromagnetic semiconductor. *Nat. Mater.*, Vol. 9, pp. 898–903, 9 2010.

[37] C. M. Jaworski, J. Yang, S. Mack, D. D. Awschalom, R. C. Myers, and J. P. Heremans. Spin-seebeck effect: A phonon driven spin distribution. *Phys. Rev. Lett.*, Vol. 106, p. 186601, May 2011.

[38] Hiroto Adachi, Ken-ichi Uchida, Eiji Saitoh, Jun-ichiro Ohe, Saburo Takahashi, and Sadamichi Maekawa. Gigantic enhancement of spin Seebeck effect by phonon drag. *Appl. Phys. Lett.*, Vol. 97, p. 252506, 12 2010.

[39] Hiroto Adachi, Jun-ichiro Ohe, Saburo Takahashi, and Sadamichi Maekawa. Linear-response theory of spin seebeck effect in ferromagnetic insulators. *Phys. Rev. B*, Vol. 83, p. 094410, Mar 2011.

[40] T. Kikkawa, K. Uchida, Y. Shiomi, Z. Qiu, D. Hou, D. Tian, H. Nakayama, X.-F. Jin, and E. Saitoh. Longitudinal spin seebeck effect free from the proximity nernst effect. *Phys. Rev. Lett.*, Vol. 110, p.

067207, Feb 2013.

[41] J. Flipse, F. K. Dejene, D. Wagenaar, G. E. W. Bauer, J. Ben Youssef, and B. J. van Wees. Observation of the spin peltier effect for magnetic insulators. *Phys. Rev. Lett.*, Vol. 113, p. 027601, Jul 2014.

[42] Shunsuke Daimon, Ryo Iguchi, Tomosato Hioki, Eiji Saitoh, and Ken-ichi Uchida. Thermal imaging of spin Peltier effect. *Nat. Commun.*, Vol. 7, p. 13754, 12 2016.

[43] S. Mizukami, Y. Ando, and T. Miyazaki. Ferromagnetic resonance linewidth for $\mathrm{NM80NiFe/NM}$ films $(\mathrm{NM = Cu,\ Ta,\ Pd\ and\ Pt})$. *J. Magn. Magn. Mater.*, Vol. 226-230, pp. 1640 – 1642, 2001. Proceedings of the International Conference on Magnetism (ICM 2000).

[44] Yaroslav Tserkovnyak, Arne Brataas, and Gerrit E. W. Bauer. Spin pumping and magnetization dynamics in metallic multilayers. *Phys. Rev. B*, Vol. 66, p. 224403, Dec 2002.

[45] Th. Gerrits, M. L. Schneider, and T. J. Silva. Enhanced ferromagnetic damping in Permalloy/ Cu bilayers. *J. Appl. Phys.*, Vol. 99, p. 023901, 1 2006.

[46] S. I. Kiselev, J. C. Sankey, I. N. Krivorotov, N. C. Emley, R. J. Schoelkopf, R. A. Buhrman, and D. C. Ralph. Microwave oscillations of a nanomagnet driven by a spin-polarized current. *Nature*, Vol. 425, pp. 380–383, 9 2003.

[47] Y. Ji, C. L. Chien, and M. D. Stiles. Current-induced spin-wave excitations in a single ferromagnetic layer. *Phys. Rev. Lett.*, Vol. 90, p. 106601, Mar 2003.

[48] K. Ando, S. Takahashi, K. Harii, K. Sasage, J. Ieda, S. Maekawa, and E. Saitoh. Electric manipulation of spin relaxation using the spin hall effect. *Phys. Rev. Lett.*, Vol. 101, p. 036601, Jul 2008.

[49] Y. Kajiwara, K. Harii, S. Takahashi, J. Ohe, K. Uchida, M. Mizuguchi, H. Umezawa, H. Kawai, K. Ando, K. Takanashi, S. Maekawa, and E. Saitoh. Transmission of electrical signals by spin-wave interconversion in a magnetic insulator. *Nature*, Vol. 464, pp. 262–266, 2010.

[50] A. A. Thiele. Steady-state motion of magnetic domains. *Phys. Rev. Lett.*, Vol. 30, pp. 230–233, Feb 1973.

[51] Stuart S. P. Parkin, Masamitsu Hayashi, and Luc Thomas. Magnetic Domain-Wall Racetrack Memory. *Science*, Vol. 320, pp. 190–194, 4 2008.

[52] F. Jonietz, S. Muhlbauer, C. Pfleiderer, A. Neubauer, W. Munzer, A. Bauer, T. Adams, R. Georgii, P. Boni, R. A. Duine, K. Everschor, M. Garst, and A. Rosch. Spin Transfer Torques in MnSi at Ultralow Current Densities. *Science*, Vol. 330, pp. 1648–1651, 12 2010.

[53] T. Schulz, R. Ritz, A. Bauer, M. Halder, M. Wagner, C. Franz, C. Pfleiderer, K. Everschor, M. Garst, and A. Rosch. Emergent electrodynamics of skyrmions in a chiral magnet. *Nat. Phys.*, Vol. 8, pp. 301–304, 2 2012.

[54] X.Z. Yu, N. Kanazawa, W.Z. Zhang, T. Nagai, T. Hara, K. Kimoto, Y. Matsui, Y. Onose, and Y. Tokura.

Skyrmion flow near room temperature in an ultralow current density. *Nat. Commun.*, Vol. 3, p. 988, 8 2012.

[55] J. Iwasaki, M. Mochizuki, and N. Nagaosa. Universal current-velocity relation of skyrmion motion in chiral magnets. *Nat. Commun.*, Vol. 4, p. 1463, 2013.

[56] L. J. Cornelissen, J. Liu, J. B. Youssef R. A. Duine, and B. J. van Wees. Long-distance transport of magnon spin information in a magnetic insulator at room temperature. *Nat. Phys.*, Vol. 11, pp. 1022–1026, 2015.

[57] Sai Li, Wang Kang, Xichao Zhang, Tianxiao Nie, Yan Zhou, Kang L. Wang, and Weisheng Zhao. Magnetic skyrmions for unconventional computing. *Mater. Horiz.*, Vol. 8, No. 3, p. 854, 2021.

[58] S. Mühlbauer, B. Binz, F. Jonietz, C. Pfleiderer, A. Rosch, A. Neubauer, R. Georgii, and P. Böni. Skyrmion Lattice in a Chiral Magnet. *Science*, Vol. 323, No. 5916, pp. 915–919, 2009.

[59] Jung Hoon Han. *Skyrmions in Condensed Matter*. Springer International Publishing, 2017.

[60] I. Dzyaloshinsky. A thermodynamic theory of “weak” ferromagnetism of antiferromagnetics. *J. Phys. Chem. Solids*, Vol. 4, No. 4, pp. 241–255, 1958.

[61] Tôru Moriya. Anisotropic Superexchange Interaction and Weak Ferromagnetism. *Phys. Rev.*, Vol. 120, pp. 91–98, Oct 1960.

[62] C Thessieu, C Pfleiderer, A N Stepanov, and J Flouquet. Field dependence of the magnetic quantum phase transition in MnSi. *J. Phys.: Condens. Matter*, Vol. 9, No. 31, pp. 6677–6687, aug 1997.

[63] X. Z. Yu, Y. Onose, N. Kanazawa, J. H. Park, J. H. Han, Y. Matsui, N. Nagaosa, and Y. Tokura. Real-space observation of a two-dimensional skyrmion crystal. *Nature*, Vol. 465, pp. 901–904, 6 2010.

[64] Wanjun Jiang, Xichao Zhang, Guoqiang Yu, Wei Zhang, Xiao Wang, M. Benjamin Jungfleisch, John E. Pearson, Xuemei Cheng, Olle Heinonen, Kang L. Wang, Yan Zhou, Axel Hoffmann, and Suzanne G. E. te Velthuis. Direct observation of the skyrmion Hall effect. *Nat. Phys.*, Vol. 13, pp. 162–169, 9 2016.

[65] Kai Litzius, Ivan Lemesh, Benjamin Krüger, Pedram Bassirian, Lucas Caretta, Kornel Richter, Felix Büttner, Koji Sato, Oleg A. Tretiakov, Johannes Förster, Robert M. Reeve, Markus Weigand, Iuliia Bykova, Hermann Stoll, Gisela Schütz, Geoffrey S. D. Beach, and Mathias Kläui. Skyrmion Hall effect revealed by direct time-resolved X-ray microscopy. *Nat. Phys.*, Vol. 13, pp. 170–175, 12 2016.

[66] H. Kurebayashi, O. Dzyapko, V. E. Demidov, D. Fang, A. J. Ferguson, and S. O. Demokritov. Controlled enhancement of spin-current emission by three-magnon splitting. *Nat. Mater.*, Vol. 10, p. 660, 2011.

[67] H. Sakimura, T. Tashiro, and K. Ando. Nonlinear spin-current enhancement enabled by spin-damping tuning. *Nat. Commun.*, Vol. 5, No. 5730, 2014.

[68] S. Watanabe, D. Hirobe, Y. Shiomi, R. Iguchi, S. Daimon, M. Kameda, S. Takahashi, and E. Saitoh. Generation of megahertz-band spin currents using nonlinear spin pumping. *Sci. Rep.*, Vol. 7, No. 4576,

pp. 2045–2322, 2017.

[69] L. Landau and E. Lifshits. ON THE THEORY OF THE DISPERSION OF MAGNETIC PERMEABILITY IN FERROMAGNETIC BODIES. *Phys. Zeitsch. der Sow.*, Vol. 8, pp. 153–169, 1935.

[70] Thomas L. Gilbert. A Phenomenological Theory of Damping in Ferromagnetic Materials. *IEEE Trans. Magn.*, Vol. 40, No. 6, 2004.

[71] B L Gyorffy, A J Pindor, J Staunton, G M Stocks, and H Winter. A first-principles theory of ferromagnetic phase transitions in metals. *Journal of Physics F: Metal Physics*, Vol. 15, No. 6, p. 1337, 1985.

[72] B. Skubic, J Hellsvik, L Nordström, and L Eriksson. A method for atomistic spin dynamics simulations: implementation and examples. *J. Phys.: Condens. Matter*, Vol. 20, No. 31, pp. 315–203, 2008.

[73] C. H. Woo, Haohua Wen, A. A. Semenov, S. L. Dudarev, and Pui-Wai Ma. Quantum heat bath for spin-lattice dynamics. *Phys. Rev. B*, Vol. 91, p. 104306, Mar 2015.

[74] Koji Hukushima and Koji Nemoto. Exchange Monte Carlo Method and Application to Spin Glass Simulations. *J. Phys. Soc. Jpn.*, Vol. 65, No. 6, pp. 1604–1608, 1996.

[75] R. C. O'Handley. Physics of ferromagnetic amorphous alloys. *J. Appl. Phys.*, Vol. 62, pp. R15–R49, 11 1987.

[76] T. Kaneyoshi. *Amorphous Magnetism*. CRC-Press, 1984.

[77] T. Kaneyoshi. *Introduction to Amorphous Magnets*. World Scientific Publishing, 1992.

[78] J. Barker, U. Atxitia, T. A. Ostler, O. Hovorka, O. Chubykalo-Fesenko, and R. W. Chantrell. Two-magnon bound state causes ultrafast thermally induced magnetisation switching. *Sci. Rep.*, Vol. 3, p. 3262, 11 2013.

[79] T. Kaneyoshi. Contribution to the Spin-Wave Theory of a Dilute Heisenberg Ferromagnet. *Prog. Theor. Phys.*, Vol. 42, No. 3, p. 477, 1969.

[80] T Kaneyoshi and R Honmura. Spin wave theory of amorphous ferromagnets. *J. Phys. C, Solid State Phys.*, Vol. 5, No. 7, pp. L65–L69, apr 1972.

[81] C.F. Kittel. *Introduction to Solid State Physics*. Wiley, New York, 1953.

[82] R. M. White. *Quantum Theory of Magnetism*. New York: McGraw-Hill, Inc, 1970.

[83] R. W. Cochrane and G. S. Cargill. Magnetization of AmorphousCoP Alloy—Spin Waves in Noncrystalline Ferromagnets. *Phys. Rev. Lett.*, Vol. 32, pp. 476–478, 3 1974.

[84] G. S. Cargill. Dense random packing of hard spheres as a structural model for noncrystalline metallic solids. *J. Appl. Phys.*, Vol. 41, p. 2248, 1970.

[85] J. L. Finney. Random packings and the structure of simple liquids. i. the geometry of random close packing. *Proc. Math. Phys. Eng. Sci.*, Vol. 319, No. 1539, pp. 479–493, 1970.

[86] Laura M. Roth. Analysis of effective-medium approximation for a tight-binding model of a liquid metal. *Phys. Rev. B*, Vol. 11, pp. 3769–3779, May 1975.

[87] G. David Scott. Radial Distribution of the Random Close Packing of Equal Spheres. *Nature*, Vol. 194, pp. 956–957, 6 1962.

[88] D. G. Henshaw. Pressure effect in the atomic distribution in liquid helium by neutron diffraction. *Phys. Rev.*, Vol. 119, pp. 14–21, Jul 1960.

[89] R. L. McGreevy and L. Pusztai. Reverse monte carlo simulation: A new technique for the determination of disordered structures. *Mol. Simul.*, Vol. 1, No. 6, pp. 359–367, 1988.

[90] O. Gereben, P. Jóvári, L. Temleitner, and L. Pusztai. A new version of the rmc++ reverse monte carlo programme, aimed at investigating the structure of covalent glasses. *J. Optoelectron. Adv. Mater.*, Vol. 9, No. 1, pp. 3021–3027, 2007.

[91] P. H. Gaskell. On the structure of simple inorganic amorphous solids. *J. Phys. C, Solid State Phys.*, Vol. 12, No. 21, p. 4337, 1979.

[92] M. Kruzík and A. Prohl. Recent developments in the modeling, analysis, and numerics of ferromagnetism. *SIAM Review*, Vol. 48, No. 3, pp. 439–483, 2006.

[93] A. Altland and B. Simons. *Condensed Maatter Field Theory*. Cambridge University Press, 2010.

[94] W. Marshall and S. W. Lovesey. *Theory of Thermal Neutron Scattering*. Oxford University Press, 1971.

[95] E. Price, editor. *International Tables for Crystallography Vol. C*, chapter 4.4, pp. 430–487. International Union of Crystallography, 2006.

[96] J Durand and M F Lapierre. NMR of co59in amorphous CoP alloys. *Journal of Physics F: Metal Physics*, Vol. 6, No. 6, pp. 1185–1192, jun 1976.

[97] Naohiro Ito, Takashi Kikkawa, Joseph Barker, Daichi Hirobe, Yuki Shiomi, and Eiji Saitoh. Spin Seebeck effect in the layered ferromagnetic insulators $\mathrm{CrSiTe_3}$ and $\mathrm{CrGeTe_3}$. *Phys. Rev. B*, Vol. 100, p. 060402, 8 2019.

[98] Joseph Barker, Dimitar Pashov, and Jerome Jackson. Electronic structure and finite temperature magnetism of yttrium iron garnet. *Electron. Struct.*, Vol. 2, p. 044002, 12 2020.

[99] M A Continentino and N Rivier. On the apparent spin wave stiffness of amorphous ferromagnets. *J. Phys. F: Met. Phys.*, Vol. 9, pp. L145–L150, 8 1979.

[100] Levente Rózsa, András Deák, Eszter Simon, Rocio Yanes, László Udvardi, László Szunyogh, and Ulrich Nowak. Skyrmions with Attractive Interactions in an Ultrathin Magnetic Film. *Phys. Rev. Lett.*, Vol. 117, p. 157205, Oct 2016.

[101] Y. Tokunaga, X. Z. Yu, J. S. White, H. M. Rønnow, D. Morikawa, Y. Taguchi, and Y. Tokura. A new class of chiral materials hosting magnetic skyrmions beyond room temperature. *Nat. Commun.*, Vol. 6,

p. 7638, 7 2015.

[102] X. Z. Yu, W. Koshibae, Y. Tokunaga, K. Shibata, Y. Taguchi, N. Nagaosa, and Y. Tokura. Transformation between meron and skyrmion topological spin textures in a chiral magnet. *Nature*, Vol. 564, pp. 95–98, 12 2018.

[103] T. Nagase, M. Komatsu, Y. G. So, T. Ishida, H. Yoshida, Y. Kawaguchi, Y. Tanaka, K. Saitoh, N. Ikarashi, M. Kuwahara, and M. Nagao. Smectic Liquid-Crystalline Structure of Skyrmions in Chiral Magnet $\mathrm{Co}_{8.5}\mathrm{Zn}_{7.5}\mathrm{Mn}_4$(110) Thin Film. *Phys. Rev. Lett.*, Vol. 123, p. 137203, 2019.

[104] T.H.R. Skyrme. A unified field theory of mesons and baryons. *Nucl. Phys.*, Vol. 31, pp. 556–569, 1962.

[105] I. Kézsmárki, S. Bordács, P. Milde, E. Neuber, L. M. Eng, J. S. White, H. M. Ronnow, C. D. Dewhurst, M. Mochizuki, K. Yanai, H. Nakamura, D. Ehlers, V. Tsurkan, and A. Loidl. Néel-type skyrmion lattice with confined orientation in the polar magnetic semiconductor $\mathrm{GaV_4S_8}$. *Nat. Mater.*, Vol. 14, No. 11, pp. 1116–1122, 2015.

[106] S. Bordács, A. Butykai, B. G. Szigeti, J. S. White, R. Cubitt, A. O. Leonov, S. Widmann, D. Ehlers, H.-A. Krug von Nidda, V. Tsurkan, A. Loidl, and I. Kézsmárki. Equilibrium Skyrmion Lattice Ground State in a Polar Easy-plane Magnet. *Sci. Rep.*, Vol. 7, No. 1, p. 7584, 2017.

[107] S. Seki, X. Z. Yu, S. Ishiwata, and Y. Tokura. Observation of Skyrmions in a Multiferroic Material. *Science*, Vol. 336, pp. 198–201, 4 2012.

[108] S. Seki, S. Ishiwata, and Y. Tokura. Magnetoelectric nature of skyrmions in a chiral magnetic insulator $\mathrm{Cu_2OSeO_3}$. *Phys. Rev. B*, Vol. 86, p. 060403(R), Aug 2012.

[109] T. Adams, A. Chacon, M. Wagner, A. Bauer, G. Brandl, B. Pedersen, H. Berger, P. Lemmens, and C. Pfleiderer. Long-Wavelength Helimagnetic Order and Skyrmion Lattice Phase in $\mathrm{Cu_2OSeO_3}$. *Phys. Rev. Lett.*, Vol. 108, p. 237204, Jun 2012.

[110] Masahito Mochizuki and Yoshio Watanabe. Writing a skyrmion on multiferroic materials. *Appl. Phys. Lett.*, Vol. 107, No. 8, p. 082409, Aug 2015.

[111] Masahito Mochizuki and Shinichiro Seki. Dynamical magnetoelectric phenomena of multiferroic skyrmions. *J. Phys.: Condens. Matter*, Vol. 27, No. 50, p. 503001, dec 2015.

[112] Eugen Ruff, Sebastian Widmann, Peter Lunkenheimer, Vladimir Tsurkan, Sandor Bordács, Istvan Kézsmárki, and Alois Loidl. Multiferroicity and skyrmions carrying electric polarization in $\mathrm{GaV_4S_8}$. *Sci. Adv.*, Vol. 1, No. 10, p. e1500916, 2015.

[113] Stefan Heinze, Kirsten von Bergmann, Matthias Menzel, Jens Brede, André Kubetzka, Roland Wiesendanger, Gustav Bihlmayer, and Stefan Blügel. Spontaneous atomic-scale magnetic skyrmion lattice in two dimensions. *Nat. Phys.*, Vol. 7, pp. 713–718, 7 2011.

[114] Niklas Romming, Christian Hanneken, Matthias Menzel, Jessica E. Bickel, Boris Wolter, Kirsten

von Bergmann, André Kubetzka, and Roland Wiesendanger. Writing and Deleting Single Magnetic Skyrmions. *Science*, Vol. 341, pp. 636–639, 8 2013.

[115] Niklas Romming, André Kubetzka, Christian Hanneken, Kirsten von Bergmann, and Roland Wiesendanger. Field-Dependent Size and Shape of Single Magnetic Skyrmions. *Phys. Rev. Lett.*, Vol. 114, p. 177203, May 2015.

[116] Christian Hanneken, Fabian Otte, André Kubetzka, Bertrand Dupé, Niklas Romming, Kirsten von Bergmann, Roland Wiesendanger, and Stefan Heinze. Electrical detection of magnetic skyrmions by tunnelling non-collinear magnetoresistance. *Nat. Nanotechnol.*, Vol. 10, No. 12, pp. 1039–1042, 2015.

[117] Pin-Jui Hsu, André Kubetzka, Aurore Finco, Niklas Romming, Kirsten von Bergmann, and Roland Wiesendanger. Electric-field-driven switching of individual magnetic skyrmions. *Nat. Nanotechnol.*, Vol. 12, No. 2, pp. 123–126, 2017.

[118] Seonghoon Woo, Kai Litzius, Benjamin Krüger, Mi-Young Im, Lucas Caretta, Kornel Richter, Maxwell Mann, Andrea Krone, Robert M. Reeve, Markus Weigand, Parnika Agrawal, Ivan Lemesh, Mohamad-Assaad Mawass, Peter Fischer, Mathias Kläui, and Geoffrey S. D. Beach. Observation of room-temperature magnetic skyrmions and their current-driven dynamics in ultrathin metallic ferromagnets. *Nat. Mater.*, Vol. 15, No. 5, pp. 501–506, 2016.

[119] Olivier Boulle, Jan Vogel, Hongxin Yang, Stefania Pizzini, Dayane de Souza Chaves, Andrea Locatelli, Tevfik Onur Menteş, Alessandro Sala, Liliana D. Buda-Prejbeanu, Olivier Klein, Mohamed Belmeguenai, Yves Roussigné, Andrey Stashkevich, Salim Mourad Chérif, Lucia Aballe, Michael Foerster, Mairbek Chshiev, Stéphane Auffret, Ioan Mihai Miron, and Gilles Gaudin. Room-temperature chiral magnetic skyrmions in ultrathin magnetic nanostructures. *Nat. Nanotechnol.*, Vol. 11, No. 5, pp. 449–454, 2016.

[120] Wanjun Jiang, Wei Zhang, Guoqiang Yu, M. Benjamin Jungfleisch, Pramey Upadhyaya, Hamoud Somaily, John E. Pearson, Yaroslav Tserkovnyak, Kang L. Wang, Olle Heinonen, Suzanne G. E. te Velthuis, and Axel Hoffmann. Mobile Néel skyrmions at room temperature: status and future. *AIP Adv.*, Vol. 6, No. 5, p. 055602, 2016.

[121] Takashi Kurumaji, Taro Nakajima, Max Hirschberger, Akiko Kikkawa, Yuichi Yamasaki, Hajime Sagayama, Hironori Nakao, Yasujiro Taguchi, Taka-hisa Arima, and Yoshinori Tokura. Skyrmion lattice with a giant topological Hall effect in a frustrated triangular-lattice magnet. *Science*, Vol. 365, pp. 914–918, 8 2019.

[122] Nguyen Duy Khanh, Taro Nakajima, Xiuzhen Yu, Shang Gao, Kiyou Shibata, Max Hirschberger, Yuichi Yamasaki, Hajime Sagayama, Hironori Nakao, Licong Peng, Kiyomi Nakajima, Rina Takagi, Taka-hisa Arima, Yoshinori Tokura, and Shinichiro Seki. Nanometric square skyrmion lattice in a

centrosymmetric tetragonal magnet. *Nat. Nanotechnol.*, Vol. 15, pp. 444–449, 5 2020.

[123] Tsuyoshi Okubo, Sungki Chung, and Hikaru Kawamura. Multiple-q States and the Skyrmion Lattice of the Triangular-Lattice Heisenberg Antiferromagnet under Magnetic Fields. *Phys. Rev. Lett.*, Vol. 108, p. 017206, Jan 2012.

[124] Ajaya K. Nayak, Vivek Kumar, Tianping Ma, Peter Werner, Eckhard Pippel, Roshnee Sahoo, Franoise Damay, Ulrich K. Rößler, Claudia Felser, and Stuart S. P. Parkin. Magnetic antiskyrmions above room temperature in tetragonal Heusler materials. *Nature*, Vol. 548, No. 7669, pp. 561–566, 2017.

[125] Licong Peng, Rina Takagi, Wataru Koshibae, Kiyou Shibata, Kiyomi Nakajima, Taka-hisa Arima, Naoto Nagaosa, Shinichiro Seki, Xiuzhen Yu, and Yoshinori Tokura. Controlled transformation of skyrmions and antiskyrmions in a non-centrosymmetric magnet. *Nat. Nanotechnol.*, Vol. 15, pp. 181–186, 1 2020.

[126] Xuebing Zhao, Chiming Jin, Chao Wang, Haifeng Du, Jiadong Zang, Mingliang Tian, Renchao Che, and Yuheng Zhang. Direct imaging of magnetic field-driven transitions of skyrmion cluster states in FeGe nanodisks. *Proc. Natl. Acad. Sci.*, Vol. 113, No. 18, pp. 4918–4923, 2016.

[127] K. Karube, J. S. White, N. Reynolds, J. L. Gavilano, H. Oike, A. Kikkawa, F. Kagawa, Y. Tokunaga, H. M. Rønnow, Y. Tokura, and Y. Taguchi. Robust metastable skyrmions and their triangular–square lattice structural transition in a high-temperature chiral magnet. *Nat. Mater.*, Vol. 15, pp. 1237–1242, 9 2016.

[128] Kosuke Karube, Jonathan S. White, Daisuke Morikawa, Charles D. Dewhurst, Robert Cubitt, Akiko Kikkawa, Xiuzhen Yu, Yusuke Tokunaga, Taka-hisa Arima, Henrik M. Rønnow, Yoshinori Tokura, and Yasujiro Taguchi. Disordered skyrmion phase stabilized by magnetic frustration in a chiral magnet. *Sci. Adv.*, Vol. 4, p. eaar7043, 9 2018.

[129] K. Karube, J. S. White, V. Ukleev, C. D. Dewhurst, R. Cubitt, A. Kikkawa, Y. Tokunaga, H. M. Rønnow, Y. Tokura, and Y. Taguchi. Metastable skyrmion lattices governed by magnetic disorder and anisotropy in β-Mn-type chiral magnets. *Phys. Rev. B*, Vol. 102, p. 064408, Aug 2020.

[130] K. Karube, J. S. White, D. Morikawa, M. Bartkowiak, A. Kikkawa, Y. Tokunaga, T. Arima, H. M. Rønnow, Y. Tokura, and Y. Taguchi. Skyrmion formation in a bulk chiral magnet at zero magnetic field and above room temperature. *Phys. Rev. Materials*, Vol. 1, p. 074405, Dec 2017.

[131] X. Z. Yu, N. Kanazawa, Y. Onose, K. Kimoto, W. Z. Zhang, S. Ishiwata, Y. Matsui, and Y. Tokura. Near room-temperature formation of a skyrmion crystal in thin-films of the helimagnet FeGe. *Nat. Mater.*, Vol. 10, No. 2, pp. 106–109, 2011.

[132] Akira Tonomura, Xiuzhen Yu, Keiichi Yanagisawa, Tsuyoshi Matsuda, Yoshinori Onose, Naoya Kanazawa, Hyun Soon Park, and Yoshinori Tokura. Real-Space Observation of Skyrmion Lattice in Helimagnet MnSi Thin Samples. *Nano Lett.*, Vol. 12, pp. 1673–1677, 2 2012.

[133] A. O. Leonov, Y. Togawa, T. L. Monchesky, A. N. Bogdanov, J. Kishine, Y. Kousaka, M. Miyagawa, T. Koyama, J. Akimitsu, Ts. Koyama, K. Harada, S. Mori, D. McGrouther, R. Lamb, M. Krajnak, S. McVitie, R. L. Stamps, and K. Inoue. Chiral Surface Twists and Skyrmion Stability in Nanolayers of Cubic Helimagnets. *Phys. Rev. Lett.*, Vol. 117, p. 087202, Aug 2016.

[134] S. D. Yi, S. Onoda, N. Nagaosa, and J. H. Han. Skyrmions and anomalous Hall effect in a Dzyaloshinskii-Moriya spiral magnet. *Phys. Rev. B*, Vol. 80, p. 054416, 2009.

[135] B. M. A. G. Piette, B. J. Schroers, and W. J. Zakrzewski. Multisolitons in a two-dimensional Skyrme model. *Z. Phys. C: Part. Fields*, Vol. 65, No. 1, pp. 165–174, 1995.

[136] H. Wilhelm, M. Baenitz, M. Schmidt, U. K. Rößler, A. A. Leonov, and A. N. Bogdanov. Precursor Phenomena at the Magnetic Ordering of the Cubic Helimagnet FeGe. *Phys. Rev. Lett.*, Vol. 107, p. 127203, Sep 2011.

[137] Shi-Zeng Lin and Satoru Hayami. Ginzburg-landau theory for skyrmions in inversion-symmetric magnets with competing interactions. *Phys. Rev. B*, Vol. 93, p. 064430, Feb 2016.

[138] A. O. Leonov and I. Kézsmárki. Asymmetric isolated skyrmions in polar magnets with easy-plane anisotropy. *Phys. Rev. B*, Vol. 96, p. 014423, Jul 2017.

[139] X. Z. Yu, Y. Tokunaga, Y. Kaneko, W. Z. Zhang, K. Kimoto, Y. Matsui, Y. Taguchi, and Y. Tokura. Biskyrmion states and their current-driven motion in a layered manganite. *Nat. Commun.*, Vol. 5, No. 1, p. 3198, 2014.

[140] Wenhong Wang, Ying Zhang, Guizhou Xu, Licong Peng, Bei Ding, Yue Wang, Zhipeng Hou, Xiaoming Zhang, Xiyang Li, Enke Liu, Shouguo Wang, Jianwang Cai, Fangwei Wang, Jianqi Li, Fengxia Hu, Guangheng Wu, Baogen Shen, and Xi-Xiang Zhang. A Centrosymmetric Hexagonal Magnet with Superstable Biskyrmion Magnetic Nanodomains in a Wide Temperature Range of 100–340 K. *Adv. Mater.*, Vol. 28, No. 32, pp. 6887–6893, 2016.

[141] Börge Göbel, Jürgen Henk, and Ingrid Mertig. Forming individual magnetic biskyrmions by merging two skyrmions in a centrosymmetric nanodisk. *Sci. Rep.*, Vol. 9, No. 1, p. 9521, 2019.

[142] D. Capic, D. A. Garanin, and E. M. Chudnovsky. Biskyrmion lattices in centrosymmetric magnetic films. *Phys. Rev. Research*, Vol. 1, p. 033011, Oct 2019.

[143] David Foster, Charles Kind, Paul J. Ackerman, Jung-Shen B. Tai, Mark R. Dennis, and Ivan I. Smalyukh. Two-dimensional skyrmion bags in liquid crystals and ferromagnets. *Nat. Phys.*, Vol. 15, No. 7, pp. 655–659, 2019.

[144] D. Capic, D. A . Garanin, and E. M. Chudnovsky. Skyrmion–skyrmion interaction in a magnetic film. *J. Phys.: Condens. Matter*, Vol. 32, No. 41, p. 415803, jul 2020.

[145] P Bak and M H Jensen. Theory of helical magnetic structures and phase transitions in MnSi and FeGe.

J. Phys. C, Solid State Phys., Vol. 13, No. 31, pp. L881–L885, nov 1980.

[146] Yuki Kawaguchi, Yukio Tanaka, and Naoto Nagaosa. Skyrmionic magnetization configurations at chiral magnet/ferromagnet heterostructures. *Phys. Rev. B*, Vol. 93, p. 064416, Feb 2016.

[147] N. Gao, S. G. Je, M. Y. Im, J. W. Choi, M. Yang, Q. Li, T. Y. Wang, S. Lee, H. S. Han, K. S. Lee, W. Chao, C. Hwang, J. Li, and Z. Q. Qiu. Creation and annihilation of topological meron pairs in in-plane magnetized films. *Nat. Commun.*, Vol. 10, p. 5603, 12 2019.

[148] S. L. Zhang, A. Bauer, H. Berger, C. Pfleiderer, G. van der Laan, and T. Hesjedal. Imaging and manipulation of skyrmion lattice domains in Cu_2OSeO_3. *Appl. Phys. Lett.*, Vol. 109, No. 19, p. 192406, 2016.

[149] I. Stasinopoulos, S. Weichselbaumer, A. Bauer, J. Waizner, H. Berger, S. Maendl, M. Garst, C. Pfleiderer, and D. Grundler. Low spin wave damping in the insulating chiral magnet Cu_2OSeO_3. *Appl. Phys. Lett.*, Vol. 111, No. 3, p. 032408, 2017.

[150] Kazuaki Shimizu, Hiroshi Maruyama, Hitoshi Yamazaki, and Hideki Watanabe. Thermal Expansion in Weak Itinerant Ferromagnets $Fe_xCo_{1-x}Si$ (x =0.48 and 0.77). *J. Phys. Soc. Jpn.*, Vol. 58, No. 6, pp. 1914–1917, 1989.

[151] Nicholas A. Porter, Priyasmita Sinha, Michael B. Ward, Alexey N. Dobrynin, Rik M. D. Brydson, Timothy R. Charlton, Christian J. Kinane, Michael D. Robertson, Sean Langridge, and Christopher H. Marrows. Giant topological Hall effect in strained $Fe_{0.7}Co_{0.3}Si$ epilayers. *arXiv*, p. 1312.1722, 2013.

[152] Alexander Mook, Börge Göbel, Jürgen Henk, and Ingrid Mertig. Magnon transport in noncollinear spin textures: Anisotropies and topological magnon hall effects. *Phys. Rev. B*, Vol. 95, p. 020401, Jan 2017.

[153] Xichao Zhang, Yan Zhou, and Motohiko Ezawa. Magnetic bilayer-skyrmions without skyrmion Hall effect. *Nat. Commun.*, Vol. 7, p. 10293, 1 2016.

[154] Sebastián A. Díaz, Tomoki Hirosawa, Daniel Loss, and Christina Psaroudaki. Spin Wave Radiation by a Topological Charge Dipole. *Nano Lett.*, Vol. 20, pp. 6556–6562, 8 2020.

[155] Christina Psaroudaki and Christos Panagopoulos. Skyrmion Qubits: A New Class of Quantum Logic Elements Based on Nanoscale Magnetization. *Phys. Rev. Lett.*, Vol. 127, p. 067201, Aug 2021.